

Design and Fabrication of Precision Carbon Nanotube-Based Flexural Transducers

by

Michael A. Cullinan

S.M. Mechanical Engineering
Massachusetts Institute of Technology, 2008

B.S. Engineering
B.A. Economics
Swarthmore College, 2006

Submitted to the Department of Mechanical Engineering
in Partial Fulfillment of the Requirements for the Degree of

Doctor of Philosophy in Mechanical Engineering

at the

Massachusetts Institute of Technology

February 2011

© 2011 Massachusetts Institute of Technology
All rights reserved.

Signature of Author.....
Department of Mechanical Engineering
January 20, 2011

Certified by.....
Martin L. Culpepper
Associate Professor of Mechanical Engineering
Thesis Supervisor

Accepted by.....
David E. Hardt
Professor of Mechanical Engineering
Graduate Officer

Design and Fabrication of Precision Carbon Nanotube-Based Flexural Transducers

by

Michael A. Cullinan

Submitted to the Department of Mechanical Engineering
on January 20, 2011 in Partial Fulfillment of the
Requirements for the Degree of
Doctor of Philosophy in Mechanical Engineering

ABSTRACT

As mechanical devices move towards the nanoscale, smaller and more sensitive force and displacement sensors need to be developed. Currently, many biological, materials science, and nanomanufacturing applications could benefit from multi-axis micro- and nanoscale sensors with fine force and displacement resolutions. Unfortunately, such systems do not yet exist due to the limitations of traditional sensing techniques and fabrication procedures. Carbon nanotube-based (CNT) piezoresistive transducers offer the potential to overcome many of these limitations. Previous research has shown the potential for the use of CNTs in high resolution micro- and nanoscale sensing devices due to the high gauge factor and inherent size of CNTs. However, a better understanding of CNT-based piezoresistive sensors is needed in order to be able to design and engineer CNT-based sensor systems to take advantage of this potential.

The purpose of this thesis is to take CNT-based strain sensors from the single element test structures that have been fabricated and turn them into precision sensor systems that can be used in micro- and nanoscale force and displacement transducers. In order to achieve this purpose and engineer high resolution CNT-based sensor systems, the design and manufacturing methods used to create CNT-based piezoresistive sensors were investigated. At the system level, a noise model was developed in order to be able to optimize the design of the sensor system. At the element level, a link was established between the structure of the CNT and its gauge factor using a theoretical model developed from quantum mechanics. This model was confirmed experimentally using CNT-based piezoresistive sensors integrated into a microfabricated test structure. At the device level, noise mitigation techniques including annealing and the use of a protective ceramic coating were investigated in order to reduce the noise in the sensor. From these investigations, best practices for the design and manufacturing of CNT-based piezoresistive sensors were established. Using these best practices, it is possible to increase the performance of CNT-based piezoresistive sensor systems by more than three orders of magnitude.

These best practices were implemented in the design and fabrication of a multi-axis force sensor used to measure the adhesion force of an array of cells to the different material's surfaces for the development of biomedical implants. This force sensor is capable of measuring forces in the z-axis as well as torques in the θ_x and θ_y axis. The range and resolution of the force sensor were determined to be 84 μN and 5.6 nN, respectively. This corresponds to a dynamic range of 83 dB, which closely matches the dynamic range predicted by the system noise model used to design the sensor. The accuracy of the force sensor is better than 1% over the device's full range.

Thesis Supervisor: Martin L. Culpepper
Title: Associate Professor of Mechanical Engineering

ACKNOWLEDGEMENTS

I would like to thank my advisor Professor Martin Culpepper for providing valuable help in selecting and performing the research for this project. Without him none of this work would have been possible. Also, I would like to thank my committee members Professor Carol Livermore and Professor Michael Strano for providing valuable feedback on various aspects of the project throughout the research process. I would especially like to thank Paul Barone and Andrew Hilmer from Professor Strano's group for providing me with purified samples of (6,5) CNTs for some of the testing performed in this thesis.

I would also like to thank my fellow members of the Precision Compliant Systems Laboratory at MIT for help and advice throughout this project. I would especially like to thank Christopher DiBiasio for his help when I was starting this project and Robert Panas for working with me on the noise modeling and electronics designs presented in Chapter 2 of this thesis. In addition I would like to thank the LMP students in room 35-135 for providing a collegial atmosphere and discussing various research problems with me.

I would also like to thank the various technicians and staff members who made this project possible. First, I would like to thank Richard Brickman and David Rodriguera for providing the administrative support for this project. Also, I would like to thank Pat McAtamney and Bill Buckley for helping me with machining various parts in the machine shop. In addition, I would like to thank Dave Terry, Dennis Ward, Kurt Broderick, and Bernard Alamariu for help with the design and microfabrication of the MEMS test structures and force sensors. Finally, I would like to thank Shiahn Chen and Yong Zhang from the MIT Center for Materials Science and Engineering for their help with the electron microscopy equipment.

CONTENTS

Abstract	3
Acknowledgements.....	5
Contents.....	7
Figures	13
Tables.....	19
Chapter 1	21
1.1 Introduction	21
1.1.1 Outline of Thesis	24
1.2 CNT Background.....	25
1.3 Scaling Sensors Down to the Nanoscale.....	28
1.3.1 Introduction.....	28
1.3.2 Need for NEMS and Nanoscale Sensors	28
1.3.3 Scaling MEMS Sensors Down to the Nanoscale	30
1.3.3.1 Capacitance Sensors	30
1.3.3.2 Piezoresistive Sensors.....	32
1.3.3.3 Hall Effect Sensors	33
1.3.3.4 Piezoelectric Sensors	34
1.3.3.5 Inductance Sensors	35
1.3.3.6 Interferometry	35
1.3.3.7 Comparison	37
1.3.4 Novel Sensors for the Nanoscale	38
1.3.4.1 CNT-Based Piezoresistors	39
Review of CNT-Based Piezoresistive Sensors.....	39
Scaling of CNT-Based Piezoresistors.....	41
1.3.4.2 Resonance Sensors	44
Introduction to Resonance Sensors.....	44

Resonance-based Mass Sensors	45
Resonance Based Strain Sensors	46
1.3.4.3 Tunneling Sensors	48
1.3.5 Sensor Selection for Case Study	49
1.4 Prior Art	50
1.4.1 CNT Assembly.....	50
1.4.1.1 Grow-in-Place	50
1.4.1.2 Pick-and-Place.....	51
1.4.1.3 Dielectrophoresis.....	52
1.4.1.4 Transfer Printing	53
1.4.2 Sorting of CNTs.....	53
1.4.3 Multi-Axis MEMS Force Sensors.....	54
1.5 Scope.....	55
1.5.1 Technical Approach	55
1.5.2 Case Study: 3-Axis Force Sensor with CNT-Based Piezoresistors	58
Chapter 2.....	61
2.1 Introduction	61
2.2 Background	61
2.3 DC Piezoresistive Sensor System Model.....	63
2.3.1 System Layout and Model.....	63
2.3.2 Flexure Model.....	65
2.3.3 Wheatstone Bridge Model.....	66
2.3.4 Instrumentation Amplifier Model	67
2.3.5 Source Voltage Model.....	68
2.3.6 Bias Voltage Model.....	68
2.3.7 Power Supply Model.....	69
2.3.8 Digital Model.....	69
2.3.9 Dominant Noise Sources and System Characteristics	70
2.3.10 Performance Metrics	71
2.4 Insights from the Model.....	72
2.4.1 Electronic Sources.....	72

2.4.2	Mechanical Sources	73
2.4.3	Thermal Sources	73
2.5	Johnson and Flicker Noise	73
2.6	Experimental Measurements and Model Verification.....	74
2.7	Piezoresistive Sensor Design and Optimization.....	76
2.7.1	Reduced Piezoresistive Sensor System Model.....	76
2.7.2	Optimization Process.....	78
2.7.3	Analytical Optimization	80
2.8	Computational Optimization.....	83
2.9	Conclusion.....	86
Chapter 3	87
3.1	Introduction	87
3.2	Prior Art	88
3.3	Theoretical Model.....	89
3.3.1	Background on Tight-Binding Model.....	89
3.3.2	CNT Gauge Factor Model.....	93
3.4	Model Evaluation	97
3.5	Design of a Device that Uses Many CNTs in Parallel.....	100
Chapter 4	105
4.1	Test Setup.....	105
4.2	Fabrication of CNT Test Structures.....	107
4.3	Results for Multiple Chirality Experiments	108
4.4	Results for Single Chirality Experiments	109
4.4.1	Predicted Results.....	109
4.4.2	CNT Enrichment	110
4.4.3	Measured Gauge Factor of Enriched (6,5) CNT Sample	112
4.4.4	Monte-Carlo Simulation for Enriched (6,5) CNT Sample	113
4.4.5	Electrical Breakdown of CNTs in Sensor	115
4.4.6	Results for Electrical Breakdown Experiments	116
4.5	Discussion	119

Chapter 5	121
5.1 Sources of Performance Limitations	121
5.1.1 Flicker Noise.....	121
5.1.2 Contact Resistance	123
5.2 Noise Measurement	124
5.3 Noise Mitigation Techniques and Results	126
5.3.1 Increasing Number of CNTs.....	126
5.3.2 Coating CNTs	127
5.3.3 Annealing CNTs	129
5.4 Methods to Reduce Contact Resistance	131
5.4.1 Effect of Electrode Material	131
5.4.2 Platinum Coating.....	131
5.4.3 Annealing.....	132
5.5 Conclusions about Best Practices	133
5.5.1 Design and Manufacturing	133
5.5.2 Materials Selection.....	133
5.6 Comparison to Conventional MEMS Piezoresistors	133
Chapter 6	137
6.1 3-Axis Force Sensor	137
6.1.1 Introduction.....	137
6.1.2 Need and Description	138
6.1.3 Design of a Three-Axis Force Sensor	139
6.1.3.1 Functional Requirements	139
6.1.3.2 Polysilicon Piezoresistor Force Sensor Design.....	140
6.1.3.3 CNT-Based Piezoresistive Force Sensor Design	141
6.1.3.4 HexFlex Motion Stage.....	143
6.1.3.5 System Dynamics	147
6.1.4 Fabrication.....	148
6.2 Testing.....	153
6.2.1 Setup.....	153
6.2.2 Calibration Procedure.....	155

6.3	Calibration Results	156
6.4	Results.....	157
6.4.1	Range.....	157
6.4.2	Resolution.....	158
6.5	Possible Improvements	158
6.5.1	Recommended Changes in Design and Manufacturing	158
6.5.2	Estimates of Future Device Performance	159
Chapter 7	161
7.1	Summary	161
7.2	Best Practices for Design and Manufacturing.....	162
7.3	Use in Non-photolithographic MEMS.....	164
7.3.1	Introduction.....	164
7.3.2	Test Structure Design.....	165
7.3.3	Fabrication.....	166
7.3.4	Results	169
7.3.4.1	Metal Trace Deposition	169
7.3.4.2	Gap Fabrication with Tungsten Wire	169
7.3.4.3	Gap Fabrication with FIB & CNT Deposition.....	171
7.3.5	Test Structure Performance	172
7.3.6	Conclusions and Future Work for Non-photolithographic MEMS	174
7.4	Possible Future Applications.....	174
7.4.1	Heated Center Stage Tests.....	174
7.4.2	Self Sensing Nanoscale Bearings.....	176
References	179
Appendix A	199
A.1	Variable Definitions.....	199
Appendix B	203
B.1	Mask 1 – Polysilicon Piezoresistor.....	203
B.2	Mask 2 – Aluminum Bond Pads.....	204
B.3	Mask 3 – Frontside DRIE	206

B.4 Mask 4 – Backside DRIE.....208

FIGURES

Figure 1.1: (a) CNT-based linear motion stage (b) CNT-based tunable resonator.....	24
Figure 1.2: Chiral vector definition on a graphene sheet [9].....	25
Figure 1.3: Zig-zag (a) and armchair (b) carbon nanotube chiralities [11].....	27
Figure 1.4: (a) comb drive and (b) parallel plate capacitive sensors.	31
Figure 1.5: Piezoresistive displacement sensor.	32
Figure 1.6: Large range Michelson-type heterodyne interferometer for 6-DOF position measurement [42].....	36
Figure 1.7: Comparison of sensor dynamic ranges versus size for MEMS sensing.....	38
Figure 1.8. (a) CNT film strain gauge [65] (b) Single suspended CNT displacement sensor [66] (c) Pressure sensor with CNT piezoresistors [66]	40
Figure 1.9: Sensor dynamic ranges versus size for piezoresistive various sensing materials.	44
Figure 1.10: CNT-Based Resonating Strain Sensor.....	47
Figure 1.11: Natural Frequency vs. Strain for CNT Resonator.....	48
Figure 1.12: Sensor Comparison for Case Study.....	50
Figure 1.13: Experimental test structure.	56
Figure 1.14: Flowchart of technical approach.	58
Figure 1.15: (a) Polysilicon piezoresistor based force sensor (b) Force sensor/HexFlex assembly	59
Figure 2.1. Schematic layout of DC piezoresistive sensor system.	63
Figure 2.2. Block diagram layout of full system model.....	64
Figure 2.3. Block diagram representation of signal domain with main signal propagation path highlighted in bold	64
Figure 2.4. Block diagram representation of flexure domain with main signal propagation path highlighted in bold	65
Figure 2.5. Block diagram representation of flexure domain with main signal propagation path highlighted in bold.	66

Figure 2.6. Block diagram representation of the amplifier domain with main signal propagation path highlighted in bold.....	67
Figure 2.7. Block diagram representation of the source voltage domain with main signal propagation path highlighted in bold.	68
Figure 2.8. Block diagram representation of the bias voltage domain with main signal propagation path highlighted in bold.	68
Figure 2.9. Block diagram representation of the power supply domain with main signal propagation path highlighted in bold.	69
Figure 2.10. Block diagram representation of the digital domain with main signal propagation path highlighted in bold.....	69
Figure 2.11. Spectral distribution of signal and relevant noise.	71
Figure 2.12. Polysilicon piezoresistive sensor noise spectrum compared to predictions.	74
Figure 2.13. Measurement of noise spectral densities with and without thermal shielding.....	75
Figure 2.14. Optimization process for maximizing sensor system performance.....	78
Figure 2.15. Comparison of PR sensor materials given conditions described in the example case.	79
Figure 2.16. Dynamic range vs. resistance plot for amplifier and Johnson noise co-dominated system where metal film piezoresistors are used.....	81
Figure 2.17. Operating surface of constraint based optimization. Constraints are mapped to this surface.	84
Figure 2.18. Dynamic range vs. resistance plot for flicker noise dominated system where polysilicon piezoresistors are used.....	85
Figure 3.1. Band structure of graphene.	91
Figure 3.2. Γ -K axis projection.	92
Figure 3.3. Γ -M axis projection.	93
Figure 3.4: (a) CNT chiral vectors (b) Graphene first Brillouin zone with allowed electronic states.....	94
Figure 3.5. Gauge factor vs. strain for CNTs with diameters of 1.38 nm.....	98
Figure 3.6. Resistance vs. strain for CNTs with diameters of 1.38 nm.....	99
Figure 3.7. MEMS multi-axis force sensor with CNT-based strain sensors.	101

Figure 3.8. Resistance vs. strain for a 100 CNT resistor network, with segregated contributions from metallic and semiconducting CNTs.....	102
Figure 3.9. Gauge Factor vs. strain for a 100 CNT resistor network consisting of metallic, semiconducting or all CNTs.	103
Figure 4.1. CNT parallel resistor network between two electrodes on the test structure.....	105
Figure 4.2. CNT resistor network between two electrodes on the test structure.	106
Figure 4.3. Measured change in resistance vs. strain for CNT resistor networks.	108
Figure 4.4. Predicted $\Delta R/R$ vs. Strain for (6,5) CNT.	109
Figure 4.5. Enrichment of (6,5) CNT sample.	110
Figure 4.6. UV-vis-nIR absorption spectrum for (6,5) enriched CNT Sample.	111
Figure 4.7. Measured $\Delta R/R$ vs. Strain for enriched (6,5) CNT sample.	112
Figure 4.8. $\Delta R/R$ vs. Strain predicted from Monte-Carlo simulations of enriched (6,5) CNT sample.....	113
Figure 4.9. Measured results from enriched (6,5) CNT sample overlaid on theoretical prediction from Monte-Carlo simulations with 0.2% strain offset.....	114
Figure 4.10. Measured results from low-strain electrical breakdown of enriched (6,5) CNT sample overlaid on theoretical prediction from Monte-Carlo simulations with 0.2% strain offset.	117
Figure 4.11. Measured results from high-strain electrical breakdown of enriched (6,5) CNT sample overlaid on theoretical prediction from Monte-Carlo simulations with 0.2% strain offset.	118
Figure 5.1. Experimental setup consisting of (1) a Wheatstone bridge, (2) a precision bridge circuit with a precision voltage reference and instrumentation amplifier, (3) a DC power supply and (4) an analog-to-digital converter.....	125
Figure 5.2. Test Structure with SWCNTs connected between the two central electrodes.....	126
Figure 5.3. Power spectral densities of CNT-based piezoresistive sensors with dielectrophoresis deposition times of 5 and 10 minutes.....	127
Figure 5.4. Power spectral densities of as deposited, Al_3O_2 and annealed CNT-based piezoresistive sensors.	128
Figure 5.5. Power spectral densities of CNR-based sensor annealed at 525 °C.....	130
Figure 5.6. I-V Curve for CNT-based sensor showing ohmic contact.....	132

Figure 5.7. Performance of various piezoresistive materials.....	134
Figure 6.1. Exploded view of Hexflex-force sensor assembly.....	139
Figure 6.2. 3-axis force sensor with polysilicon piezoresistors.....	141
Figure 6.3. 3-axis force sensor with CNT-based piezoresistors.....	142
Figure 6.4. HexFlex with polysilicon piezoresistive sensors.....	143
Figure 6.5. (clockwise from top) Al 1100 HexFlex being machined in the micromill, Al 1100 HexFlex, Al 6061-T6 HexFlex.....	145
Figure 6.6. Hardware setup for micromilling HexFlex nanopositioners.....	146
Figure 6.7. First resonant mode of force sensor.....	147
Figure 6.8. First resonant mode of Hexflex - force sensor assembly.....	148
Figure 6.9. Fabricated 3-axis force sensor with CNT-based piezoresistors.....	153
Figure 6.10. Force sensor stiffness testing setup with top and side view.....	154
Figure 6.11. Force sensor calibration setup.....	155
Figure 6.12. Calibration curve for each CNT-based sensor on the force sensor.....	157
Figure 7.1. Test Structure Schematic (Units in Inches).....	166
Figure 7.2. Shadow Mask with Tungsten Wire.....	167
Figure 7.3. Test Structure with Metal Trace.....	168
Figure 7.4. Flaking of Pd wire on Aluminum Beam.....	169
Figure 7.5. Trace fabricated with tungsten wire on the top of shadow mask.....	170
Figure 7.6. Trace fabricated with tungsten wire on the bottom of shadow mask.....	170
Figure 7.7. Test structure with gap cut with FIB.....	171
Figure 7.8. CNTs deposited on test structure.....	172
Figure 7.9. Results for FIB Cut and Tungsten Wire Gaps.....	173
Figure 7.10. Force Sensor assembly with heated central stage.....	175
Figure 7.11. Force Sensor assembly with heated central stage.....	175
Figure 7.12. Nanoscale linear motion bearing with CNT-based flexures/sensors.....	176
Figure 7.13. Deformation of CNT in linear motion bearing.....	177
Figure B.1. Mask 1 defining polysilicon piezoresistors.....	203
Figure B.2. Blowup of alignment mark in mask 1.....	204
Figure B.3. Mask 2 defining aluminum bond pads and electrodes.....	205
Figure B.4. Electrode pattern for CNT-based force sensor in mask 2.....	206

Figure B.5. Mask 3 defining frontside photoresist pattern.	207
Figure B.6. Frontside alignment mark in mask 3.....	208
Figure B.7. Mask 4 defining backside photoresist pattern.	209
Figure B.8. Backside alignment mark in mask 3.	210

TABLES

Table 1.1: Bearing functional requirements.	37
Table 2.1: Common forms of flexure gain, ϵ_F	65
Table 4.1: Estimated chiral distribution of enriched sample from absorption spectrum.	111
Table 4.2: Resistance normalized to (6,5) CNT resistance for CNTs in enriched CNT sample at various strain levels.	116
Table 5.1: Measured noise and dynamic range for CNT-based sensors produced under various processing conditions.	129
Table 5.2: Measured noise as a function of annealing time and temperature.	130
Table 6.1: Force Sensor Functional Requirements.	140
Table 6.2: CNT-Based Force Sensor Design.....	143
Table 6.3: Process parameters for HexFlex machining.....	146
Table 6.4: Processing steps for force sensor fabrication.....	150
Table 6.5: Results for each piezoresistor in the force sensor.	158
Table 7.1: Comparison of Potential performance of Microfabricated and Machined Hexflex Designs.	174
Table A.1: Nomenclature for System Design Section	199

INTRODUCTION AND BACKGROUND

1.1 Introduction

As mechanical devices move towards the nano-scale, smaller and more sensitive force and displacement sensors become necessary. Currently, many biological, materials science, and nano-manufacturing applications could benefit from multi-axis micro- and nano-scale sensors with fine displacement resolution (nanometers) and/or force resolution (piconewtons). Unfortunately, because of the limitations of traditional sensing techniques and fabrication procedures, such sensing systems do not yet exist.

Traditional sensing techniques become increasingly impractical at the micro/nano-scale due to scaling constraints. For example, the resolution of capacitance sensors scales with sensor area, making high resolution sensors too large for many micro/nano-scale sensor systems. Similarly, interferometry becomes impractical at the micro/nano-scale because of the relatively large optics required. High resolution silicon-based piezoresistive sensing techniques work well for meso-scale devices, but become increasingly hard to fabricate in micro/nano-scale devices due to the constraints of photolithography and ion implantation.

Carbon nanotube-based (CNT) piezoresistive transducers offer the potential to overcome the limitations of traditional sensing systems in high resolution micro- and nano-scale sensing systems. CNTs have been shown to have piezoresistive gauge factors in excess of 2900 [1], which is about an order or magnitude larger than silicon-based piezoresistors. Nanoscale fabrication of CNT-based transducers is also not limited by the same fabrication difficulties as other sensors, since CNTs are inherently nanoscale materials. These properties make CNTs ideal sensors for fine resolution micro/nano-scale flexural transducers.

Previous research has shown the potential for the use of CNTs in high resolution sensing devices. However, much more work needs to be done in order to be able to design and engineer CNT-based sensor systems to take advantage of this potential. The purpose of this research is to take CNT-based strain sensors from the single element test structures that have been fabricated, and develop them into high precision sensor systems that can be used in micro- and nano-scale force and displacement transducers. Several steps are necessary to be able to engineer such CNT-based high resolution sensor systems:

1. A clear link between the CNT's structure and its strain sensitivity must be established.
2. The mechanical and electrical interactions between the substrate/electrodes and CNTs must be tested and modeled in order to optimize the strain sensitivity of the CNT-based sensor system.
3. Noise models based on experimental data for the CNTs and CNT-based sensors must be developed in order to optimize the device design and CNT system-level integration.
4. The effects of temperature on the resistance and gauge factor of the CNT sensors must be characterized to enable the design of a bridge circuit that can compensate for these temperature effects.

The ability to engineer CNT-based strain sensors is necessary in order to design integrated microelectromechanical systems (MEMS) and nanoelectromechanical systems (NEMS) devices that have large range and fine resolution. The ratio of range to resolution is important because it sets the fundamental limits of device performance. Flexure-based devices with integrated strain sensors can be designed to achieve a specific range or resolution by changing the device stiffness. However, these devices cannot be designed to achieve a range and a resolution requirement simultaneously. This is because there is a tradeoff between range and resolution based on sensor sensitivity and the yield strain of the flexure material. In order to increase the dynamic range of the MEMS/NEMS device it is necessary to either increase the sensitivity of the sensor or increase the yield strain of the flexure material. These requirements make CNT-based sensors ideal for high dynamic range devices due to their large failure strain (>25% [2]) and high gauge factor. The large failure strain allows the CNTs to be subject to large displacements before failure. This means that the flexure itself, and not the CNT, will be the

range- limiting element in CNT-based sensor systems. This is in contrast with other sensing techniques such as capacitance or tunneling where the sensor is the range-limiting element. Also, if it becomes possible to design and engineer CNT-based sensor systems, CNT-based strain sensors are capable of achieving at least an order of magnitude better resolution than silicon-based sensors due to their higher gauge factor.

CNT-based strain sensors may be useful in many fields including biology, nanomanufacturing, aerospace, and nano-scale electromechanical systems. One possible medical application, for example, involves measuring how well bone cells adhere to newly developed medical implants in order to choose the best implant materials, surface coatings and surface textures for the implant, and to estimate how the strength of the joint will develop over time. At present, the state-of-the-art in this field is for researchers to visually observe the behavior of the cells and to infer from certain visual cues, such as the shape of the cell on the surface, the quality of the cell-surface bonding [3]. There are no instruments that can measure the adhesion force between an array of cells and the surface. This type of instrument would require piconewton resolution, micronewton range, and the ability to operate in an aqueous environment. These requirements eliminate conventional sensing techniques such as capacitance, tunneling, and interferometry. Similarly, silicon-based strain sensors would not be able to meet the range and resolution requirements for this application simultaneously, since the best silicon-based strain sensors are typically limited to dynamic ranges of less than 80 dB at 1 kHz [4]. A properly engineered CNT-based sensing system, however, should be able to achieve all of the requirements of this device. The case study explored in this research is the design and manufacturing of a force sensor to meet the requirements of this type of application.

Other conventional MEMS devices could also be improved markedly by incorporating CNT-based strain sensors. For example, MEMS-based nanopositioners for nanomanufacturing such as the HexFlex [5] could improve their range and/or resolution by using CNT-based strain sensors. This would result in improved quality and higher throughput of products manufactured using such positioners. CNT-based strain sensors could be incorporated with AFM cantilevers to achieve atomic scale resolutions without the need for expensive optics or time consuming laser adjustments [6]. In addition, CNT-based AFM cantilevers could be used to reduce the cost and improve the rate of AFM-based nanomanufacturing techniques such as dip-pen lithography [7].

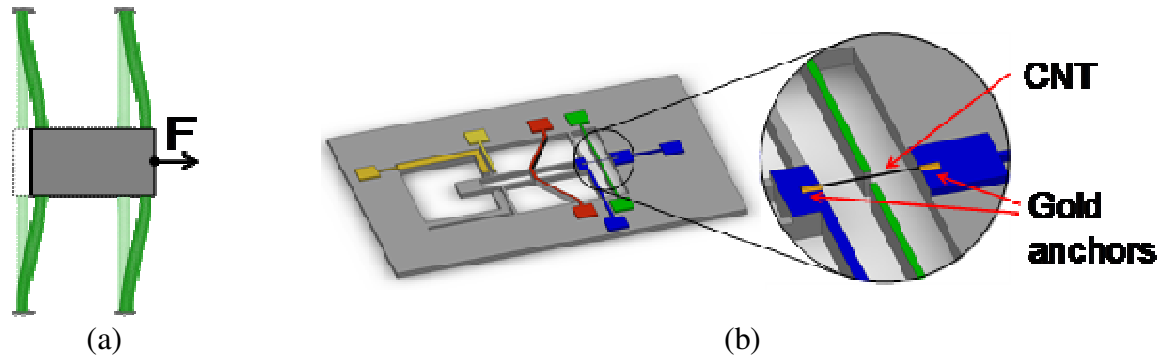


Figure 1.1: (a) CNT-based linear motion stage (b) CNT-based tunable resonator

CNT-based strain sensors will become important in NEMS devices that are too small for conventional sensing systems. For example, the NEMS device in Figure 1.1a is a linear motion stage that incorporates CNTs as the flexural bearings [8]. These bearings could be used to sense the strain in the device, thereby turning the linear motion stage in to a nano-scale force sensor or positioner. The resonator in Figure 1.1b uses a CNT as the resonating element. A set of thermal actuators is used to stretch the CNT, which causes a shift in the CNT's resonant frequency, allowing the resonator to be tuned to a specific frequency. In addition to being used as a resonator, the CNT could also be used as a strain sensor to measure its own pretension as well as its vibration amplitude and frequency. This would help ensure that the resonator was operating correctly without the need for additional electronics and sensors that would increase the cost and size of the device.

1.1.1 Outline of Thesis

This thesis focuses on the development of CNT-based piezoresistive strain sensors for micro- and nanoscale force and displacement measurements. Chapter 1 introduces this topic, provides background on CNT properties, manufacturing methods and mechanical sensors, and discusses why CNT-based piezoresistive sensors were chosen for this project. Chapter 2 goes over the system-level design of a piezoresistive sensor, and discusses the major noise sources in the system and the optimization of the piezoresistor design. Chapter 3 focuses on the theory of CNT-based piezoresistors and presents a quantum mechanical model which can be used to predict the behavior of the CNTs based on their chiral indices. Chapter 4 presents the experimental setup and gauge factor measurements for both random chirality and single chirality CNT-based piezoresistive sensors. These gauge factor measurements are used to verify the

theoretical models presented in Chapter 3. Chapter 5 discusses manufacturing techniques that can be used to reduce the amount of noise in the CNT-based piezoresistive sensors. Chapter 6 presents the design, fabrication, and results from the 3-axis force sensor case study. Finally, the conclusions and possible future research directions of this work are discussed in Chapter 7.

1.2 CNT Background

CNTs are carbon molecules that are a member of the fullerene structural carbon family. They may be thought of as rolled up sheets of graphene. Graphene is a single planar sheet of carbon atoms whose lattice consists of carbon atoms arranged in a hexagonal structure. This hexagonal structure means that each carbon atom is bonded aromatically to its neighboring atoms via sp^2 hybridized bonds with a bond length of 0.142 nm. The C-C sp^2 bond configuration is one of the strongest found in nature, which gives CNTs excellent mechanical properties.

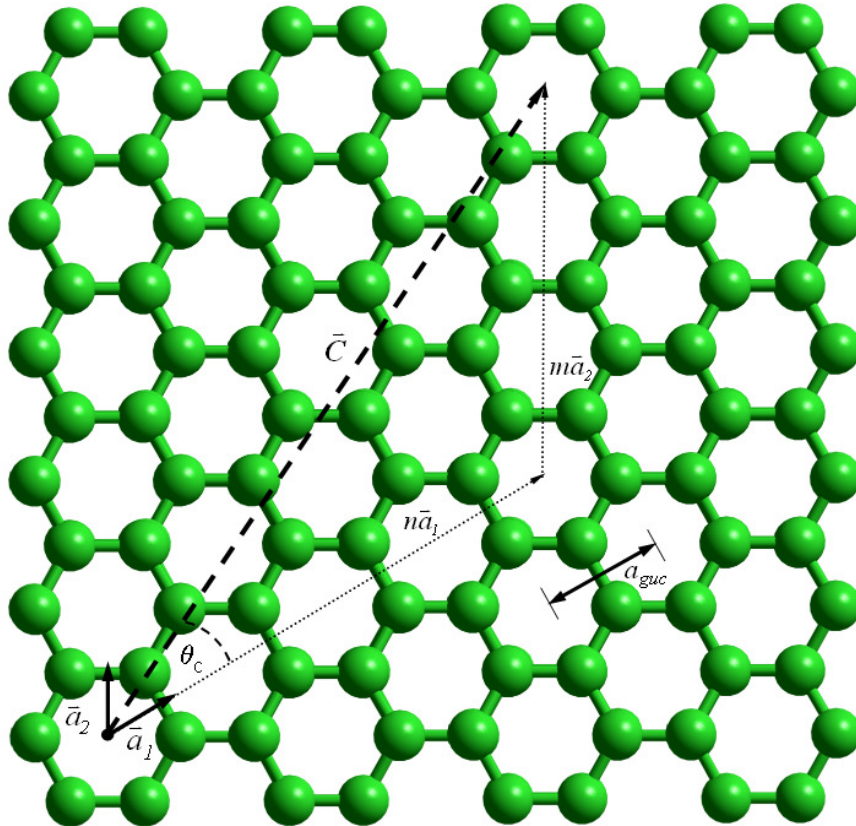


Figure 1.2: Chiral vector definition on a graphene sheet [9].

In the CNT structure, each carbon atom is bonded to three other carbon atoms by σ bonds with 120° of spacing. The carbon atom's fourth valence shell electron forms a delocalized π bond which is oriented perpendicular to the plane of carbon-carbon σ bonding.

A single-walled CNT (SWCNT) may be thought of as graphene sheet rolled along some chiral vector, \vec{C} , as shown in Figure 1.2. The chiral vector is a linear combination of two base vectors, \vec{a}_1 and \vec{a}_2 , which are oriented at 60° from each other. The chiral vector may be used to define the diameter of a SWCNT, d_{cnt} , of a carbon nanotube, as shown in Equation (1.1) [10], where a_{guc} is the distance between the centers of two unit cells and n and m are the lengths of the basis vectors.

$$d_{cnt} = a_{guc} \frac{\sqrt{n^2 + nm + m^2}}{\pi} \quad (1.1)$$

The energy per atom required to roll a graphene sheet into a CNT, U_r , is inversely proportional to the square of the CNT diameter [10], as shown in Equation (1.2), where E_g is the elastic modulus of graphene and t_g is the thickness of a graphene sheet.

$$U_r = \frac{\sqrt{3}E_g t_g^3 a_{guc}^2}{24d_{cnt}^2} \quad (1.2)$$

In general, CNTs may be classified into three types: 1) zig-zag, 2) armchair, and 3) chiral. The zig-zag and armchair types are shown in Figure 1.3. Zig-zag CNTs have $m = 0$, leading to a wrapping angle of 0° and diameters that are directly proportional to n . Armchair nanotubes have $m = n$, leading to a wrapping angle of 30° and diameters that are proportional to $\sqrt{3}n$. Chiral nanotubes thus have wrapping angles between 0° and 30° .

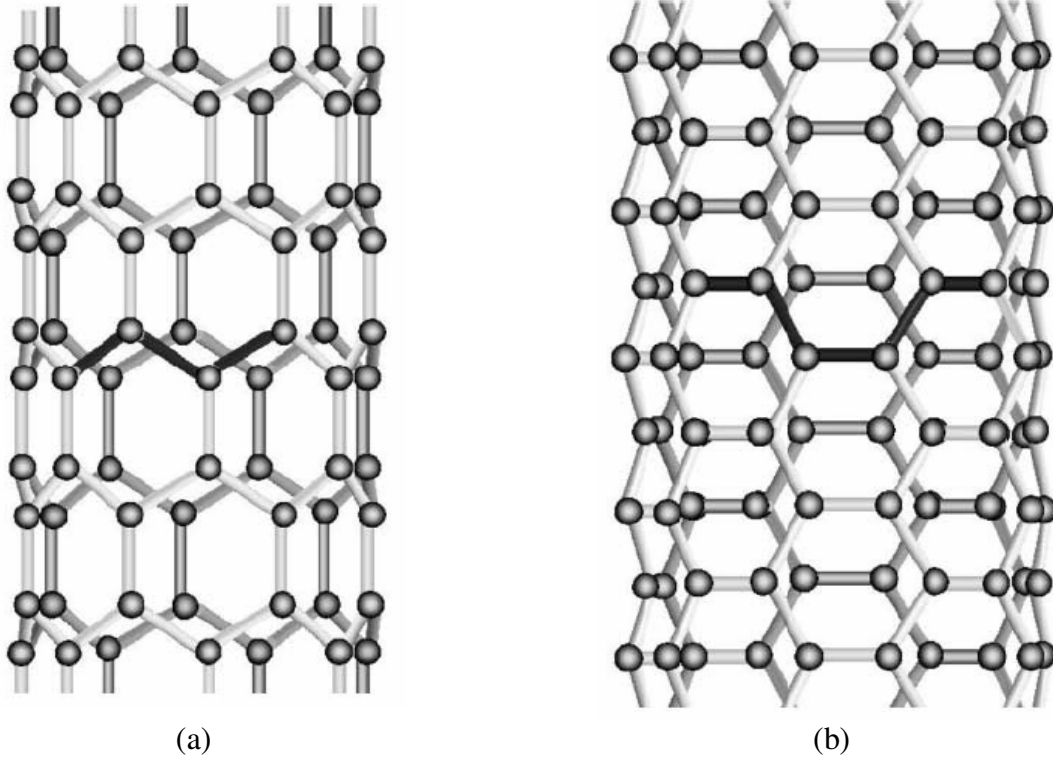


Figure 1.3: Zig-zag (a) and armchair (b) carbon nanotube chiralities [11].
Reprinted with permission from Elsevier Copyright 2003

The structure of the CNT also has a large effect on the electrical properties of the CNT. For example, electrically conductive tubes or metallic tubes always have a difference of their basis indices equal to an integer, q , multiple of three, as shown in Equation (1.3) [10]. This means that armchair nanotubes are always conductive.

$$3q = |n - m| \quad \text{where } q = 0, 1, 2, \dots \quad (1.3)$$

If the difference between the basis indices is not equal to an integer multiple of three, the tube is semiconducting, with a band gap, U_{gap} , that is proportional to a hopping parameter, γ , as is shown in Equation (1.4) [12].

$$U_{gap} = a_{guc} \frac{\gamma}{d_{cnt}} \quad (1.4)$$

For multi-walled CNTs (MWCNT) each wall may be treated as a resistor in parallel. This means that MWCNTs with many walls will likely be conducting because each shell has a one-in-three chance of being conductive.

1.3 Scaling Sensors Down to the Nanoscale

1.3.1 Introduction

As mechanical devices are scaled down to the nanoscale, it becomes difficult to measure and control their motion. Nanoscale mechanical devices offer the potential to overcome many of the speed and sensitivity limitations of macro- and microscale devices. However, traditional MEMS sensing techniques are not adequate for many nanoscale sensing applications, because MEMS sensing techniques generally suffer from poor resolution or become difficult to fabricate when scaled down to the nanoscale. Therefore, new sensors must be developed in order to meet the requirements of nanoscale sensing.

Nanoscale mechanical devices typically rely on flexure beams to guide their motion and set the stiffness of the system. Based on the stiffness of the flexure it is generally possible to trade range for resolution. For example, compliant flexures are generally good for high resolution force measurements but tend to fail at relatively low forces. Therefore, it is the ratio of range to resolution, known as dynamic range, which is the best metric of nanoscale sensor performance. Throughout this thesis the viability of different sensor systems is judged on the basis of the dynamic range of the sensor. Typically, nanoscale sensing applications require a minimum dynamic range of at least 40 dB (range to resolution ratio of 100:1). However, dynamic ranges of greater than 80 dB are desirable for many positioning [13] and force sensing applications [14].

1.3.2 Need for NEMS and Nanoscale Sensors

Nanoelectromechanical systems (NEMS) offer a promising area of research due to their small size and potential to operate at high speeds. NEMS can operate in locations that larger machines can generally not fit into, such as inside the human body. Also, because of their size, NEMS can outperform their macro-scale counterparts in terms of speed and resolution. Microelectromechanical systems (MEMS) are already being used in a number of consumer

applications such as accelerometers in car airbags, microphones in cell phones, ink jets in printers, and micromirrors in televisions. The ability of MEMS to accurately position fiber optics have also allowed for the creation of communication systems that perform tasks that were not previously possible at the macro-scale. MEMS have allowed devices to become smaller and lighter without reducing performance benefits. In fact, MEMS have helped increase the resolution of ink jet printers and the picture quality of televisions that rely on digital light processing. Also, MEMS have helped reduce the cost of many devices due to their small materials costs and the ability to fabricate many MEMS devices at once. NEMS have the potential to build upon the benefits of miniaturization that were seen for MEMS by further increasing the performance and reducing the cost of such devices.

Another major advantage of NEMS devices is that they eliminate the scale mismatch problem that is often seen when macro- and micro-scale devices are used to perform nano-scale tasks. In order for macro- and micro-scale devices to interact with nano-scale systems, it is typically necessary to de-amplify the motion of the macro- and micro-scale mechanisms because the displacement and force outputs of the macro- and micro-scale mechanisms are at least three orders of magnitude larger than the intended output motion for nano-scale systems. Flexures are commonly used to de-amplify force and displacement outputs from an actuator, but in order to de-amplify an actuator displacement input, the flexure's compliance must be a small fraction of the actuator's compliance. Unfortunately, adding a high compliance flexure lowers the natural frequency of the system because the frequency scales with the square root of the system's effective spring constant. This may be a problem because it leads to an increase in the system's sensitivity to low frequency vibrations such as floor vibration, fan vibration in electronics, footsteps, and electrical noise. This sensitivity to low frequency vibrations can introduce large errors into the system (nanometers to microns) which can easily cause nano-scale structures to fail. Fortunately, these vibration problems caused by scale mismatch may be avoided by using stiff nano-scale devices to perform nano-scale tasks. Overall, this elimination of the scale mismatch problem could allow nano-scale devices to have a large impact on a number of fields where nano-scale phenomena are important, such biology, chemistry, physics, and nano-fluidics, by allowing machines to interact with individual molecules.

Another big advantage of NEMS is that they have a small footprint, which allows many devices to be packed into a small area, thereby increasing information density. For example,

NEMS transistors, relays, and non-volatile memory could help increase how many processors may be fitted on a chip. Such chips would also consume less power due to the high Q factor of NEMS and thus would not become as hot as current electronic processors, allowing more processors to fit into the chip without the chip melting. Denser fiber optic interconnections could also be made using NEMS devices, which would have a large impact on the communications industry.

One of the greatest challenges for mechanical devices as they move towards the nanoscale is the incorporation of sensors. Sensors are critical in numerous mechanical applications because the ability to measure and control forces and displacements in mechanical systems can greatly improve device performance. This thesis will examine the potential of scaling down traditional MEMS sensing techniques to the nanoscale and new measurement techniques only available at the nanoscale.

1.3.3 Scaling MEMS Sensors Down to the Nanoscale

1.3.3.1 Capacitance Sensors

Capacitance sensors are widely used at the macro-, meso-, and micro-scale for measuring displacements on the order of nanometers [15-17]. There are two architectures for capacitive sensors at the MEMS scale [18], comb drive fingers and parallel plate capacitors, as shown in Figure 1.4. Comb drives produce a linear change in capacitance in response to a change in displacement, while parallel plate capacitors produce a nonlinear change. The dynamic range, DR, of a parallel plate capacitor can be found from Eq. (1.5) [18].

$$DR = \frac{\varepsilon \cdot A}{g \cdot \Delta C} \quad (1.5)$$

In Eq. (1.5), g is the initial gap size, δ is the resolution of the sensor, ε is the permittivity of the medium, A is the area of one of the parallel plates, and ΔC is the change in capacitance at maximum range due to a change of δ in position. At large ranges (gap sizes), the sensitivity, $\Delta C/\delta$, of the sensor decreases. The main noise source in capacitive sensors is stray capacitance in the environment which can vary from 1 fF [16] to 180 pF [19] depending on system shielding. Because the dynamic range of parallel plate capacitive sensors is dependent on the sensor area,

these types of sensors do not scale down well to the nanoscale. For example, in order to achieve an 80 dB dynamic range, large sensor areas are required (10's of mm² to 10's of cm²).

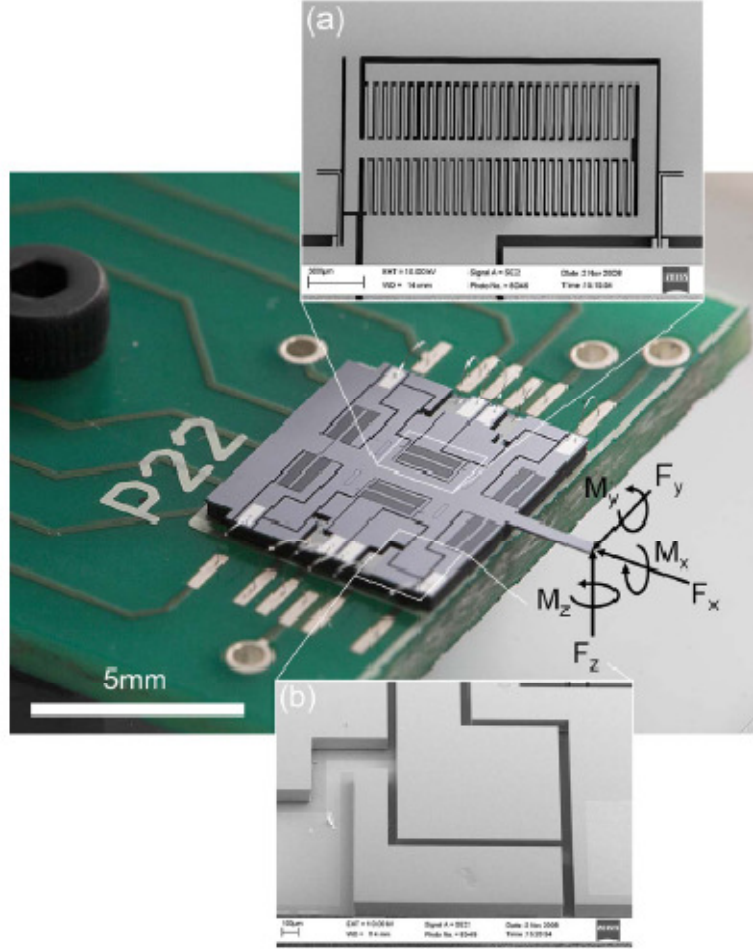


Figure 1.4: (a) comb drive and (b) parallel plate capacitive sensors.

The dynamic range in a comb drive sensor can be found from Eq. (1.6) [18].

$$DR = \frac{\epsilon \cdot (N-1) \cdot L \cdot t}{g \cdot \Delta C} \quad (1.6)$$

In Eq. (1.6), N is the total number of comb fingers, L is the overlapping length of the comb fingers, and t is the device thickness. Equation (1.6) shows that as the range of the sensor is increased the sensitivity, $\Delta C/\delta$, is not changed. In order to achieve an 80 dB dynamic range, a large number of fingers per axis are necessary (10³ to 10⁸). Typically in MEMS devices the

fingers are on the order of 10 microns wide and are an order of magnitude longer than the overlapping area each axis. These sensors, therefore, have a best case footprint of 1 cm x 100 microns in order to achieve an 80 dB dynamic range. Again because the dynamic range of these sensors scales with sensor area, comb drive sensors become impractical at the nanoscale.

1.3.3.2 Piezoresistive Sensors

Piezoresistive sensors are commonly used to measure displacements on the micro- and nano-scale due to their small size [20-22]. The electrical resistance of piezoresistive sensors changes as strain is applied to the sensor, and is typically measured using a Wheatstone bridge. This measurement of the strain in the sensor, and thus the strain in the beam, makes it possible to determine the displacement of the beam. A typical application of a piezoresistive sensor is shown in Figure 1.5.

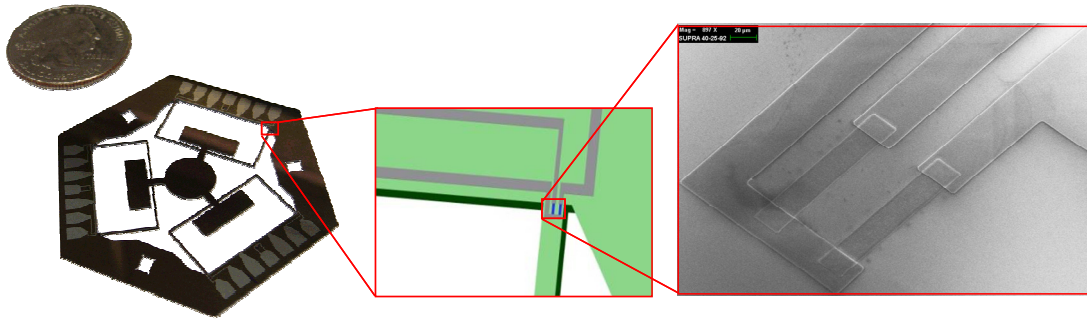


Figure 1.5: Piezoresistive displacement sensor.

The major noise sources in piezoresistive sensors are flicker noise caused by conductance fluctuations and Johnson noise caused by thermal agitation of electrons in the conductor [23,24]. The total noise, σ_V , is the sum of the squares of the Johnson and flicker noise, as seen in Eq. (1.7) where k_b is the Boltzmann constant, T is the temperature, R is the bridge resistance, f is the frequency in Hertz, α is the Hooge constant, N is the number of charge carriers, and V_s is the voltage across the resistors.

$$\sigma_V = \sqrt{4k_bTR(f_{\max} - f_{\min}) + \frac{\alpha V_s^2}{N} \ln\left(\frac{f_{\max}}{f_{\min}}\right)} \quad (1.7)$$

The dynamic range of a piezoresistive sensor is given by Eq. (1.8) where ε_y is the maximum safe strain of the flexure (usually 1/3 the yield strain), N_ε is the bridge strain number, and G_F is the gauge factor.

$$DR = \frac{\varepsilon_y V_s N_\varepsilon G_F}{\sigma_V} \quad (1.8)$$

For doped silicon piezoresistors, the dynamic range can be on the order of 10^6 [4]. However, both the resistance and gauge factor of piezoresistors are sensitive to thermal variations. Therefore, it is critical to either include thermal compensation, such as span temperature compensation [25] and a thermally symmetric bridge design [21], or to precisely control the temperature of the environment, in order to make high accuracy measurements. As piezoresistive sensors are scaled down to the nanoscale, flicker noise becomes the dominant noise source and the sensor's dynamic range starts to scale with the inverse of the square root of the resistor volume. This typically limits the performance of nanoscale piezoresistors to less than 60 dB dynamic range.

1.3.3.3 Hall Effect Sensors

Hall Effect sensors have also been used to measure sub-micron displacements in MEMS devices [26,27]. Equation (1.9) shows the sensitivity of the Hall Effect sensor output voltage, V_H , to motion of the sensor, δ . This sensitivity scales with an applied magnetic field, $B(x)$, which varies as a function of the distance, x , from the magnet. In Eq. (1.9), R_h is the Hall coefficient, I_s , is the energizing current, and t is the sensor thickness [28].

$$\partial V_H = \frac{R_h I_s}{t} \cdot \frac{\partial B(x)}{\partial x} \cdot \delta \quad (1.9)$$

The main sources of noise in a Hall effect sensor are Johnson noise and 1/f noise [26,28], as described by Eq. (1.7). Typically these noise sources range from 100's nV to microvolts [28]. The maximum Hall coefficient in doped silicon is approximately $1.4 \times 10^{-3} \text{ m}^3/\text{C}$ with a doping concentration of $n = 4.5 \times 10^{15} \text{ cm}^{-3}$ [28]. For a MEMS sensor with a thickness of approximately 100 microns and a typical current of roughly 1-10 mA [26,29] the sensor's minimum detectable

field is approximately 7 μT . The dynamic range of this sensor can be approximated by Eq. (1.10), assuming linearity of the field over the range, r , of the sensor.

$$DR \approx \frac{R_h I_s f_r r_s}{\sigma_v t} \cdot \frac{\partial B(r_s)}{\partial x} \quad (1.10)$$

In Eq. (1.10) r_s is the separation of the sensor from the field source, σ_v is the electronic noise in the system, and f_r is the fraction of the sensor to magnet separation over which the field gradient falls within the desired bounds for the sensor to function effectively. Note that there may be significant variation in the magnetic field gradient over the range of the sensor. A common bound is that a minimum sensitivity as calculated through Eq. (1.9) must be met over the whole sensor range, giving the gradient a lower bound. Magnetic fields used for Hall effect sensing typically decay at a high (2nd, 3rd) power and thus the gradient condition is met at all displacements up to a maximum, r_s and thus f_r approaches unity [29]. The main challenge in implementing Hall Effect sensors in nanoscale systems is minimizing the nonlinear stray magnetic field from the environment as a positioning stage moves through a work volume. If these fields exceed the minimum detectable magnetic field they can adversely affect the sensor accuracy and/or resolution.

1.3.3.4 Piezoelectric Sensors

Piezoelectric sensors are not good candidates for many nanoscale sensing applications because they are not capable of making static measurements [30]. This is because the electric potential generated in the piezoelectric material by a static force results in a fixed amount of charge generated. Therefore, a static load generates a potential that decays until all the free electrons in the material are dissipated via the sensor's internal impedance. The lower frequency cutoff limit for measurement is given by Eq. (1.11).

$$f = \frac{1}{2\pi RC} \quad (1.11)$$

A 1.8x1.8 mm, 40 μm thick PZT sensor corresponds to a lower cutoff of roughly 10 Hz [31]. MEMS piezoelectric accelerometers have been known to go as low as 0.5 Hz [32].

1.3.3.5 Inductance Sensors

There are two types of inductance sensors that are commonly used to measure displacements, linear variable differential transformers (LVDT) and eddy current proximity sensors [33]. In order for LVDT's to achieve nanometer resolution the motion in the other orthogonal axes must be minimized. Therefore, multi-degree-of-freedom devices are difficult to implement with LVDT sensing. In eddy current proximity sensors, an AC current is driven over a reference coil to generate a sensing magnetic field. This field induces eddy currents in the target, which itself produces a magnetic field in opposition to the sensing field. The opposing field, which is a function of the coil to target separation, alters the effective inductance of the reference coil. The coil inductance can be measured by the sensing electronics to determine the coil to target separation [33]. MEMS eddy current sensors have been shown to have resolutions of 100's of nanometers [34-36] when used with metallic targets. MEMS eddy current sensors have also been shown to be sensitive to motion in the axes orthogonal to the measurement axis [34-36]. Due to their reliance on magnetic fields for accurate location measurement, eddy current sensors are sensitive to magnetic interference. At the nanoscale eddy current sensors become hard to fabricate and the maximum current in the coil decreases significantly, which limits the sensor resolution. Therefore, eddy current sensors are not practical for nanoscale sensing applications.

1.3.3.6 Interferometry

Optical Interferometry is mainly used in fine precision equipment, especially in cases which require both large range and fine resolution displacement measurement [37-42]. The basic form for this method of sensing relies on splitting coherent light into two beams, arranging the beam paths such that one path length is dependent on the displacement of interest and recombining the beams to generate an interference pattern [37,42-44]. This pattern will vary with the displacement measurement, and can be measured to infer the change in the path length. A common interferometry setup is the Michelson Type Heterodyne interferometer [37,40,42,43], which passes lasers of different frequencies along the measurement and reference optical path, combining them at the end to generate a signal at the beat frequency determined by the frequency difference between the two beams. The lower frequency beat signal allows for greater range and is more easily measured by the electronics, resulting in reduced noise [37,43].

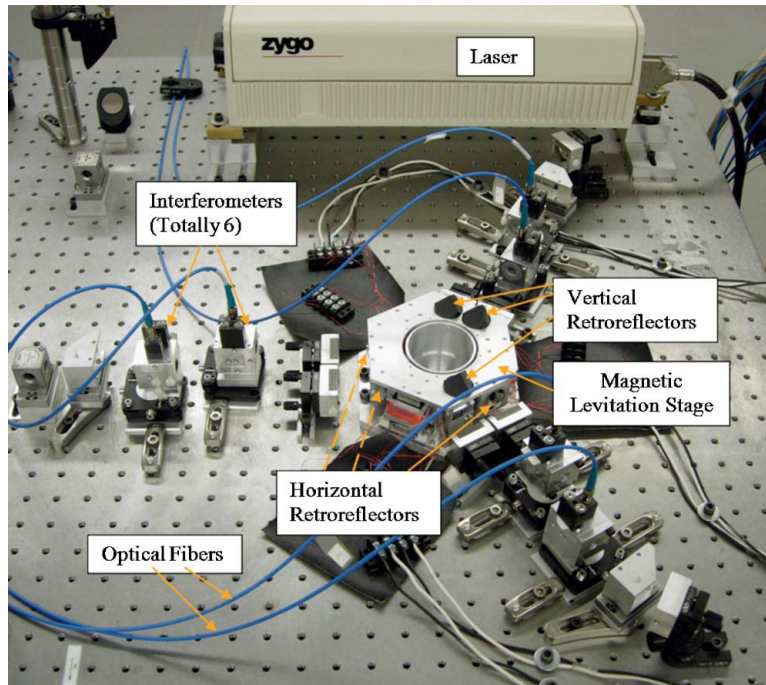


Figure 1.6: Large range Michelson-type heterodyne interferometer for 6-DOF position measurement [42].

Optical Heterodyne Interferometers are extremely sensitive to environmental conditions such as temperature and pressure, both of which change the optical properties of the medium through which the beam travels [37,42,44]. The range of measurement of an optical heterodyne interferometer is effectively decoupled from its resolution because the relative phase measurement cyclically shifts only through 0 to 2π as the displacement value changes. Interferometers are generally limited in range by either a scaling of error due to environmental sensitivity or the spatial coherence of the interferometer [37,42]. High performance interferometers are capable of reaching ranges of multiple meters [37,40,42,45]. Interferometry position sensors are only capable of accurate displacement measurement up to a maximum velocity on the scale of a 1-3 m/s [37,42], however, above which the fringe count rate exceeds the ability of the electronics to perform accurate counting. The displacement resolution, d , of an optical heterodyne interferometer can be written as a function of the phase resolution capability of the electronics, ϕ_{\min} , lasing wavelength, l , and number of reflections of the beam through the measurement arm, N , as [37,42,45]:

$$\delta_{min} = \frac{\Delta\phi_{min}\lambda}{2\pi N} \quad (1.12)$$

State of the art interferometry systems are capable of resolving down to roughly 1 part in 5000 of the lasing wavelength [37,40-42,45], of which a He:Ne laser is a common choice [37], with a wavelength of around 630 nm. The resulting resolution is roughly 130 pm. Multi-axis interferometry setups generally utilize a single high precision large lasing source which is multiplexed to allow multiple degree-of-freedom measurements [40-42]. This requires a large optical layout on the order of .01-1 m on a side [39,41,42]. The complexity of the optical setup increases rapidly as the number of measured axes is increased, resulting in increased system environmental sensitivity. The cost for a single axis optical heterodyne interferometer is in the range of \$10,000, and can rise upwards of \$100,000 for a complex multi-axis system [37]. A state-of-the-art optical heterodyne laser interferometer is capable of reaching and exceeding 180 dB dynamic range. However, the cost and size of interferometry setups limit their utility at the nanoscale.

1.3.3.7 Comparison

The MEMS sensors described above are compared in Table 1.1 based on the general categories of Resolution (Res), Dynamic Range (DR), Cost, Size, Bandwidth (BW), Sensitivity to Environment (Env.) and Sensitivity to Temperature (Temp).

Table 1.1: Bearing functional requirements.

Sensor Type	Res (nm)	DR (dB)	Cost per Axis (\$)	Size (μm^2)	BW (kHz)	Sensitivity	
						Env.	Temp
Capacitive	0.1	100	100	10^8	E	High	Low
Inductance	600	70	600	10^7	1-100	High	Low
Hall Effect	500	60	200	10^7	100	High	Low
Piezoelectric	0.1	120	100	10^8	0.2-100	Low	High
Piezoresistive	0.1	120	100	10^2	E	Low	High
Interferometer	0.1	215	10,000	10^9	30	High	High

E = electronics limited bandwidth (~30 kHz)

As shown in Table 1.1, interferometry is the most effective sensing system if cost and system complexity are not a concern. On the low cost end, if size is not a large concern,

capacitive sensors are the most effective, as their DR will scale with their area. However, for nanoscale sensing systems where size is a major restriction, piezoresistive sensors become the most effective sensing system.

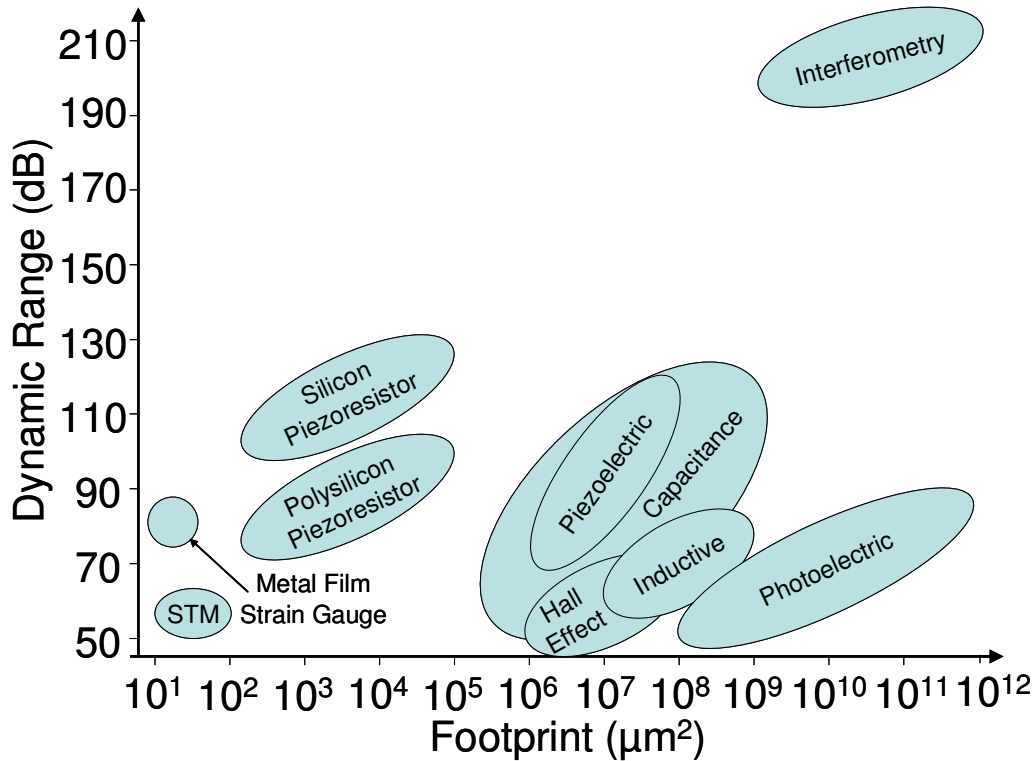


Figure 1.7: Comparison of sensor dynamic ranges versus size for MEMS sensing.

1.3.4 Novel Sensors for the Nanoscale

As shown in the previous section, most traditional MEMS sensor systems do not scale down well to the nanoscale due to noise, sensitivity and fabrication limits. Therefore, new types of sensors and sensing systems must be investigated to improve sensing at the nanoscale. For example, nanoscale materials such as carbon nanotubes and quantum phenomena such as electron tunneling can be used to vastly increase the dynamic range of nanoscale sensors.

1.3.4.1 CNT-Based Piezoresistors

Review of CNT-Based Piezoresistive Sensors

The first experiments that showed the potential of using CNTs as high quality strain sensors involved using an atomic force microscope (AFM) tip to push down on a suspended CNT. This method was used by Tombler et al. to show that the conductance of a CNT can change by up to two orders of magnitude when strain is applied to the CNT [46]. Similarly, using this method Minot et al. showed that the band structure of a CNT can be altered by the application of strain to the CNT [47]. However, simulations have shown that these results may have been due to local deformations in the CNT structure around the AFM tip as opposed to uniform strain in the CNT [48,49]. More recently, experiments that have uniformly strained the entire CNT have showed that the CNT gauge factor could be as high as 2900 [1]. The CNT gauge factor has also been shown to vary widely based on the electrical structure of the CNT [50]. For example, Grow et al. showed that the CNT gauge factor could be either positive or negative based on the CNT structure [51]. This result offers the interesting possibility that a full Wheatstone could be formed at one location on a MEMS flexure using CNTs that increase and CNTs that decrease resistance as the flexure is strained.

Theoretical modeling and simulations have been used to understand the link between CNT structure and gauge factor. These models and simulations typically are used to estimate the change in the band-gap of different types of CNTs. The band-gap changes are then related back to CNT resistance to obtain an estimate of the gauge factor. For example, Chen et al. showed that a 1 percent strain of a (12,0) CNT should result in a 6.4 percent decrease in resistance [52]. Similarly, Yang et al. [53] used tight-binding models to show that CNT band-gap could increase or decrease depending on the chirality of the CNT, confirming the qualitative result given by Grow et al. Unfortunately, there has been little quantitative work used to link specific CNT geometries to specific gauge factors. Also, there has been little theoretical or experimental work done to understand how interactions between the CNT and the substrate/electrodes affect the properties of the CNT-based strain sensor.

Several prototype devices have been fabricated using CNTs as strain sensors. The most common devices use films of randomly oriented films of CNTs as the sensing element. These films are popular due to their ease of assembly and large size. These properties allow CNT-

based film sensors to be integrated into many macroscale sensor systems [54-57]. CNT-based films also offer the advantage that they can easily be integrated into rubber and polymer-based composites [58-64]. Such composites are commonly used in microfluidic systems, structural health monitoring, artificial skin, and acoustic wave diagnostics. Overall, these CNT-based piezoresistive films tend to show good linearity but generally have low gauge factors due to the random orientation of the CNTs in the films and the poor transmittance of the strain in the substrate to the CNTs in the films [65].

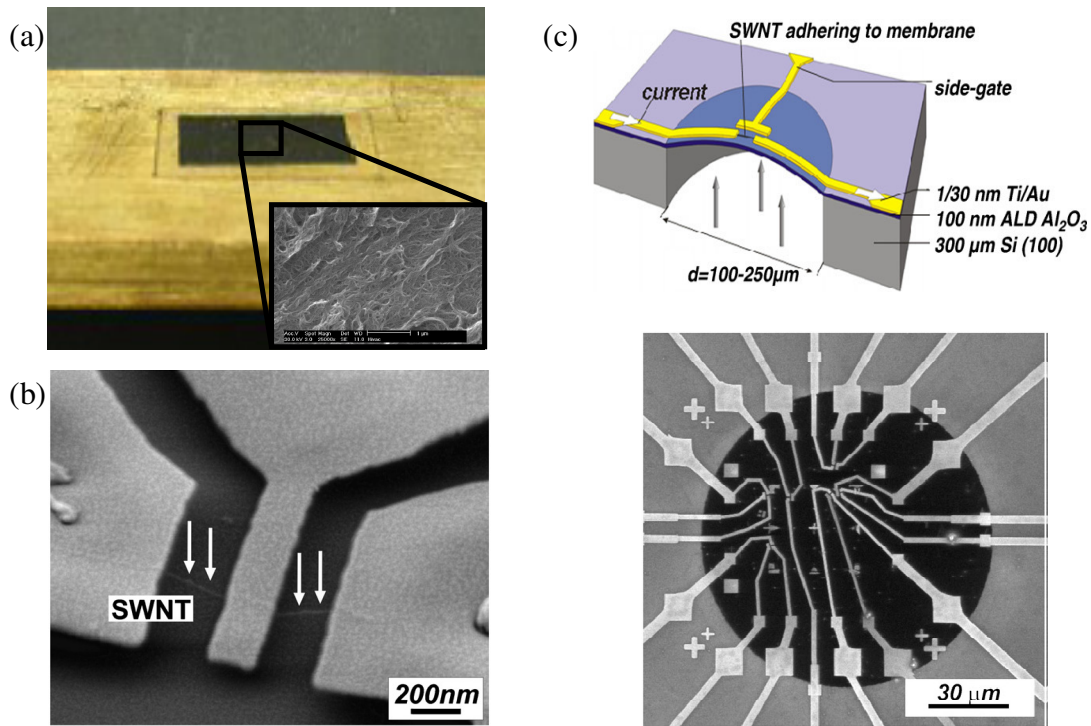


Figure 1.8. (a) CNT film strain gauge [65] (b) Single suspended CNT displacement sensor [66] (c) Pressure sensor with CNT piezoresistors [66]

There have been several devices fabricated using individual or a small number of CNTs as the sensing elements. For example, CNT-based piezoresistive sensors have been used to measure the force applied to meso-scale beams [6,9,67-69] and the strain applied to flexible substrates [70,71]. In these devices strain is applied to the CNTs through the bending or stretching of the substrate. MEMS pressure sensors have also been fabricated using CNT piezoresistors as the sensing element [72]. These CNT-based pressure sensors are capable of pressure resolutions of about 1 psi. These devices are fabricated by dispersing a random

assortment of SWCNTs on a surface and then selecting a few to pattern the MEMS device around, as seen in Figure 1.8. When pressure is applied to the substrate, the CNTs are strained and their resistance changes, making it possible to measure the pressure. Force and displacement sensors have also been fabricated by suspending individual CNTs between electrodes and attaching a beam to the center of the CNT [73]. When the beam is deflected, the CNT is stretched, causing the resistance to change. Such devices are capable of sub-nanonewton force resolution. In addition to these devices based on applying tension to the CNT, several CNT-based piezoresistive devices have been demonstrated where compression [74] or torsion [75] is applied to the CNT.

Scaling of CNT-Based Piezoresistors

As piezoresistive sensors are scaled down to the nanoscale, flicker noise becomes the dominant noise source. This is because the conductance fluctuations of the piezoresistor are dependent on the number of charge carriers in the resistor. The number of charge carriers in the resistor is, in turn, dependent on the carrier concentration and the volume of the piezoresistor. For most classic piezoresistor materials such as silicon, polysilicon, and metals, flicker noise scales with the square root of the resistor volume, as shown in Equation (1.13) where C_C is the carrier concentration and Ω is the resistor volume. Also, since dynamic range is inversely proportional to the sensor noise, dynamic range will scale with $\Omega^{-1/2}$.

$$\sigma_v = \sqrt{\frac{\alpha V_s^2}{\Omega C_C} \ln \left(\frac{f_{\max}}{f_{\min}} \right)} \quad (1.13)$$

The noise in carbon-nanotube-based piezoresistive sensors, however, scales with the number of CNTs in the sensor [76,77] as well as the geometry of the CNTs [78,79]. Therefore, the dynamic range of CNT-based piezoresistive sensors will not scale with $\Omega^{-1/2}$.

When flicker noise is the dominant noise source in the piezoresistive sensor system, the optimal size of the piezoresistor will tend to scale with the flexure size. For example, when flicker noise is the dominant noise source, the optimal length of the silicon, polysilicon, or metal-based piezoresistor is 1/3 of the beam length for a cantilever beam [23]. Therefore, the volume of the piezoresistor scales in direct proportion to the length of the flexure beam.

Similarly, the thickness of the piezoresistor is generally set by the thickness of the flexure beam. For example, for a silicon-based piezoresistive sensor, the optimal maximum ion implantation depth is 1/3 of the beam thickness [23]. For piezoresistors that sit on top of the flexure beam, such as metal and polysilicon piezoresistors, the maximum resistor thickness is generally set to be less than $1/10^{\text{th}}$ of the flexure thickness. This thickness ensures that the performance of the flexure is not affected significantly by the presence of the piezoresistor. Therefore, the volume of the piezoresistor scales linearly with the thickness of the flexure. Finally, the maximum width of the piezoresistor is set by the width of the flexure beam, since the piezoresistor cannot exist outside the confines of the flexure. These scaling rules mean that when flicker noise is the dominant noise source, the volume of the piezoresistor scales with the flexure volume. Therefore, noise in these sensors scales with the flexure volume to the 1/2 power.

Carbon-nanotube-based sensors, however, are not subject to the same scaling laws. The size of high performance CNT-based piezoresistors is generally set by the inherent size of the CNTs. CNT-based piezoresistors are a single monolayer of CNTs, so their thickness is a set constant no matter what the beam thickness is. Further, CNT-based piezoresistive sensors are generally less than 1 μm in length to ensure that each CNT is connected between two electrodes. This eliminates the need for CNT-CNT connections, which can significantly decrease the sensor's strain sensitivity [65], and allows the CNTs to behave as ballistic conductors [80,81]. Therefore, the size of the CNT-based sensor is not affected as the flexure length is scaled down until the flexure beam is a few microns in length. Even when the length of the CNT-based sensors is reduced, the noise in the sensor should not be affected. This is because flicker noise in ballistic conductors is not affected by the number of charge carriers in the resistor [82]. The number of charge carriers only plays a central role in the noise of diffusive conductors where the scattering of different carriers is uncorrelated. However, this scattering is not relevant in devices where the length of the device is below the mean free path length of the electrons. Therefore, the noise in the ballistically conducting CNT-based piezoresistive sensors should not be dependent on the sensor length.

The width of the flexure, however, will have an effect on the noise in the CNT-based piezoresistor. This is because the width of the flexure controls the width of the sensor, which in turn sets the number of CNTs which can fit in parallel in the sensor. Each CNT acts as a

conduction channel through which electrons can flow. Therefore, decreasing the sensor width reduces the number of conduction channels, which increases the noise in the sensor system [76]. This means that the noise in CNT-based piezoresistive sensors scales with the square root of the sensor volume. Overall, these factors make CNT-based piezoresistive sensor systems much less sensitive to sensor size than traditional silicon, polysilicon, and metal thin film piezoresistors.

Using these scaling equations and basic material properties, it is possible to estimate the performance of silicon, polysilicon, metal thin films and CNT-based piezoresistive sensors as a function of flexure size. If we assume a constant 10:10:1 length to width to thickness ratio flexure system, it is possible to plot the optimal performance of each type of piezoresistive sensor. As shown in Figure 1.9, the ideal CNT-based piezoresistors have the potential to outperform traditional piezoresistive sensors at most size scales if their strain sensitivity can be optimized by selecting the CNT chiralities with the highest strain sensitivities for the piezoresistive sensor [9]. This difference between ideal CNTs and traditional piezoresistors is magnified when the flexure is less than about 10 μm in length, as a result of differences in sensor scaling. Currently, CNT-based piezoresistors are capable of outperforming silicon based sensors when the flexure length is less than about 1 micron, and polysilicon sensors when the flexure length is less than about 100 microns.

The silicon piezoresistors are competitive with ideal CNT-based piezoresistors for flexure lengths of about 100 μm . At larger flexure lengths, the silicon piezoresistors are limited by Johnson noise and their dynamic range stops increasing. At lower flexure lengths, the silicon-based piezoresistor's performance drops off significantly as a result of the sensor scaling rules discussed previously. The polysilicon sensors perform similarly to the silicon piezoresistors, except that they have a lower gauge factor and greater Hooge constant, so their performance starts to drop off when the flexure length decreases below about 1 mm. The metal thin film piezoresistors have a dynamic range limited to about 80 dB because of their low gauge factor. They, however, do not start to see a drop off in performance in dynamic range until the flexure length decreases below about 10 μm due to their high carrier concentration. The metal thin film piezoresistors are, therefore, able to outperform current CNT-based piezoresistors for flexure lengths between 1 and 100 microns, as seen in Figure 1.9.

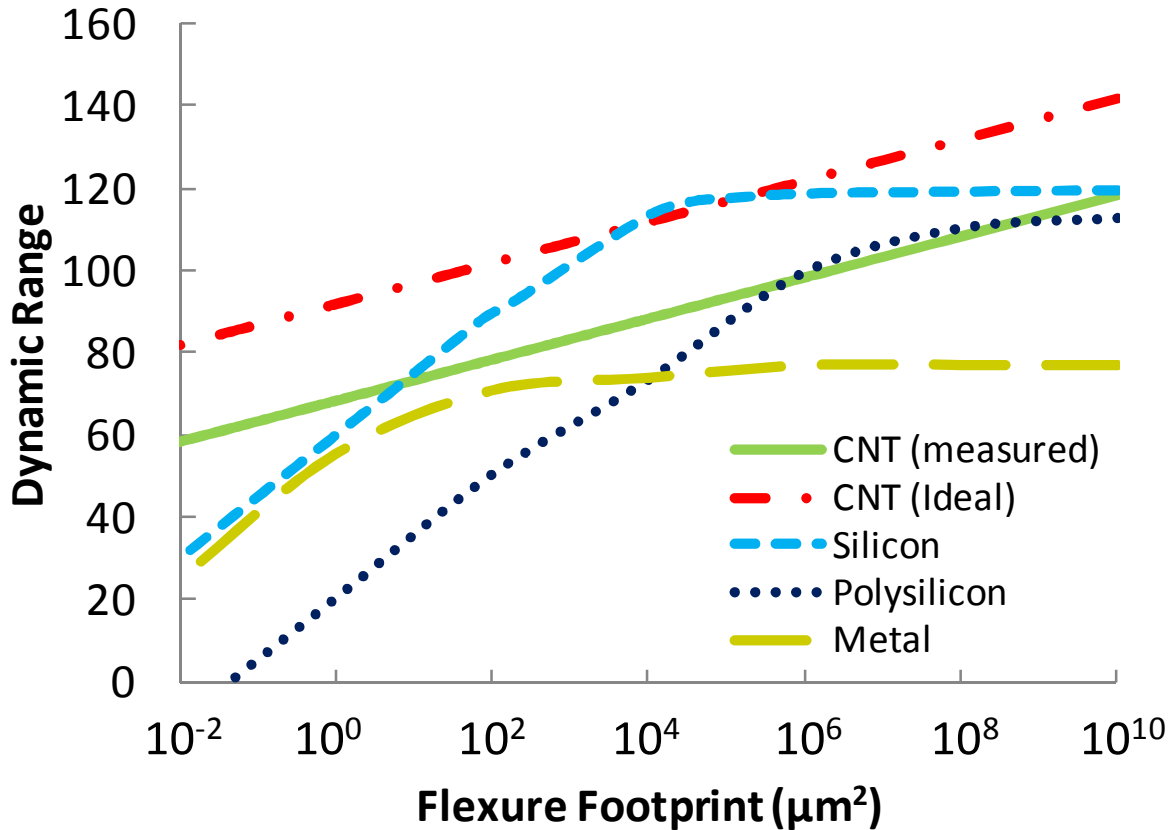


Figure 1.9: Sensor dynamic ranges versus size for piezoresistive various sensing materials.

Overall, therefore, as piezoresistive sensors are scaled down to the nanoscale, CNT-based piezoresistors are the only viable option for high-dynamic-range sensing. However, more work needs to be done to improve these sensors and to optimize their performance before they can be incorporated into real high-dynamic-range nanoscale sensor systems.

1.3.4.2 Resonance Sensors

Introduction to Resonance Sensors

Resonant NEMS sensors are a promising new class of sensors that have been made possible at the nanoscale by the small mass, high natural frequency and high quality factor of nanoscale resonators. The small mass of NEMS devices allows such devices to operate at high frequencies. As was seen in Equation (1.14), the natural frequency of the device is inversely proportional to the square root of the mass.

$$f = \frac{1}{2\pi} \sqrt{\frac{k}{m}} \quad (1.14)$$

Therefore, by reducing the mass of the device, the device may be run at much higher speeds. For example, while micro-scale devices typically run in the 10 kHz to 10 MHz range [83], NEMS devices can run at frequencies that are greater than 1 GHz [84]. This increased natural frequency can improve signal processing speeds and increase the sensitivity of nanoscale sensors and transducers that rely on the resonance of a beam.

The small mass of NEMS devices also makes the amount of power dissipated by NEMS devices small, thus giving NEMS devices high quality or Q factors. The Q factor is defined in Equation (1.15), where ω is the angular frequency, m is the mass, K is the stiffness, and R is the mechanical resistance.

$$Q = \omega \times \frac{\text{Energy Stored}}{\text{Power Loss}} = \frac{\sqrt{mK}}{R} \quad (1.15)$$

The Q factor of NEMS devices may be hundreds of times better than similar high frequency electrical resonators [85]. NEMS are intrinsically low power devices due to these high Q factors. The fundamental power scale is defined by the thermal energy divided by the response time, which equals the Q factor divided by the natural frequency. For NEMS devices, this value is typically in the 10^{-18} watts range. This means that even if the NEMS device is only driven with a picowatt of power, the signal to noise ratio is still on the order of 10^6 . Therefore, NEMS devices have the ability act as fine precision sensors because of their high damping and signal to noise ratios.

Resonance-based Mass Sensors

Resonance-based mass sensors work by creating a frequency shift, Δf , that is directly proportional to the change in mass. When mass is added to a resonating beam the natural frequency of the beam changes, as described by Equation (1.16) [86].

$$\Delta f = -\frac{1}{2} f \frac{\Delta m}{m} \quad (1.16)$$

Nanoscale resonators are ideal for such sensors due to their extremely low mass and high natural frequency. The sensitivity of these sensors is generally limited by thermomechanical noise, which is caused by energy exchange between the flexure and the environment [87]. These thermomechanical vibrations generally limit the dynamic range of resonant mass sensors to about 60 dB [88].

Nanoscale resonators, however, are still capable of high mass sensitivity. For example, silicon-based nanoscale cantilevers and doubly clamped beams have been used to measure masses down to an attogram [20,89]. In addition, carbon nanotube-based nanomechanical resonators have been proposed that would be capable of mass resolutions of up to a zeptogram [90].

Resonance Based Strain Sensors

Resonance-based strain sensors are based upon the principle of strain stiffening. For small strains, the pseudo-rigid-body large-deflection beam bending model given by Equation (1.17) can be used to predict the strain stiffening behavior of a clamped-clamped flexure beam [8]. Equation (1.17) relates the applied force, F , to the change in length of the beam, ΔL , via the initial clamped-clamped beam length, L_0 , the position along the beam, x , the stiffness coefficient K_θ , the characteristic radius factor, γ , flexural rigidity, $(EI)_{bend}$, and $(EA)_{axial}$.

$$F = \frac{2\Delta L (EA)_{axial}}{L_0 + \Delta L} \sin^{-1} \left(\frac{x}{\sqrt{x^2 + \gamma^2 L_0^2}} \right) + \frac{8\gamma^2 K_\theta (EI)_{bend} \tan^{-1} \left(\frac{x}{\gamma L_0} \right)}{x^2 + \gamma^2 L_0^2} \quad (1.17)$$

When tension is applied to the beam, the beam elongates and ΔL increases, which causes the stiffness to increase. This increase in stiffness then results in a higher natural frequency of the beam. This increased natural frequency can be described by Equation (1.18) where μ is the mass per unit length of the flexure and ε is the axial strain applied to the flexure [91].

$$f = \frac{4.73^2}{2\pi L_0^2} \sqrt{\frac{(EI)_{bend}}{\mu} + \frac{(EA)_{axial} L_0}{4\pi^4 \mu} \varepsilon} \quad (1.18)$$

Therefore, based on the change in natural frequency of the resonating beam, it is possible to measure the strain applied to the beam.

Resonant strain sensors are not as commonly used as macroscale strain sensors because of the range limitations created by the low failure strains of most macroscale materials. However, CNT-based resonant strain sensors have recently been shown to be able to overcome some of these limitations [91-94]. A schematic of a CNT-based resonant strain sensor is given in Figure 1.10.

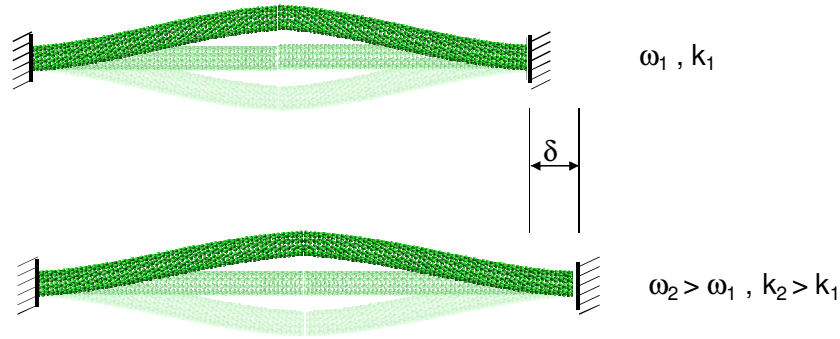


Figure 1.10: CNT-Based Resonating Strain Sensor.

Carbon nanotubes are ideal for resonance-based strain sensors due to their high elastic modulus [95], high strength [96], and failure strain of greater than 20 percent [2]. These properties give CNT-based resonant strain sensors a high natural frequency and a large range. For example, based on molecular dynamics simulations of a 15.28 nm long, (5,5) single walled carbon nanotube, CNT-based resonant sensors can have a strain sensitivity of about 1 picostrain per hertz, as seen in Figure 1.11. For the 15.28 nm long, (5,5) CNT this translates to a force sensitivity of approximately 1 pN/MHz and a displacement sensitivity approximately of 10 pm/GHz, with a range of approximately 3.7 nm. These sensors can therefore be very good at measuring small strains over nanoscale displacement ranges.

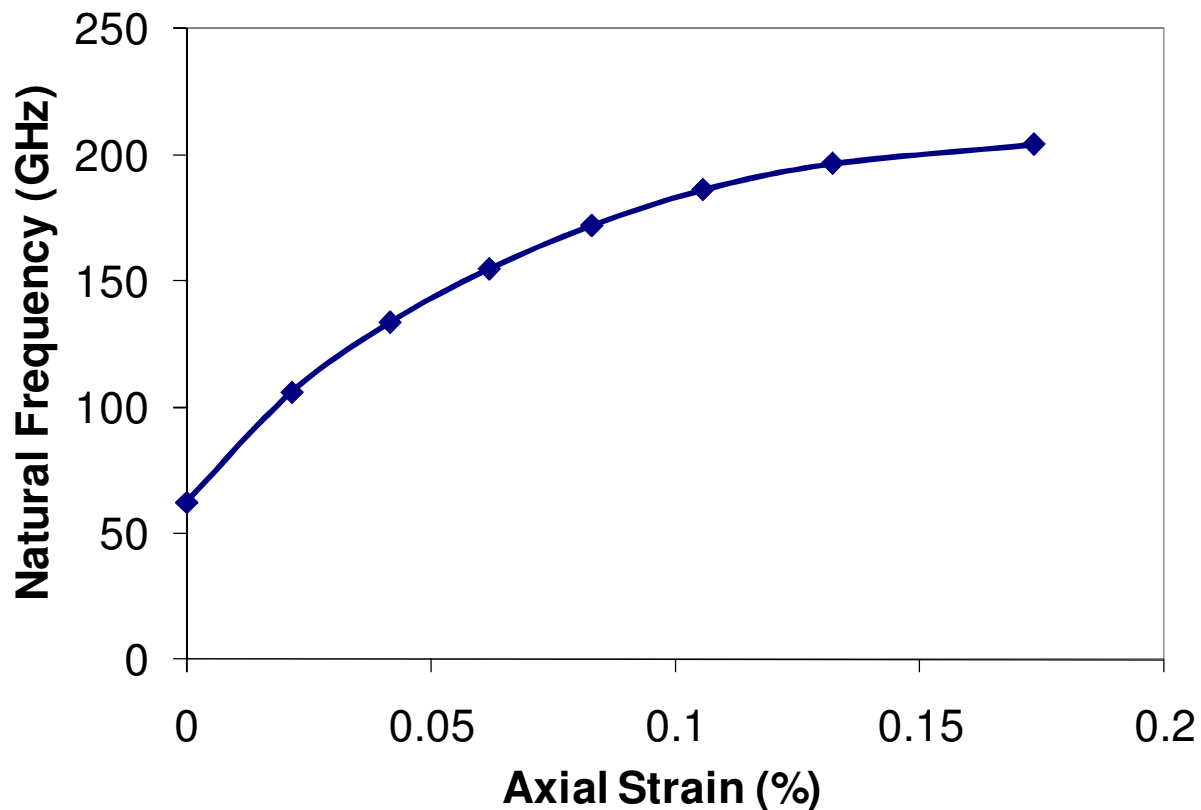


Figure 1.11: Natural Frequency vs. Strain for CNT Resonator.

1.3.4.3 Tunneling Sensors

Tunneling sensors have had great success in measuring subatomic displacements, but have been limited at the macroscale due to their lack of range. Tunneling sensors generally consist of a sharp tip placed within a nanometer of a moving surface. As the gap between the tip and the surfaces changes, the tunneling current changes, as shown in Equation (1.19), where V is the DC bias voltage, κ is decay constant for the electron wave-function within the gap, and d is the gap size [97].

$$i = \rho_s(E_F) V e^{-2\kappa d} \quad (1.19)$$

This results in a high displacement sensitivity but small range, because of the exponential decline in tunneling current as the gap size increases. For example, an electronic circuit with 1 percent

variation in a 1 nA current from a 100 M Ω source is capable of detecting displacements as small as 0.3 pm, but has a range of less than 1 nm [98]. In order to improve these range limitations, feedback control systems are often used to maintain a fixed gap distance over a range of displacements [99]. These feedback sensors, however, are not able to maintain the fine displacement resolution of the tunneling sensor over the full range of the device, since large motions must be measured by an external sensor on the feedback platform.

While non-feedback tunneling sensors are limited at the macro and micro scales, they may have some utility at the nanoscale. As devices are scaled down to the nanoscale, the necessary range of these devices tends to decrease as well. Therefore, the limited range of the tunneling sensors may not be that limiting in nanoscale sensing. Non-feedback tunneling sensors are also scalable down to the nanoscale, since the tunneling occurs between the nearest pair of atoms on each side of the tip-surface gap [99]. Therefore, the tunneling sensor does not need to be any larger than a few atoms and the sensor range and resolution do not scale with the sensor size. This makes tunneling sensors ideal for nanoscale sensing applications that require high resolution but that do not have a large range.

1.3.5 Sensor Selection for Case Study

For the case study examined in this thesis, CNT-based piezoresistors were selected for the sensing element. CNT-based piezoresistive strain sensors were chosen because of their ability to meet the footprint and dynamic range requirements of the case study, as seen in Figure 1.12. Also, CNT-based piezoresistive strain sensors are easy to integrate into multi-axis sensors and are inexpensive to fabricate. This combination of sensor properties makes CNT-based piezoresistive sensors the ideal choice for the 3-axis MEMS force sensor case study presented in Section 1.4.3.

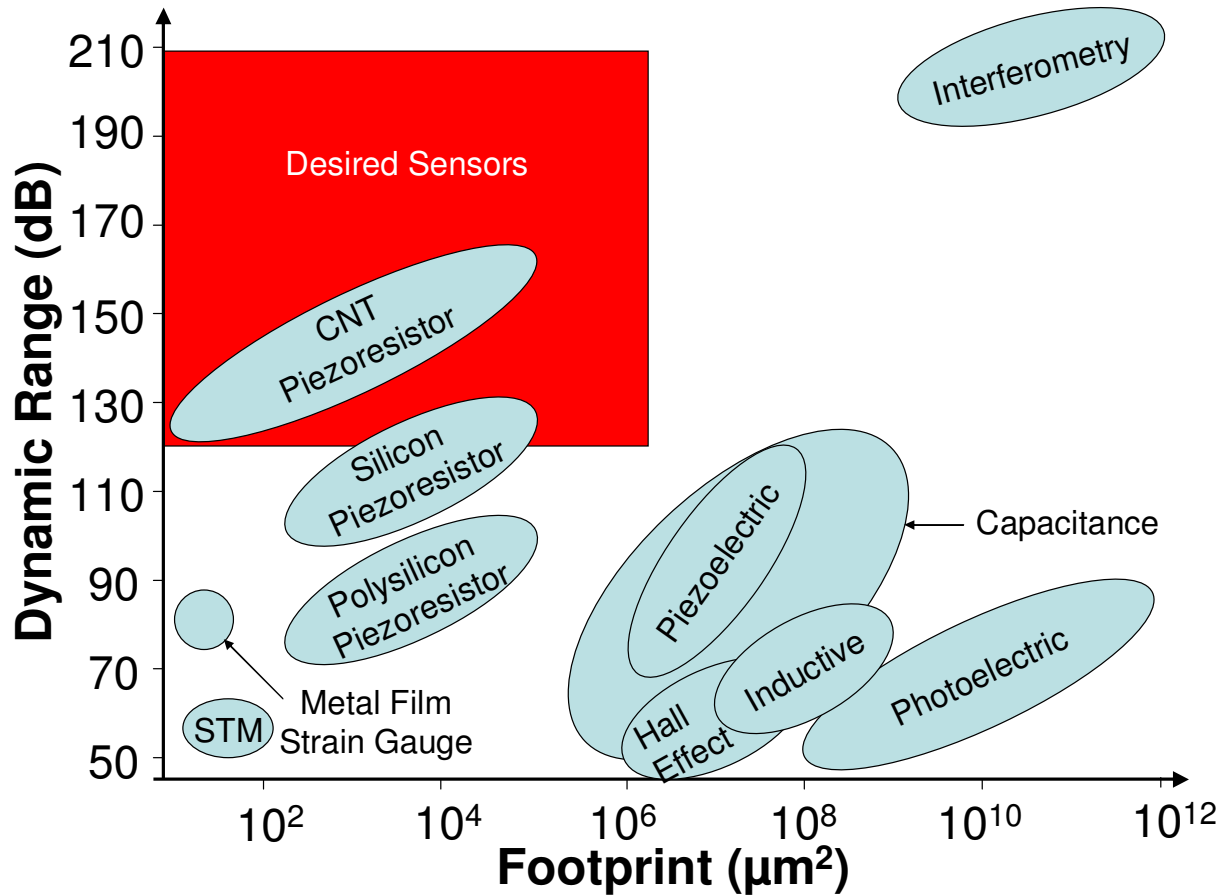


Figure 1.12: Sensor Comparison for Case Study.

1.4 Prior Art

1.4.1 CNT Assembly

Accurate and reliable assembly of CNTs into micro- and nanoscale devices is critical in order to maximize the performance of these devices. This section reviews several techniques used to assemble CNTs into MEMS/NEMS devices and discusses their advantages and disadvantages.

1.4.1.1 Grow-in-Place

Several methods have been used to guide the direction of growth of CNTs on a substrate. These techniques typically focus on structuring the substrate to promote growth between specific locations or using an electric field to direct the growth of the CNTs. For example, suspended

CNTs have been fabricated by growing the CNTs on top of pillars and allowing them to form bridges between neighboring pillars [100,101]. Similar methods have been used to connect CNTs between an electrode and a cantilever beam to create a CNT-based strain sensor [102]. In addition, researchers have demonstrated the growth of CNTs across trenches to produce sensors [103] and electronic circuits [104,105]. In order to enhance CNT placement accuracy, electric fields are commonly used to direct the direction of CNT growth [106,107]. The electric field induces a dipole in the growing CNT parallel to the CNT's principal axis. The electric field then exerts a torque on this induced dipole. The torque exerted on the CNT by the electric field is given by Equation (1.20), where α_{zz} is the polarizability tensor, E is the electric field intensity, L is the length of the CNT, and ϕ is the angle between the CNT and the electric field [108].

$$T = \frac{1}{2} \alpha_{zz} L E^2 \sin 2\phi \quad (1.20)$$

This torque causes the CNTs to align along the direction of the electric field. Therefore, by controlling the direction and intensity of the electric field during CNT growth, the placement of CNTs onto a structure can be accurately controlled. The main advantage of the growth-in-place assembly technique is that it can be done in parallel to facilitate the fabrication of a large number of devices at the same time. However, it can be difficult to control the exact location, type and number of CNTs in the device. Also, the high temperatures required for growth of CNTs are not compatible with the fabrication of many types of materials and devices.

1.4.1.2 Pick-and-Place

The typical pick-and-place setup consists of a three degree-of-freedom nanopositioning stage inside a scanning electron microscope (SEM) [109-111]. The nanopositioner system typically has a range of 10's of millimeters and sub-nanometer resolution [112]. The SEM is used to image the CNT while the nanopositioner is used to direct a probe into contact with the CNT. Once in contact with the probe, the CNTs are then welded to the probe using electron beam-induced deposition of a carbon or organometallic compound [112,113]. Alternatively, microfabricated grippers have been used instead of a probe to pick-and-place CNTs inside an SEM [114,115]. Once the CNT has been secured to the nanomanipulator, the nanopositioner can be used to move the CNT to the desired location, where it can be welded in place and the

nanomanipulator can be removed. This process allows great control over the exact position and type of CNT placed onto the device. However, pick-and-place assembly is a slow, serial fabrication process, making it impractical for large scale manufacturing of devices.

1.4.1.3 Dielectrophoresis

In assembly by dielectrophoresis, CNTs are dispersed in an aqueous or alcohol-based solution [116] and directed into a desired location through the use of an alternating electric field [117,118]. In dielectrophoresis, a non-uniform electric field is applied with unequal field strength around a particle, leading to imbalanced forces on the induced dipole. This drives the CNT towards the field maximum and results in a torque that aligns the CNT with the electric field. The force and torque on the CNT can be calculated using Equations (1.21) and (1.22), where r is the radius of the CNT, l is the length of the CNT, ϵ_p and ϵ_m are the complex dielectric permittivities of the CNT and the medium, and E is the electric field [119].

$$F_{DEP} = \frac{1}{2} \pi r^2 l \epsilon_m \operatorname{Re} \left(\frac{\epsilon_p - \epsilon_m}{\epsilon_m} \right) \nabla |E|^2 \quad (1.21)$$

$$T_{DEP} = \frac{1}{2} \pi r^2 l \epsilon_m E^2 \sin \theta \cos \theta \operatorname{Re} \left(\frac{(\epsilon_p - \epsilon_m)^2}{\epsilon_m (\epsilon_m + \epsilon_p)} \right) \quad (1.22)$$

Process parameters such as the CNT concentration, the magnitude of the electric field, and the deposition time all affect the assembly of CNT by dielectrophoresis. For example, experiments have shown that the number of assembled CNTs increases with concentration of the CNT solution, the magnitude of the applied voltage, and the duration of the electric field [120]. In addition, experiments have shown that higher frequency alternating currents tend to result in better alignment of the CNTs to the electric field [121]. Also, depending on the processing conditions it is possible to control whether both semiconducting and metallic or just metallic CNTs are deposited onto the device [122-124].

The major advantage of dielectrophoretic assembly is that many carbon nanotubes can be assembled into a device at the same time at room temperature [125,126]. Using dielectrophoresis, millions of CNTs can be assembled onto a single device in a matter of minutes [127]. This is critical for the nanomanufacturing of nanoscale, CNT-based devices [128]. In

addition, individual CNTs can be assembled onto NEMS devices by measuring the magnitude of both the direct and low frequency current to determine when a nanotube has made electrical contact and to halt the dielectrophoretic process [129]. Using these dielectrophoretic assembly techniques, several different types of nanoscale sensors and electronics components have been fabricated [130,131].

1.4.1.4 Transfer Printing

Transfer printing can be used to remove CNTs from the substrate on which they were grown or deposited and assemble them into nanoscale devices. In this process a polydimethylsiloxane (PDMS) stamp is laminated against a donor substrate and is quickly peeled away, pulling the CNTs from the donor substrate onto the stamp. The stamp is then brought into contact with the receiving substrate and slowly peeled away, transferring the CNTs to the receiving substrate. This works because the peeling rate determines the strength of adhesion and, therefore, the direction of transfer [132,133]. This technique can be used to print CNTs with a wide variety of shapes and sizes on to virtually any smooth surface [134-136]. Overall, transfer printing is a quick and simple method to assemble CNTs onto a substrate. Unfortunately, the utility of this method is limited because the CNTs must already have the correct relative spatial location and orientation before the transfer printing process can be preformed.

1.4.2 Sorting of CNTs

The ability to sort CNTs by diameter, chirality, electronic structure and handedness is required for numerous sensor and electronic applications. CNTs can be sorted either through precise control of the growth conditions [137] or through post-growth separation [138]. Controlled growth of CNTs has been successful in setting the length, diameter, and number of walls in the CNT [139-146]. However, precise control of chirality has proven more difficult, with only a few limited successes [147,148].

Post-growth sorting generally relies on chemical reactions that vary as a function of the physical or electronic structure of the CNT [149]. The first step in these post-growth sorting methods is to disperse the CNTs in solution [116]. Then electrophoresis, chromatography, or ultracentrifugation techniques can be used to separate CNTs by specific physical or electrical

properties. Electrophoresis and chromatography have mainly been used to separate CNTs into semiconducting and metallic varieties [149-151].

Density-gradient ultracentrifugation (DGU), however, is commonly used to separate CNTs by size and chirality [149]. In DGU, CNTs are distributed into a density gradient that is formed in a centrifuge tube. A centrifuge is used to produce a driving force that causes the CNTs to move towards the point where the buoyant density of the SWCNT matches the local density gradient of the centrifugal field. Specific types of CNTs can then be extracted from the centrifugal field. In order to increase the density difference between different types of CNTs, the CNTs are commonly attached to other molecules [152,153]. For example, co-surfactant mixtures of sodium cholate and sodium dodecyl sulfate (SDS) have been shown to be successful in separating CNTs by diameter or electronic structure [154]. In addition this method has been used to isolate specific CNT enantiomers by taking advantage of the fact that some surfactants bind preferentially to either left-handed or right handed CNTs [155-158]. Recently, it has been demonstrated that specific strands of DNA will attach preferentially to specific chiralities of carbon nanotubes, making it possible to effectively sort CNTs by their (n,m) chiral indices [159-161].

1.4.3 Multi-Axis MEMS Force Sensors

MEMS force sensors tend to rely on one of three sensing methods: capacitive sensing, optical detection, and piezoresistive sensing. Several multi-axis force sensors have been developed using capacitive sensors [17,162-165]. Two degree-of-freedom capacitive force sensors have been demonstrated that rely on interdigitated fingers to measure displacement and transduce force. These sensors are capable of achieving sub- μN resolutions and mN ranges [162]. Six-axis force sensors have also been demonstrated that rely on both comb drive and parallel plate capacitive sensors [163]. In general, multi-axis capacitive force sensors are difficult to fabricate and require relatively large sensor areas (mm^2) for each axis in order to achieve high force resolution. This makes capacitive sensing impractical for small, inexpensive, multi-axis force sensors.

Optical sensors are commonly used in single-axis MEMS force sensors. For example, photodiodes are used in atomic force microscopes (AFM) to measure the deflection of an AFM cantilever beam. In this process, a laser beam is directed at the end of the cantilever and is

reflected to a photodiode. When the cantilever is deflected, the angle at which the laser is reflected changes, which can be measured by the change in the photodiode current [166]. From this deflection measurement it is possible to calculate the force applied to the cantilever based on the cantilever stiffness. In addition, other optical methods such as measuring the displacement of a stage using optical gratings in an SEM and laser interferometry have been used in force sensing applications [167,168]. However, optical methods have rarely been used to make multi-axis force measurements at the microscale.

To date, most MEMS force sensors have used piezoresistors as the active sensing element [22]. Piezoresistors offer the advantages of small size and low cost. For example, silicon-based piezoresistors have been used to make nanonewton level single axis force sensors [4,169] and AFM cantilevers [21]. In general, the design of these sensors is optimized by the proper selection of piezoresistive material, sensor geometry, and fabrication procedure [170-172].

However, the design and fabrication process becomes significantly more challenging for multi-axis piezoresistive sensors [14]. There are two common configurations for two-axis silicon based force sensors. These sensors can either be fabricated by putting two sensors in series and using sidewall ion implantation to measure lateral forces [173] or by placing the piezoresistors off the neutral axis of the beam so that they change resistance when both vertical and lateral loads are applied [174-176]. These sensing methods, however, significantly increase the complexity of the fabrication process and result in significantly worse resolution in one direction relative to the other. Multi-axis silicon-based piezoresistive sensors have the added complexity that the piezoresistivity of silicon is dependent on its crystallographic orientation. Therefore, for multi-axis force sensors, other piezoresistive materials such as polysilicon and metals are commonly used [13,14,20].

1.5 Scope

1.5.1 Technical Approach

In order to be able to engineer high quality, CNT-based piezoresistive strain sensors, work needs to be done in three areas: the CNT sensing element itself, integration of the CNT sensing element into MEMS/NEMS devices, and overall system level design and optimization. As discussed in the background section, previous research has shown that there can be a wide

variance in the CNT gauge factor depending on the structure of the CNT, but there has been no quantitative link established between CNT structure and gauge factor. The purpose of this thesis is to establish such a link so that it is possible to select the optimal CNT structure for a given sensing application.

In order to examine the link between CNT structure and gauge factor, a MEMS test structure, which is used to measure CNT gauge factor, has been designed and fabricated. As seen in Figure 1.13, this test structure consists of a fixed-fixed flexure beam with electrodes connected to the base of the flexure. The outer four sets of electrodes are connected to polysilicon piezoresistors, while the inner two electrodes are left empty so that CNTs can be connected across them. These central electrodes are spaced 1 micron apart. This architecture allows the strain in the flexure to be measured simultaneously by both the polysilicon and CNT piezoresistors. The center of the flexure has a locating hole where weights can be placed to load the structure and strain the CNTs.

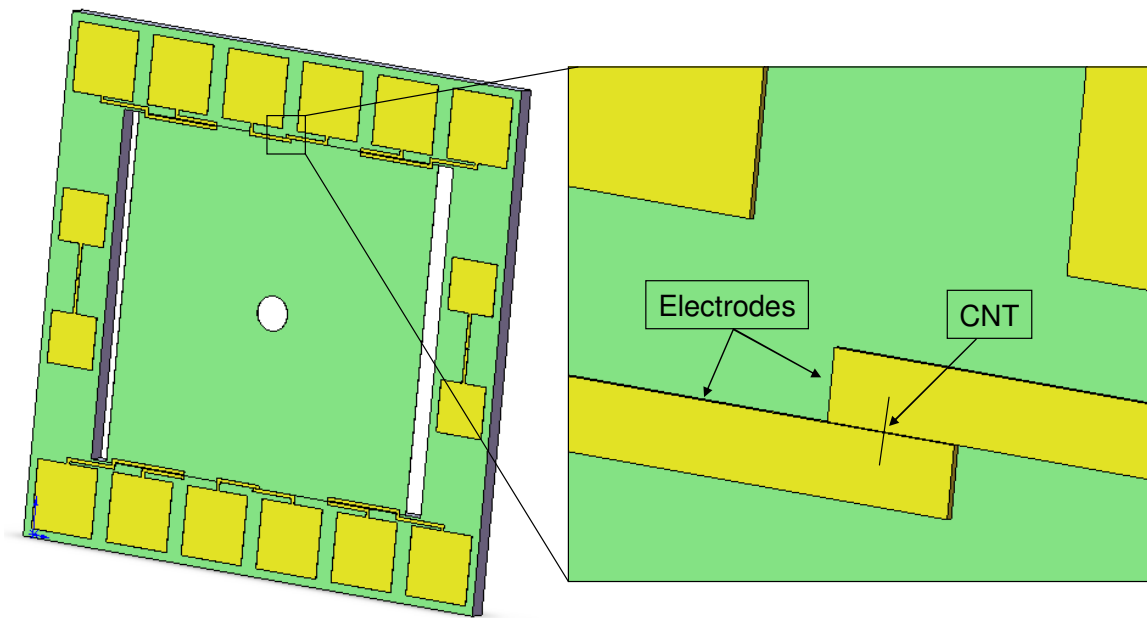


Figure 1.13: Experimental test structure.

CNTs are deposited on to the test structure by dielectrophoresis. The (n,m) chiral indices of the CNTs placed on the test structure are set through a pre-deposition sorting process. By determining both the electromechanical response of the CNTs and their chiral indices, it is possible to obtain a better understanding of the physics relating the two. In addition to

measuring the electromechanical response of the CNTs to strain, the temperature sensitivity of resistance and gauge factor is also measured. This is done by placing the test structure in a furnace and measuring how the resistance and gauge factors of the CNTs change as the structure is heated and cooled. Polysilicon piezoresistors which have well-known thermal properties are used to isolate the CNT temperature effects from the thermal effects on the test structure itself. Knowing the thermal coefficients for different CNT chiralities makes it possible to mitigate the effects of temperature fluctuations in the CNT-based strain sensors by implementing span temperature compensation and proper Wheatstone bridge design.

At the device level, the test structure is used to test the mechanical interactions between the CNT and the substrate/electrodes. For example, it is important to determine how well the strain in flexures is being transferred to the CNTs. This can be done by looking for stick-slip during the device loading and for changes in the orientation of the CNT before and after loading. Also, different anchoring techniques are used to fix the CNT in place on the substrate to see if the strain response changes. The information gained from these tests is used in combination with theory and simulations to optimize the strain transfer from the substrate to the CNT and to improve the device performance.

In addition to the mechanical interactions between the CNT and the MEMS device, the electrical interactions between the CNTs and the electrodes are investigated. For example, contact resistance between CNTs and the electrodes can be large depending on the electrode material [177,178] and anchoring technique [179,180]. Bench level tests are performed using the MEMS test structures to determine the effect of using different techniques and materials to anchor the CNTs to the electrodes. These results were used to create CNT/electrode contact resistance models and establish “best practice” techniques for manufacturing CNT-based sensor systems.

At the system level, the biggest concern limiting device performance is noise. In order to optimize the sensor performance a system-level noise model is developed that includes the noise from both the sensors and the electronics. This is done by measuring the noise from each component and feeding this noise through the electronic circuit. This makes it possible to determine the major noise sources in the system. The sensor system is then redesigned to reduce this noise by changing things such as the number of CNTs in the sensor. A flow chart of the technical approach is given in Figure 1.14.

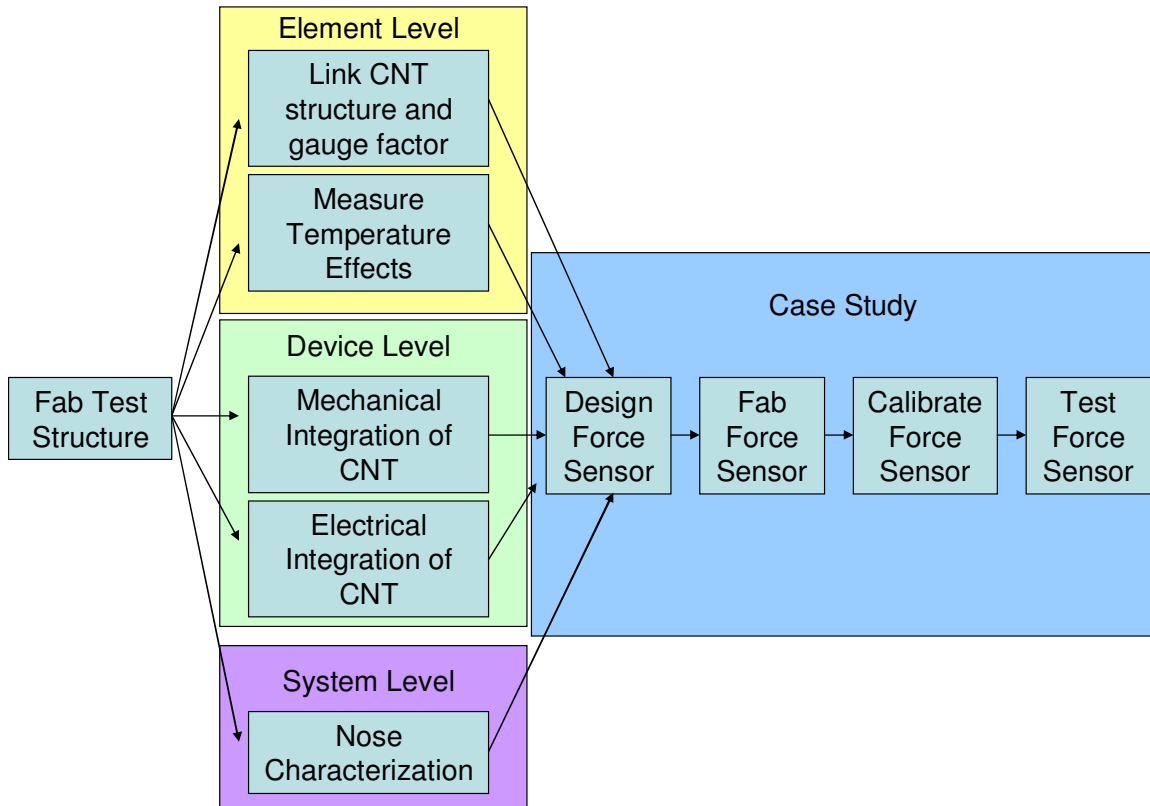


Figure 1.14: Flowchart of technical approach.

1.5.2 Case Study: 3-Axis Force Sensor with CNT-Based Piezoresistors

The purpose of the case study undertaken for this research is to use the knowledge gained in the technical approach section to design and manufacture a 3-axis force sensor with pN resolution and μN range that can be actuated using the HexFlex nanopositioner. The 3-axis force sensor is designed to fit on top of the HexFlex's central stage, as seen in Figure 1.15. In theory this may seem simple, but the knowledge gained from this research is necessary for the development of such a sensor because traditional sensing techniques cannot meet all of the 3-axis force sensor's functional requirements. Sensors such as capacitive comb drives and laser interferometry are too bulky to fit onto the central stage of the HexFlex nanopositioner. Silicon-based piezoresistors would fit into the space requirement but are not capable of achieving both the force range and resolution requirements due to their limited dynamic range. Also, silicon-based piezoresistors are sensitive to crystallographic orientation. This means that silicon

piezoresistors do not work well on structures that have nonparallel beams such as the 3-axis force sensor because the beams have different crystallographic orientations. Therefore, the CNT-based piezoresistors developed in this study are the only sensor system available that has the potential to meet all of the requirements of this sensing system.

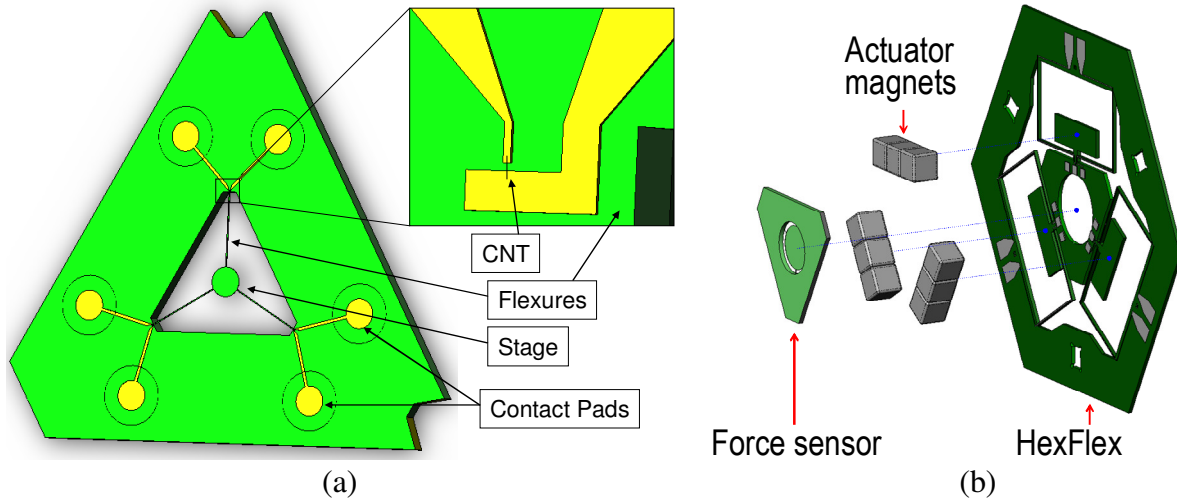


Figure 1.15: (a) Polysilicon piezoresistor based force sensor (b) Force sensor/HexFlex assembly

One application of this device is to perform the cell adhesion tests described in Section 1.1. In these tests, the HexFlex will be used to bring the stage of the force sensor into contact with the cells on the test surface. The force sensor will measure the force applied to the cells in the z-axis. Also, the measurements of the torques around the θ_x and θ_y rotations will be fed back to the HexFlex nanopositioner to ensure that constant pressure is maintained across the surface. This will allow the sensor to accurately and precisely measure the interaction between the array of cells on the surface and the surface itself. With the knowledge gained from this device, researchers may more rapidly assess how new materials, material surface designs/textures, and drug coatings improve the performance of a biomedical device. As a result, they will be able to set biological standards that will allow them to more rapidly weed-out less promising designs/materials and thereby reduce the time to market of biomedical implants.

SYSTEM LEVEL DESIGN

2.1 Introduction

Piezoresistors are widely used in microsystem sensing due to their low cost, small size, low phase lag, and large dynamic range. They have been used to create MEMS nanomanipulators [181], biocharacterization instruments [169], pressure sensors [182], inertial sensors [183], mass sensors [20], and elements of high-speed atomic force microscopes (AFMs) [20,21,23]. Designers often consider only the performance of the transducing element in the full sensing system, leading to the perception that these sensors are ‘too noisy’ for precision applications. However, excellent performance may be obtained if the design properly manages the tradeoffs between size, bandwidth, resolution, power, and dynamic range. This requires the ability to accurately predict the effect of all relevant noise sources on the performance of the full sensing system.

This chapter presents a systems approach that makes piezoresistive sensor system optimization possible. The emphasis here is on the conceptual layout of a system model, the technical details of modeling the noise sources associated with its components, and the insights and results that come from integrating the individual components to form an overview of the system’s performance. The systems approach is a reinforcement of best practices that are familiar to precision engineers, but less common for microsystem/MEMS designers. The variables used in this chapter are defined in Appendix A of this thesis.

2.2 Background

High-resolution micro-sensor systems are typically based upon piezoresistive, capacitive, or optical sensing methods. Optical methods are capable of high dynamic ranges (>200 dB [37]) but tend to be too large and expensive (>\$10,000 [37]) for low-cost microsystems. Capacitive

sensors are orders of magnitude less expensive than laser interferometers, but require large sensor areas to achieve a high dynamic range. For example, the force sensor developed by Beyeler et al. has a footprint of approximately 100 mm^2 [163] and exhibits a dynamic range of 57 dB at 30 Hz. A comparable piezoresistive sensor with the same dynamic range could be three orders of magnitude smaller. This type of comparison must be made in order to ‘squeeze’ every ounce of performance from piezoresistive systems. Such optimization is only possible, in turn, if all aspects of the systems are modeled, allowing the designer to assess the best ways to tune all components relative to each other. System models also provide more certainty in the design process, thereby reducing guesswork as well as the time required to converge on a best design.

In those applications where piezoresistive sensors can replace capacitive and optical methods, the designer must determine which type of piezoresistive material will best fit the intended use. The most common materials that are used in microsystems are single crystal silicon, polysilicon and metal film piezoresistors. Single crystal silicon piezoresistors typically have the highest dynamic range due to their high gauge factors (20 to 100 depending on doping concentration [4,171]) and low flicker noise. The gauge factor of single crystal silicon depends upon crystallographic orientation [184], however, and therefore this material is typically only used in single axis, cantilever-type force sensors [4,21,171].

For multi-axis devices, polysilicon and metal piezoresistors are typically used, given that their gauge factors are largely isotropic [14]. Polysilicon piezoresistors tend to have a lower gauge factor (10-40 depending on doping [184]) and higher flicker noise than single crystal silicon, due to the effect of grain boundaries [185,186]. Metal film piezoresistors have a significantly lower gauge factor (~ 2) than single crystal and polysilicon piezoresistors but also have nearly non-existent flicker noise due to their higher carrier concentration [20]. The optimal material choice is dependent on the measurement frequency, type of device and device footprint. the following sections discuss the information needed to make good material and geometry/design decisions that yield the best device performance.

2.3 DC Piezoresistive Sensor System Model

2.3.1 System Layout and Model

The layout in Figure 2.1 is used in this study to model the limits that noise imposes upon the sensing system. A typical piezoresistive sensor system contains a voltage source that energizes a span-temperature-compensated (STC) Wheatstone bridge and a piezoresistive element within the bridge. An instrumentation amplifier is used to boost the bridge signal, which is nulled with a bias voltage and read by an Analog-to-Digital Converter (ADC). This layout may be used to model sensors that measure a force or displacement that is applied to a compliant element.

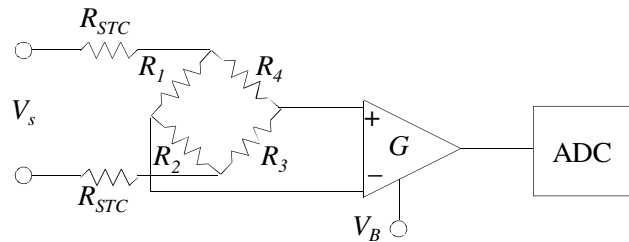


Figure 2.1. Schematic layout of DC piezoresistive sensor system.

The system model includes the relevant thermal, electrical and mechanical noise sources. These noise sources are included in the model for each subsection, as shown in Figure 2.3-2.10. The subsections are arranged as shown in Figure 2.2 to create the full system model. These figures are a visual representation the characteristic equation of each part of the sensor system. The Laplace transform of all filters, $F(s)$, in the model are assumed to be non-dimensional and to have unity, steady-state gain. All n noise sources, σ_n , are considered to be unbiased, uncorrelated, and normally distributed with spectral densities, $S_n(f)$.

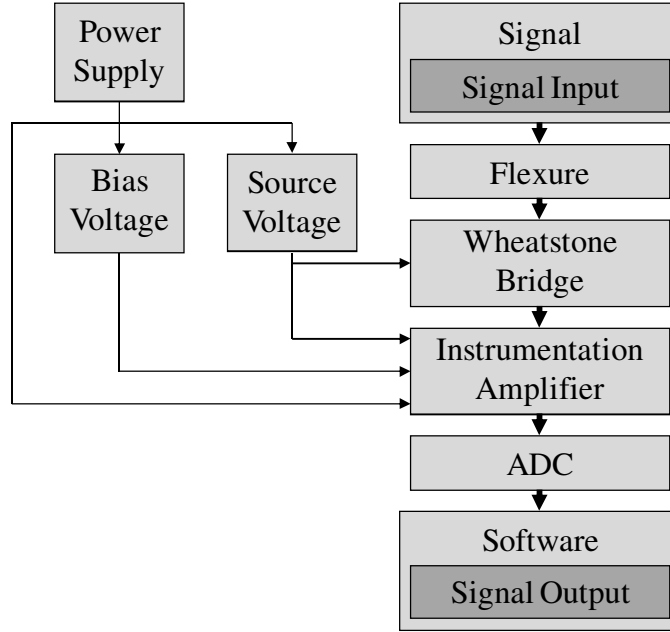


Figure 2.2. Block diagram layout of full system model.

The following inputs are applied to the compliant element: (i) a force or displacement signal, Ψ_M , (ii) mechanical noise, σ_{Mv} , e.g. vibrations, and (iii) thermomechanical noise, σ_{Mt} , with the spectral density [187]:

$$S_{M_t}(f) = 4k_B T \left(\frac{2\zeta}{k\omega_n} \right). \quad (2.1)$$

The mechanical noise scaling factor, Λ , is used to convert between displacements and forces. This factor has a unity value for displacement signals or a value of k for force signals.

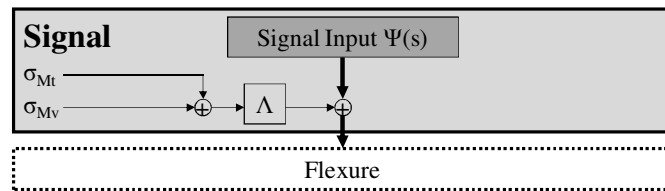


Figure 2.3. Block diagram representation of signal domain with main signal propagation path highlighted in bold

2.3.2 Flexure Model

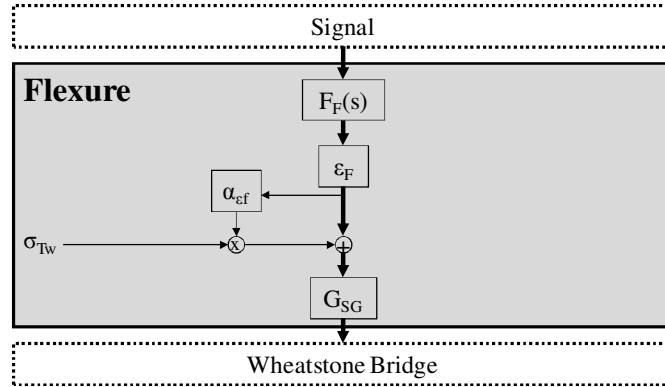


Figure 2.4. Block diagram representation of flexure domain with main signal propagation path highlighted in bold

The flexure acts as a (a) mechanical filter and (b) transducer that converts a force or displacement into a strain. The flexure behavior is therefore integrated as a gain, ϵ_F , within the model. The appropriate gain depends upon the intended use of the sensor (force vs. displacement sensing) and the grounding of the flexure (fixed-guided or fixed-free boundary). Table 2.1 lists the gains that should be used for commonly used flexures in both force and displacement sensing.

Table 2.1: Common forms of flexure gain, ϵ_F

Type of sensing	Fixed-guided	Fixed-free
Displacement	$3h_f/L_f^2$	$3h_f/(4L_f^2)$
Force	$3L_f/(N_b b_f h_f^2 E)$	$6L_f/(N_b b_f h_f^2 E)$

The strain geometry gain factor is obtained via Equation (2.2).

$$G_{SG} = \frac{1}{L_r h_r} \int_0^{h_r} \int_{L_o}^{L_o+L_r} \epsilon(x, y) \partial x \partial y = \left(1 - \frac{L_r + 2L_o}{\gamma L_f}\right) \left(1 - \frac{h_r}{h_f}\right) \quad (2.2)$$

This value is based upon an average of the strain field that is directly sensed by the piezoresistor. The strain field constant, γ , captures the effect of different flexural end conditions and has value of 1 for fixed-guided, or 2 for fixed-free boundary conditions.

2.3.3 Wheatstone Bridge Model

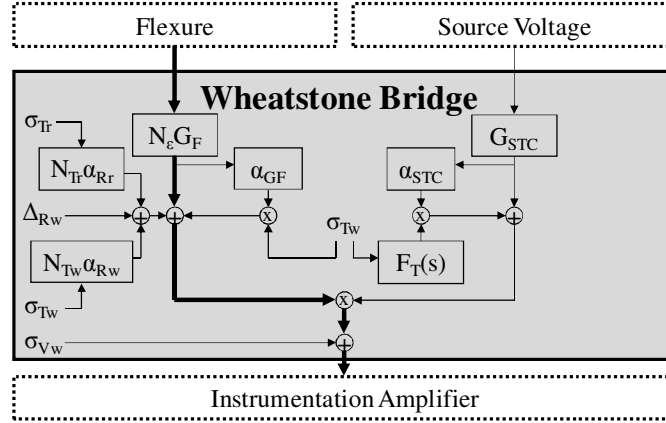


Figure 2.5. Block diagram representation of flexure domain with main signal propagation path highlighted in bold.

The signal is transformed from the mechanical domain to the electrical domain via a Wheatstone bridge. The bridge's sensitivity depends upon the bridge type. The type is defined as the number of strain sensitive resistors within the bridge divided by 4. The bridge thermal type determines how the bridge output changes with temperature and is calculated by averaging the directional (\pm) normalized thermal sensitivity for each of the piezoresistors mounted on the device. The normalization is carried out using the characteristic thermal sensitivity of the piezoresistors mounted on the device, α_{Rw} . The off-bridge thermal type is calculated in the same manner, but for the resistors located off the device such as the resistors in the electronics. The sensor noise is composed of Johnson and flicker noise. The spectral density [23,188] of this noise source is:

$$S_{V_w}(f) = 4k_B T R + \frac{V_S^2}{16} \sum_i \frac{\alpha_i}{C_{Ci} \Omega_i f} \quad (2.3)$$

The bridge voltage is attenuated by the gain of the STC, which describes the loss in bridge voltage caused by the STC resistors in series with the bridge. This gain is specifically set to have a thermal sensitivity that cancels out the thermal sensitivity of both the piezoresistors and flexure.

$$G_{STC}(dT) = \frac{\overbrace{R_W}^{G_{STC}}}{R_W + R_{STC}} \left[1 + \frac{\overbrace{R_{STC}}^{\alpha_{STC}}}{R_{STC} + R_W} (\alpha_{Rw} - \alpha_{Rstc}) dT \right] \quad (2.4)$$

The STC gain has a thermal sensitivity intended to passively cancel the gauge factor and flexure gain thermal sensitivities [25].

$$R_{STC} = \frac{R_W (\alpha_{GF} + \alpha_{Ff})}{\alpha_{Rstc} - \alpha_{Rw} - \alpha_{GF} - \alpha_{Ff}} \quad (2.5)$$

The STC and bridge resistors may be separated by some distance; therefore they may experience different temperatures. The bridge thermal filter can be used to characterize this frequency-dependent effect. Thermal variations occurs at relatively low frequencies, therefore the bandwidth of $F_T(s)$ is normally large enough to approximate as unity over the frequencies of interest.

2.3.4 Instrumentation Amplifier Model

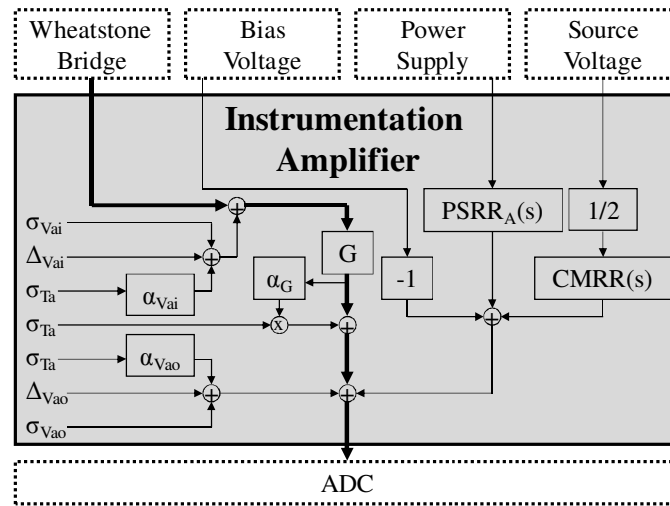


Figure 2.6. Block diagram representation of the amplifier domain with main signal propagation path highlighted in bold.

The Wheatstone bridge output signal is boosted via the instrumentation amplifier in order to scale it to the full usable range of the ADC. The required amplifier gain is calculated by constraining the maximum input to the ADC to v , which is generally 0.9, or 90% of the ADC's

full voltage range. The maximum signal is found by inputting the maximum strain safely achievable in the flexure after the flexure gain.

$$G = \frac{\nu V_{range} E \eta}{2 \sigma_Y G_{SG} N_\epsilon G_F G_{STC} V_S} \quad (2.6)$$

2.3.5 Source Voltage Model

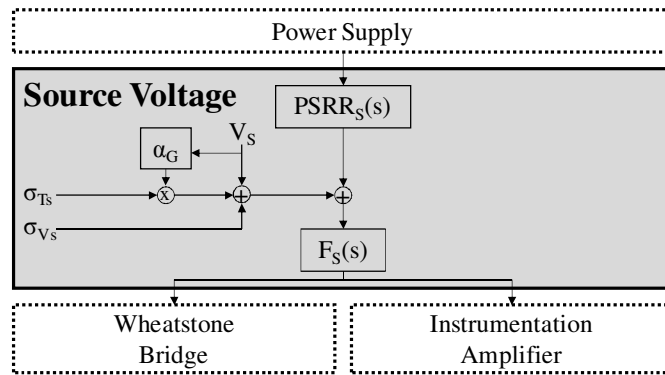


Figure 2.7. Block diagram representation of the source voltage domain with main signal propagation path highlighted in bold.

The source voltage chip provides a steady energizing voltage to the Wheatstone bridge. It is subject to electronic and thermal noise, but a filter may be used to attenuate this noise on the DC signal. Any variation in the source voltage will erroneously appear as a force or displacement signal.

2.3.6 Bias Voltage Model

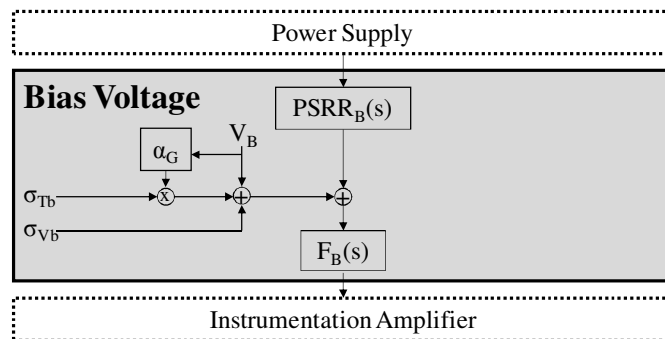


Figure 2.8. Block diagram representation of the bias voltage domain with main signal propagation path highlighted in bold.

The signal can be adjusted to the center of the operating range through the use of the bias voltage. This voltage simply provides a steady state offset for the output of the instrumentation amplifier. A filter may likewise be used to attenuate electrical or thermal noise.

2.3.7 Power Supply Model

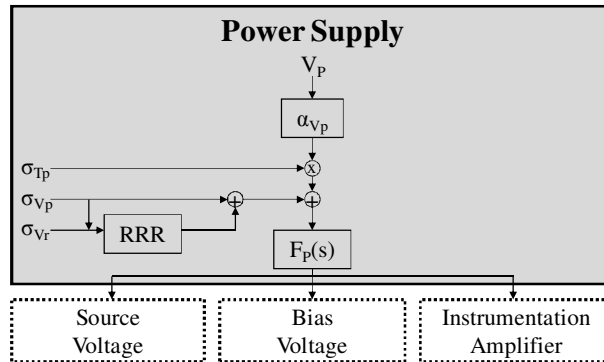


Figure 2.9. Block diagram representation of the power supply domain with main signal propagation path highlighted in bold.

The power supply can produce variations in the force or displacement signal by varying the voltage supply to the main chips in the piezoresistive sensor circuit: the source voltage, the bias voltage and the instrumentation amplifier. These effects are in general highly attenuated through power supply rejection ratios in each of the chips. A low pass filter may be used to further attenuate the electronic and thermal noise in the power supply.

2.3.8 Digital Model

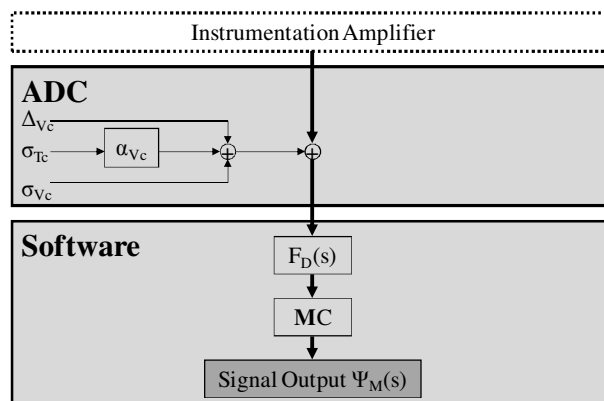


Figure 2.10. Block diagram representation of the digital domain with main signal propagation path highlighted in bold.

The ADC reads the signal into the digital domain, where it is passed through a digital filter which can be adjusted to attenuate noise outside of the signal spectrum. The signal is scaled by a calibration coefficient which is found by enforcing equality between Ψ_M and Ψ ,

$$C = \frac{1}{\epsilon_F G_{SG} N_\epsilon G_F G_{STC} V_S G}. \quad (2.7)$$

When multiple sensors are used to obtain multi-axis measurements, uncorrelated noise from each sensor is attenuated by the averaging effect of combining the multiple sensor readings, which may be written as a vector to calculate the performance of the j axes of interest. The coordinate transform matrix acts on the vector of sensor readings to produce the coordinates of the device in the desired axes.

$$M_j = \sqrt{\sum_k \mathbf{A}_{j,k}^2} \quad (2.8)$$

2.3.9 Dominant Noise Sources and System Characteristics

Partial derivatives of the model yield the sensitivity of system to noise sources. The noise spectrum is obtained by considering the effect of all noise sources. Partial derivatives for the dominant noise sources, σ_{Vw} , σ_{Vai} , σ_{Tw} , are listed below.

$$\begin{aligned} \frac{\partial \Psi_M(s)}{\partial \sigma_{Vw}} &= MCF_D(s)G \\ \frac{\partial \Psi_M(s)}{\partial \sigma_{Vai}} &= MCF_D(s)G & \frac{\partial \Psi_M(s)}{\partial \sigma_{Vao}} &= MCF_D(s) \\ \frac{\partial \Psi_M(s)}{\partial \sigma_{Tw}} &= MCF_D(s)GG_{STC}F_S(0)V_S \left[\Delta_{Rw}F_T(s)\alpha_{STC} \dots \right. \\ &\quad \left. + N_T\alpha_{Rw} + \Psi F_F(0)G_{SG}N_\epsilon G_F (\alpha_{GF} + \alpha_{\epsilon_f} + F_T(s)\alpha_{STC}) \right] \end{aligned} \quad (2.9)$$

The spectral densities from each of the n noise sources are scaled by their respective frequency dependent sensitivities and geometrically summed to obtain the full system noise spectral density:

$$S_{\psi_m}(f) = \sum_n \left| \frac{\partial \Psi_M(2\pi if)}{\partial \sigma_n} \right|^2 S_n(f) \quad (2.10)$$

The act of zeroing the sensor at the start of operation will cause attenuation of the low frequency noise. This effect may be modeled as a high-pass filter with pole frequency at $\sqrt{12} f_m$. The noise spectrum lies between f_m and f_n as seen in Figure 2.11. At frequencies greater than f_n , anti-aliasing filters heavily attenuate the noise [189].

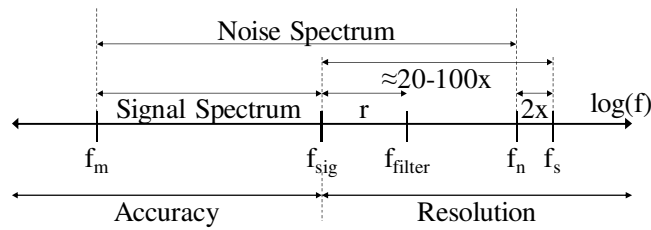


Figure 2.11. Spectral distribution of signal and relevant noise.

The signal spectrum defines the bandwidth over which a useful signal may occur. In real-time operation, oversampling by roughly 20x - 100x higher than the signal bandwidth results in minimal phase delay. The noise between f_{sig} and f_n is attenuated by the placement of a digital filter, generally located roughly 10x higher than the signal bandwidth to minimize phase delay in the signal [189].

2.3.10 Performance Metrics

The system spectral noise density is integrated over the frequency range to produce an estimate of the noise variance. The sensor accuracy is considered the pseudo-steady state measurement error ($\Psi_M - \Psi$), namely error which remains relatively constant over changes in the signal. The sensor resolution is considered the high frequency measurement error, which changes faster than the signal. From the spectral analysis viewpoint, the noise below f_{sig} is a measure of accuracy and noise above f_{sig} is a measure of resolution. The spectral range of the sensor accuracy is set 100x below f_m to ensure the estimate is within 5 percent of the actual value, up to f_{sig} .

$$\sigma_{Acc} = \sqrt{\int_{\frac{f_m}{100}}^{f_{sig}} S_{\psi_m}(f) \partial f} \quad (2.11)$$

The spectral range of the sensor resolution is set from f_{sig} up to f_n .

$$\sigma_{Res} = \sqrt{\int_{f_{sig}}^{f_n} S_{\psi_m}(f) \partial f} \quad (2.12)$$

2.4 Insights from the Model

2.4.1 Electronic Sources

The model is generalized so that it may be used with a wide range of applications. This model allows insights on best design of general and specific sensor systems. The model assumes the use of high-performance electrical components – instrumentation amplifier (Analog Devices AD624), voltage source and bias (Texas Instruments REF50xx series), and ADC (National Instruments 9215 ADC). This is essentially a best practice that ensures that these electronics are not a significant source of noise. The relevant noise values for these components are provided in the references. As shown below, sensor noise is the dominant noise source in well-designed sensing systems; therefore AC bridges are only rarely required to reduce amplifier noise. Amplifier noise is typically only dominant in metal film sensor systems that have strict limitations on power dissipation at the sensor. Metal film sensors require high amplification and show low flicker noise, allowing the amplifier noise to be dominant in these cases. An AC bridge will attenuate this noise, but adds new noise sources to the system and the secondary sources are often not far below the amplifier noise, meaning little gain in dynamic range.

When the resistance of the piezoresistor is low, noise from the instrumentation amplifier may become significant. The input noise from the amplifier is added to the signal before the signal is amplified, therefore reducing the signal output by the bridge may make the amplifier input noise the dominant source. If the signal is small, thermomechanical noise, i.e. random vibration in the beam caused by energy exchange between the flexure and environment, may become a major noise source once propagated through the electronics.

2.4.2 Mechanical Sources

The mechanical noise sources do not significantly contribute to the overall noise in most well-designed sensor systems because this is attenuated by physical filters (e.g. via optical tables) before reaching the sensor.

2.4.3 Thermal Sources

Errors caused by thermal fluctuations can generally be avoided by proper system design. The Wheatstone bridge may be thermally balanced by placing the bridge resistors close together so that they are subject to the same temperature. Similarly, STC resistors may be used to make the gauge factor and flexure gain effectively thermally insensitive.

Bridge offsets generated by manufacturing inaccuracies are compensated for by the bias voltage. The thermal sensitivity of the bridge offset, however, is unaffected by the bias voltage, as may be discerned from Equation (2.9). STC compensation is therefore only beneficial when the signal offset is less than the signal range. Thermal fluctuations can be minimized through the use of insulation or active temperature controls in cases where the manufacturing inaccuracies are large. This type of thermal control is not necessary in most cases, since relative manufacturing inaccuracies are typically small in MEMS. The noise in the piezoresistor itself generally limits the resolution of the sensor system.

2.5 Johnson and Flicker Noise

The noise in the sensor may be separated into two dominant sources: (1) Johnson noise caused by the thermal agitation of electrons in a conductor and (2) flicker noise caused by conductance fluctuations that manifest during the capture and release of charge carriers in the piezoresistor [188]. Dopant concentration affects resistivity, gauge factor and carrier concentration of silicon piezoresistors, therefore silicon piezoresistors may be Johnson- or flicker-noise dominated. There is a tradeoff between noise and sensitivity as dopant concentration is varied. Optimization for C_c as an extra variable may be performed if the link between dopant concentration, gauge factor, resistivity, and carrier concentration are known.

In the case where the performance of the sensor is limited by flicker noise, an optimal sensor length and thickness will exist. As the length and thickness of the sensor increases, the sensor volume and therefore number of carriers increases. This acts to decrease flicker noise.

The average amount of strain in the sensor also decreases as the length and thickness of the sensor increase. In balancing these two effects, optimal length and thickness may be found. The optimal sensor to flexure length ratio is $\gamma/3$. The fixed-guided condition and other boundary conditions are often found in multi-axis flexures. The optimal sensor to flexure thickness ratio for sensors embedded in the flexure is $1/3$, which is consistent with prior force sensor work [23].

2.6 Experimental Measurements and Model Verification

The noise characteristics of a simple quarter bridge ($N_e = 1/4$) polysilicon piezoresistive sensor was compared to model predictions as shown in Figure 2.12. The sensor and electronics are shielded from external noise sources. The sensor is located on a large aluminum thermal reservoir within a Faraday cage. The flicker noise characteristics of the polysilicon piezoresistive sensor were experimentally determined. The spectral density of the noise was measured from 0.01 Hz to 5 kHz, corresponding roughly to the common range of operation for such sensors.

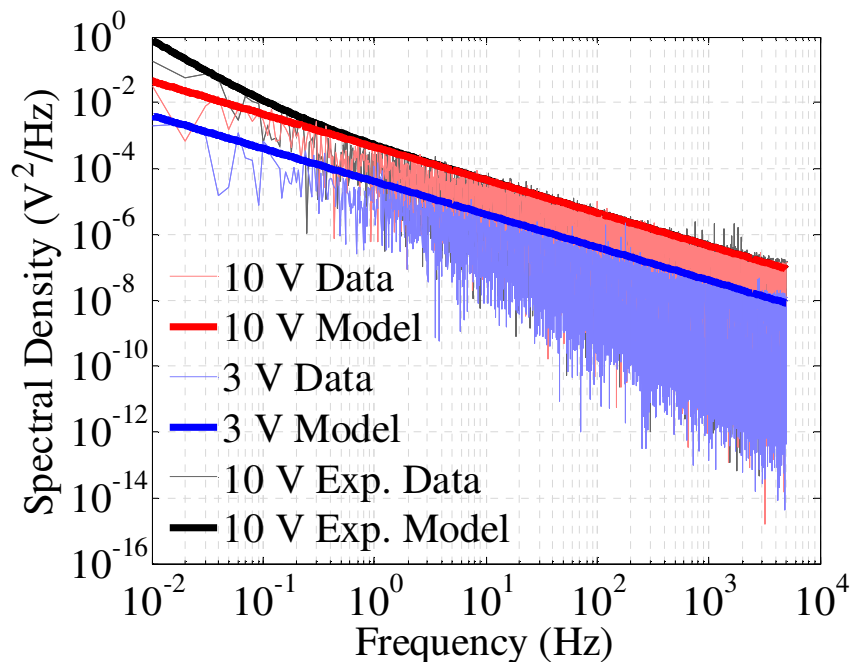


Figure 2.12. Polysilicon piezoresistive sensor noise spectrum compared to predictions.

The model indicates that the sensor flicker noise should be the dominant source over the full range of measurement when the bridge is energized at 10 V. This prediction is verified by the measured spectral density. The predicted and measured noises are 77 mV and 78 mV respectively. The model also correctly predicts the change in noise spectral density resulting from a reduction in the bridge energizing voltage from 10 V to 3 V. In the reduced voltage scenario, the predicted and measured noises are 23 mV and 21 mV respectively.

In the third scenario studied in the experiment, the electrical and thermal shielding surrounding the polysilicon piezoresistor was removed to expose the sensor to random temperature variations ('Exp. Data'). The spectral density of these temperature variations was measured and propagated through the system model to predict the effect of exposing the sensor on the noise spectral density. The electrical noise prediction was unaffected by this change, however the noise component of the prediction due to thermal effects rose significantly to become a dominant source over the low frequencies (0.01 to 1 Hz) as shown in Figure 1.13. This effect was observed in the measurements of the spectral densities with and without thermal shielding. This indicates that thermal effects on system noise can effectively be integrated into a cohesive model as described in the previous sections.

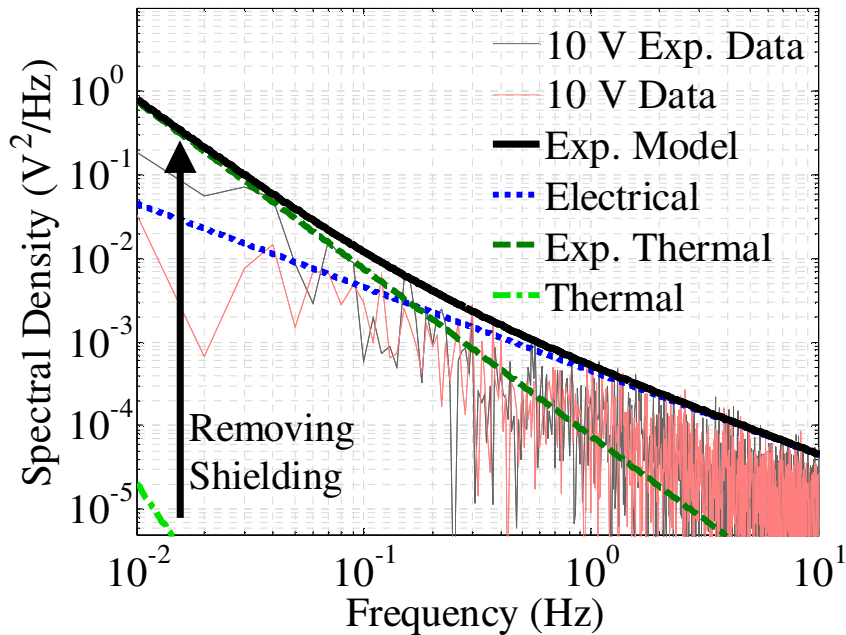


Figure 2.13. Measurement of noise spectral densities with and without thermal shielding.

2.7 Piezoresistive Sensor Design and Optimization

2.7.1 Reduced Piezoresistive Sensor System Model

One of the most important system parameters is the dynamic range, that is, the ratio of range to resolution of the system. The range and resolution are functions of the flexure geometry but the dynamic range is typically dependent only on the piezoresistor itself. Therefore, it is generally good practice to optimize the sensor system to achieve the highest practical dynamic range.

From the model it was determined that the three largest noise sources were the Johnson noise, flicker noise and instrumentation amplifier noise. In the reduced model, only these three noise sources are passed through the system to create a simplified expression for the resolution of the sensor. The dynamic range of the sensor is given in Equation (2.13),

$$DR = \frac{\sigma_y N_\varepsilon G_F G_{STC} V_S G_{SG}}{\eta EM \sqrt{4k_b TRB + \frac{V_S^2}{16} \sum_i \frac{\alpha_i}{C_{Ci} \Omega_i} \ln(r) + S_{vai} B}} \quad (2.13)$$

$$R = \frac{\rho N_r^2 L_r}{b_r h_r} \quad \Omega = L_r b_r h_r$$

The serpentine factor, N_r , describes the number of segments in the resistor. For example, $N_r = 1$ corresponds to a resistor with current flow from end to end, while $N_r = 2$ corresponds to a resistor with current flowing in a U shape through the same volume. This U-shaped flow is formed by cutting a line through nearly the full length of the piezoresistors, such that the current enters and leaves the piezoresistors on the same side. The resistor volume is the same in both cases, but the resistance has been roughly quadrupled.

The bandwidth of the noise may be written as a function of the signal frequency where the pole of the software first order, low pass filter is located at a multiple of the signal frequency. The approximation of this bandwidth is given by Equation (2.14) [188].

$$B = \frac{\pi}{2} (r-1) f_{sig} \quad (2.14)$$

This simplified model makes it possible to optimize the dynamic range of the sensing system for most cases. However, when extremely small forces or displacements are being measured, the thermomechanical noise may become greater than the noise from the instrumentation amplifier and must be added as a fourth term to the dynamic range expression. This term is dependent only on the flexure geometry, so will require a computational optimization, as described below.

Optimization of the sensor system may be carried out using a constraint based maximization procedure. In the general case, the objective function is the maximization of the dynamic range as given by Equation (2.13). However, alternate objective functions such as minimization of the force resolution may also be used. The objective function is subject to several sets of constraints. The maximization of the objective function is performed by adjusting the values of the seven system variables: L_f , h_f , b_f , L_r , h_r , b_r , and V_s . The doping concentration is another variable that may be set for some types of materials such as doped silicon.

The constraints on these variables fall into four major categories: (i) fabrication constraints, (ii) geometric constraints, (iii) voltage constraints, and (iv) performance constraints. Fabrication constraints set limits on the minimum dimensions of the flexure beams and piezoresistors. Some common geometric constraints are the device footprint, which sets the maximum size of the flexures, and flexure geometry, which sets limits on the size of the resistors. Voltage constraints are composed of power and voltage limits. Power limits are based on how much heat may be dissipated by the resistors on the flexure. This limit is used to help set the supply voltage and the resistance of the resistors in the Wheatstone bridge. Voltage limits are based on the limitations of the voltage source. Performance constraints are based on the desired operation of the device. Several common performance constraints are minimum stiffness, minimum natural frequency, maximum displacement, and maximum force.

The constraint-based solver uses a search procedure to find the maximum dynamic range for the given constraints. This is done by adjusting the values of the geometry and voltage variables. As may be seen from Equation (2.13) and the constraints, there are clear tradeoffs between variables. For example, by increasing the resistor length, the flicker noise and G_{SG} term decrease but the Johnson noise increases. The dynamic range may either increase or decrease depending on the supply voltage, Hooge constant, carrier concentration and temperature. Similar tradeoffs occur when the dimensions of the flexure are varied, since many of the resistor

constraints are directly linked to the flexure dimensions. A computer-based solver is used to optimize the sensor design due to the coupling of the resistor and flexure geometries. However, in the analytical case, a simple procedure may be used to optimize the sensor design.

2.7.2 Optimization Process

The flexure geometry may be coupled or decoupled with the sensor performance depending on the sensor system. A flow chart is shown in Figure 2.14 to illustrate the overall optimization process. The first step in the optimization is to define the basic parameters of the sensor system, f_{sig} , P_{max} , and V_{max} . The signal frequency is set by defining the signal of interest, while P_{max} and V_{max} are set by design limits. The initial values chosen for these limits should lie safely within the present constraints of the full design. For example, P_{max} is initially set such that the power generated at the sensor can be safely dissipated in the MEMS structure.

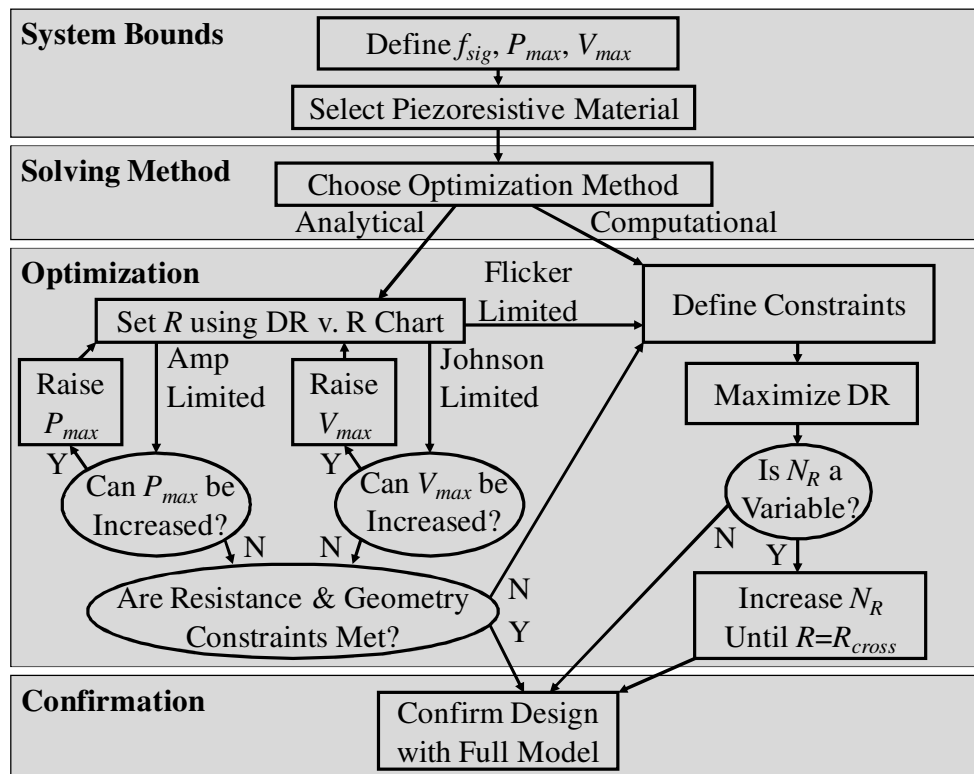


Figure 2.14. Optimization process for maximizing sensor system performance.

The three system parameters can then be used to generate a comparison between the performances of different piezoresistor materials using Figure 2.15. The material comparison

was calculated using the assumptions that $P_{max} = 100$ mW, $V_{max} = 10$ V and that the volume limit is defined by the layout of a three-axis sensor with a footprint of 100 mm² [14]. Variations in these assumptions will result in slight changes in the materials' relative performance. The proper piezoresistive material for use in a particular application may be identified from Figure 2.15. The optimal dynamic range for each material and signal frequency was calculated using the optimizing process defined in this chapter. The Johnson noise-limited regime of the chart is represented by the sloped sections of the lines and scales with $\sqrt{P_{max}}$. The amplifier-limited regime of the chart, which creates a limit parallel to the Johnson noise limit, scales with V_{max} . The flicker noise-limited regime is represented by the flat regions of the lines and scales with $\sqrt{\Omega}$. The majority of the other parameters in Equation (2.13), including the yield strain and bridge strain type, scale the material curves equally over all frequencies.

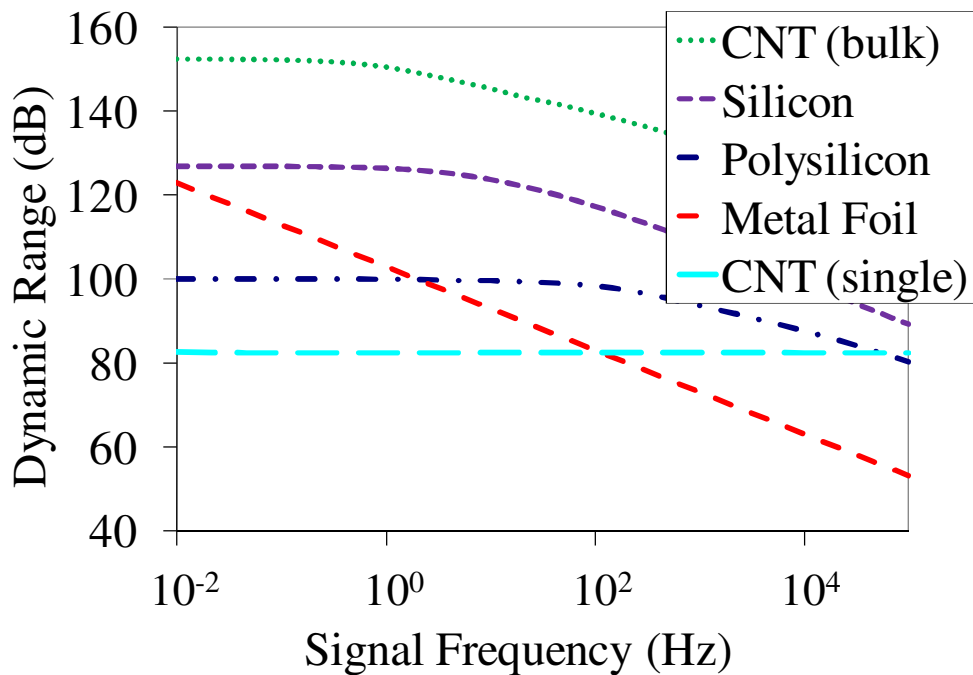


Figure 2.15. Comparison of PR sensor materials given conditions described in the example case.

Several other factors may be included when choosing a piezoresistive material. Doped silicon piezoresistors will generate the highest performance but provide the least design freedom because the piezoresistors must be aligned along specific crystal planes for maximum gauge factor. Metal foil and polysilicon piezoresistors have lower performance but offer significantly greater design freedom through a wider range of substrate materials and possible orientations.

Carbon Nanotubes (CNTs) have the lowest performance but offer the greatest design freedom due to their scale and post-fabrication assembly. Also, if multiple CNTs may be combined into a single piezoresistor with the same properties demonstrated by individual CNTs, they have the potential to outperform the dynamic range of doped silicon by up to an order of magnitude, due to their high gauge factors [9].

Two different regimes of optimization exist, analytical and computational. In the computational case, the sensor is flicker noise-limited. The piezoresistor size is increased up to the bounds defined by the flexural geometry to reduce flicker noise, but this creates a coupling between the flexure geometry and dynamic range of the sensor. In the analytic case the flexure geometry does not affect the dynamic range of the sensor as the piezoresistor size is significantly below the bounds defined by the flexure geometry. If the system is not flicker noise-limited, then a range of resistor volumes is possible, all of which generate roughly the same performance. The range is bounded on the lower end by the resistor volume becoming small enough that the sensor is again flicker noise-limited. The range of volumes means that the flexural geometry is decoupled from performance in this resistor volume range. A near-optimal solution can thus be worked out using a significantly simpler graphical process in the analytic case. The general optimization process will still provide a design with maximum performance, but may result in a more complex design process than necessary.

2.7.3 Analytical Optimization

An estimate of the resistor volume must be made to provide a rough calculation of flicker noise so that the dominant noise source can be identified. The volume estimate is found through assuming that the resistor is $\gamma/3$ times the length of the flexure, as wide as possible to fit the number of active resistors on the flexure and roughly 1/10 the thickness of the flexure for thin film resistors or 1/3 if the piezoresistor is fabricated in the flexural material. As with power and voltage limits, this produces a volume upper limit which satisfies the constraints of the present design. The upper limit on the piezoresistor length was found through maximizing for the tradeoff of volume based performance gains versus the reduction in the strain geometry gain. Length ratios above $\gamma/3$ will show overall reduced dynamic range due to G_{SG} attenuation.

The volume, power and voltage limits provide sufficient information to generate a plot of the dynamic range versus the resistance for each of the three dominant terms. The voltage term

in the Johnson and amplifier noise expressions is maximized until either the power or voltage limit is reached. Both of these expressions show a transition from power-limited to voltage-limited operation at the regime crossover resistance.

$$R_{cross} = \frac{V_{max}^2}{P_{max}} \quad (2.15)$$

The chart generated by Equation (2.13) is shown in Figure 2.13 for the example case described above. The dynamic range limits of each noise source are independently graphed. The dynamic range of the full piezoresistive sensor system traces out the limiting factor at each resistance, and at the crossover from one limiting source to another it will fall about 3 dB below the asymptotic approximations.

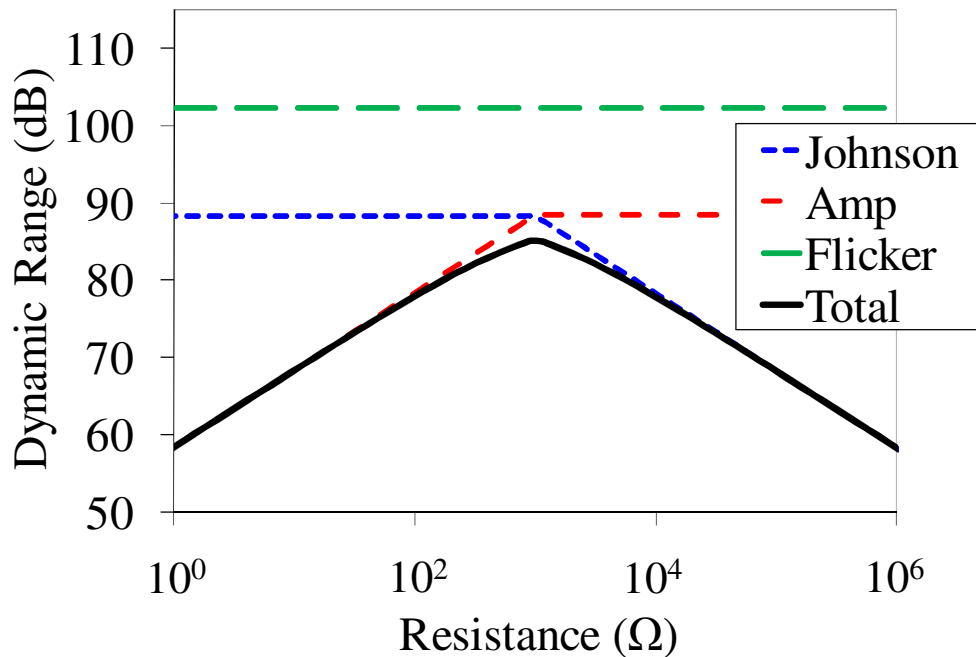


Figure 2.16. Dynamic range vs. resistance plot for amplifier and Johnson noise co-dominated system where metal film piezoresistors are used.

Johnson noise produces a constant dynamic range in the power-limited regime, and then falls off at a slope of -1 in the voltage-limited regime. When this is the dominant factor, the design should be reanalyzed with the goal of raising P_{max} . This will shift the Johnson noise

asymptotic line up. Amplifier noise produces an increasing dynamic range of slope +1 in the power-limited regime, and then holds at a constant dynamic range in the voltage-limited regime. When this is the dominant factor, the design should be reanalyzed with the goal of raising V_{max} , which will shift the amplifier noise asymptotic line up. Flicker noise produces a constant dynamic range limit over all resistances. When this is the dominant term, computational analysis is required because any further improvement in performance requires adjustment of the flexural geometry. It is usually the case that a single noise source is dominant and thus defines either a single value or a range of resistances over which nearly optimal dynamic range may be found. In the case of the example however, the volume and power limits happen to make amplifier and Johnson noise co-dominant. Therefore, both V_{max} and P_{max} would need to be raised to further increase the performance of the sensor.

After each change in the design parameters, the chart is redrawn to determine the new dominant noise source at maximum performance. If this noise source is still Johnson or amplifier noise after all possible design changes have been made, then an analytical optimization is possible. The optimal sensor design meets all three of the underlying requirements: (i) the resistance should lie on the peak or plateau of maximum dynamic range in Figure 2.16, (ii) the piezoresistor dimensions must lie within the limits described by the flexural dimensions, and (iii) the piezoresistor volume must be lie between Ω_{min} and Ω_{max} . The minimum piezoresistor volume is defined by the resistor volume at which the flicker noise rises to become equal to that of the present dominant noise source--amplifier or Johnson.

$$\Omega_{min} = \frac{\alpha \ln(r)}{C_c \frac{\pi}{2} (r-1) f_{sig}} \cdot \begin{cases} \frac{V_{max}}{S_{vai}} & \text{if amplifier limited} \\ \frac{\sqrt{P_{max}}}{4k_B T} & \text{if Johnson limited} \end{cases} \quad (2.16)$$

The variables L_r , b_r , h_r , C_c and N_r are used in this optimization. There may be a range of solutions for near optimal performance since this is no longer an optimization process: any solution which fits within the resistance, volume and geometric bounds is adequate. One method to check for possible solutions is to map the volume range, using Equation (2.17), to an effective resistance range, R_{min} to R_{max} , and compare these with the range of resistances for the optimal dynamic range described in condition (ii) above. The intersection of these two sets contains the

resistance values which meet all criteria for a valid solution. If there is no intersection between these two sets or if the solution is otherwise infeasible, then the computational optimization method is required. The serpentine factor in Equation (2.16) should be set to the minimum and maximum values available to the designer to find the resistance bounds.

$$\begin{aligned}
 R_{min} &= \frac{\rho N_r^2 \gamma^2 L_f^2 \Omega_{min}}{9 \Omega_{max}^2} \\
 R_{max} &= \frac{\rho N_r^2 \beta^2 L_f^2}{\Omega_{min}}
 \end{aligned}
 \tag{2.17}$$

2.8 Computational Optimization

The solution to the sensor optimization is dependent on the imposed constraints when flicker noise is dominant. The type and number of constraints are unique to each design. A constraint-based solver is used to maximize the dynamic range of the sensor system.

In the flicker noise-limited regime, the dynamic range of the sensor system may be rewritten as a function of R and L_r . The term G_{SG} reduces to a constant because optimal resistor-to-beam length and thickness ratios exist for the flicker regime. This simplification removes the dependence of Equation (1.13) on L_f and h_f . The resistor volume may be written as a function of both the R and L_r variables as shown in Equation (2.18). The supply voltage is also a function of R and is set by either the voltage limit of the voltage source or the power limit of the resistor.

$$\Omega = \frac{\rho N_r^2 L_r^2}{R}
 \tag{2.18}$$

The removal of the two flexural variables in the flicker noise regime simplifies the dynamic range expression sufficiently to allow the operating surface of the optimizer to be visualized for the example design, as shown in Figure 2.17.

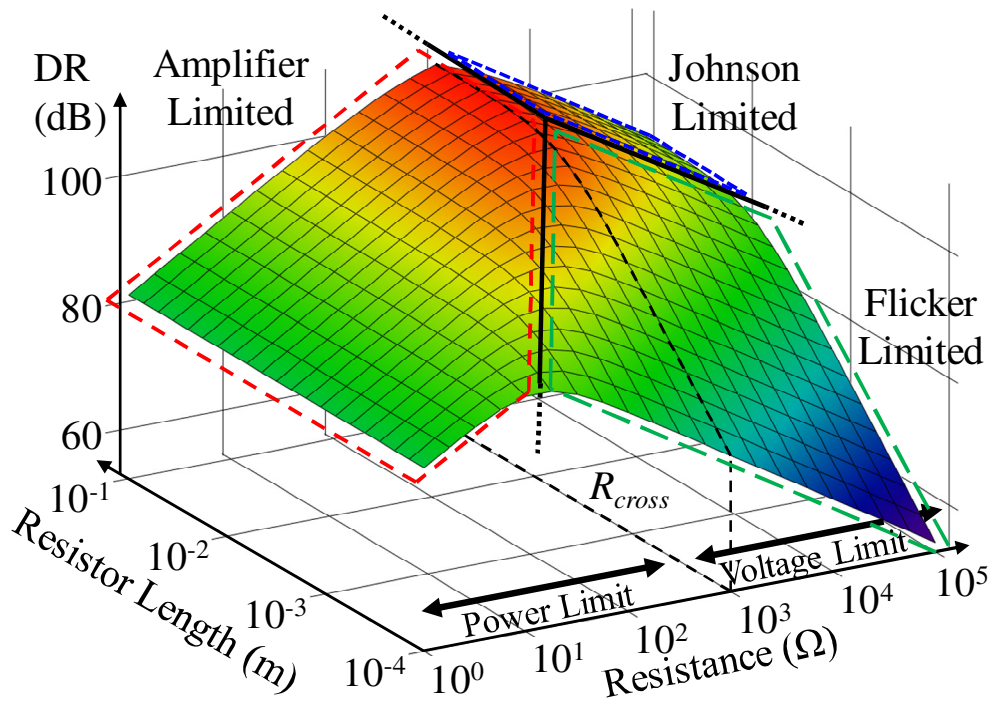


Figure 2.17. Operating surface of constraint based optimization. Constraints are mapped to this surface.

A constant L_r slice of Figure 2.17 differs from Figure 2.14 in that the resistance is now directly linked to the volume. In Figure 2.16 it was assumed that $L_r \ll L_f$ so that L_r could be freely varied to effectively decouple R and Ω . In the coupled flicker noise regime, L_r is not necessarily able to change, as it is optimized to a maximum. This results in an apparent inverse relationship between R and Ω .

The optimal value on this surface is found by mapping all of the constraints onto this surface. Unfortunately, far more than two variables are needed to define the constraints, so these boundaries cannot be plotted on a three dimensional surface plot. It is possible to see from the surface plot that the maximum dynamic range in the flicker noise-dominated regime trends towards the low resistance corner at the intersection of flicker and amplifier noise asymptotes. The constraint-based solver will tend towards the lower resistance end of the plateau defined by the flicker noise line in Figure 2.18 to increase the volume of the resistor and thus boost the sensor dynamic range.

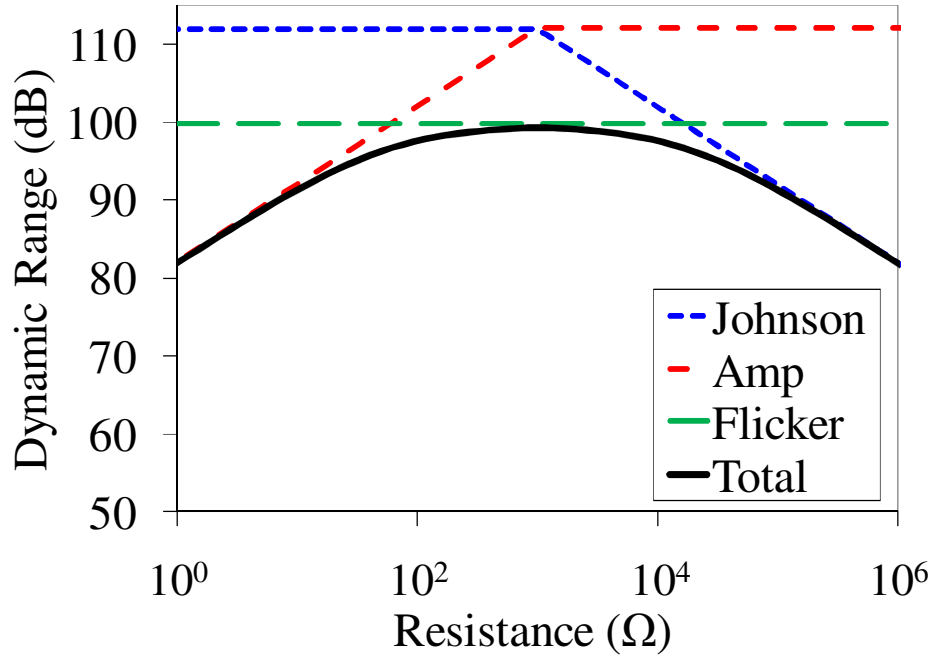


Figure 2.18. Dynamic range vs. resistance plot for flicker noise dominated system where polysilicon piezoresistors are used.

A measure of decoupling may be gained in the design through N_r . This is because N_r may be used in Equation (2.18) to increase the resistance without further reducing the piezoresistor volume. The benefit of this increase is that raising R up to R_{cross} increases the dynamic range of the sensor by reducing the subordinate noise sources. However, care needs to be taken when adjusting N_r in the optimization process since highly folded resistor geometries can significantly increase the complexity of the MEMS fabrication process, while only resulting in small performance gains.

A successful computational optimization will always result in a higher-performance device than the analytical optimization. The analytical optimization is focused only on minimizing the dominant noise source when used for Johnson- and amplifier-limited systems. In fact, the subordinate flicker noise still marginally contributes to the dynamic range. The computational optimization takes this into account and maximizes the dynamic range of both the dominant and subordinate noise sources. The tradeoff between the two optimizations is between the level of coupling/complexity in the design and the performance. In the flicker noise-limited regime there is a strong link between these two, so large gains in performance may be found through increasing the complexity of the design process. In the other two regimes the link may

be very weak such that little performance is gained for the same increase in the design process complexity.

2.9 Conclusion

As shown in this chapter, the piezoresistor itself is generally the limiting element in the piezoresistive sensor system when proper modeling and optimization procedures are used to design the systems. In order to improve the performance of piezoresistive sensor systems, better piezoresistors should be developed. Novel materials, such as carbon nanotubes, offer the potential to increase sensor performance by more than an order of magnitude due to their high gauge factors [9]. However, more research needs to make these types of sensors feasible for MEMS piezoresistive sensor systems.

CNT PIEZORESISTOR THEORY

3.1 Introduction

As mechanical devices move towards the nano-scale, smaller and more sensitive force and displacement sensors are required to measure and control their behavior. For example, multi-axis micro- and nano-scale sensors with nanometer displacement resolution and/or piconewton force resolution are needed in many biological, materials science, and nanomanufacturing applications. Unfortunately, these resolutions are difficult to achieve given the size, sensitivity and fabrication limitations associated with existing small-scale sensing techniques. Carbon nanotube-(CNT) based strain sensors are attractive as force and displacement sensors since they are not subject to the same limitations. However, CNT-based sensors cannot be realized in a practical way unless their performance in strain sensing systems can be modeled and predicted.

The physics and fabrication of traditional MEMS sensing technologies do not scale favorably with geometric downscaling. Therefore, the practical utility of traditional sensing technologies is limited at the micro/nanoscale. For example, the resolution of capacitive sensors scales with sensor area, making fine resolution sensors too large for many micro/nanoscale sensor systems. Similarly, interferometry becomes impractical at the micro/nanoscale because of the relatively large optics that are required. Fine resolution, silicon-based piezoresistive sensing techniques are easily fabricated within meso-scale devices, but are difficult to realize in nano-scale devices due to limitations associated with photolithography and ion implantation.

These factors foster the need to identify technologies that are less problematic and advance their performance via new approaches. The dominant physics of CNT-based strain sensors do not preclude practical utility at the micro- and nano-scales. Nanoscale fabrication of CNT-based transducers is not limited by lithography or ion implantation since CNTs are inherently nanoscale materials. Also, CNTs have characteristics that yield increased performance and

sensitivity. CNTs have been shown to have gauge factors in excess of 2900 [1]. This is about an order of magnitude larger than silicon-based piezoresistors. These properties make CNTs the optimal sensors for fine resolution micro- and nanoscale flexural transducers.

A better understanding of the link between applied strain and resistance is required in order to realize the potential of CNT-based transducers. This chapter presents a theoretical model of CNT gauge factor that is based upon tight binding and zone-folding approximations. With this model, it is possible to (i) identify the types of CNTs that are most sensitive to strain and therefore best-suited for use in high-resolution CNT-based flexural transducers, and (ii) evaluate the piezoresistance of CNT films.

3.2 Prior Art

Early experiments have showed that CNTs have the potential to be high quality strain sensors. For example, Tombler et al. [46] used AFM tips to depress, and therefore strain, a suspended CNT. Using this method they showed that the conductance of a CNT may change by two orders of magnitude when strain is applied. Simulations showed that this result may have been the result of local deformations in the CNT structure around the AFM tip as opposed to uniform strain in the CNT [48,49]. However, later experiments that uniformly strained the entire CNT showed that CNT gauge factor could be as high as 2900 [1]. Also, gauge factor has been shown to vary widely with the electrical structure of a CNT [47,50,51]. For example, Grow et al. showed that CNT gauge factor could be positive or negative [51]. Given the sensitivity and variability of gauge factor with structure, the creation of practical devices can only happen if one has the ability to specify the CNT that is best suited for a specific sensing application.

Theory and simulation have been used to predict the relationship between structure and gauge factor. These models and simulations are typically used to estimate the change in band-gap between different types of CNTs. Gauge factor is then found by relating the band-gap to CNT resistance. For example, Chen et al. showed that a 1 percent strain of a (12,0) CNT should result in a 6.4 percent decrease in resistance [52]. Yang et al. [190] used tight-binding models to show that CNT band-gap could increase or decrease depending upon the chirality of the CNT. These results have been confirmed using more detailed molecular mechanics simulations [191] and first principles calculations based on the generalized gradient approximation which includes

effects due to σ^* - π^* hybridization [192]. Unfortunately, little quantitative work has been undertaken to link specific CNT geometries to gauge factors.

3.3 Theoretical Model

3.3.1 Background on Tight-Binding Model

In general, there are two approximation methods that can be used to calculate the electronic energy bands in a material: free-electron approximation and tight binding approximation. In the free-electron approximation, electrons are allowed to move as free particles in the crystal, subject only to the periodic potential produced by the atoms in the crystal lattice and interacting only with other electrons. This approach allows the electrons to be modeled as plane waves and starts from the parabolic dispersion of a free particle. In the tight binding approximation, electrons are assumed to be tightly bound to the atoms in the solid and to be spaced at periodic atomic distances. This causes the valence electrons in different atoms to interact because of the overlap between electronic wave functions from different atoms. Because of these interactions, electronic bands are formed in the solid which can be used to predict the electronic structure of the material. For carbon based materials such as graphene and CNTs, the tight-binding approximation works exceptionally well and is commonly used to calculate the valence and conduction bands [193].

Since CNTs are rolled-up sheets of graphene, it is useful to look at the tight-binding description of graphene. In graphene, electronic wave functions from different carbon atoms overlap when they are placed in the hexagonal lattice of graphene. However, the p_z orbital does not overlap with the s , p_x , or p_y orbitals because the p_z orbital is out of the plane of the graphene sheet while the other orbitals are in its plane. Therefore, the p_z orbital can be treated independently from the other orbitals. This is important because it is the p_z orbital which forms the π -bonds in graphene and is responsible for the electronic structure of graphene.

In order to find the electronic band structure of the graphene π -orbitals it is necessary to solve Schrodinger's equation

$$H\Psi(\mathbf{k}) = E(\mathbf{k})\Psi(\mathbf{k}) \quad (3.1)$$

where H is the Hamiltonian, $E(\mathbf{k})$ are the eigenvalues at wave vector \mathbf{k} , and $\Psi(\mathbf{k})$ are the eigenfunctions. The eigenfunctions can then be written as a linear combination of Bloch functions $\Phi(\mathbf{k})$.

$$\Psi(\mathbf{k}) = \sum_l C_l \Phi_l \quad (3.2)$$

When the tight-binding approximation is employed, the Bloch functions can be written for each sub-lattice (A or B) in the unit cell as linear combinations of the atomic wave functions for each unit cell as seen in Equation (3.3), where N is the number of unit cells in the solid, \mathbf{R} is a lattice vector and $\varphi(\mathbf{r})$ is the isolated $2p_z$ orbital in the carbon atom.

$$\Phi_{A,B} = \frac{1}{\sqrt{N}} \sum_{\mathbf{R}_{A,B}} e^{i\mathbf{k}\cdot\mathbf{R}_A} \varphi(\mathbf{r} - \mathbf{R}_{A,B}) \quad (3.3)$$

To solve Equation (3.1), we can substitute in the linear combination of the Bloch functions as described in Equation (3.2) and solve for the determinant of the Hamiltonian and overlap matrix. If we assume that only the nearest neighbor atoms interact with each other, then we can solve for the electronic band structure as shown in Equation (3.4), where k_x and k_y are reciprocal lattice vectors, ε_{2p} is the energy of the $2p_z$ orbital modified by the periodic potential of the crystal Hamiltonian, γ_0 is the carbon-carbon interaction energy known as the tight-binding integral, s_0 is the overlap integral and $f_{xy}(\mathbf{k})$ is given by Equation (3.5). This nearest neighbor approximation is only valid for the small part of the Brillouin zone near the K point.

$$E^\pm(k_x, k_y) = \frac{\varepsilon_{2p} \pm \gamma_0 \sqrt{f_{xy}(k_x, k_y)}}{1 \pm s_0 \sqrt{f_{xy}(k_x, k_y)}} \quad (3.4)$$

$$f_{xy}(k_x, k_y) = 3 + 2 \cos(a_0 y) + 4 \cos\left(\frac{a_0 \sqrt{3}}{2} x\right) \cos\left(\frac{a_0}{2} y\right) \quad (3.5)$$

Based on these equations the band structure of graphene can be calculated as shown in Figure 3.1.

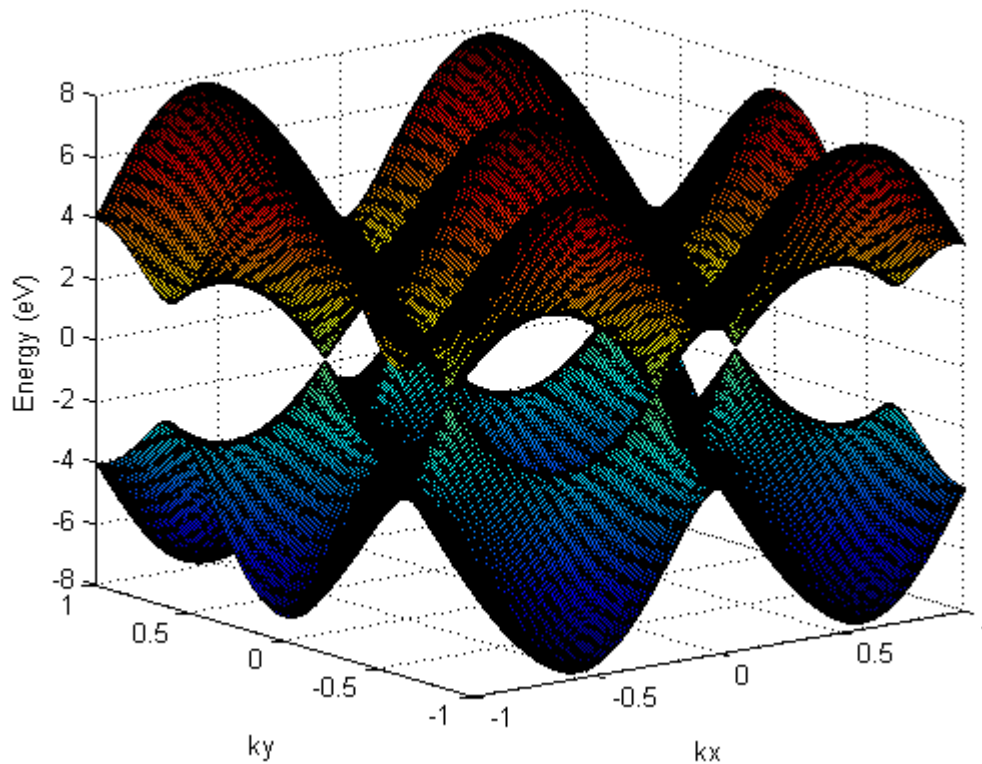


Figure 3.1. Band structure of graphene.

From the band structure of graphene, the electronic properties of CNTs can be found by utilizing the zone-folding approximation. In this approximation, the electronic band structure of the nanotube is given by the graphene electronic energies along allowed wave vectors. In the carbon nanotube, the allowed wave vectors around the nanotube circumference are quantized and only take discrete values while along the nanotube axis the wave vectors are continuous. This means that the length, number and orientation of the allowed wave vectors in the carbon nanotube depend on the chiral indices of the CNT. The band structure of a carbon nanotube can be found by tracing the allowed wave vectors on Brillouin zone of graphene. For example, the projection of the valence and conduction bands of a zigzag CNT is found by setting $k_x=0$ as shown in Figure 3.2.

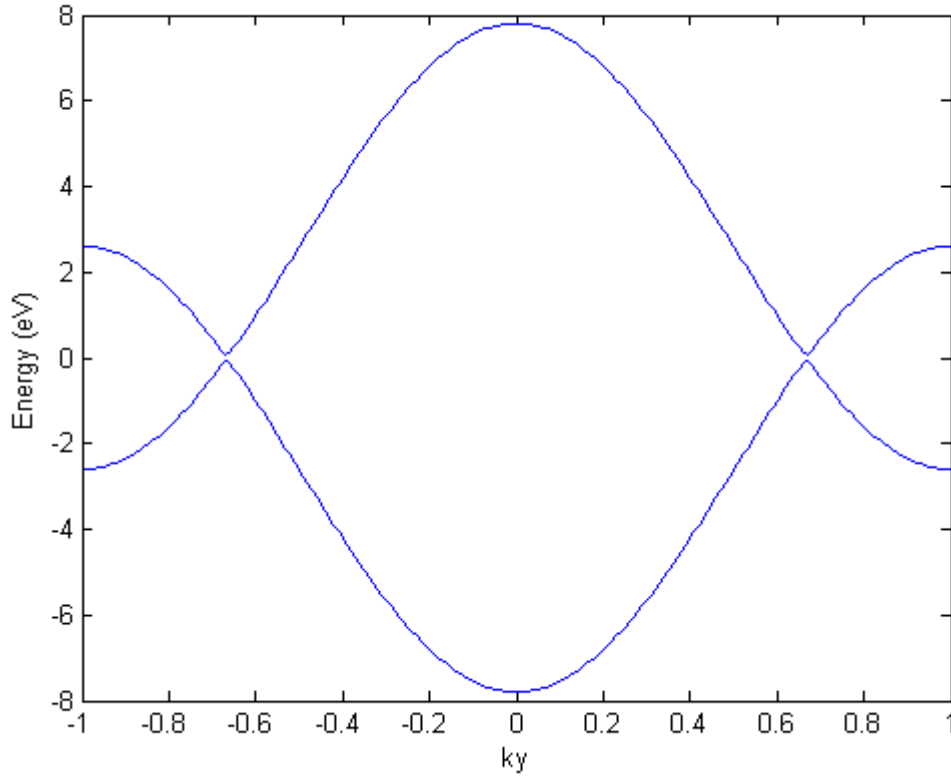


Figure 3.2. Γ -K axis projection.

From Figure 3.2, it can be seen that for zigzag CNTs the band gap is maximized at the Γ point ($k_x = 0, k_y = 0$) and is equal to $6\gamma_0$. Also, for zigzag CNTs the band gap is zero at the K point ($k_x = 0, k_y = 2/3$). Similarly, the band structure of armchair CNTs can be found from the graphene projection along the Γ -M axis by k_y to zero as shown in Figure 3.3. From Figure 3.3 it can be seen that the band gap is maximized at the Γ point ($k_x = 0, k_y = 0$), where it is equal to $6\gamma_0$ and is minimized at the M point ($k_x = \frac{1}{\sqrt{3}}0, k_y = 0$), the band gap is reduced to $2\gamma_0$. These representative band structures show why zigzag CNTs are always metallic while armchair CNTs can be semiconducting.

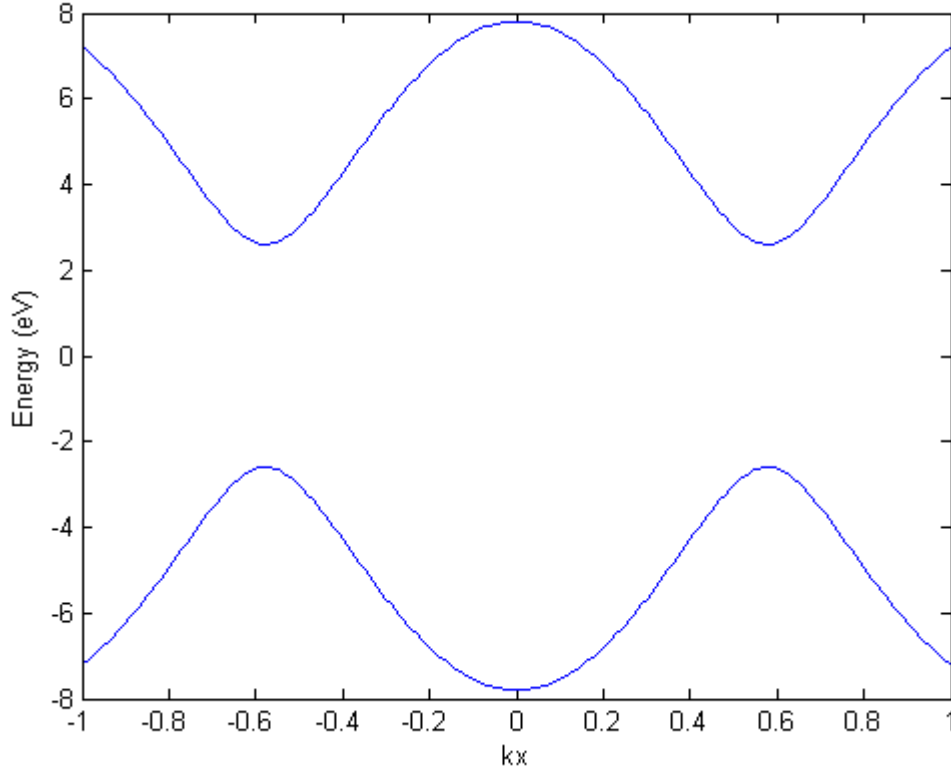


Figure 3.3. Γ -M axis projection.

3.3.2 CNT Gauge Factor Model

The approach used in this study is based upon the tight binding model Mintmire and White [194,195] use to predict the electronic structure of an undeformed CNT near the Fermi level. Yang and Han [53] showed that this model could be extended to relate chiral angle and strain to the shift of the Fermi point, \mathbf{k}_F , away from Brillouin zone vertices. The CNT may be thought of as a graphene sheet rolled up into a cylinder along the lattice vectors \mathbf{a}_1 and \mathbf{a}_2 , as shown in Figure 1a.

The electronic states near the Fermi point may be analyzed using the first Brillouin zone of graphene as defined by the reciprocal lattice vectors \mathbf{K}_1 and \mathbf{K}_2 . In an undeformed lattice, the Fermi points lie on the vertices of hexagonal Brillouin zone. The allowed electronic states, given by the Born-von Karman boundary condition, lie on parallel lines, \mathbf{k} , which are perpendicular to the lattice vector \mathbf{C} , as seen in Figure 3.4b. The variations in electronic states that are induced by

strain may be found by measuring how the Fermi point moves with respect to the lines as strain is applied.

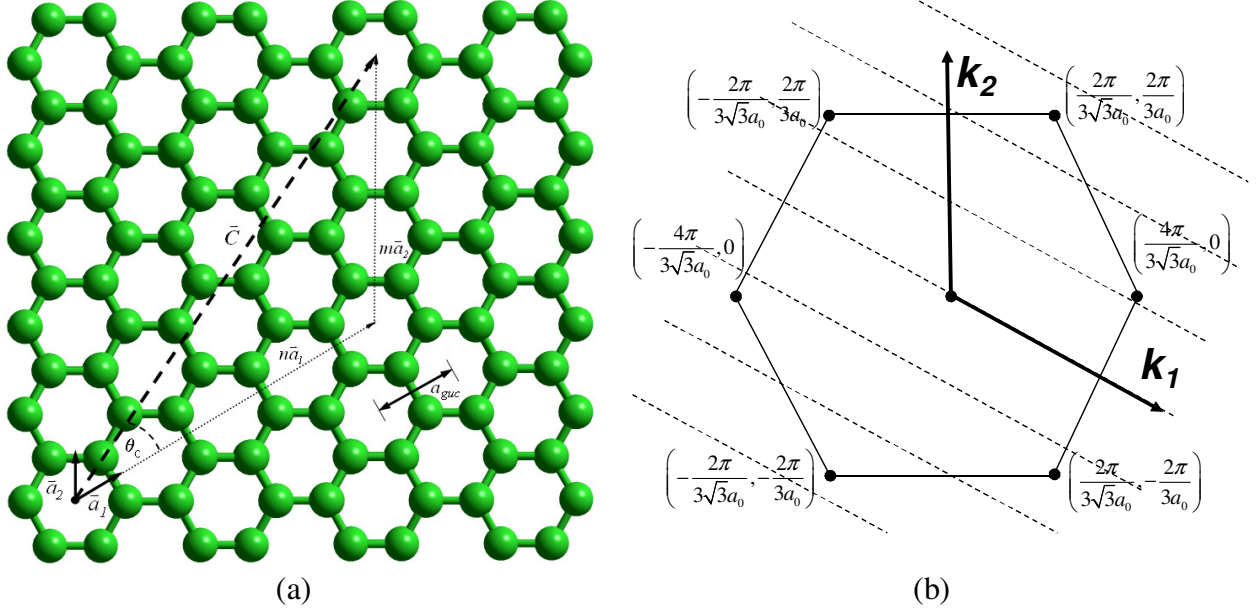


Figure 3.4: (a) CNT chiral vectors (b) Graphene first Brillouin zone with allowed electronic states.

The Fermi point may be found by solving the tight-binding equation:

$$E(k_F) = \left| \sum \frac{t_0 r_0^2}{r_i^2} e^{ik \cdot \mathbf{R}_i} \right| \quad (3.6)$$

where r_0 is the original bond length, r_i is the deformed bond length, t_0 is the tight-binding overlap integral and \mathbf{R}_i is the deformed bond vector. Yang et al. [190] solved this equation and showed that

$$\Delta k_F r_0 = (1 + \nu) \varepsilon \cos 3\theta + \gamma \sin 3\theta \quad (3.7)$$

where ν is the Poisson's ratio, θ is the chiral angle, ε is the axial strain and γ is the torsional strain. The dispersion relation of the deformed graphene may then be found by expanding $E(k)$ at k_F :

$$E(\mathbf{k} - \mathbf{k}_F) = \pm \frac{3}{2} t_0 r_0 |\mathbf{k} - \mathbf{k}_F| \quad (3.8)$$

When Equations (3.7) and (3.8) are combined, the change in band gap for small strains may be calculated, as shown in Equation (3.9). The sign of the band gap change is determined by the chiral indices such that $p = -1, 0$, or 1 depending on the value of $\text{mod}(n-m, 3)$ [53].

$$\Delta E_{gap} = \text{sgn}(2p + 1) 3t_0 \left[(1 + \nu) \varepsilon \cos 3\theta + \gamma \sin 3\theta \right] \quad (3.9)$$

This equation works well for semiconducting and armchair CNTs with diameters larger than 1 nm [196]. For smaller CNTs and for primarily metallic CNTs, curvature may play a large role in the gauge factor and therefore must be accounted for in the band-gap theory [197-199]. In this case a similar, nearest neighbor tight binding approach is used that captures the intrinsic curvature of the CNT. For primarily metallic CNTs, Kleiner and Eggert [200] showed that:

$$\Delta E_{gap} = -\text{sgn} \left(\frac{t_0 a^2}{4d^2} - \frac{ab\sqrt{3}}{2} \right) \frac{ab\sqrt{3}}{2} \varepsilon \cos 3\theta \quad (3.10)$$

where a is the length of the graphene lattice unit vector, d is the diameter of the CNT, and b is the change in the transfer integral with change in bond length.

The change in electrical resistance due to strain can be calculated based on band-gap changes. The resistance of a CNT can be accurately modeled by considering electron transport to occur by thermal activation [47]. This model is given in Equation (3.11), where lt^2 is the transmission probability that electrons with $|E - E_F| > E_{Gap}$ will cross the energy barrier, R_c is the contact resistance, h is Plank's constant, e is the charge on an electron, k is Boltzman's constant and T is temperature in degrees Kelvin.

$$R = R_c + \frac{1}{|t|^2} \frac{h}{8e^2} \left[1 + \exp \left(\frac{E_{Gap}^0 + \frac{dE_{Gap}}{d\varepsilon} \varepsilon}{kT} \right) \right] \quad (3.11)$$

The zero strain band gap, E_{Gap}^0 , is [10]

$$E_{Gap}^0 = \frac{2t_0 a}{\sqrt{3}d} \quad (3.12)$$

for a semiconducting CNTs and [198]

$$E_{Gap}^0 = \frac{t_0 a^2}{4d^2} \quad (3.13)$$

for a metallic CNTs.

The gauge factor for any set of chiral indices may be calculated using Equations (3.11)-(3.13). Gauge factor for any material is defined by Equation (3.14).

$$G_F \varepsilon = \frac{\Delta R}{R} \quad (3.14)$$

When Equation (3.11) is substituted into Equation (3.14), it can be shown that when $R_c \ll R$:

$$G_F = \frac{\frac{dE_{Gap}}{d\varepsilon} \exp\left(\frac{E_{Gap}^0 + \frac{dE_{Gap}}{d\varepsilon} \varepsilon}{kT}\right)}{kT \left[\exp\left(\frac{E_{Gap}^0 + \frac{dE_{Gap}}{d\varepsilon} \varepsilon_0}{kT}\right) + 1 \right]} \quad (3.15)$$

where ε_0 is the pretension strain. Using this equation, the gauge factor for a specific CNT may be calculated by inserting Equations (3.9) and (3.12) for semiconducting CNTs, or Equations (3.10) and (3.13) for metallic CNTs, into Equation (3.15).

3.4 Model Evaluation

Equation 10 predicts an exponential dependence of gauge factor upon strain, which is consistent with observations [1]. From Equations (3.9)-(3.15), it may be seen that (i) the maximum magnitude of gauge factor occurs in zig-zag (n,0) CNTs and (ii) the gauge factor decreases as the chiral angle increases, until a gauge factor of zero is reached for armchair CNTs (n,n). This trend, seen in Figure 3.5, shows the behavior for five CNTs with diameters of ~1.38 nm.

The CNTs in Figure 3.5 show two distinct trends. The gauge factors of CNTs where $p=1$ are positive and increase towards infinity with increasing strain. This trend is consistent with the results observed by Stampfer et al [1]. The gauge factors of the CNTs where $p=-1$ are negative and increase towards zero with increasing strain. This is consistent with results observed by Grow et al [51]. These two trends are the result of the exponential term in Equation (3.15), where the sign of $dE_{Gap}/d\varepsilon$ determines whether the exponential increases toward infinity or approaches zero. Also, Figure 3.5 shows that the (10,10) CNT has a gauge factor of zero for all strains. This result is consistent with previously results for armchair CNTs [201].

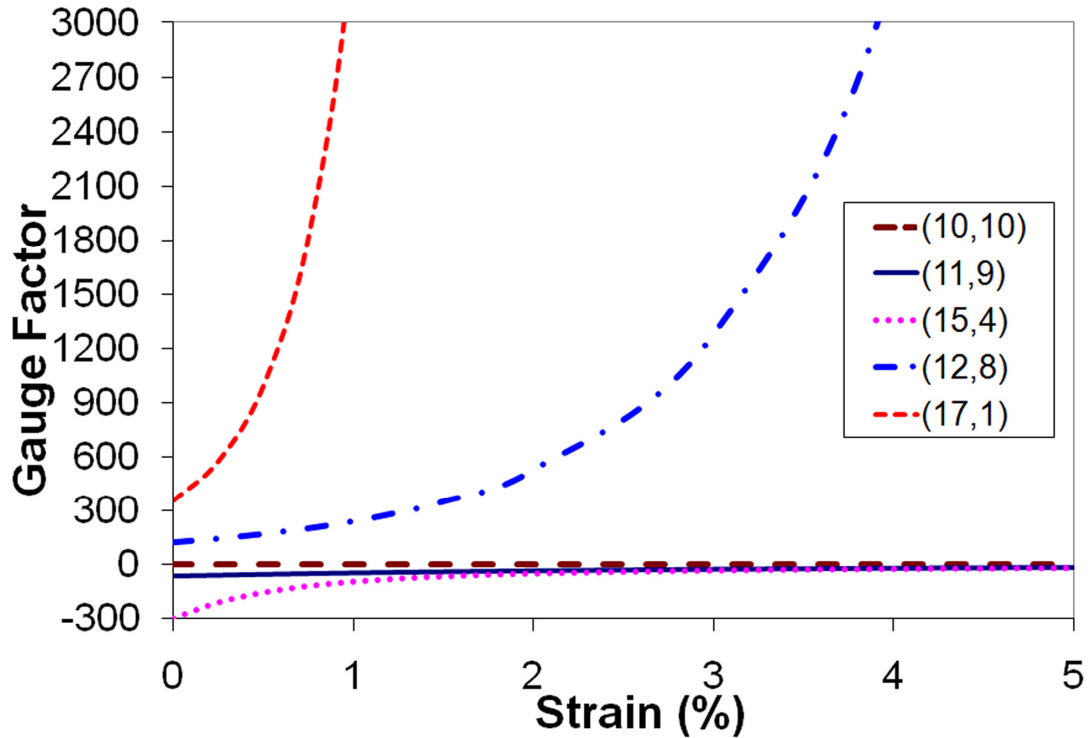


Figure 3.5. Gauge factor vs. strain for CNTs with diameters of 1.38 nm.

These trends may be better understood by examining how resistance changes with strain. From Figure 3.6 it may be seen that the resistance of (17,1) and (12,8) CNTs increases exponentially with strain, while the resistance of (15,4) and (11,9) CNTs decreases exponentially with strain. These trends give rise to the observed exponential dependence of gauge factor with strain as seen in Figure 3.5. It is also important to note the magnitude of the slope of resistance vs. strain in Figure 3.6. The magnitude decreases as the chiral angle increases. This is responsible for the differences in gauge factor sensitivity to strain that was shown in Figure 3.6. In general, the constant gauge factor approximation (i) holds over large strain ranges as the chiral angle increases and (ii) is more accurate for metallic CNTs than semiconducting CNTs with similar chiral angles.

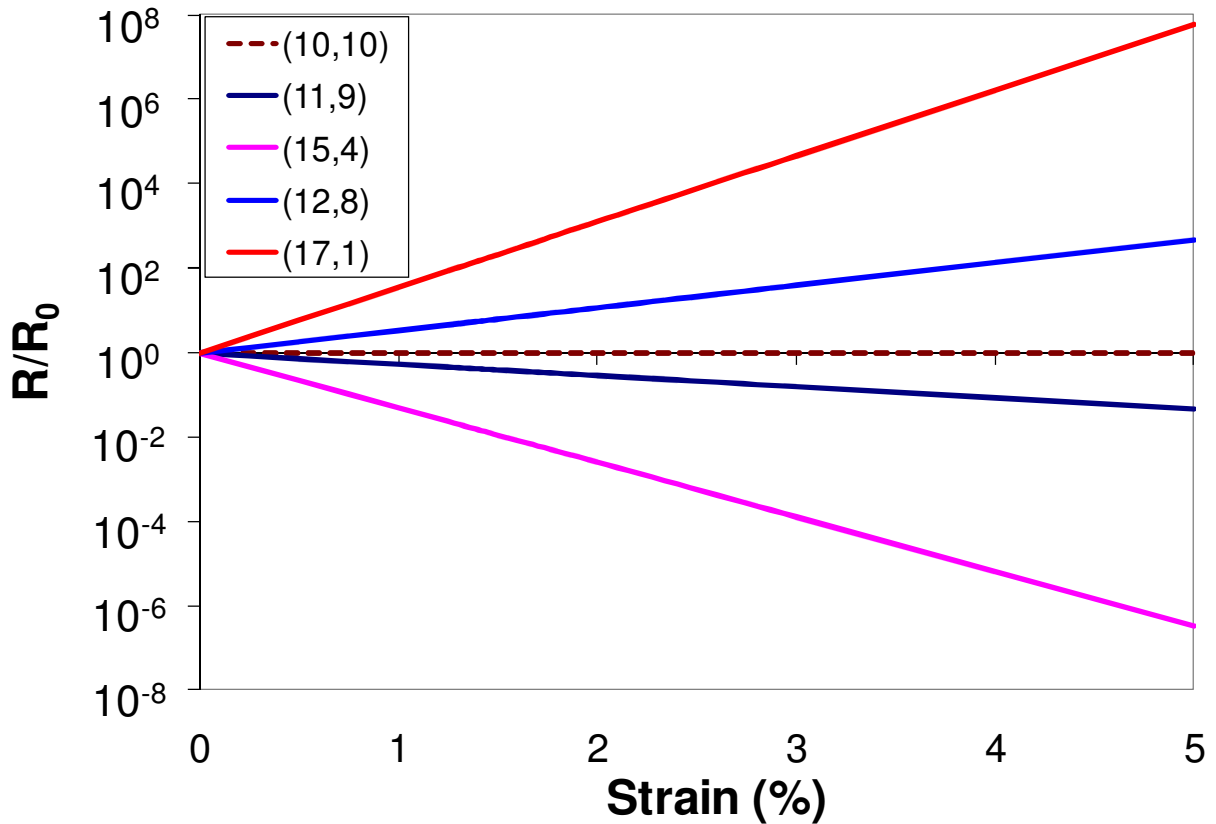


Figure 3.6. Resistance vs. strain for CNTs with diameters of 1.38 nm.

Overall, near zero strain the maximum gauge factor for a semiconducting CNT is 362 while the maximum gauge factor for a metallic CNT is 292. These values are much lower than the measured gauge factors reported by Stampfer et al [1], Cao et al [50] and Grow et al [51]. There are three likely explanations for these differences.

A small pretension on a CNT results in large increases in gauge factors when the CNT has a small chiral angle. Pretension could be induced during fabrication or within experimental setups. For example, the substrate the CNT is placed upon can induce a strain due to van der Waals interactions. Molecular mechanics simulations and experimental measurements have estimated deformations as large as 2-3 percent for a CNT on a SiO₂ surface [202,203]. This level of pretension would cause higher-than-expected gauge factors.

Another possibility is that previous experiments may have unknowingly measured the characteristics of CNT bundles rather than individual SWCNTs. The CNTs measured by Grow et al. [51] ranged from 2-6 nm in diameter, therefore it is likely that some of the larger diameter

CNTs were bundles of smaller SWCNTs. Bundling reduces band gap of semiconducting CNTs, opens a secondary band-gap in metallic CNTs, and changes electronic dispersion [77].

Some of the difference could be a result of effects that are not captured by the model. Increased electron scattering and changes in the Schottky barrier may also affect gauge factor, though at this point it is unclear how large the effect is. Isolating the magnitude of error associated with the possible causes will require a larger study that links chiral indices to resistance and gauge factor at different temperatures. This is a rather involved study that will be taken up in the future. As will be seen in Chapter 4, the model presented matches experimental results for networks of CNTs with less than 7 percent error.

3.5 Design of a Device that Uses Many CNTs in Parallel

The theory discussed in section 3.3 may be used to design devices with CNTs, for example the force sensor shown in Figure 3.7. This sensor consists of three flexural beams that are used to measure out-of-plane forces and torque about an axis that is normal to the plane of the device and aligned with its axis of symmetry. In this design, several CNTs are placed in a parallel resistor network upon the flexure beams. When the beams strain, the CNTs also strain, and this may be used to measure force and/or displacement.

The resolution of a strain sensor is set by sensitivity of the device output to strain (i.e. gauge factor) and noise. In CNT-based strain sensors, the dominant noise source is flicker noise [77]. Flicker noise is caused by the capture and release of charge carriers in localized trap states within the CNT [188]. The flicker noise in a CNT is given by Equation (3.16), where α is the Hooge constant, V_s is the source voltage, f is the frequency, and N is the number of charge carriers in the resistor.

$$\sigma_{1/f} = \sqrt{\frac{\alpha V_s^2}{N} \ln\left(\frac{f_{\max}}{f_{\min}}\right)} \quad (3.16)$$

From this equation, it is possible to decrease the flicker noise by increasing the number of charge carriers in the resistor. This may be accomplished, without reducing sensitivity, by replacing a single CNT sensor with a network of parallel CNTs [76].

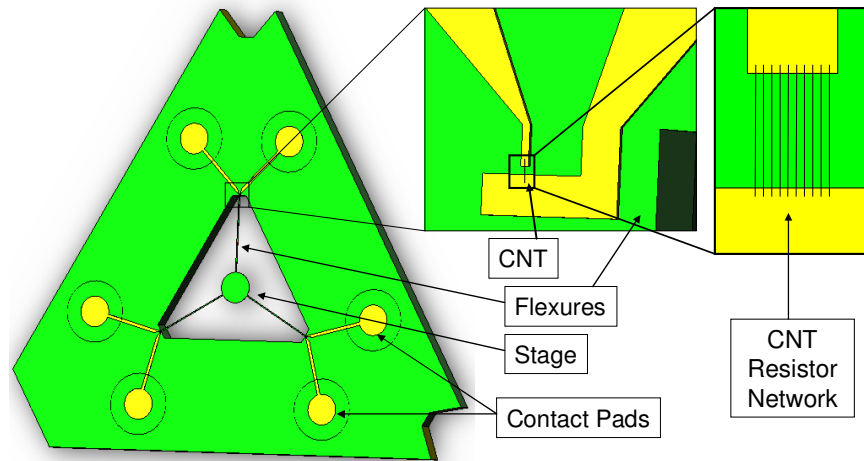


Figure 3.7. MEMS multi-axis force sensor with CNT-based strain sensors.

The feasibility of this design was investigated via a Monte-Carlo simulation of a 100 CNT resistor network. In this simulation, the carbon nanotubes are modeled as independent resistors in parallel with equal amounts of strain applied to each CNT. The Monte-Carlo simulation was run 10,000 times at strain intervals of 0.1 percent from 0 percent to 5 percent strain. Each of the CNT's chiral indices was randomly selected from the pool of CNTs with diameters between 0.5 nm and 4 nm with each chiral index given equal weighting. The average resistance and gauge factor results of these simulations at each strain level are presented in Figure 3.8 and Figure 3.9.

For small strains, the network resistance is dominated by the metallic CNTs because they have a lower resistance. Initially, the change in resistance is small and slightly negative. This is due to the closing of the secondary band gap in the metallic CNTs. At approximately 0.3 percent strain, the band gap in the metallic CNTs is zero and a new energy gap starts to open, thereby causing the band-gap to increase. This results in the observed increase in resistance between 0.3 percent and 2 percent strain. Over this range, the change in resistance is close to linear with an R^2 of 0.997 and a gauge factor of 78.5 ± 0.4 . This is close to the results reported in the literature of gauge factors of 79 to 134 for aligned CNT films [6]. At 2.5 percent strain, the contributions from the semiconducting CNTs become significant and the resistance starts to decrease. In

practice, most devices are likely to work within the linear regime between 0.3 percent and 2 percent strain due to the initial strain imposed on the CNT through interactions with the substrate or through other pretensioning effects [202,203].

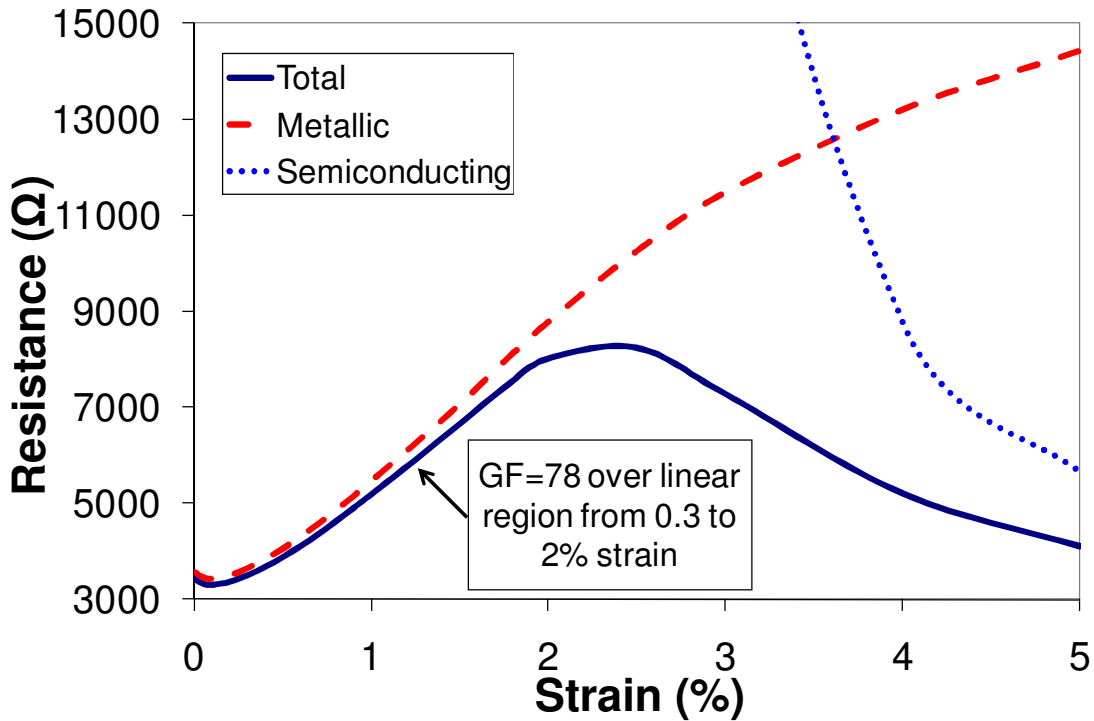


Figure 3.8. Resistance vs. strain for a 100 CNT resistor network, with segregated contributions from metallic and semiconducting CNTs.

These resistance trends are the cause of the nonlinear gauge factor vs. strain curves seen in Figure 3.9. The network gauge factor follows the metallic CNT behavior closely until approximately 2.5 percent strain. This is when the contributions from semiconducting CNTs become relevant. Initially, the semiconducting CNTs have a gauge factor of zero because the $p=1$ CNTs increase in resistance with increasing strain, while the $p=-1$ CNTs decrease in resistance with increases in strain. These effects cancel out initially, but as strain increases, the behavior of the $p=-1$ CNTs start to dominate. This occurs because increasing strain causes more of the current in the network to be carried through the lower resistance, $p=-1$ CNTs. At high strains, the semiconducting CNTs act as $p=-1$ CNTs.

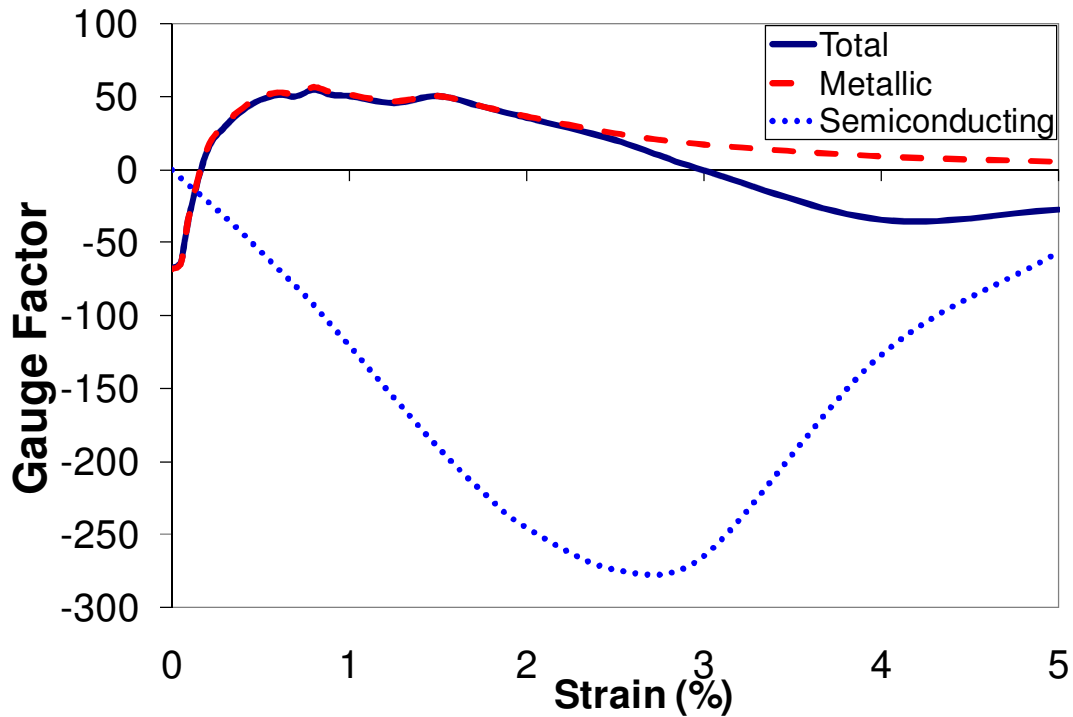


Figure 3.9. Gauge Factor vs. strain for a 100 CNT resistor network consisting of metallic, semiconducting or all CNTs.

From Figure 3.8 and Figure 3.9 it is clear that the gauge factor of unsorted CNTs or CNTs sorted only into metallic and semiconducting CNTs is at least an order of magnitude smaller than for individual CNT sensors. A small number of $p=0$, $p=-1$ or other low gauge factor CNTs can significantly reduce the sensitivity of the network. Therefore it is important to sort CNTs by chirality before constructing the networks if low noise and high strain sensitivity are desired [153,158,159,161].

EXPERIMENTAL SETUP AND RESULTS

4.1 Test Setup

A MEMS test structure was designed and microfabricated in order to test the predictions made in Chapter 3. This test structure was incorporated into an experiment to measure the gauge factor of CNTs. As seen in Figure 4.1, the test structure consists of a fixed-fixed flexure beam and electrodes connected to the base of the flexure. The outer four sets of electrodes are connected to polysilicon piezoresistors while the inner two electrodes are left empty so that CNTs may be connected across them. These central electrodes are spaced $1\mu\text{m}$ apart. This architecture allows strain to be measured simultaneously and independently with the polysilicon and CNT piezoresistors. The center of the flexure has a locating hole where small, known weights may be placed, thereby loading the structure and straining the CNTs.

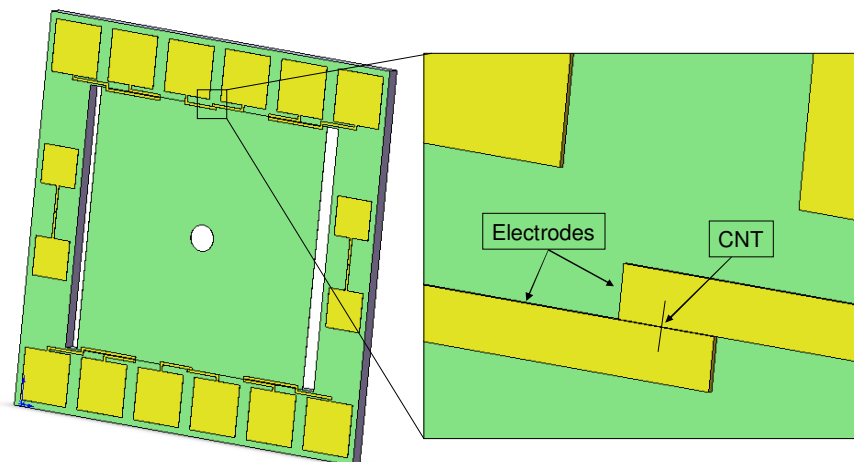


Figure 4.1. CNT parallel resistor network between two electrodes on the test structure.

CNTs were deposited onto these test flexures via dielectrophoresis. A droplet of a 3 $\mu\text{g}/\text{mL}$ solution of SWCNTs in deionized (DI) water was placed on the middle electrodes of the test structure and a 5 MHz, 5V peak-to-peak AC voltage was used to direct the deposition of the SWCNTs. After 5 minutes, the test structure was rinsed with DI water and dried. The results of this deposition process are shown in Figure 4.2.

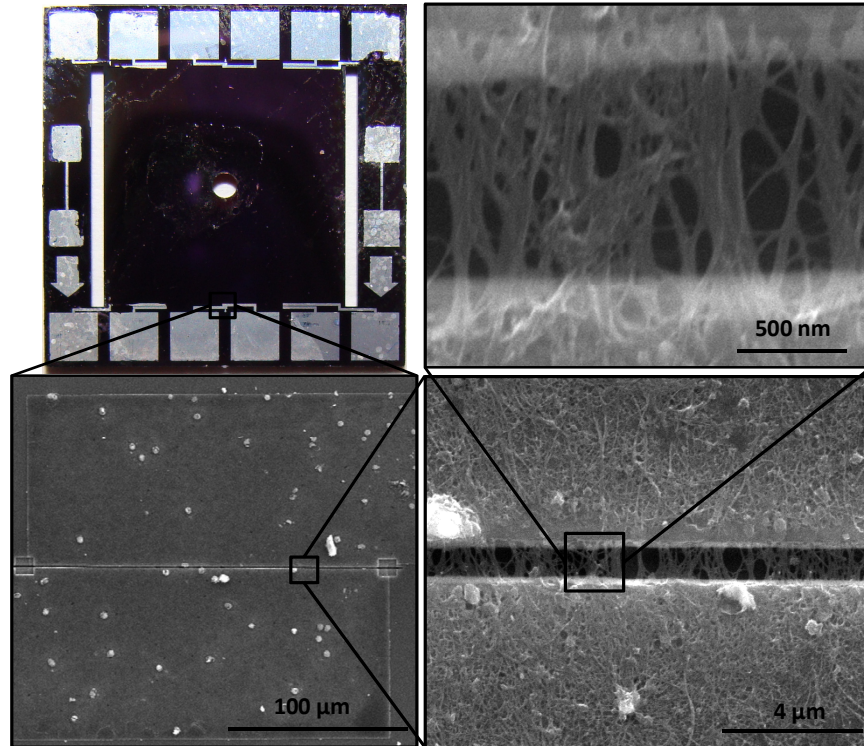


Figure 4.2. CNT resistor network between two electrodes on the test structure.

A low noise sensor system was connected in order to measure the gauge factor of the CNT network. The noise in the sensor electronics was more than an order of magnitude lower than the noise in the CNT sensor itself. The CNT network was incorporated into a DC Wheatstone bridge in a quarter bridge configuration. An instrumentation amplifier was used to boost the signal from the bridge, which is nulled with a bias voltage and read by an Analog-to-Digital Converter (ADC).

4.2 Fabrication of CNT Test Structures

The CNT test structures were fabricated using standard microfabrication procedures. For the microfabrication a Silicon-on-Insulator (SOI) wafer with a 10 μm handle layer, a 500 nm insulating layer and a 500 μm handle layer was used. First, a 300 nm layer of SiO_2 was grown on the SOI wafer by wet oxidation. This layer provides electrical insulation between the wire traces and the silicon wafer. Next, polycrystalline silicon was deposited on the SOI wafer by low pressure chemical vapor deposition (LPCVD). This polysilicon layer was then patterned into piezoresistors that can be used to give an independent measurement of the strain on the test structure.

After the polysilicon piezoresistors were patterned by photolithography and etching, aluminum was sputtered onto the SOI wafer. This aluminum layer was then patterned by photolithography and etched to create the wire traces that connected the polysilicon piezoresistors to the bond pads. In addition, in the center of each chip, a separate set of traces were patterned for the CNT-based piezoresistors.

After the aluminum traces were patterned, the front side of the silicon wafer was etched to define the flexure geometry in the device layer. The device layer was then coated in photoresist to protect it during the backside etch. For the backside etch the wafer was mounted to a quartz wafer so that once the backside etch was complete the wafer would not fall apart. The backside etch was performed using deep reactive ion etching (DRIE), and was used to release the flexures in the device layer and separate the chips. Finally, the SOI wafer was released from the quartz wafer and diced into individual devices.

After the test structures had been fabricated, they were taken to the focused ion beam (FIB) where a small gap was cut between the wire traces in the center of the flexure. The gap was cut using 0.92 nA beam current and a 1.5 μm beam depth with an aluminum setting. This small 500nm gap is where the CNT-based piezoresistors are placed during dielectrophoresis.

The dielectrophoresis process, as described in the previous section, consists of placing a drop of a solution with CNTs suspended in it on the wire traces, then running an alternating electrical current through the traces. This causes the CNTs to align with the electrical field and produce CNT suspended across the gap the FIB cut in the electrical traces. Using this method, test structures with both CNT-based and polysilicon piezoresistors were fabricated.

4.3 Results for Multiple Chirality Experiments

The change in normalized resistance vs. the change in strain was measured using the test structure setup. The change in strain is used since the exact strain is unknown due to the pretension strain imposed on the CNT through its interaction with the SiO₂ substrate. Based on molecular mechanics simulations and experimental measurements, this pretension strain is estimated to be approximately 0.2 percent for our setup [202,203]. The maximum change in strain that could be measured with this test setup was 0.1 percent because of the fracture limit of the silicon beams. Using this test setup, the gauge factors of three different CNT resistor networks were measured, as shown in Figure 9. Each of these resistor networks was produced using the same dielectrophoresis process conditions described above. Sample 1 was measured to have a gauge factor of 73 ± 9 , while samples 2 and 3 were measured to have gauge factors of 82 ± 9 and 70 ± 6 , respectively. Overall, the average gauge factor of the three samples was calculated to be 75 ± 5 . This result is within experimental error of the predicted value of 78.5 ± 0.4 that was presented in the last chapter.

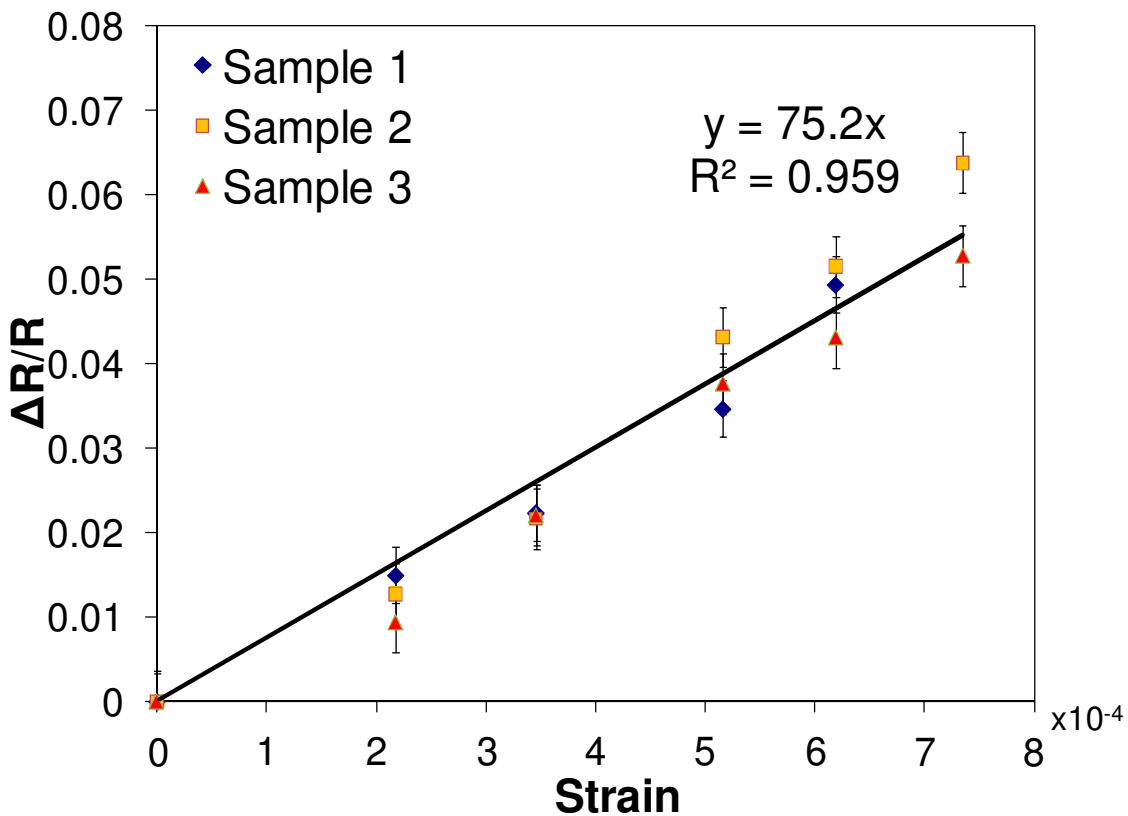


Figure 4.3. Measured change in resistance vs. strain for CNT resistor networks.

This result indicates that the theory and models presented in Chapter 3 accurately capture the performance of CNT-based piezoresistors. This is important because using the theory and models from Chapter 3 it is possible to predict which CNTs will make the best piezoresistive sensors. In addition, the verification of the theory and models from Chapter 3 makes it possible to analyze and predict the performance of samples with a distribution of CNTs. This is useful in cases where pure samples are not available or when determining the effect of a small number of impurities in a sample. Therefore, the use of the Monte-Carlo simulations to predict the performance of CNT-based piezoresistive sensors can help to determine the sensitivity-limiting factors and suggest ways to improve the performance of the sensors.

4.4 Results for Single Chirality Experiments

4.4.1 Predicted Results

In order to further analyze the accuracy and reliability of the theory and models presented in Chapter 3, experiments were performed on enriched samples of (6,5) CNTs. (6,5) CNTs were chosen because there has been a great amount of success in enriching (6,5) CNT samples from bulk samples. (6,5) CNTs are predicted to have a gauge factor of 57, as shown in Figure 4.4.

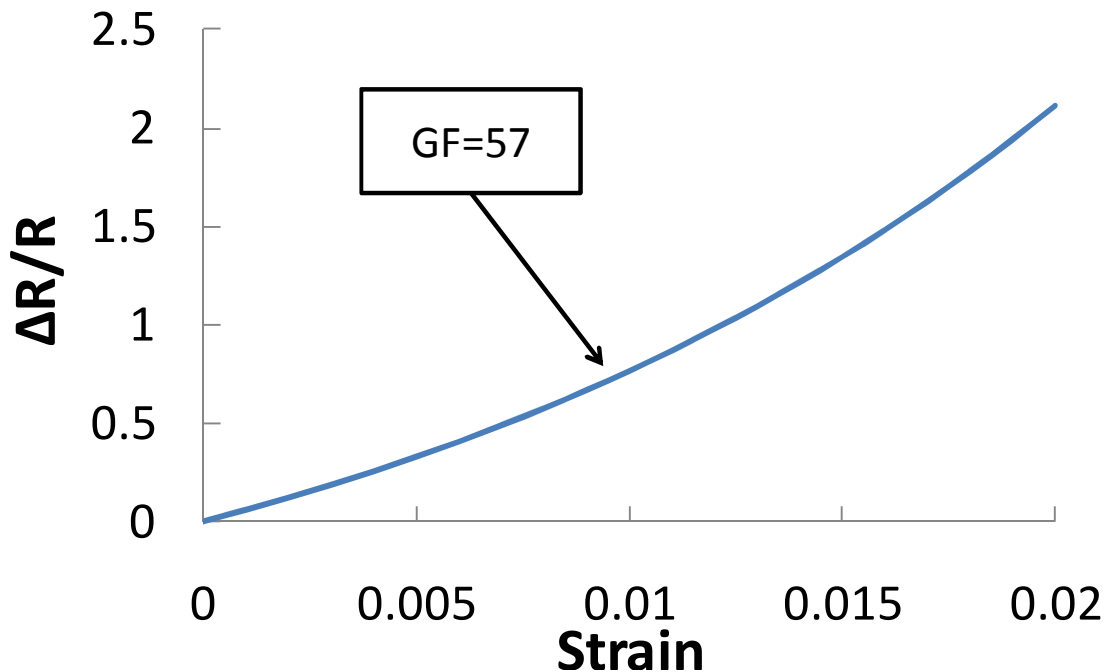


Figure 4.4. Predicted $\Delta R/R$ vs. Strain for (6,5) CNT.

4.4.2 CNT Enrichment

For this experiment, the (6,5) CNTs were enriched from a solution of SWCNTs suspended in water with a sodium cholate surfactant. The (6,5) CNTs were separated out using density gradient ultracentrifugation. Overall, this method produces enriched (6,5) CNT samples that are about 85 percent pure. The results of the ultracentrifugation process are shown in Figure 4.5.

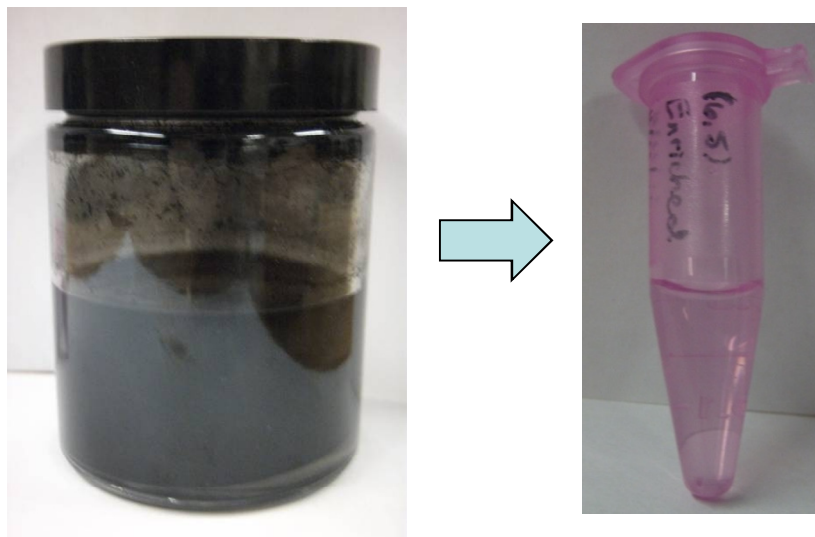


Figure 4.5. Enrichment of (6,5) CNT sample.

In order to determine the purity of the enriched (6,5) CNT sample, the absorption of the sample was measured over the ultraviolet (UV), visible (vis) and near-infrared (nIR) spectrums. From this absorption spectrum it is possible to determine the chiralities of the CNTs in the sample as well as the concentration of each type of CNT [204,205]. Based on the absorption spectrum, it was determined that the sample contained several other types of CNTs including (7,5), (7,6), (9,1), (6,4), (8,3), (8,4), and (9,2) CNTS as shown in Figure 4.6.

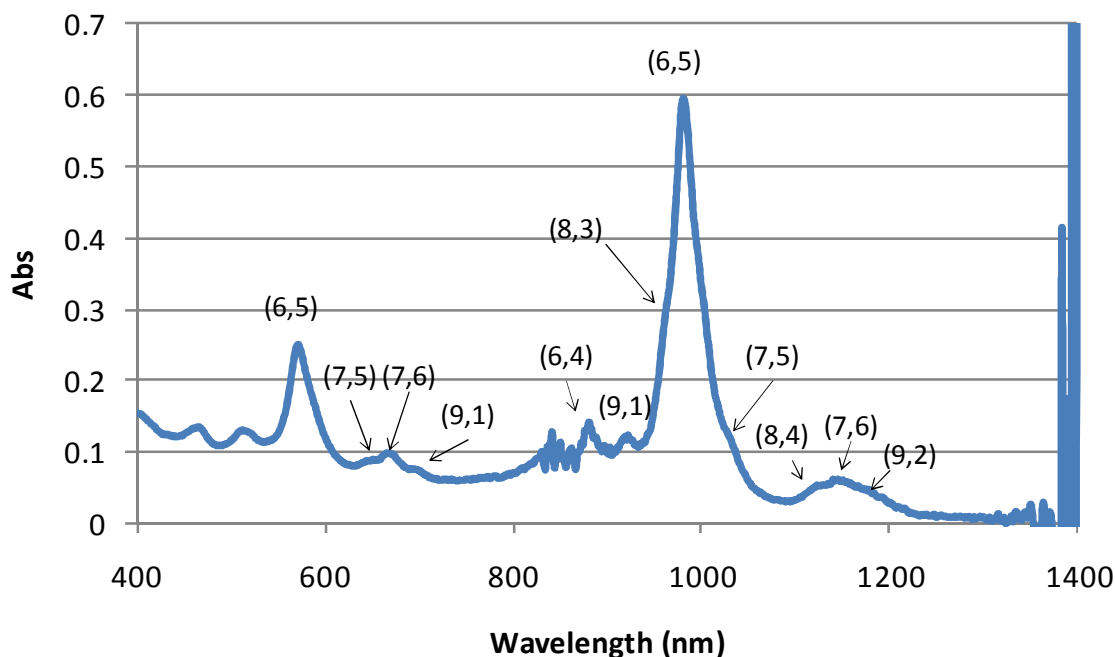


Figure 4.6. UV-vis-nIR absorption spectrum for (6,5) enriched CNT Sample.

From this absorption, the percentage of each type of CNT in the sample was calculated by integrating the area under each of the absorption peaks and dividing the area for each type of CNT by the total area under the curve. The results of this calculation are presented in Table 4.1 along with the gauge factor predicted from theory for each of the CNT chiralities. Overall, the sample contains 82.6 percent (6,5) CNTs.

Table 4.1: Estimated chiral distribution of enriched sample from absorption spectrum.

CNT	Percentage	Predicted Gauge Factor
(6,5)	82.60%	57
(7,6)	5.60%	48
(7,5)	1.70%	-103
(9,1)	1.60%	-348
(6,4)	1.00%	-122
(8,4)	3.50%	196
(9,2)	1.70%	315
(8,3)	0.70%	-252
Other	1.60%	NA

4.4.3 Measured Gauge Factor of Enriched (6,5) CNT Sample

Based on the high purity of the sample it might be expected that the CNT-based piezoresistors made from the enriched sample of (6,5) CNTs should behave like (6,5) CNTs in isolation since the number of (6,5) CNTs in the sample is at least an order of magnitude greater than any of the other types of CNTs in the sample. However, as shown in Figure 4.7, the measured gauge factor for the enriched (6,5) sample is -22.7 as opposed to the predicted gauge factor of 57 for a pure (6,5) sample. This result indicates that even a small number of impurities can have a substantial impact on both the sensitivity and sign of the CNT-based piezoresistor.

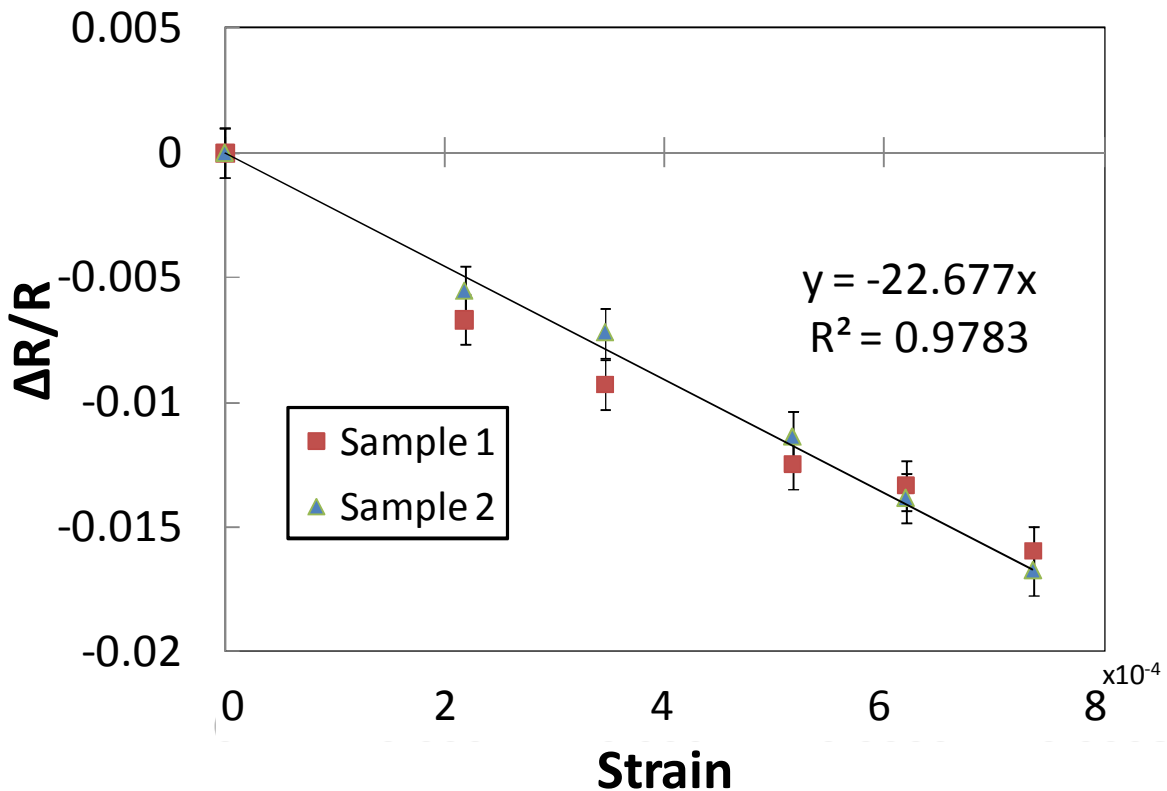


Figure 4.7. Measured $\Delta R/R$ vs. Strain for enriched (6,5) CNT sample.

In order to understand this result it is necessary to look at the component CNTs that make up the CNT-based piezoresistor created from the enriched (6,5) sample and to understand how the sensor operates. Based on how the CNT-based piezoresistive sensor was fabricated, the CNTs can be modeled as independent, parallel resistors in a resistor network. Based on this model, the voltage drop across each of the resistors is equal but the current is not. Therefore, the

overall resistance of the sample is dominated by the CNTs with the highest current, which are the lowest resistance CNTs. In this sample, the lowest initial resistance CNTs are the (7,6), (7,5) and (8,4) CNTs. Both the (7,6) and (8,4) CNTs have positive gauge factors and thus increase resistance as the sample is strained. However, the (7,5) CNTs have a negative gauge factor and thus decrease in resistance when strained. Therefore, the presence of (7,5) CNTs in the sample might help to explain the measured negative gauge factor of the sample.

4.4.4 Monte-Carlo Simulation for Enriched (6,5) CNT Sample

In order to determine the overall theoretical effect of the impurities in the enriched (6,5) sample a Monte-Carlo simulation was created. The Monte-Carlo simulation was setup much like the Monte-Carlo simulation presented in Chapter 3 for the random assortment of CNTs in a parallel resistor network, except that uniform probability distribution across all chiralities of CNTs used to select each CNT in the sensor was replaced by the measured probability distribution function of the CNT chirality content of the sample. The results of this simulation are given in Figure 4.8.

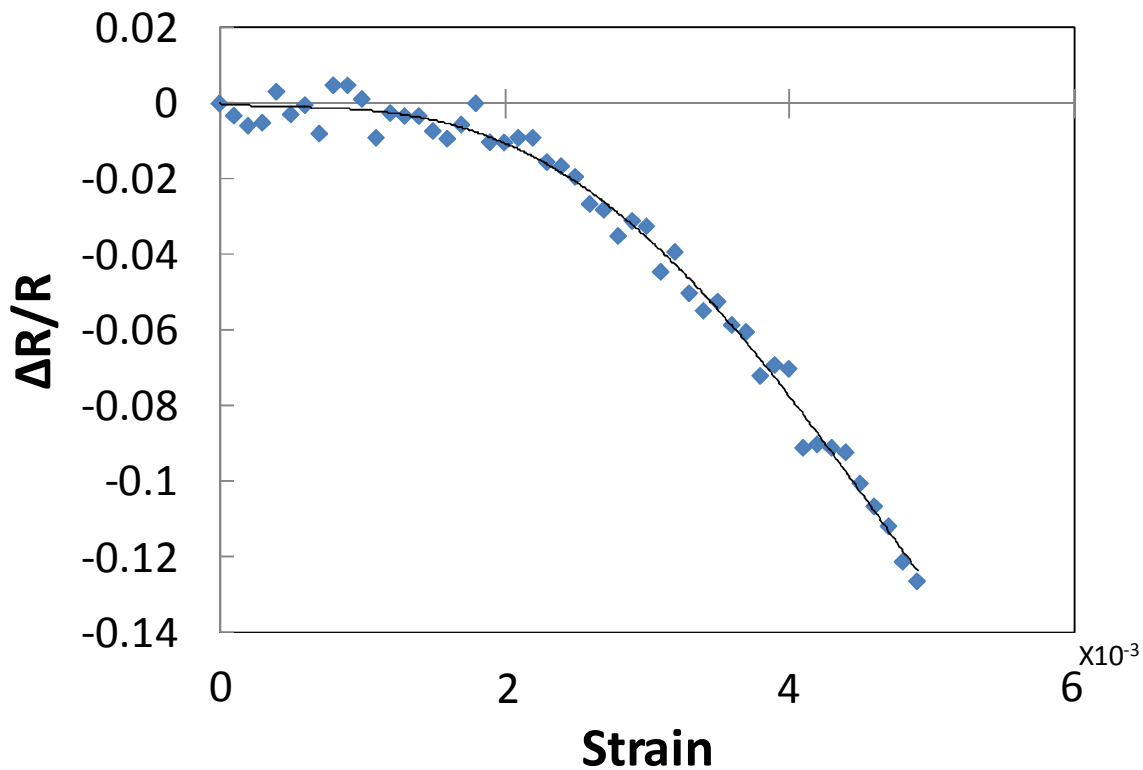


Figure 4.8. $\Delta R/R$ vs. Strain predicted from Monte-Carlo simulations of enriched (6,5) CNT sample.

Overall, the predicted results from the Monte-Carlo simulation of the enriched (6,5) CNT sample show that the gauge factor of the sample should be negative and the magnitude of the gauge factor depends on the initial strain on the sample. Based on the fabrication methods and molecular dynamics simulations of CNT interacting with an SiO₂ surface it is estimated that the initial pretension strain on the CNTs is approximately 0.2 percent. The results of the Monte Carlo simulation with an initial strain offset of 0.2 percent are given in Figure 4.8 along with the experimental measurements from the piezoresistors fabricated with the enriched (6,5) CNT solution.

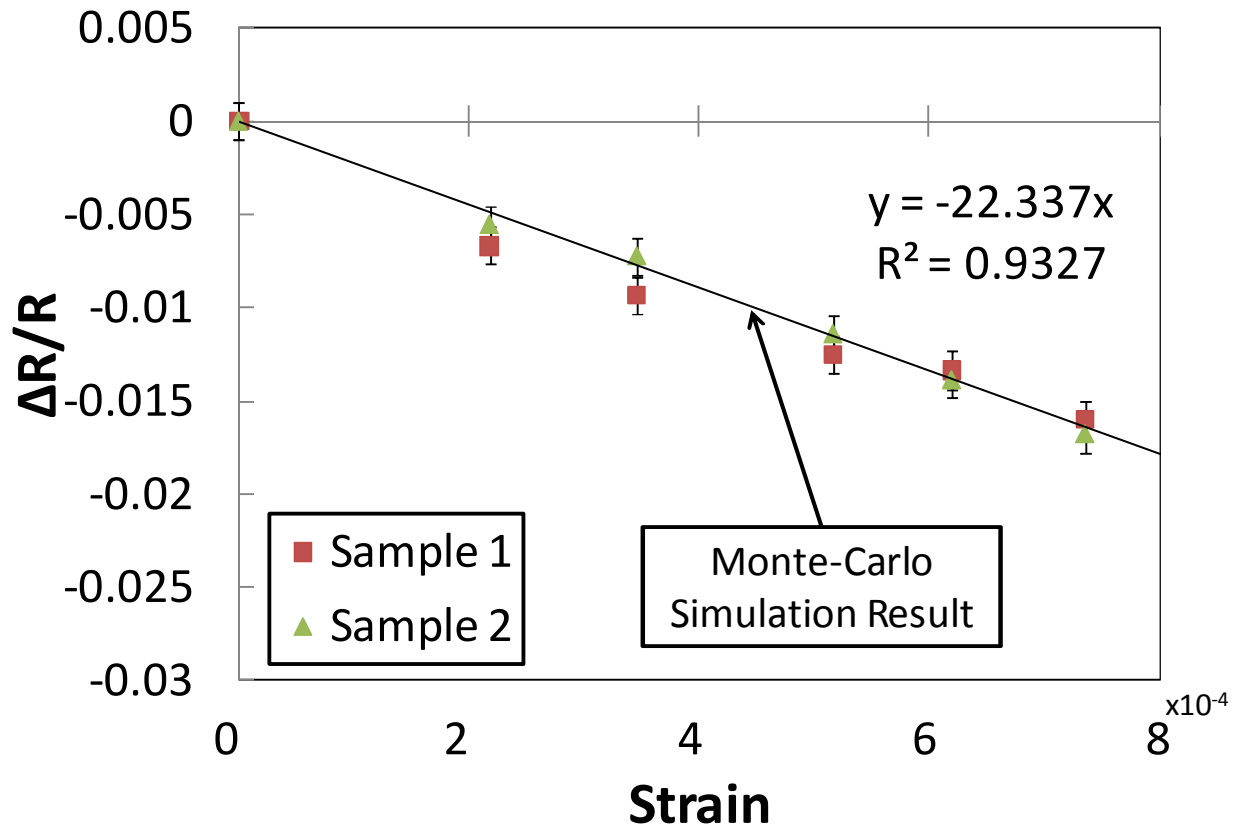


Figure 4.9. Measured results from enriched (6,5) CNT sample overlaid on theoretical prediction from Monte-Carlo simulations with 0.2% strain offset.

Overall, the results from the Monte-Carlo simulations are within experimental error of the experimental results for the enriched (6,5) CNT. The Monte-Carlo simulations predict the gauge factor of the enriched (6,5) CNT sample to be -22.3 while the experimentally determined gauge factor was -22.7 ± 0.5 . This result shows that the presence of other types of CNTs in the enriched (6,5) CNT sample explains both the sign and the magnitude of the measured gauge

factor for the enriched (6,5) CNT sample as well as its deviation from the theoretical gauge factor for a pure (6,5) CNT sample.

4.4.5 Electrical Breakdown of CNTs in Sensor

In order to produce sensors with the maximum strain sensitivity it is necessary to eliminate the low resistance and low gauge factor CNTs that limit the strain sensitivity of the sensor. As was shown in the previous section, a small number of these CNTs can have a large effect on the strain sensitivity of the sensor since most of the current in the parallel resistor network runs through these CNTs. This high amount of current causes the lower resistance CNTs to heat up much more than the higher resistance CNTs that make up the majority of the CNTs in the sample. This Joule heating of the low resistance CNTs can be used to eliminate these CNTs through a process known as the electrical breakdown technique [206]. This technique takes advantage of the increased reactivity of CNTs at high temperature to create a rapid oxidation of the low resistance CNTs in the sample. This process creates a break in the CNT structure and eliminates the low resistance CNTs from the sample. The resistances of each of the chiralities of CNTs in the enriched (6,5) CNT sample normalized to the resistance of the (6,5) CNT are given in Table 4.2.

From these normalized resistances it is clear that at low strains, the (7,6), (7,5), (8,4) and (9,2) CNTs all have resistances that are at least an order of magnitude less than the (6,5) CNTs. Therefore, using the electrical breakdown technique it should be possible to eliminate these CNTs from the sensor. For large strains some of the CNTs increase in resistance and some of the CNTs decrease in resistance, changing the normalization between the (6,5) CNTs and the rest of the CNTs in the sample. For example, at 1% strain, the (7,6), (7,5) and (8,4) CNTs are still all an order of magnitude lower resistance than the (6,5) CNTs while the (9,2) CNTs are now higher resistance than the (6,5) CNTs. In addition, the (9,1) and (8,3) CNTs now have a resistance that is an order of magnitude lower in resistance than the (6,5) CNTs. Therefore, by performing an electrical breakdown at both low and high strains it should be possible to eliminate all of the CNTs in the sample except for the (6,5) CNTs and the (6,4) CNTs.

Table 4.2: Resistance normalized to (6,5) CNT resistance for CNTs in enriched CNT sample at various strain levels.

CNT	Diameter	Normalized Resistance for a Given Strain			
		0%	0.2%	0.3%	1%
(6,5)	0.76 nm	1	1	1	1
(7,6)	0.89 nm	0.003	0.003	0.003	0.003
(7,5)	0.83 nm	0.037	0.027	0.023	0.007
(9,1)	0.76 nm	1.000	0.444	0.296	0.017
(8,4)	0.84 nm	0.023	0.030	0.035	0.092
(6,4)	0.69 nm	36.76	25.69	21.48	6.13
(9,2)	0.80 nm	0.101	0.169	0.218	1.333
(8,3)	0.78 nm	0.301	0.162	0.119	0.014

4.4.6 Results for Electrical Breakdown Experiments

The electrical breakdown technique was used to eliminate some of the impurities from the sensor created from the enriched (6,5) CNT sample. First, electrical breakdown was performed on the enriched (6,5) sample with no load applied to the flexure. 17.7 volts was applied between the two electrodes in order to cause the electrical breakdown of the (7,6), (7,5), (8,4) and (9,2) CNTs and to eliminate them from the sensor.

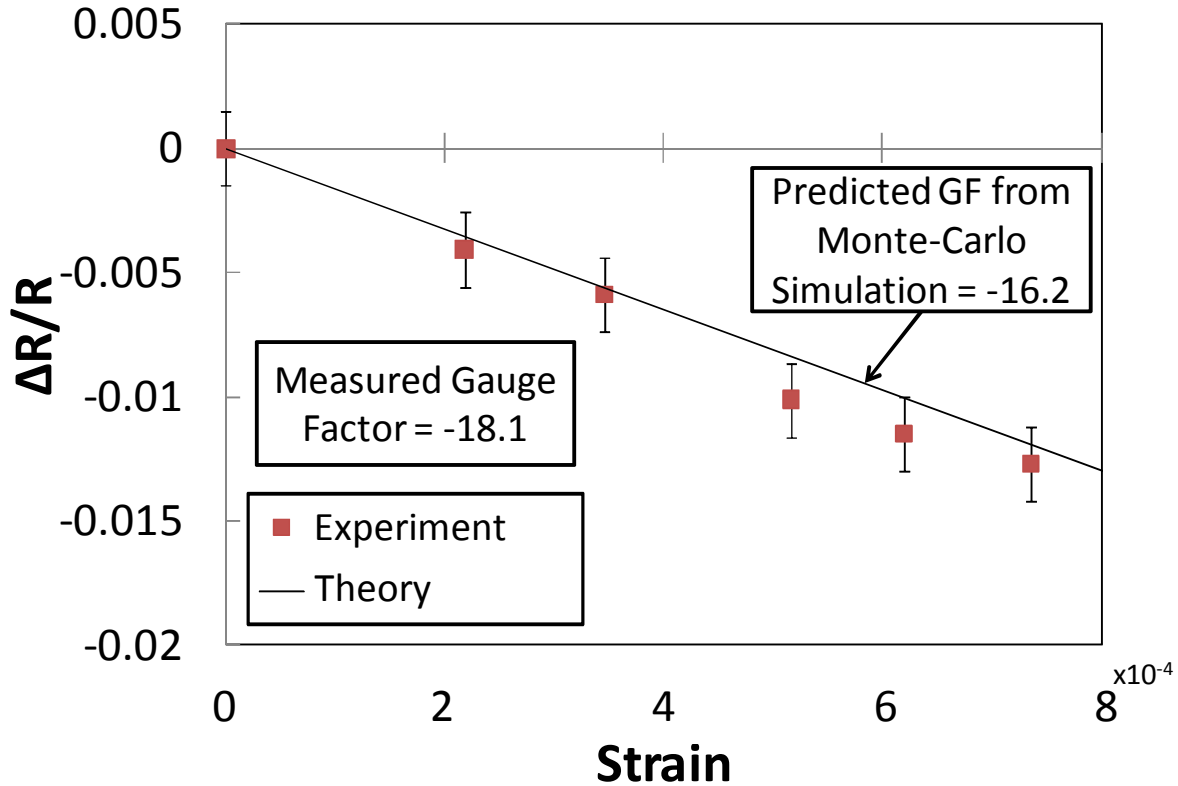


Figure 4.10. Measured results from low-strain electrical breakdown of enriched (6,5) CNT sample overlaid on theoretical prediction from Monte-Carlo simulations with 0.2% strain offset.

This low strain electrical breakdown was successful in increasing the gauge factor of the sensor from -22.7 ± 0.5 to -18.1 ± 0.4 as shown in Figure 4.10. Overall this result is in good agreement with the result predicted from the Monte-Carlo simulations when the (7,6), (7,5), (8,4) and (9,2) CNTs are removed from the sample. These Monte-Carlo simulations predict that the gauge factor of the sensor will increase to -16.2 after the low-strain electrical breakdown, while the measured gauge factor is -18.1 ± 0.4 . This overestimate of the sensor gauge factor is likely due to incomplete removal of the (7,6), (7,5), (8,4) and (9,2) CNTs during the low strain electrical breakdown. However, the increase in gauge factor does indicate that most of low resistance CNTs were removed.

In order to further increase the gauge factor of the sensor, an electrical breakdown of low resistance CNTs was performed at high strain. In addition to the (7,6), (7,5), (8,4) and (9,2) CNTs removed in the previous low strain electrical breakdown step, it should be possible to remove the (9,1) and (8,3) CNTs with electrical breakdown at high strains. As shown in Figure 4.11, the gauge factor of the enriched (6,5) CNT-based piezoresistive sensor increased from -

18.1 ± 0.4 for the low strain electrical breakdown sensor to 34 ± 1 for the high strain electrical breakdown sensor.

The increase in resistance and the change in sign of the gauge factor indicate that most of the low resistance and low gauge factor CNTs were removed during the two electrical breakdown steps. However, the Monte-Carlo simulations for the (6,5) enriched samples after the (7,6), (7,5), (8,4), (9,2), (9,1) and (8,3) CNTs are removed from the probability distribution function significantly overestimate the gauge factor of the sensor, as shown in Figure 4.11. This indicates that while the electrical breakdown technique was successful in eliminating most of the unwanted CNTs in the sample, it was not capable of completely removing all impurities from the sensor.

Overall, the results from this section show that the performance of the CNT-based piezoresistors created from enriched samples of single chirality CNTs can be significantly improved through the use of the electrical breakdown technique. This makes it possible to achieve near-optimal results from enriched samples even if the samples are not initially 100 percent pure

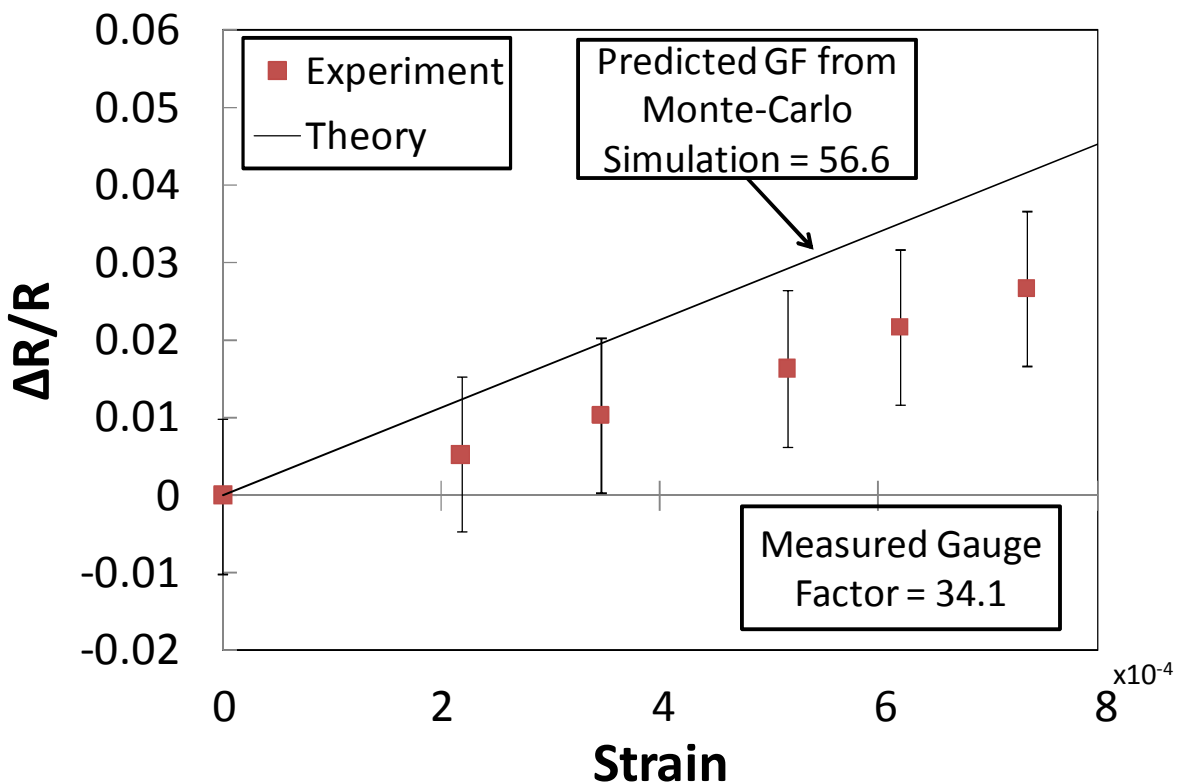


Figure 4.11. Measured results from high-strain electrical breakdown of enriched (6,5) CNT sample overlaid on theoretical prediction from Monte-Carlo simulations with 0.2% strain offset.

4.5 Discussion

CNT-based piezoresistors offer the potential to become versatile, high resolution sensing systems. Existing CNT-based piezoresistive sensor systems are competitive with metal strain gauges in terms of performance. The theory and modeling approach presented here enables the prediction of gauge factor in general CNTs. The theoretical framework presented in Chapters 3 and 4 suggests that the performance of CNT-based piezoresistive sensor systems could be improved by almost an order of magnitude if it becomes possible to accurately sort CNTs by chirality [23-26]. This would allow CNT-based piezoresistive sensor systems to overcome many limitations presently found in micro- and nanoscale sensor systems.

However, this work shows that even a small number of low resistance or low gauge factor CNTs in the CNT-based sensor system can have a large effect on the performance of the sensor. Therefore, it is critical to be able to produce pure enriched samples of single chirality CNTs or to be able to remove these unwanted CNTs after the sorting process is finished. As shown in this chapter, it is possible to remove many of the unwanted CNTs from the sensor system using the electrical breakdown technique. Using this method it is possible to both increase the sensitivity of the sensor system and to change the sign of the gauge factor from negative to positive. Using similar methods it should be possible to create CNT-based piezoresistive sensor systems with gauge factors in excess of 300. In order to accomplish this goal, however, it is necessary to improve both the sorting techniques and the electrical breakdown technique in order to ensure that only the highest gauge factor CNTs are present in the sensor system.

The theoretical framework presented in Chapters 3 and 4 could also be extended to other types of systems such as graphene sheets and nanoribbons. The theoretical framework, which is based on tight binding calculations for strained graphene sheets, suggests that graphene sheets and nanoribbons could be used to produce high gauge factor strain sensors. The primary difference in the theoretical analysis of carbon nanotubes and graphene sheets is that the band gap created by the curvature of the graphene sheet must be accounted for in the analysis of carbon nanotubes where as curvature does not have to be accounted for in the analysis of graphene sheets and nanoribbons. Also, in order to properly analyze the effects of strain on the electronic structure of graphene sheets and nanoribbons, the Born-Von Karman boundary condition around the circumference of the carbon nanotube would need to be replaced by a

particle in a particle-in-a-box-like boundary condition. Both of these changes to the theoretical framework could have a major impact on the sensitivity of the strain sensing element. Therefore, more work needs to be done in this area to determine the ultimate viability of graphene sheets and nano-ribbons as high quality strain sensors.

CNT INTEGRATION AND NOISE

5.1 Sources of Performance Limitations

5.1.1 Flicker Noise

Carbon nanotube-based piezoresistive strain sensors have the potential to outperform many traditional MEMS force and displacement sensors due to their high strain sensitivity [1]. However, CNT-based sensors typically suffer from large amounts of flicker noise which limits the resolution of these sensors [77]. Flicker noise is believed to be caused by the capture and release of charge carriers in localized trap states in the CNT [188]. The flicker noise in a CNT is given by Equation (5.1), where α is the Hooge constant, V_s is the source voltage, f is the frequency, and N is the number of charge carriers in the resistor.

$$\sigma_{1/f} = \sqrt{\frac{\alpha V_s^2}{N} \ln\left(\frac{f_{\max}}{f_{\min}}\right)} \quad (5.1)$$

Overall, the Hooge constant for CNT-based sensors has been measured to be similar to other semiconducting materials such as polysilicon [79]. However, as sensor systems are scaled down to the nanoscale, the number of charge carriers is reduced and flicker noise increases. Therefore, due to the small number of charge carriers in the CNT-based devices, the noise in these devices tends to be dominated by flicker noise.

In general, the amount of noise in the CNT sensor scales with the resistance of the sensor [77]. However, the total amount of noise in the in the CNT-based sensor system is highly dependent on a number of sources related to the design of the sensor system and the conditions under which the sensor is manufactured and tested. For example, the amount of flicker noise in

the sensor is higher when the sensor is exposed to the environment compared to when it is tested in a vacuum [207]. This indicates that molecules that are absorbed onto the surface of the CNT can act as extra scattering sites and significantly increase the noise in the sensor [208]. Similarly, the gate voltage used during testing can have a significant effect on the sensor noise by altering the number of charge carriers in device [209,210]. Even the surface on which the CNTs are deposited can have a significant effect on the noise in the sensor since the motion of charged defects in the dielectric surface or at the dielectric/CNT interface can result in increased noise in the CNT [211]. For example, it has been shown that CNTs on a SiO₂ substrate have 10-20 times greater flicker noise than suspended CNTs [212,213].

In addition, the type of CNTs in the sensor can have a significant effect on the sensor noise. For example, metallic CNTs have been shown to have up to two orders of magnitude less flicker noise than semiconducting CNTs [214]. Also, if the CNTs are longer than the ballistic conduction length, the length of the CNT can also affect the amount of noise in the sensor [82,209,210]. Finally, the temperature at which the CNT-based sensors are tested can have a significant effect on the flicker noise. For example, samples tested at room temperature can have up to three orders of magnitude greater noise power than samples tested at 8° K [215]. It is thought that this decrease in noise power can be attributed to reduced noise in the contact between the electrode and the CNT [216].

In general, sensors based on CNT network films tend to have higher 1/f noise than single CNTs, due to the noise from tube-tube junctions [217]. Therefore, the percolation process is the primary physical mechanism influencing the noise level in a CNT film and percolation theory can be used to describe the noise in these films [218]. This means that the noise in CNT films is sensitive to the disorder of the film and the quality of the film [219,220]. For example, it has been shown that the signal-to-noise ratio of CNT network films can be increased by up to two orders of magnitude by improving the alignment of the CNTs within the film [221]. In addition, it has been shown that flicker noise in CNT films scales inversely with the device size for a given resistance [78].

In order to reduce the amount of flicker noise in CNT-based sensors and transistors, several noise mitigation techniques have been investigated. For example, one of the major sources of flicker noise in CNT sensors is the adsorption and desorption of gas molecules on the surface of the CNT [222]. This adsorption and desorption of gas molecules changes the number

of mobile carriers in the carbon nanotube, which leads to a change in electron mobility, resulting in increased flicker noise. This source of flicker noise can be reduced in CNT-based sensors and transistors by encapsulating the CNTs in a ceramic coating in order to protect the CNTs from the outside environment. For example, it has been shown that encapsulating CNTs in 100 nm of atomic-layer-deposited aluminum oxide can increase device stability and decrease noise by almost an order of magnitude [223]. Similar results have been demonstrated for top-gated transistors where the ceramic encapsulation layer is used as the gate dielectric and passivation layer [224,225].

In addition to adding an encapsulation layer, annealing has also been used to reduce noise in the sensors. Annealing improves both the inter-tube coupling and the CNT-electrode coupling. These improvements can lead to an order of magnitude decrease in flicker noise in CNT-based sensors [226,227]. Similarly, increasing the number of CNTs in the sensor has been shown to reduce the noise power, since the noise power scales with the number of carriers, which is proportional to the number of CNTs in the sensor [76]. Finally, the amount of flicker noise in a CNT-based sensor is also a function of the gate bias voltage [228]. As the gate bias is increased, the flicker noise tends to decrease, since more charge carriers are injected into the device. However, the gauge factor of the CNT-based piezoresistor decreases as the gate bias voltage increases due to the decrease in the piezoresistive effect. Therefore, the signal-to-noise ratio of such sensors tends to be maximized when the device is in the off-state [229].

5.1.2 Contact Resistance

The contact resistance of the carbon nanotubes to the electrodes can have a large effect on the resolution of the sensor system. This is because the contact resistance tends to remain approximately constant as the CNT is strained. Therefore, a high contact resistance can significantly reduce the sensitivity of the sensor system. Contact between the electrodes and the CNTs can either be Schottky or ohmic, depending on the contact metal and the processing conditions [230]. For example, thermal annealing can be used to create ohmic contacts and to decrease the contact resistance between the CNT and the electrode by up to three orders of magnitude [231]. In general, ohmic contact is preferred to Schottky contact in CNT-based piezoresistive strain sensors because the current in ohmic contacts is linear with voltage and ohmic contacts tend to have lower contact resistances due to the lack of a Schottky barrier. The

Schottky barrier is a potential barrier between the CNT and the electrode, which prevents free flow of electrons between the CNT and the electrode due to potential energy differences between them. The height of the Schottky barrier is set by the difference between the work functions of the CNT and the electrode as well as the diameter of the CNT [232].

Overall, the contact resistance is a function of the difference in work functions between the metal electrodes and the CNT as well as the wettability of the electrode [233]. The quantum coupling between the CNT and the metal electrode depends on the contact area, CNT diameter, CNT chirality, and whether the CNT is side or end contacted [234,235]. In addition, coupling between the d-orbitals in the metal and the π -orbital in the CNT plays an important role in determining both the cohesive and the electronic interactions at the contacts [177]. Therefore, metals with good quantum coupling to CNTs, good wettability and work functions similar to CNTs such as titanium tend to produce the best contacts.

5.2 Noise Measurement

In order to measure the noise in the CNT-based piezoresistors, a precision bridge circuit was set up. The bridge circuit consists of (1) a precision voltage reference, (2) a Wheatstone bridge and (3) an instrumentation amplifier. The voltage reference in the bridge circuit is used to convert the noisy supply voltage from the power supply into a low noise input reference for the Wheatstone bridge. The Wheatstone bridge is set up in a quarter bridge configuration with the CNT-based piezoresistor acting as the active element and three metal film resistors used to complete the bridge. The instrumentation amplifier is used to scale the output signal of the Wheatstone bridge so that the signal can be read accurately by an analog-to-digital converter (ADC). Both the electronics and the Wheatstone bridge are placed in metal boxes in order to shield them from electromagnetic interference, as shown in Figure 5.1. Overall, this bridge circuit design results in less than 2 μV of noise in the electronics. This is much lower than the noise in the CNT-based piezoresistors. Therefore, it is possible to get an accurate measurement of the noise in the CNT-based piezoresistive sensor using this experimental setup.

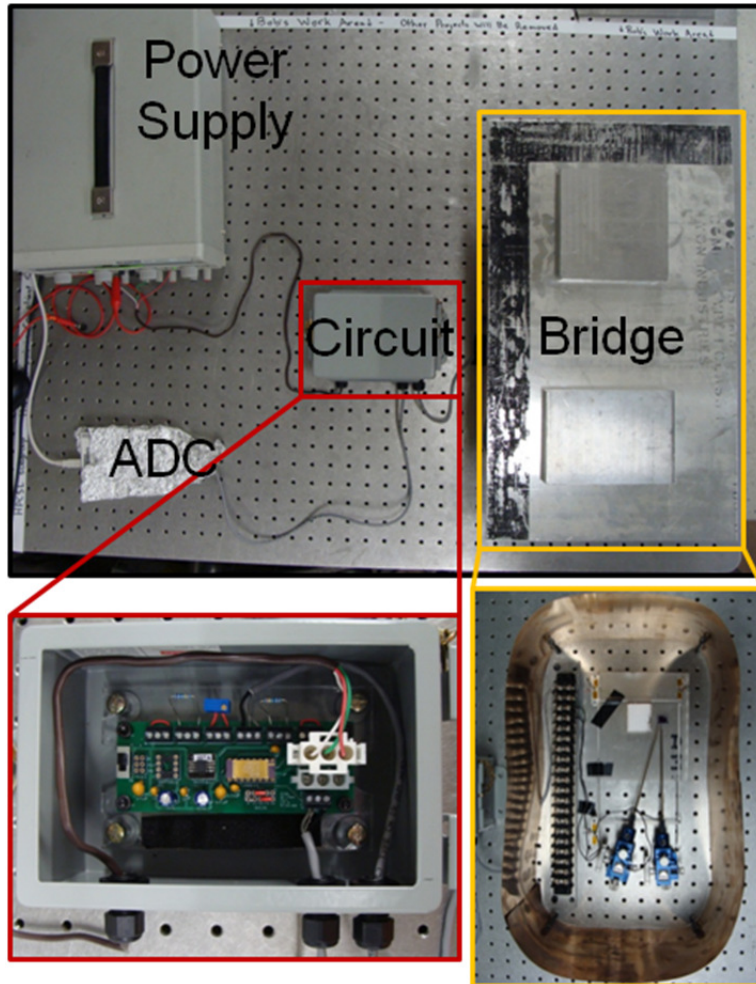


Figure 5.1. Experimental setup consisting of (1) a Wheatstone bridge, (2) a precision bridge circuit with a precision voltage reference and instrumentation amplifier, (3) a DC power supply and (4) an analog-to-digital converter.

A MEMS test structure was designed and microfabricated in order to measure the noise and gauge factor of the CNT-based piezoresistors. The test structure consists of a fixed-fixed flexure beam and electrodes connected to the base of the flexure, as seen in Figure 5.2. The outer four sets of electrodes are connected to polysilicon piezoresistors while the inner two electrodes are left empty so that CNTs may be connected across them. These central electrodes are spaced $1\mu\text{m}$ apart. This architecture enables independent measurement of strain with both the polysilicon and CNT-based piezoresistors. The center of the flexure has a locating hole where small, known weights may be placed, thereby loading the structure and straining the CNTs.

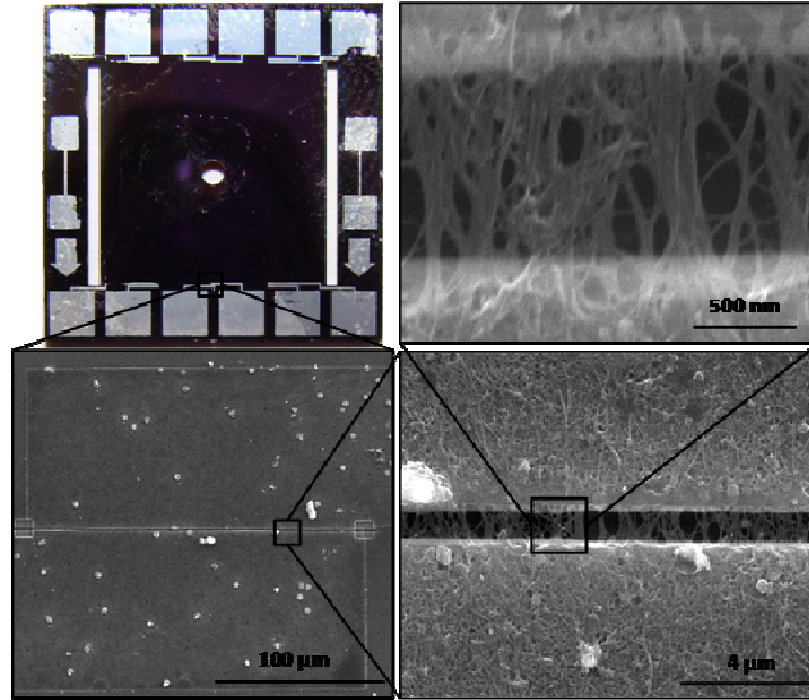


Figure 5.2. Test Structure with SWCNTs connected between the two central electrodes.

CNTs are deposited onto these test flexures via dielectrophoresis. In the typical deposition process used for these tests, a droplet of a 3 $\mu\text{g}/\text{mL}$ solution of SWCNTs in deionized water was placed on the middle electrodes of the test structure and a 5 MHz, 5V peak-to-peak AC voltage was used to direct the deposition of the SWCNTs. After 5 minutes, the test structure was rinsed with DI water and dried. The results of this deposition process are shown in Figure 5.2.

5.3 Noise Mitigation Techniques and Results

5.3.1 Increasing Number of CNTs

Several different design and fabrication methods were investigated in order to determine their effects on flicker noise in the CNT-based piezoresistive sensor. First, the effect of the number of CNTs in the sensor system was investigated. In order to increase the number of CNTs in the sensor, the deposition time in the dielectrophoresis process was increased from 5 minutes to 10 minutes. This should approximately double the number of CNTs in the sensor. As can be seen in Figure 5.3, this change in the manufacturing process resulted in a two-fold decrease in

the flicker noise in the sensor. This result is consistent with Equation (5.1), where the noise power is inversely proportional to the number of charge carriers. Increasing the number of CNTs in the sensor system should increase the number of charge carriers in the sensor since the number of CNTs is directly related number of carriers. Therefore, doubling the number of CNTs in the sensor should reduce the power spectral density by a factor of two and result in lower flicker noise.

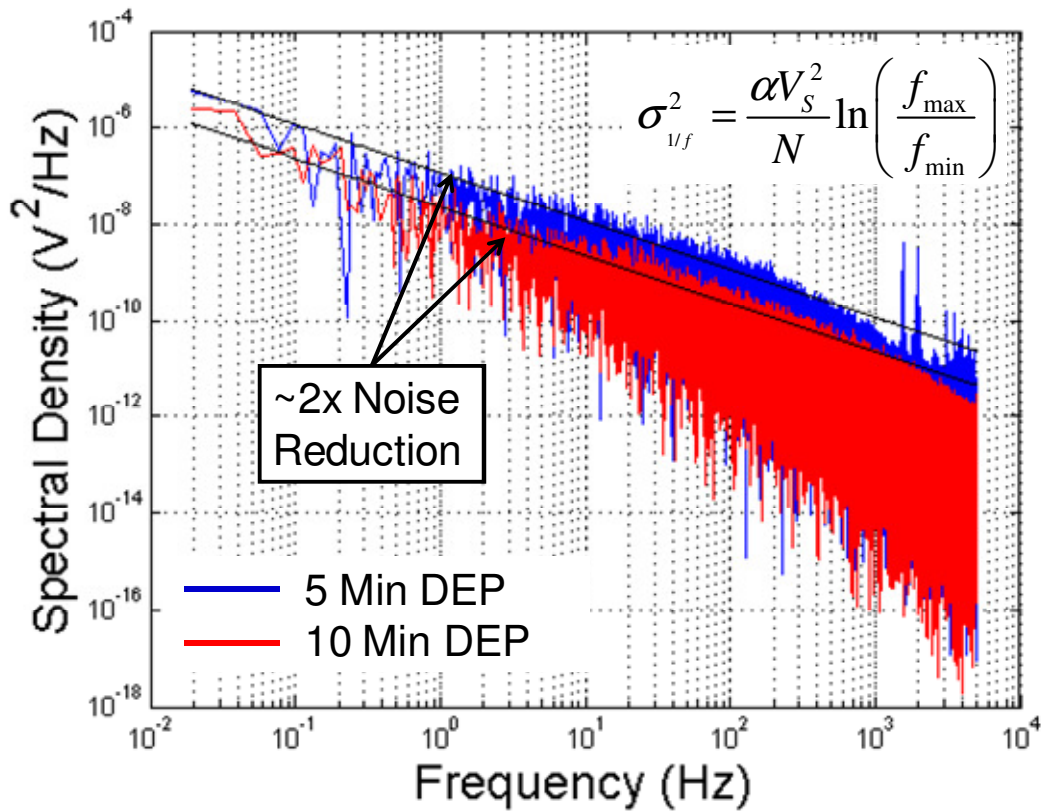


Figure 5.3. Power spectral densities of CNT-based piezoresistive sensors with dielectrophoresis deposition times of 5 and 10 minutes.

5.3.2 Coating CNTs

In addition to increasing the number of CNTs in the sensor system, several other manufacturing methods were investigated to reduce the flicker noise in the CNT-based piezoresistive sensor system. First, electron beam evaporation was used to coat the devices in 500 nm of aluminum oxide in order to isolate the CNTs from the outside environment. This

aluminum oxide coating helps to prevent molecules in the air from absorbing onto the surface of the CNT where they can become additional scattering sources and increase the noise in the CNT-based sensor. After the CNTs are coated in aluminum oxide, the samples are annealed at 500° C for 30 minutes. This annealing process helps both to reduce the contact resistance between the CNTs and aluminum electrodes and to remove some of the adsorbates from the surface of the CNTs. The effect of coating the CNTs in aluminum oxide and annealing the devices on the noise in the sensor is shown in Figure 5.4.

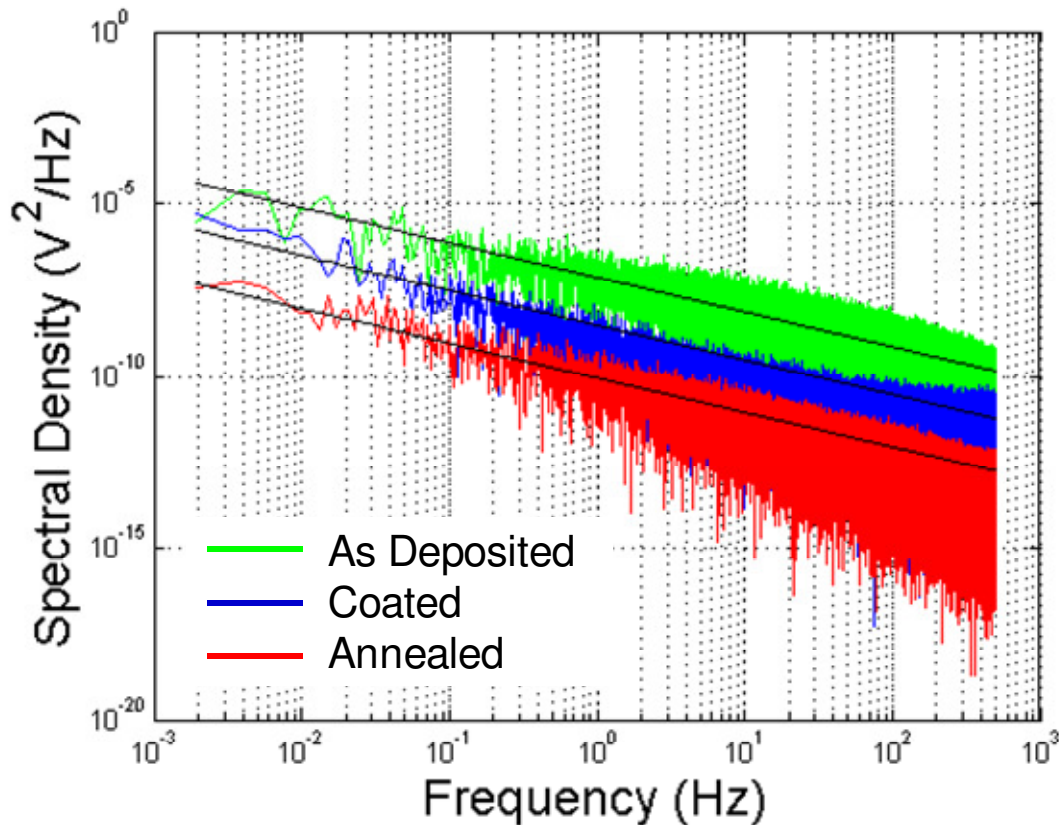


Figure 5.4. Power spectral densities of as deposited, Al₃O₂ and annealed CNT-based piezoresistive sensors.

By coating the CNT-based piezoresistors in a layer of aluminum oxide and annealing them it is possible to reduce the total noise in the sensors by almost two orders of magnitude, as shown in Table 5.1. This reduction in noise also results in a significant improvement in the dynamic range of the CNT-based piezoresistive sensors. For example, coating the CNTs in aluminum oxide increased the dynamic range by 14 dB, while annealing the samples increased

the dynamic range by another 15 dB. Overall, this demonstrates that through the use of proper design and manufacturing procedures, the resolution of CNT-based piezoresistive sensors can be significantly improved.

Table 5.1: Measured noise and dynamic range for CNT-based sensors produced under various processing conditions.

	Total Noise (μV)	α/N	Dynamic Range (dB)
As Deposited	1000	8×10^{-9}	50
Coated	200	3×10^{-10}	64
Annealed	36	1×10^{-11}	79

5.3.3 Annealing CNTs

In order to determine the optimal annealing conditions for the CNT-based piezoresistive sensors, a simple design-of-experiments (DOE) was set up to test the effects of annealing time and temperature on the noise in the sensor. A full factorial DOE was used with four temperature levels between 475 °C and 550 °C and time intervals of 30 minutes and 1 hour. Initially, as the time and temperature were increased the flicker noise in the sensors decreased, as seen in Table 5.2. This decrease in noise is likely due to improved CNT-electrode contacts and removal of adsorbed molecules. However, at high temperatures and long annealing times the flicker noise started to increase due to the degradation of the CNTs in the sensors. Overall, the optimal annealing conditions for the CNT-based piezoresistor in this test were determined to be an annealing temperature of 525 °C and an annealing time of 30 minutes. Using these processing conditions it is possible to reduce the flicker noise in the sensors by a factor of 229 over as deposited samples.

Table 5.2: Measured noise as a function of annealing time and temperature.

Temp \ Time	475 °C	500 °C	525 °C	550 °C
30 Minutes	370 μ V	190 μ V	4.37 μ V	49.7 μ V
60 Minutes	150 μ V	34.3 μ V	44.9 μ V	99.5 μ V

By using the optimal annealing conditions it is possible to start to hit the Johnson noise limit for these sensors, as shown in Figure 5.5.

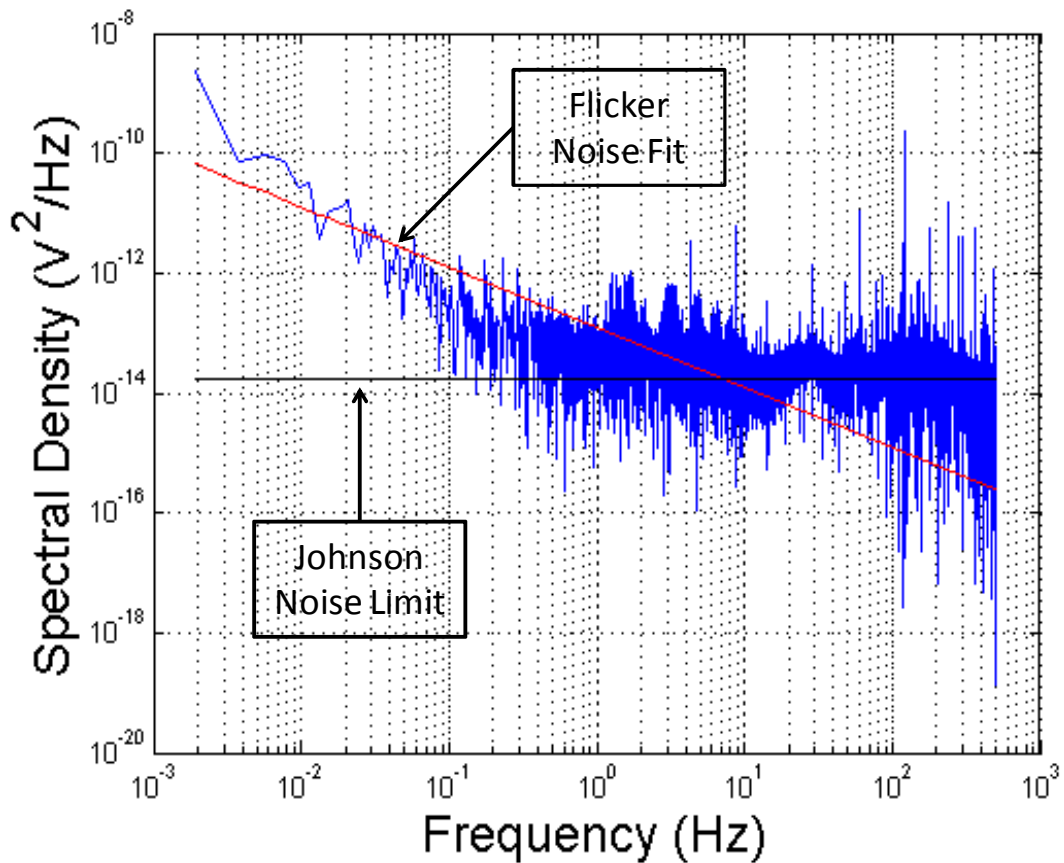


Figure 5.5. Power spectral densities of CNR-based sensor annealed at 525 °C.

The crossover frequency between the measured flicker noise and the Johnson noise limit predicted from theory is approximately 7 Hz. This indicates that for measurements that take less

that $1/10^{\text{th}}$ of a second, flicker noise is negligible and the Johnson noise becomes the dominant noise source. However, for longer experiments, flicker noise is still the dominant noise source.

5.4 Methods to Reduce Contact Resistance

5.4.1 Effect of Electrode Material

The selection of the electrode material can have a significant impact on both the magnitude and the type of contact resistance. For example, electrode materials with low work functions can sometimes produce Schottky-type contact resistances. This type of contact resistance is undesirable because it is nonlinear and can reduce the sensitivity of the sensor system. In addition, oxidation of the electrode material can increase the contact resistance and result in Schottky-type contact barriers.

For this study, aluminum, titanium and platinum contacts were tested. Both the titanium and platinum electrodes generally resulted in low resistance, ohmic contacts. However, the aluminum contacts sometimes resulted in Schottky-type resistors. This is because aluminum has a low work function and oxidizes easily. In order to overcome these limitations, the aluminum contacts were typically coated in platinum and annealed to produce low resistance ohmic contacts.

5.4.2 Platinum Coating

The platinum coating of the aluminum electrodes was performed using the gas injection system in the focused ion beam (FIB). In this process, the platinum organometallic gas is injected into the FIB vacuum chamber where it is chemisorbed onto the surface of the device. When the desired deposition area is scanned with the ion beam, the precursor gas is decomposed into volatile and non-volatile components. The non-volatile component of the gas, such as the platinum, remains on the surface while the volatile reactants are released back into the vacuum chamber. Through this process it is possible to coat both the CNTs and the aluminum electrode with platinum. This helps to improve the contact resistance by increasing the work function of the electrode, increasing the contact area between the CNT and the electrode, and by preventing oxidation of the contact area.

5.4.3 Annealing

After the platinum deposition, the aluminum contacts with the CNTs attached to them are typically annealed in order to reduce the contact resistance and improve the linearity of the contact. Annealing can be used to remove surface contaminants such as water molecules that can adhere to the electrode surface. In addition, annealing can create a composite structure between the electrode and the CNT which can significantly decrease the contact resistance and create an ohmic contact between the electrode and the CNT. A typical current-voltage curve for a CNT with the aluminum electrode after platinum deposition and annealing is shown in Figure 5.6. From this curve, it is clear that good ohmic contact has been achieved between the CNT and the aluminum electrode due to the linearity of the curve.

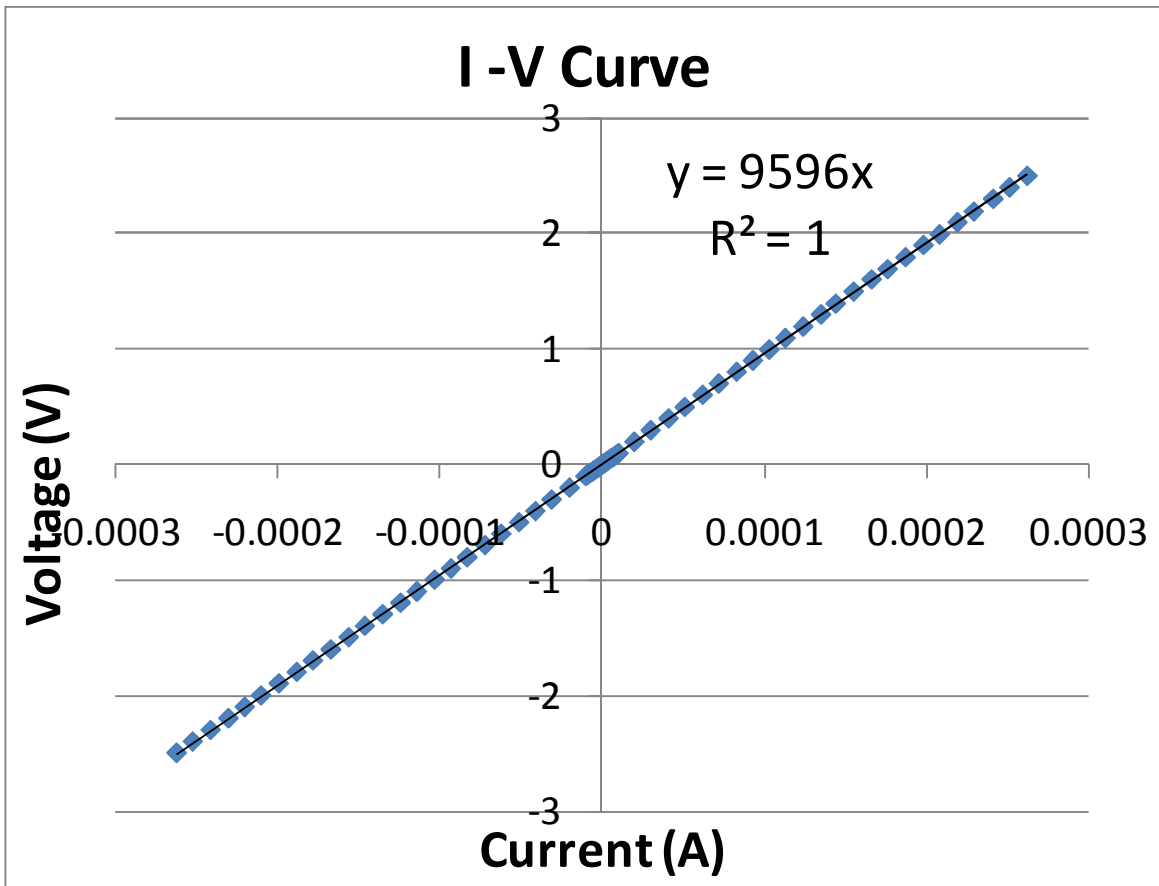


Figure 5.6. I-V Curve for CNT-based sensor showing ohmic contact.

5.5 Conclusions about Best Practices

5.5.1 Design and Manufacturing

This study found that in order to minimize the amount of noise in the CNT-based piezoresistive sensors, five basic rules should be followed.

1. Always maximize the size of the CNT-based piezoresistor.
2. Maximize the number of CNTs in the piezoresistive sensor.
3. Coat the sample CNT-electrode interface in platinum to minimize contact resistance.
4. Use ceramic coating to protect the CNT-based piezoresistor.
5. Anneal the CNT-based piezoresistive sensor at 525 °C for 30 minutes to reduce noise and improve contact resistance.

Through the use of these simple design and manufacturing rules of thumb it is possible to reduce the noise in the CNT-based piezoresistive sensors by almost three orders of magnitude.

5.5.2 Materials Selection

In general, in order to ensure low contact resistance and ohmic contact between the CNTs and the electrodes, electrode materials should be selected that have high work functions and that do not oxidize. However, these considerations must be weighed against fabrication considerations. For example, gold and palladium both have high work functions and do not oxidize easily. However, these materials tend to delaminate from the device structure and can contaminate microfabrication equipment. Alternatively, aluminum is easy to pattern and etch and does not create contamination issues. However, aluminum suffers from a low work function and it rapidly forms a surface oxide. Therefore, for much of this project aluminum was selected as the electrodes material but at the electrode-CNT interface platinum was added to ensure good ohmic contact.

5.6 Comparison to Conventional MEMS Piezoresistors

Overall, through the use of theory and experimentation this project has been able to increase the performance of CNT based piezoresistive sensors by more than three orders of magnitude over previous results [1]. These improvements make CNT-based piezoresistive sensors very competitive with more conventional MEMS piezoresistors such as metal, silicon

and polysilicon, as shown in Figure 5.7. However, more work still needs to be done on the sorting of CNTs in order to reach the theoretical maximum performance characteristics of CNT-based piezoresistive sensors.

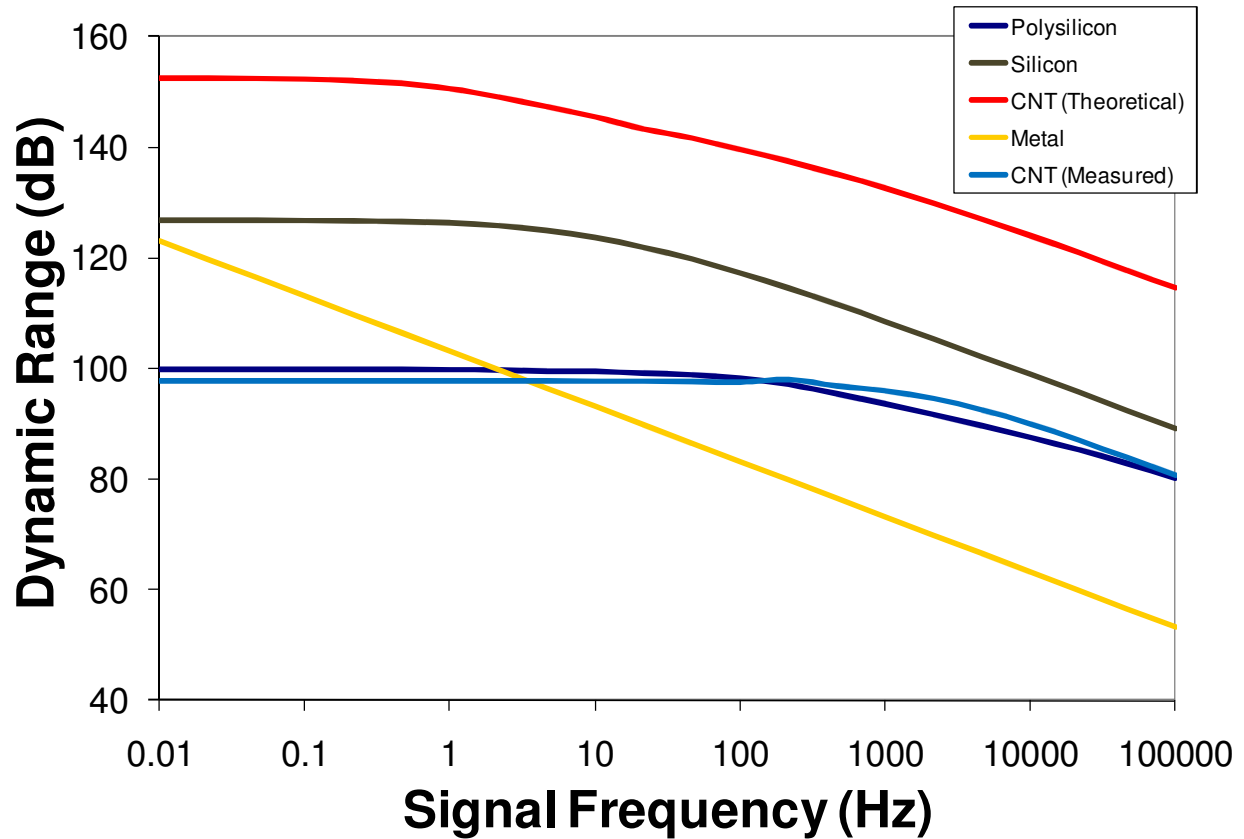


Figure 5.7. Performance of various piezoresistive materials.

As can be seen in Figure 5.7, for flexures on the scale of the flexures in the force sensor case study, current CNT-based piezoresistors outperform metal gauges for signal frequencies greater than 10 Hz. In addition, CNT-based piezoresistors perform about as well as optimized designs for polysilicon piezoresistors. Silicon based piezoresistors would outperform CNTs in a single axis device but are not capable of high performance on multi-axis devices due to the crystallographic orientation-dependent gauge factor of single crystal silicon. For smaller devices, the performance of CNT-based piezoresistors will continue to improve in comparison with silicon and polysilicon due to the scaling laws presented in Chapter 1. On the other hand, for larger devices polysilicon and silicon based piezoresistors are probably the best material selections. For slow measurements, metal gauges become a feasible option.

Based on this analysis, CNT-based piezoresistors are currently the best material for the force sensor case study. In addition, they have the potential to significantly increase in performance as chirality sorting technology improves.

6.1 3-Axis Force Sensor

6.1.1 Introduction

Multi-axis force sensing is required in biology, materials science and nanomanufacturing. Unfortunately, few fine-resolution, multi-axis MEMS force sensors exist because their creation involves substantial design and manufacturing challenges. In this chapter, the design, fabrication, and calibration of a multi-axis force sensor with integrated CNT-based piezoresistive sensors is presented as a case study for the development of such a sensor.

The focus of this case study is the design and fabrication of a 3-axis force sensor to measure the adhesion forces between an array of cells and a surface. This is important in the development of biomedical implants, for example, because it will allow researchers to determine the suitability of different types of materials in both areas where cell growth is desired and in areas where there should be no cell growth. Currently, this type of determination is done by looking at the cells in a microscope and seeing whether they tend to spread out on the surface or ball up [3,236]. However, this type of measurement is inaccurate and better measurement techniques are needed in order to optimize materials selection for biomedical implants. The development of the 3-axis force sensor described in this chapter will enable researchers to measure the adhesion of arrays of cells to surfaces more precisely and, therefore, to select the optimal materials for biomedical implants. The design and fabrication techniques presented in this case study build upon the theoretical and experimental results presented in Chapters 2-5 of this thesis.

MEMS force sensors tend to rely on one of three sensing methods: capacitive sensing, optical laser detection, and piezoresistive sensing. Several multi-axis force sensors have been

developed using capacitive sensors [163,164]. These sensors are difficult to fabricate and require relatively large sensor areas (mm^2) for each axis in order to achieve high force resolution. This makes capacitive sensing impractical for small, inexpensive, multi-axis force sensors.

Optical sensors are widely used in atomic force microscopy (AFM) to make high resolution force measurements in one axis. Optical sensors are rarely used in applications of interest due to the difficulty and cost of integrating multiple sets of optics into a small region. Also, optical sensors require relatively large lasers which make it impossible to miniaturize the force sensing system to the micro-scale.

Piezoresistive sensors offer the most promise at the micro-scale due to their small size and relative ease of integration into MEMS devices. Piezoresistive transducers are commonly found in MEMS devices such as pressure sensors, accelerometers, and AFM cantilevers [237]. Several dual-axis MEMS cantilevers with nN-level resolution have previously been demonstrated [173,175]. The modeling and design work in this case study will focus on piezoresistive sensing techniques.

6.1.2 Need and Description

The multi-axis force sensor presented in this chapter is designed to fit on top of the standard Hexflex architecture. The HexFlex is designed so that bond pads on the center stage of the HexFlex connect to the bond pads on the force sensor. The force sensor is held in place by a steel plate and a magnetic preload. In addition, rectangular magnets are placed on the tabs connected to the center stage of the HexFlex. These magnets are used in combination with a set of six Lorenz coils to actuate the center stage of the HexFlex. An exploded view of this setup is presented in Figure 6.1.

In this setup, the HexFlex nanopositioner is used to precisely move the multi-axis force sensor. The precise, six degree-of-freedom motion of the HexFlex is necessary to properly position the force sensor into place and align the center stage of the force sensor with the surface of the cells. The HexFlex can then be used to lower the force sensor stage into contact with the cells and to make sure even pressure is applied over the entire cell array. After the cells bond to the center stage of the force sensor, the HexFlex can be used to slowly retract the force sensor from the surface to which the cells are adhered. Using feedback from the force sensor, the HexFlex can be used to compensate for any torques that might be applied to the cells during this

retraction phase and to ensure that only the direct force normal to the cell surface is being measured. Overall, this setup and procedure should make it possible to accurately and precisely quantify the adhesion forces between cells and different types of surfaces.

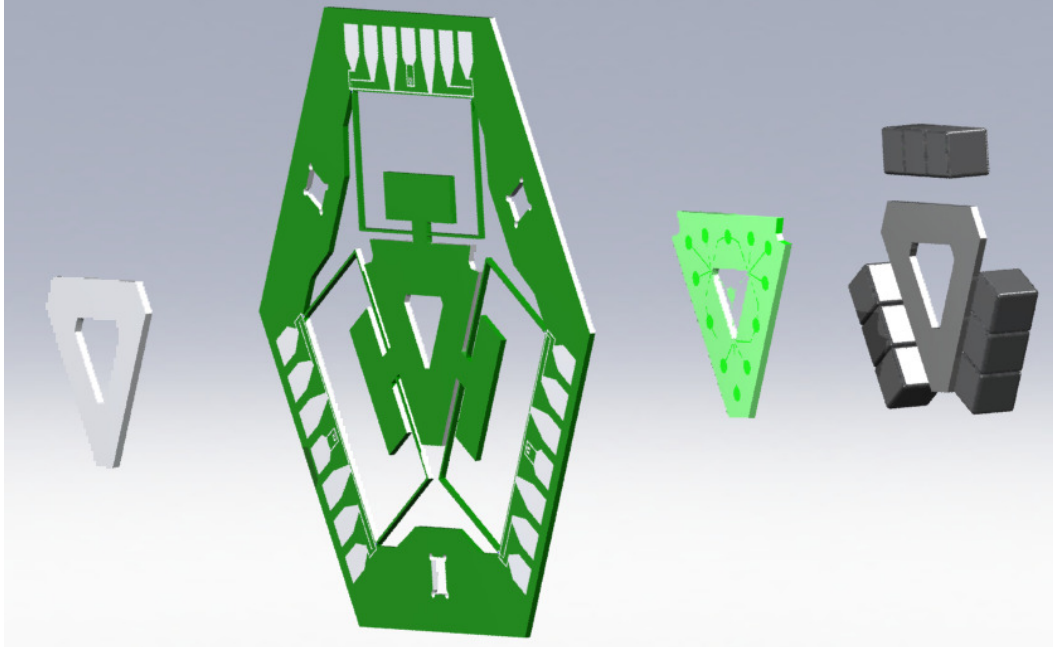


Figure 6.1. Exploded view of Hexflex-force sensor assembly.

6.1.3 Design of a Three-Axis Force Sensor

Multi-axis, precision force sensing is needed to measure adhesion forces between cells and various material surfaces. For example, these measurements enable one to know (i) how well cells bond to different types of biomedical implant materials and (ii) the effects that drug coatings have on the prevention/promotion of adhesion. This type of measurement is necessary where the mechanical properties of the cell-implant interface are critical [3].

6.1.3.1 Functional Requirements

Accurate measurement of cell adhesion forces between surfaces requires multi-axis sensing to make sure that the surfaces are suitably positioned and oriented, thereby ensuring that load is applied evenly over the surfaces during testing. Cellular adhesion forces are typically on the scale of nN [238]. When thousands of cells are arrayed on the surface being tested, the adhesion force is on the order of 100's of μN . Therefore, to be useful, the force sensor must

have 100's of μN range, nN resolution. The natural frequency of the force sensor was set to 1 kHz in order to ensure that it was capable of operating at least 1 order of magnitude faster than the HexFlex, which has a natural frequency of ~ 100 Hz. This ensures that the force sensor can be used in feedback mode with the HexFlex, even when the HexFlex is operating at its maximum speed. In addition, in order to ensure that the force sensor is applying an uniform force over the entire cell array, the force sensor must be capable of measuring forces in a direction parallel to the normal to the plane of contact (Z) and torques about axes that are parallel to the planes of contact, (θ_x, θ_y) . Also, the force sensor must fit on the central stage of the Hexflex and the force sensor must be low cost ($< \$100$) so that it can be replaced after each test.

Table 6.1: Force Sensor Functional Requirements.

<i>Functional Requirement</i>	<i>Value</i>
Measurement Axis	Z, θ_x , θ_y
Range	100's of μN
Resolution	~ 1 nN
Natural Frequency	1 kHz
Cost	$< \$100$
Footprint	$< 1 \text{ mm}^2$

6.1.3.2 Polysilicon Piezoresistor Force Sensor Design

The noise model presented in Chapter 2 was used to design both a polysilicon piezoresistive sensor and a CNT-based piezoresistive sensor 3-axis force sensor that are intended to satisfy functional requirements for measuring cell adhesion forces. These force sensors are designed to fit on top of a HexFlex nanopositioner system [5]. This makes it possible for the force sensor to be accurately positioned and oriented while minimizing the cost of the total system. Figure 6.2 shows the polysilicon-based piezoresistive force sensor, which is comprised of three coplanar flexures with integrated piezoresistors at the base of the flexures. The piezoresistors are in a half bridge arrangement. A full Wheatstone bridge was not used due to fabrication and thermal heating constraints. The piezoresistors are n-doped polycrystalline silicon deposited by chemical vapor deposition and are connected to aluminum contact pads on

the outer base of the force sensor via aluminum traces. The sensors are placed at the base of the structure to maximize the strain imposed upon the resistors.

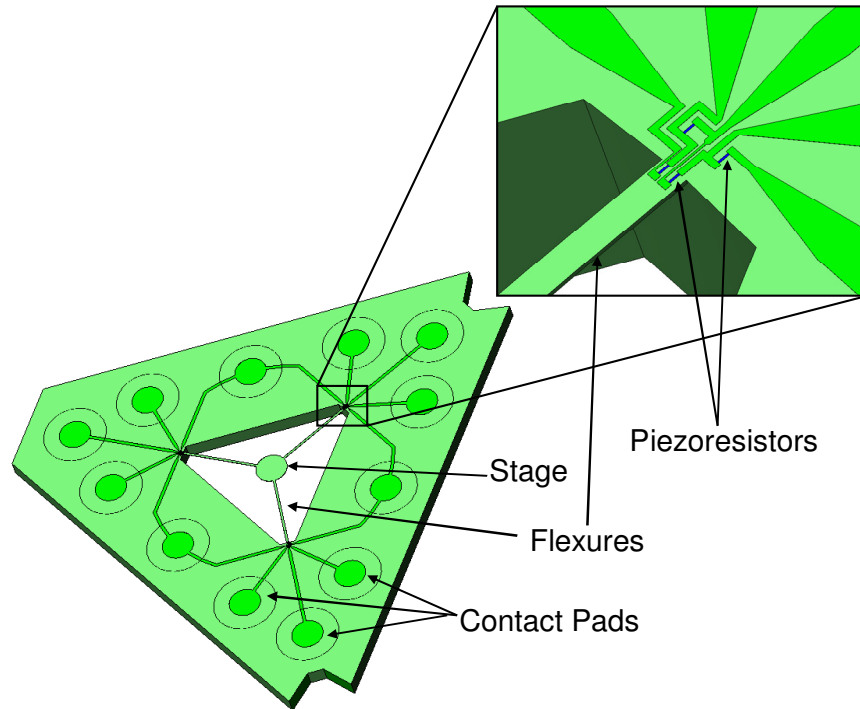


Figure 6.2. 3-axis force sensor with polysilicon piezoresistors.

The flexures in the force sensor are fabricated using deep reactive ion etching (DRIE) of a silicon-on-insulator (SOI) wafer. The flexures are connected to a 1 mm diameter central stage which is meant to contact the cells during testing. The flexures' lengths are limited to 2.5 mm due to device footprint constraints. The flexures' widths and thicknesses are set to meet both the range and resolution functional requirements using the noise flow model. A 70 μm beam width and 10 μm beam thickness were chosen.

6.1.3.3 CNT-Based Piezoresistive Force Sensor Design

The design of the CNT-based piezoresistive force sensor was based on the design of the multi-axis force sensor with polysilicon piezoresistors presented in the previous section. Several small design changes were incorporated in the CNT-based piezoresistive force sensor in order to account for the differences between the polysilicon and the CNT-based piezoresistors. For example, the half-bridge in the polysilicon-based piezoresistor design was replaced by a quarter-

bridge in the CNT-based piezoresistor design due to concerns about the uniformity in resistance between CNT-based piezoresistive sensors. The uniformity in resistance is important because if the two resistors in the half-bridge do not have the same resistance, it is difficult to balance the bridge and make a good measurement. By replacing the half bridge with a quarter-bridge, the sensitivity of the sensor system was reduced by a factor of two. Therefore, the width of the flexure beam was reduced by a factor of two in order cut the stiffness in half and to maintain the same resolution between the two sensors when the same resistors are used. A schematic of the CNT-based piezoresistive force sensor is given in Figure 6.3.

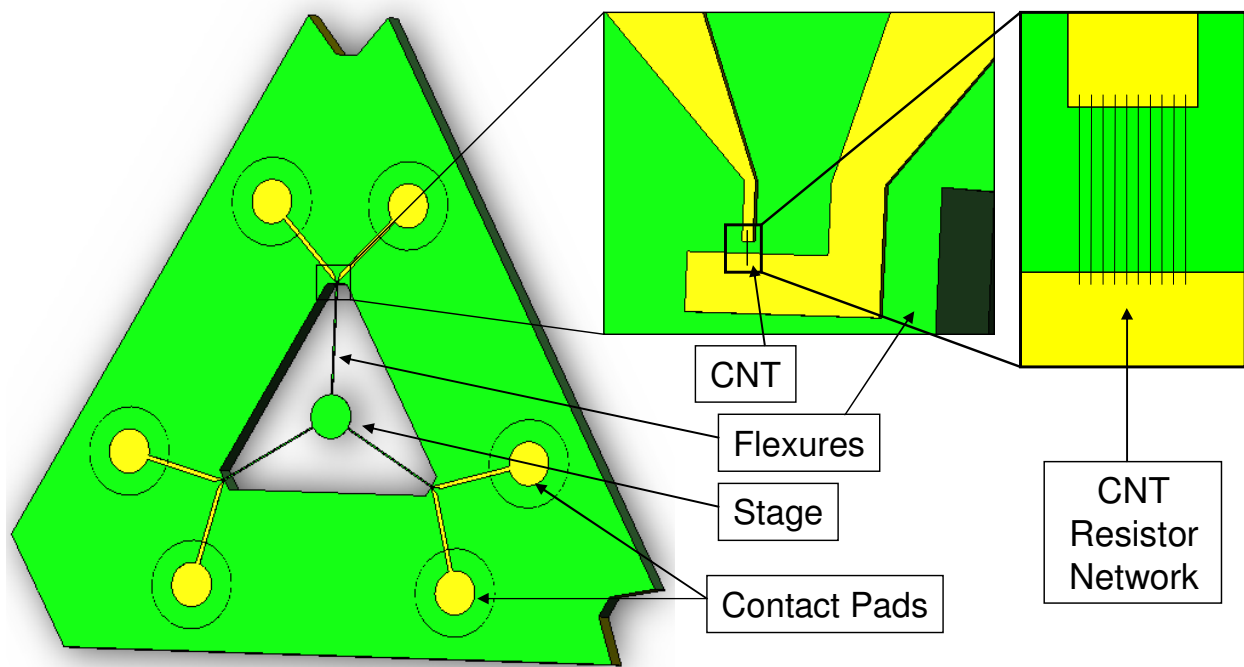


Figure 6.3. 3-axis force sensor with CNT-based piezoresistors.

The final flexure dimensions of the force sensor are a beam length of 2.5 mm, a beam width of 35 μm and a beam thickness of 10 μm . Based on this design it was estimated that the CNT-based piezoresistive force sensor should have a force resolution of approximately 100 μN and a resolution of approximately 7 nN. This works out to a dynamic range of 83 dB. In addition, the estimated natural frequency was approximately 1000 Hz. These design properties are presented in Table 6.2: CNT-Based Force Sensor Design. Table 6.2.

Table 6.2: CNT-Based Force Sensor Design.

Property	Value
Beam Length	2.5 mm
Beam Width	35 μm
Beam Thickness	10 μm
Max Force	100 μN
Natural Frequency	1000 Hz
Dynamic Range	83 dB

6.1.3.4 HexFlex Motion Stage

The HexFlex consists of (1) six bent beams with integrated piezoresistive sensors, (2) three sets of magnets, and (3) a flex circuit with mm-scale coils. The bent beams enable the stage to move in 6 DOF and the piezoresistors enable six-axis displacement sensing. The magnet arrays and flex circuit are used to create six Lorentz force actuators that control the motion of the nanopositioner. The force sensor is placed onto the central stage of the HexFlex. The bond pads on the force sensor are aligned to pads on the HexFlex so that the signal from the piezoresistors in the force sensor may be ported out of the sensor.

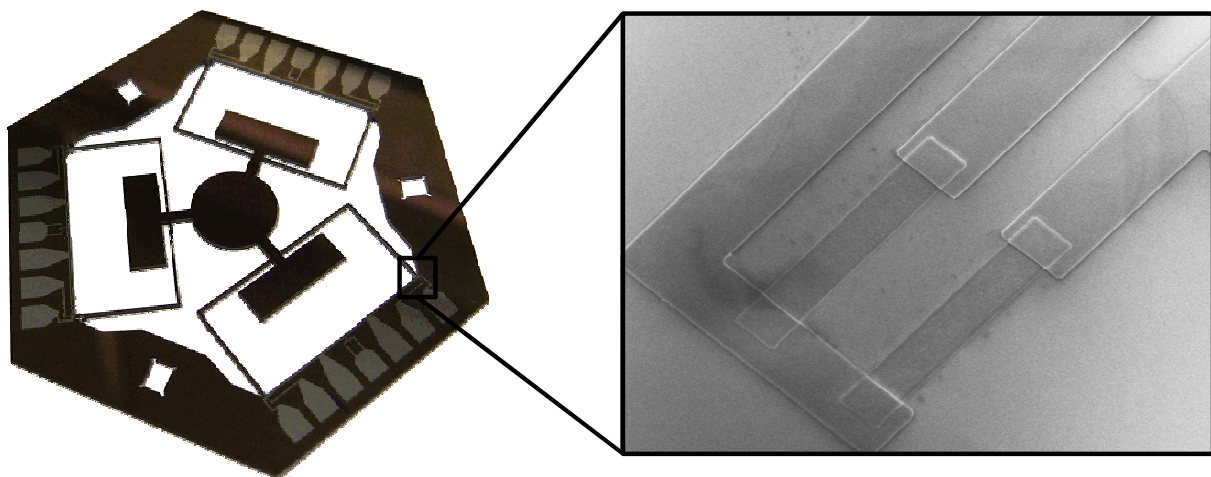


Figure 6.4. HexFlex with polysilicon piezoresistive sensors.

The mesoscale HexFlex has been traditionally fabricated using standard microfabrication procedures. First a thermal oxide insulation layer is grown on a 400 μm thick silicon wafer. Then, low pressure chemical vapor deposition is used to deposit doped polysilicon onto the wafer. Next, the polysilicon layer is patterned into piezoresistors using photolithography and etching. After the piezoresistors are fabricated a layer of aluminum is deposited onto the wafer. This aluminum layer is patterned into wire traces using photolithography and etching. These wire traces connect the polysilicon piezoresistors to bond pads so that the read out of the piezoresistive sensors can be made. Next, the physical structure of the Hexflex is created by mounting the wafer to a quartz handle wafer and using deep reactive ion etching (DRIE) to etch through the entire wafer. Finally, the Hexflex devices are released from the quartz handle wafer using an acetone bath [239].

Overall, this procedure produces HexFlex devices that have a range of about 20 μm and a resolution of 20 nm in each axis. However, this fabrication process can take months to complete and costs \$10's of thousands of dollars per batch. In addition, the yield on this fabrication technique is extremely low due to the brittleness of the silicon. Therefore, the cost per HexFlex device can be as high as several thousand dollars. In order to improve the yield and lower the cost of the mesoscale HexFlex, micromilling has been used to fabricate several HexFlex devices. These HexFlex devices have the same dimensions as the microfabricated HexFlex devices but are not brittle and take only a few minutes to fabricate. The main drawback of the micromilled HexFlex devices is the lack of piezoresistive sensing elements integrated into the structure. In chapter 7, I will present some preliminary research showing how CNT-based piezoresistive sensors may be incorporated into micromilled structures.

In this project, a Microlution 363-S 3-axis horizontal micro-milling machine was used to fabricate several HexFlex devices out of Aluminum 6061-T6 sheet stock and Aluminum 1100 shim stock. Pictures of the machined HexFlexes are shown in Figure 6.5.



Figure 6.5. (clockwise from top) Al 1100 HexFlex being machined in the micromill, Al 1100 HexFlex, Al 6061-T6 HexFlex.

Unlike conventional end-mills, this milling device has no vise to quickly secure parts and no edge-finding/zeroing process to specify a zero with respect to a desired datum surface on the workpiece. For this research, a sacrificial fixture was developed specifically for HexFlex fabrication that screws onto the micromill pallet via four 10-32 socket-head cap screws. The fixture is machined out of 6061-T6 Aluminum and has four 4-40 threaded holes lining the periphery that secure the piece of raw stock to the fixture. Double-sided adhesive is placed in between the stock and the sacrificial fixture to provide viscous damping. FEA simulations determined that the HexFlex's first 3 modes of vibration are around 400 Hz. As micromilling necessitates spindle speeds between 10,000 RPM and 50,000 RPM (166 Hz – 833 Hz), unrestrained vibration is a potential concern. The adhesive also serves to minimize large-scale

deflection of the thin (200 μm) flexural blades against normal cutting forces. The separate components and the entire pallet-fixture-stock assembly are shown in Figure 6.6.

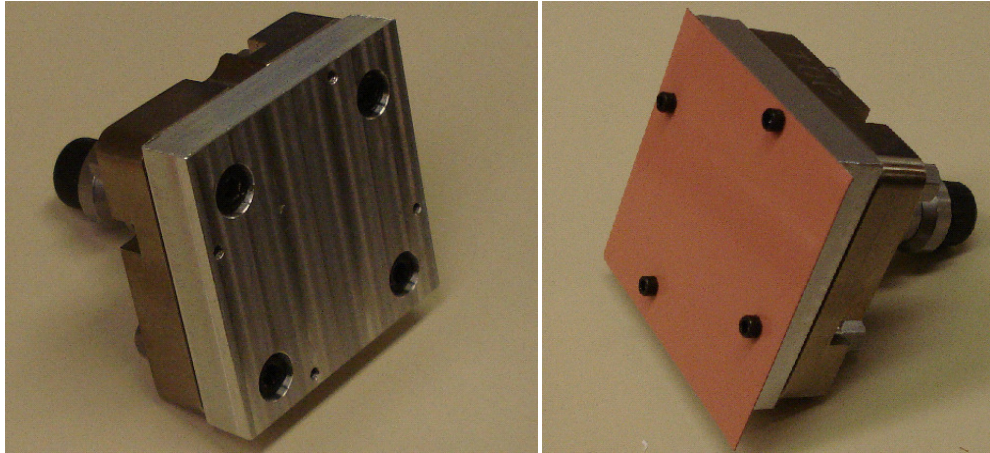


Figure 6.6. Hardware setup for micromilling HexFlex nanopositioners.

Toolpaths were generated and post-processed using HSMWorks, a CAM package developed by Dassault systems. The process consists of five steps: (1) cutting to depth (thickness of stock minus desired part thickness) and roughing out the hexagonal shape, (2) roughing out the interior pockets, (3&4) finishing the interior contours, and (5) finishing the hexagonal contour and separating the finished part from the uncut stock. The post-processed G-code was uploaded into the Microlution control panel using the process parameters summarized in Table 6.3.

Table 6.3: Process parameters for HexFlex machining.

Step	1	2	3&4	5
Toolpiece Diameter [mm]	3.175	1.016	0.381	3.175
Spindle Speed [RPM]	17,000	36,000	50,000	17,000
Cutting Feed [mm/min]	254	229	127	254
Axial DOC [mm]	0.30	0.15	0.06	0.30
Final Depth [mm]	-0.553	-0.953	-0.953	-0.953
Machining Time [min:sec]	13:55	16:58	28:12	3:16

6.1.3.5 System Dynamics

In order to analyze the dynamics of the force sensor system, several finite element dynamics simulations were carried out on both the force sensor structure and the force sensor – HexFlex assembly. The results for the first resonant mode of the force sensor are given in Figure 6.7.

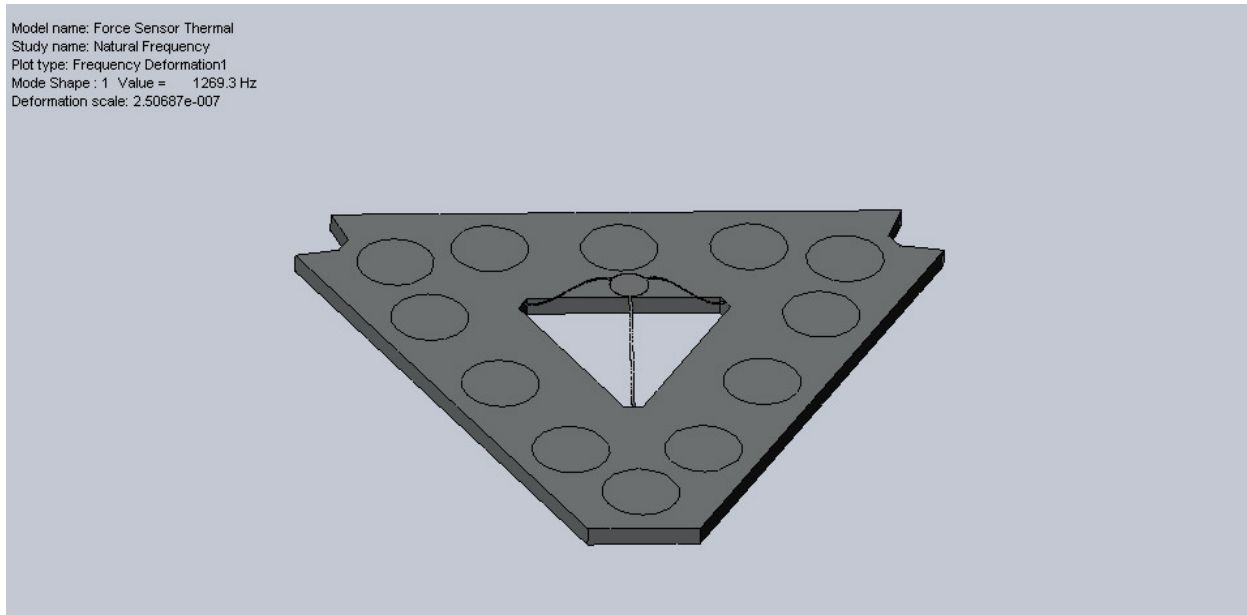


Figure 6.7. First resonant mode of force sensor.

In the dynamic simulation of the force sensor the outside structure is grounded and the center stage is free to move. The first resonant mode of the force sensor is the vibration of the center stage in the z-axis. The natural frequency of this mode is 1269 Hz, which is slightly higher than the predicted natural frequency of ~1000 Hz from the lumped element model used in the design of the force sensor.

Dynamic simulations were also performed on the overall Hexflex-force sensor assembly in order to determine the natural frequency of the overall structure. The results of this simulation are presented in Figure 6.8.

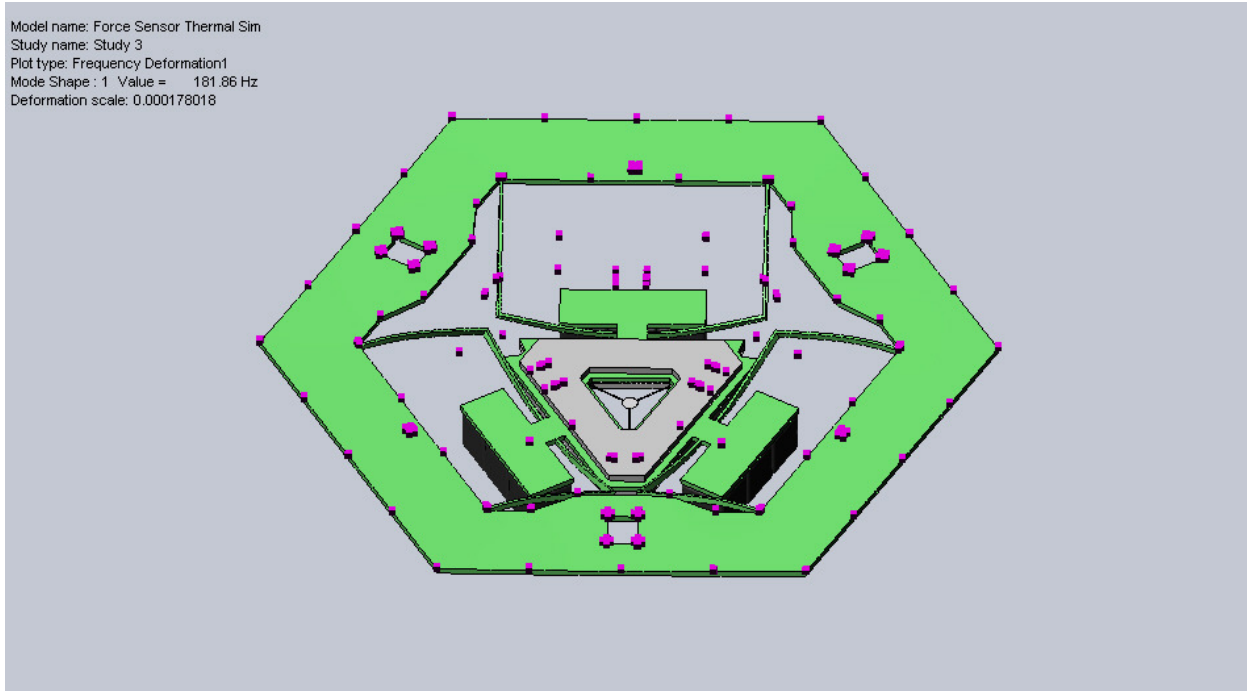


Figure 6.8. First resonant mode of Hexflex - force sensor assembly.

In this simulation, the outer structure of the Hexflex is grounded while the flexures and the center stage are free to move and deform. The weights of the magnets, steel plate, and force sensor are included in the simulation and are added to the center stage of the Hexflex. Overall, the finite element dynamic simulation predicts that the first mode of the HexFlex-force sensor assembly is the displacement of the center stage in the z-axis, and that the natural frequency of the HexFlex-force sensor assembly is 181 Hz. Therefore, the natural frequency of the HexFlex assembly is approximately equal to the design value of 100 Hz for the Hexflex and is about an order of magnitude lower than the natural frequency of the force sensor. This means that it should be possible to operate the HexFlex-force sensor assembly in force feedback mode even when the HexFlex is operating near its natural frequency.

6.1.4 Fabrication

The MEMS force sensors for this case study were fabricated using conventional microfabrication techniques, as described in Table 6.4. The process starts with a 150 mm silicon-on-insulator (SOI) wafer with a 10 μm device layer, a 500 μm handle layer, and a 1 μm oxide layer. First, an RCA clean is used to remove any contaminants from the wafer surface. This is important because it ensures that the thermal oxide will be grown properly. After the RCA clean,

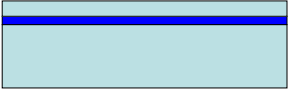

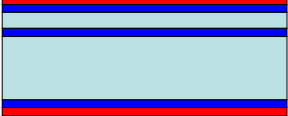





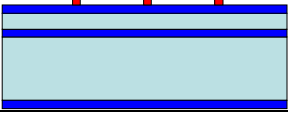



the wafer is placed in the oxide furnace and 300 nm of thermal oxide is grown on the wafer. Next the wafer is placed in the low-pressure chemical vapor deposition (LPCVD) furnace and 500 nm of polysilicon is grown on the wafer. This polysilicon is used as the piezoresistive material for half of the force sensors on the wafer. The rest of the force sensors are left blank so that CNT-based piezoresistors can be deposited after the microfabrication process is complete. After the polysilicon is deposited it is placed in an annealing furnace to improve the resistivity of the polysilicon and to ensure that the dopants are evenly distributed throughout the film.

After these high temperature processing steps are completed, a protective photoresist coating is applied to the front side of the wafer and the back side polysilicon is removed. Next photolithography with mask 1 is used to define the pattern of the polysilicon on the wafer and reactive ion etching is used to remove the polysilicon from the unwanted areas. The masks for this fabrication process are presented in Appendix B. After the polysilicon piezoresistors are defined, the wafer is cleaned using an ashers to remove the photoresist and a piranha clean to remove any other contaminates, before 500 nm of aluminum is sputtered onto the wafer. Again, photolithography mask 2 is used to define the wire traces and bond pads while etching is used to remove the excess aluminum from the wafer.

Next, a protective photoresist is applied to the front side of the wafer so that it is not damaged while a buffered oxide etch (BOE) is used to remove the thermal oxide from the back side of the wafer. After this step, photolithography with mask 3 is used to define the flexure structure on the front side of the wafer. A BOE is used to remove the oxide from the front side of the wafer and deep reactive ion etching (DRIE) is used to create the flexures in the handle layer. The ashers is used to remove excess photoresist from the front side of the wafer.

Finally, photolithography is used to pattern the back side of the wafer using mask 4. The front side of the wafer is then mounted to a quartz handle wafer. This handle wafer acts as both a protective layer for the front side as well as a mechanical structure that holds the wafer together after the DRIE step. DRIE is used to etch the back side of the wafer and to release the flexures from the handle layer of the SOI wafer. DRIE is also used to etch through the entire wafer in order to separate the wafer into devices. After the DRIE step, a vapor hydrofluoric acid (HF) step is used to remove the excess oxide from the insulating layer of the SOI wafer and the wafer is placed into an acetone bath to separate the chips from the quartz wafer. In the end, a laser ablation system is used to separate any chips that may still be attached to each other.

Table 6.4: Processing steps for force sensor fabrication.

Step	Lab	Machine	Description	Comment	
1	ICL	RCA	RCA Clean	SOI Wafer	
2	ICL	Tube 5C	Thermally grow 300 nm oxide		
3	ICL	Tube 6A	LPCVD deposit 500 nm Poly-Si		
4	ICL	Tube 5B	Anneal Poly-Si		
5	ICL	Coater6	Protective layer	Photoresist protective layer	
6	ICL	LAM490	Poly Dry Etch	Remove 500 nm Poly-Si on back	
7	ICL	Asher	Ash	Remove resist	
8	ICL/TRL	coater6, HMDS-TRL, EV1, coater6	Lithography (frontside)	Mask 1, positive, DF	
9	ICL	LAM490	Poly Dry Etch	Remove 1 μm Poly-Si	
10	ICL	Asher	Ash	Remove resist	
11	ICL	Premetal-Piranha	Pre-metal clean		
12	ICL	Endura	Sputter 500 nm Al		

13	ICL/ TRL	coater6, HMDS-TRL, EV1, coater6	Lithography (frontside)	Mask 2, positive, DF	
14	ICL	Rainbow	Etch 500 nm Al		
15	ICL	Asher	Ash	Remove resist	
16	ICL/ TRL	coater6, HMDS-TRL, EV1, coater6	Lithography (frontside)	Photoresist protective layer	
17	ICL	Oxide-etch	BOE	Removal of backside oxide	
18	ICL	Asher	Ash	Remove Resist	
19	ICL/ TRL	coater6, HMDS-TRL, EV1, coater6	Thick resist lithography (frontside)	Mask 3, positive, DF	
20	ICL	Oxide-etch	BOE	Remove oxide	
21	TRL	STS1	DRIE	10 μm, through device layer.	
22	TRL	Asher	Ash	Remove Resist	
23	TRL	HMDS-TRL, coater, prebake, EV1, postbake	Thick resist lithography (backside)	Mask 4, positive, DF	
24	TRL	coater, prebake	Mount handle wafer	Spin thick PR, quartz handle wafer mount	

25	TRL	STS1	DRIE	500 μm , through handle layer.	
26	TRL	Acidhood	Vapor HF	Removal of oxide.	
27	TRL	Photo-wet	Acetone release	24h acetone bath to release handle wafer	
28	TRL	Asher	Ash	Remove Resist	
29	ICL	Resonetics	Laser Ablation	Separate Chips	

After the microfabrication is complete, CNT-based piezoresistors are deposited onto the blank CNT force sensors using dielectrophoresis. A droplet of a 3 g/L CNT solution is placed on the gap between the electrodes on the force sensor structure. A 5V peak-to-peak ac voltage with a frequency of 5 MHz is used to align the CNTs between the two electrodes. This deposition process is continued for 15 minutes in order to ensure that the maximum number of CNTs are deposited on the force sensor structure. After the sensors are deposited by dielectrophoresis, they are coated in an aluminum oxide protective layer and annealed at 525 °C for 30 minutes as described in Chapter 5 in order to minimize the amount of noise in the sensor. The final result of this fabrication process is shown in Figure 6.9.

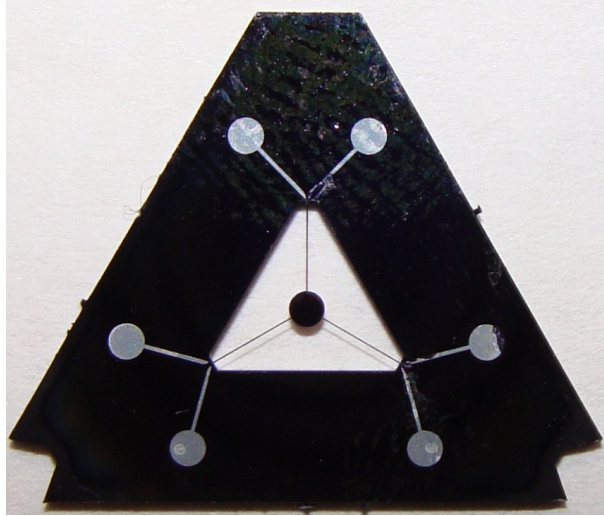


Figure 6.9. Fabricated 3-axis force sensor with CNT-based piezoresistors.

6.2 Testing

6.2.1 Setup

Two different setups are used to measure the stiffness of the force sensor and to calibrate the force sensor. The stiffness of the force sensor is measured using the Hysitron TriboIndenter. The force sensor is mounted in a test setup which allows contact to be made to the piezoresistive sensors on the flexural elements. The nanoindenter is used to deflect the center stage of the force sensor which is located in a 0.762 cm diameter hole 1 mm below the top surface of the setup, as shown in Figure 6.10. In this test, the nanoindenter is used to indent an array of points on the center stage to find the center of stiffness. The nanoindenter is then used to deflect the stage with a known force load at the center of stiffness and measure displacement of the center stage. Using this method it is possible to get an accurate measurement of the force sensor stiffness.

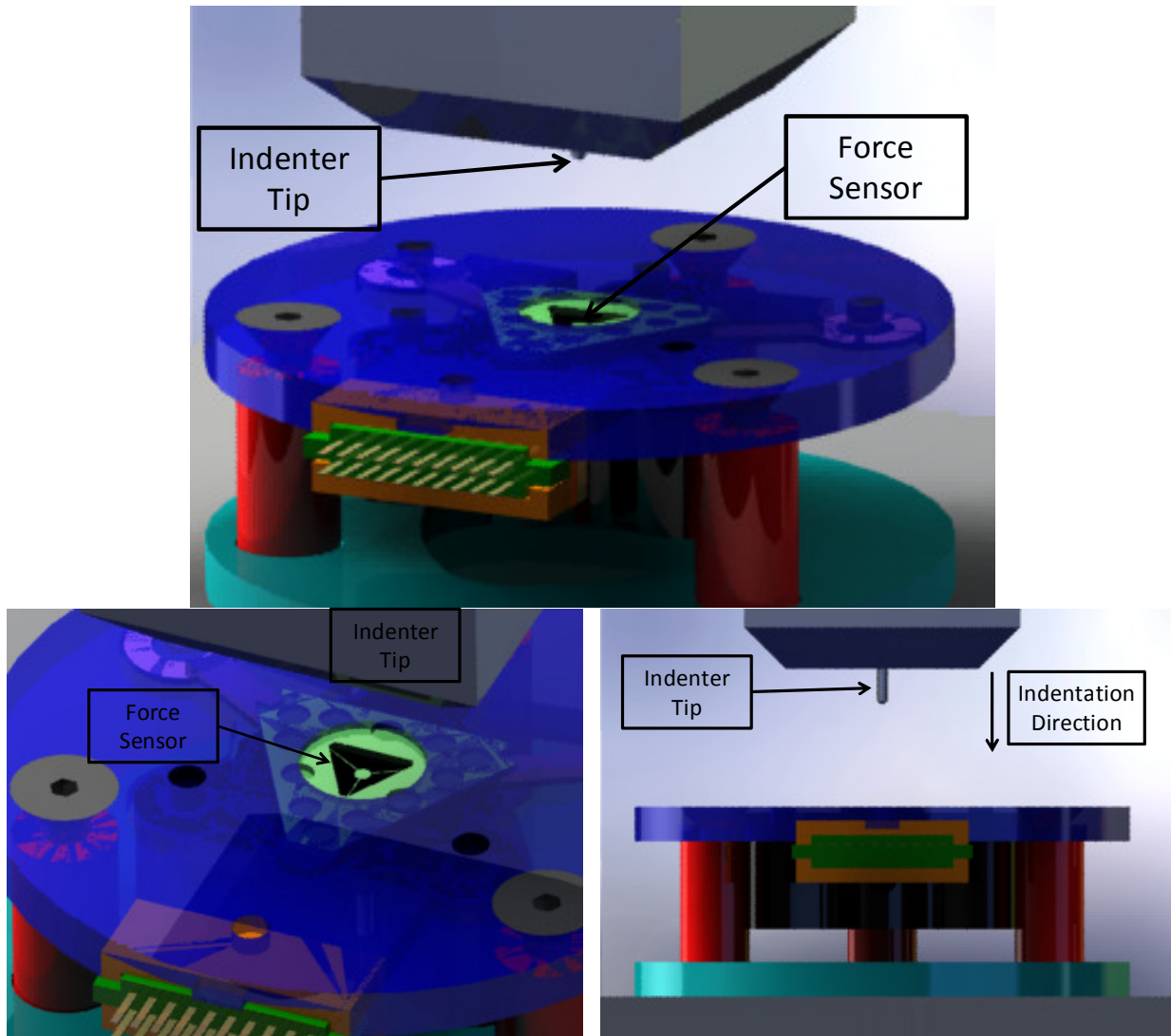


Figure 6.10. Force sensor stiffness testing setup with top and side view.

The calibration setup is similar to the stiffness measurement setup except that a micrometer is used to actuate the center stage of the force sensor. The micrometer has a digital readout with a resolution of 1 μm . Spring pins are used to connect the bond pads on the force sensor to wires that run to the Wheatstone bridge circuit. These spring pins provide a preload to the force sensor to hold it in place during testing and ensure that all of the bond pads are in contact during testing. A small 1 mm diameter ball is connected to the tip of the micrometer head in order to ensure a small contact area and to prevent torques from being transmitted to the center stage from the rotation of the micrometer head. This setup allows the force sensor to be calibrated over a much larger range since the micrometer can travel through the full range of the

force sensor while the nanoindenter is only capable of displacements of up to 5 μm . A picture of this setup is given in Figure 6.11.

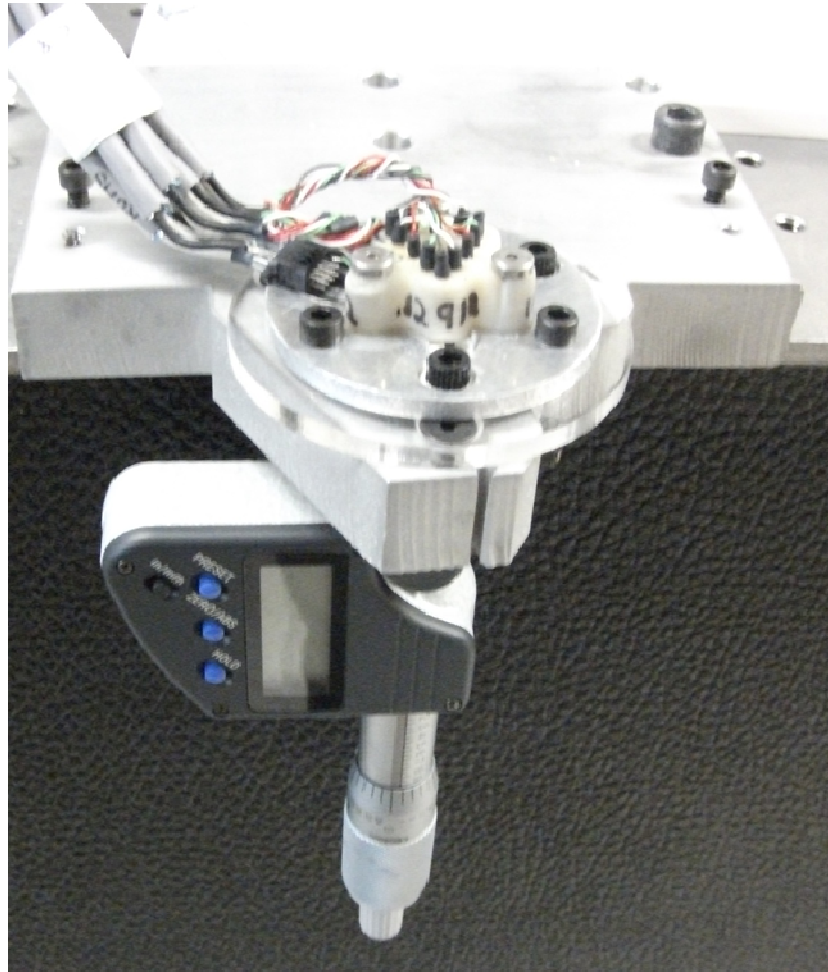


Figure 6.11. Force sensor calibration setup.

6.2.2 Calibration Procedure

The CNT-based force sensor was calibrated using the test setup described in the previous section. First the CNT-based force sensor was placed in the testing setup and fixed into place. Then the spring pins were brought into contact with the bond pads on the force sensor and a preload was applied using three bolts. Next, the micrometer was brought into contact with the center stage of the force sensor and zeroed. Finally, the readout from each of the sensors was

amplified through the Wheatstone bridge circuit and read into Labview. The noise in each sensor was measured at a measurement frequency of 1000 Hz over a time period of 1000 seconds.

An initial measurement for all three sensors was taken in Labview, then the micrometer was actuated by 1 micron and a new set of measurements was recorded. This process was continued for 35 μm or until the force sensor reached about 1/3 of its predicted maximum displacement. The output of each sensor was recorded for each 1 micron displacement. These data were then used to create calibration curves for each piezoresistor in the force sensor.

6.3 Calibration Results

The calibration results for each sensor are presented in Figure 6.12. Sensor 1 has a sensitivity of 0.79 mV per μN , while sensors 2 and 3 have sensitivities of 0.64 mV per μN and 0.59 mV per μN respectively. Each of these calibration curves explains over 95 percent of the variance in voltage with the increase in force applied to the structure. Therefore, these curves are an accurate representation of the sensors' response to a force input. The differences in force sensitivities could be due to either the differences in the gauge factors of the sensors or to asymmetric loading of the structure by the micrometer. Previous results with the test structures have shown that the gauge factor of CNT-based piezoresistive sensors can vary by up to 12 percent. This explains about half of the variation between the sensors. Asymmetric loading of the force sensor by the micrometer could also contribute to the difference in measured sensitivities by imposing torques onto the force sensor as well as z-axis displacement. These torques would cause some of the flexure beams to be strained more than others, which would result in the higher readouts from these sensors.

For example, a positive torque around the x-axis would result in an increased strain on sensor 1 but a decreased strain on sensors 2 and 3. Such a torque could be created if the location of the actuation was moved in the positive y-direction from the center of stiffness of the force sensor. Such an offset could either be created by small fabrication errors that result in the center of stiffness not being at the same location as the geometric center or by the actuator not pushing directly on the geometric center of the force sensor. Either way, this type of torque about the x-axis could help explain the remaining discrepancy between the measured sensitivities of each of the sensors.

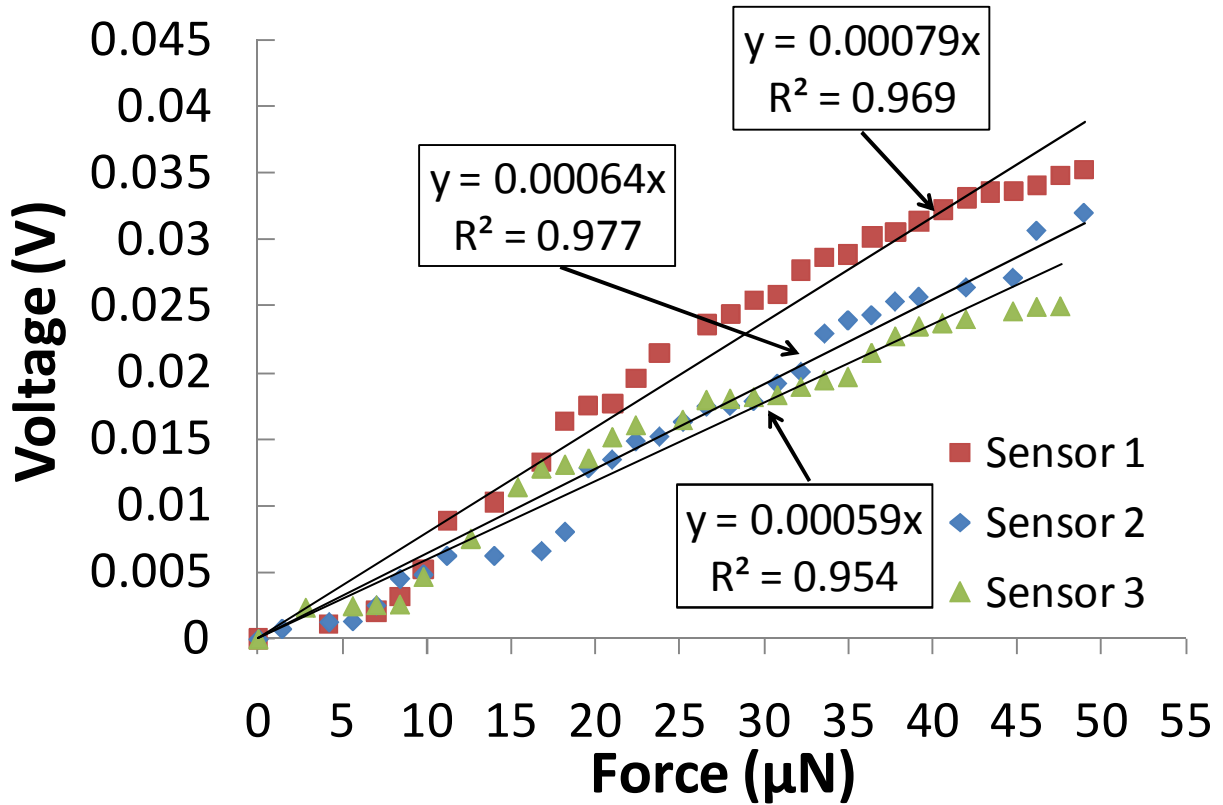


Figure 6.12. Calibration curve for each CNT-based sensor on the force sensor.

In addition to the to the linear calibration curves, each sensor appears to have a sinusoidal component. This component is likely due to thermal variations over the testing period. The total test took about 20 minutes, which is approximately equal to the thermal period of the room. Therefore, we would expect to see about 1 full thermal period in each sensor due to thermal variations of the room.

6.4 Results

6.4.1 Range

The total range of the system was measured by increasing the displacement of the micrometer head until a sharp change in the sensor readout was observed. This sharp change was caused by the fracture of one of the flexure beams, which caused the readout from the sensor on that flexure beam to return to its original value, since the strain on the CNT-based piezoresistors decreased to zero. Overall, the range of the sensor was measured to be about 60

microns. The stiffness of the force sensor measured from the nanoindentation tests was 1.4 N/m. therefore the force range of the force sensor was measured to be 84 μN .

6.4.2 Resolution

The resolution of each sensor was calculated by dividing the noise in each sensor by the sensitivity of each sensor. The measured resolution for sensor 1 was 9.5 nN and it was 11.8 nN and 6.7 nN for sensors 2 and 3, respectively. The results for each sensor along with the corresponding measured dynamic ranges for each sensor are presented in Table 6.5.

Table 6.5: Results for each piezoresistor in the force sensor.

	Sensor 1	Sensor 2	Sensor 3
Sensitivity	790 V/N	640 V/N	590 V/N
Noise	7.5 μV	7.5 μV	4 μV
Dynamic Range	78.4 dB	76.5 dB	81.3 dB

The overall resolution of the force sensor is calculated by taking the weighted sum of squares of each of the three sensors in the force sensor structure. Based on this calculation, the resolution of the force sensor is approximately 5.6 nN. This corresponds to a dynamic range of 83 dB and matches the predicted dynamic range for the sensor of 83.2 dB with less than 0.25% error. The accuracy of this prediction indicates that the system optimization method presented in Chapter 2 can be used to improve the design of the sensor system.

6.5 Possible Improvements

6.5.1 Recommended Changes in Design and Manufacturing

There are three main improvements that can be made to the force sensor system: (1) incorporate higher gauge factor CNTs, (2) increase sensor size, and (3) change the flexural material. In order to incorporate higher gauge factor CNT into the force sensor device it is

necessary to improve our ability to sort CNT by chirality. If it become feasible to sort out the highest gauge factor CNTs, it will be possible to increase the gauge factor of the piezoresistive CNT-based sensors from 75 to over 350.

Increasing the sensor size will help to reduce the noise in the sensor since the CNT-based piezoresistive sensors are flicker noise-dominated. By decreasing the thickness of the flexure beam by an order of magnitude it should be possible to increase the width of the flexure beam by up to 3 orders of magnitude while still maintain the same stiffness and range. This increase in sensor area could help reduce the noise in the sensor system by a factor of 30.

In addition, changing the flexural material could help improve the dynamic range by increasing the yield strength or reducing the elastic modulus of the flexure. Single crystal silicon is a good flexural material due to its yield strength the elastic modulus ratio. However, silicon utility in practice is limited due to its brittleness. Therefore, changing flexural material to a metallic glass or 7075 aluminum could significantly increase the dynamic range of the sensor. However, in order to achieve this increase in dynamic range it is necessary to develop new microfabrication methods for material other than silicon.

6.5.2 Estimates of Future Device Performance

Overall, the dynamic range of the force sensor can be improved through redesign of the force sensor system to decrease the flexure beam thickness and increase the flexure width as well as the incorporation of high gauge factor CNTs into the sensor. Based on these design changes, the force sensor optimization presented in Chapter 2 predicts that the dynamic range of the force sensor can be increased to 111 dB. Therefore, the sensor could achieve a resolution of about 100 pN while maintaining the same range as the current CNT-based force sensor.

CONCLUSIONS AND FUTURE WORK

7.1 Summary

Smaller and more sensitive multi-axis micro- and nanoscale sensors need to be developed for many biological, materials science, and nanomanufacturing applications. Unfortunately, such systems do not yet exist due to the limitations of traditional sensing techniques and fabrication procedures. For example, because the resolution of capacitive sensors scales with sensor area, high resolution capacitive sensors are generally too large for use in multi-axis micro/nanoscale sensor systems. Similarly, interferometry is impractical at the micro/nanoscale due to the relatively large optics required. High resolution silicon-based piezoresistive sensors work well in mesoscale devices, but become increasingly hard to fabricate in micro- and nanoscale devices due to the constraints of photolithography and ion implantation. Carbon nanotube-based (CNT) piezoresistive transducers offer the potential to overcome many of these limitations due to their high gauge factor and inherent nanoscale size. However, a better understanding of CNT-based piezoresistive sensors is needed in order to be able to design and engineer sensor systems that can capitalize on this potential.

The purpose of this research was to take CNT-based strain sensors from the single element test structures that have been fabricated and turn them into precision sensor systems that can be used in micro/nanoscale force and displacement transducers. In order to achieve this purpose and engineer high resolution CNT-based sensor systems, the design and manufacturing methods used to create CNT-based piezoresistive sensors were investigated. At the system level, a noise model was developed in order to be able to optimize the design of the sensor system. At the element level, a link was established between the structure of the CNT and its gauge factor using a theoretical model developed from quantum mechanics. This model was confirmed experimentally using CNT-based piezoresistive sensors integrated into a microfabricated test

structure. At the device level, noise mitigation techniques including annealing and the use of protective ceramic coatings were investigated in order to reduce the noise in the sensor. From these investigations, best practices for the design and manufacturing of CNT-based piezoresistive sensors were established. Using these best practices, it is possible to increase the performance of CNT-based piezoresistive sensor systems by more than three orders of magnitude over previous results.

These best practices were also implemented in the design and fabrication of a multi-axis force sensor used to measure the adhesion force of an array of cells to the different material's surfaces for the development of biomedical implants. This force sensor is capable of measuring forces in the z-axis as well as torques in the θ_x and θ_y axis. The range and resolution of the force sensor were determined to be 84 μN and 5.6 nN, respectively. This corresponds to a dynamic range of 83 dB, which closely matches the dynamic range predicted by the system noise model used to design the sensor. The accuracy of the force sensor was measured to be better than 1% over the device's full range.

7.2 Best Practices for Design and Manufacturing

Several best practice rules have been created based on the work presented in this thesis. First, in the design of MEMS sensor systems it is necessary to take account of all of the possible noise sources in the sensor system in order to maximize the performance of the system. For mechanical sensor systems, the correct figure of merit to use when evaluating sensor performance is dynamic range. This is because it is often possible to trade range for resolution in mechanical sensor systems. Therefore, it is the ratio of the range to the resolution which is important in evaluating sensor performance. Once the effects of each of the noise sources are quantified, it is possible to eliminate all but the few largest noise sources. This type of simplification makes it possible to set up a constraint based optimization system for the design of the sensor, as shown in Chapter 2. This type of optimization procedure can be used to maximize the dynamic range of the sensor while ensuring that other fabrication and design parameters such as natural frequency, maximum load, maximum footprint and minimum beam dimensions are met.

In addition to this type of systematic design optimization, the performance of the CNT-based sensors can be improved through the proper selection of CNT chirality, as shown in

Chapter 3. For example, CNTs with a low chiral angle will tend to have greater strain sensitivity than CNTs with high chiral angles. The gauge factor of an armchair CNT with a chiral angle of 30° is zero, while gauge factor can be as high as 362 for a zig-zag CNT at 0 percent strain. In addition, CNTs with $p = 0$ or 1 where $p = \text{mod}(n-m,3)$ have a positive gauge factor, while $p = -1$ CNTs have a negative gauge factor. Therefore, it is possible to maximize the sensitivity of CNT-based strain sensors by selecting only zigzag CNTs with $p = 1$ for the CNT sensors.

Unfortunately, it often proves difficult to sort out only the desired CNTs from a solution with many types of CNTs. Even when this type of sorting can be performed, it may only be possible to significantly enrich the desired CNT species without completely eliminating all other CNT species. However, as shown in Chapter 4, it is possible to use the electrical breakdown technique to eliminate many of the unwanted types of CNTs in the sensor after the CNTs have been deposited. Using this method it is possible to eliminate low resistance and low gauge factor CNTs by running high currents through these types of CNTs, causing them to heat up and rapidly oxidize. By eliminating these low performance CNTs, it is possible to both increase the sensitivity of the sensor and change the sign of the gauge factor of the sensor.

In addition to increasing the sensitivity of the CNT-based strain sensor it is possible to improve the dynamic range of the sensor by decreasing noise. As shown in Chapter 5, the noise in CNT-based is flicker noise-dominated. This means that the noise in the sensor system can be reduced either by decreasing the Hooge noise coefficient, α , or by increasing the number of carriers in the sensor. The easiest way to increase the number of carriers in the sensor is to increase the number of CNTs in the sensor, since carriers scale linearly with number of CNTs. This can either be done by increasing the density of CNTs on the parallel resistor network by increasing the deposition, or by increasing the area of the resistor through design changes. In addition to increasing the number of CNTs, the Hooge coefficient can be reduced by coating the CNTs in a ceramic protective layer and annealing them in an inert atmosphere at 525°C for 30 minutes. This procedure removes the absorbed molecules from the surface of the CNTs and protects the CNTs from having additional molecules absorb or desorb from the CNT surface. This procedure reduces the noise in the CNT-based piezoresistors by almost three orders of magnitude. Overall, through the use of the optimized design and manufacturing processes presented in this thesis it is possible to increase sensor dynamic range by up to 4 orders of

magnitude and to create a multi-axis force sensor with nN level force resolution and a range of up to 100's of μN .

7.3 Use in Non-photolithographic MEMS

In addition to the design and manufacturing best practices presented in this thesis, further improvements can be made to mesoscale MEMS sensor systems if traditional microfab-based fabrication procedures can be replaced by machining and forming operations. By eliminating cleanroom microfab, it is possible to significantly reduce the fabrication cost and fabrication time associated with these types of sensors. In addition, moving out of the microfab increases flexibility in the selection of the flexural materials used to build the sensor. This section will present the use of non-cleanroom fabrication techniques to produce CNT-based sensor systems.

7.3.1 Introduction

Current MEMS manufacturing techniques are based on IC chip fabrication techniques, such as photolithography and deep reactive ion etching (DRIE), which have been developed over the last half century. These techniques offer high dimensional resolution but are generally limited to silicon processing, which results in brittle MEMS devices. IC fabrication equipment also is extremely expensive, on the scale of \$100's millions to billions for a fabrication line. This makes MEMS manufacturing prohibitively expensive, since MEMS devices are typically produced in much smaller quantities than IC chips. Prototyping alone can cost \$10's of thousands of dollars in an IC MEMS facility and require months to a year to complete [240]. Therefore, new fabrication techniques need to be developed to meet the needs of MEMS prototyping and manufacturing if these techniques are to be cost-effective.

This section will present the initial work towards a method that enables the design and fabrication of flexure-based, meso- and micro-scale force/displacement sensors fabricated using non-photolithographic micro-machining processes. In these sensors, CNTs are used as piezoresistive sensing elements. Piezoresistive sensors transduce strain in a flexing element into a resistance change. This resistance change may be used to measure the force on and displacement of a flexible element, e.g. a flexure beam. Silicon-based piezoresistive sensors are commonly found in small-scale pressure sensors, accelerometers, AFM probes and

nanopositioners. These sensors are typically fabricated via conventional IC processing techniques within dedicated microfabrication facilities/labs.

The approach discussed here eliminates the need to use cost- and time-intensive photolithographic fabrication processes to create small-scale force/displacement sensors and thereby reduces cost and lead times for prototypes. Non-photolithographic micromachining processes are also attractive as they offer designers more flexibility in materials and geometry. These processes are not limited to IC microfabrication-compatible materials and 2½D geometries. This process integrates CNTs with the flexure elements, thereby taking advantage of the CNTs' relatively high gauge factor, which equates to greater sensitivity. CNT-based piezoresistors have been measured to have gauge factors that are an order of magnitude larger than silicon-based piezoresistors [1]. CNTs are also attractive for use as they may be assembled onto existing flexure structures and therefore do not require photolithography-based microfabrication processes. These characteristics make CNTs promising transduction elements for use with micromachining to produce fine resolution, small-scale force and displacement sensors.

7.3.2 Test Structure Design

The design and fabrication of a cantilever test structure showcases the potential capabilities of non-photolithographic MEMs manufacturing techniques. These small cantilever test structures are designed for use in testing CNT-based strain sensors. In these test structures, a 1.5 mm (0.6”) long cantilever beam is attached to a 2 mm (0.082”) thick base. Two 3.25 mm (0.128”) diameter mounting holes are drilled in the base to attach the test structure to the testing jig. A secondary 1.57 mm (0.062”) diameter hole for hanging weight on the beam is made at the end of the cantilever.

A conductive wire trace is deposited on to the top surface of the beam in order to allow CNT-based strain sensors to be placed onto the beam. These wire traces start at a contact pad on the stationary base and run out a short length of the beam before returning to a another contact pad next as seen in Figure 7.1. A small gap is made across the trace so that carbon nanotube resistors can be deposited onto the beam. These CNTs stretch between over the gap in the trace and complete the electrical circuit between the two electrodes. When the beam deflects, the

carbon nanotubes are strained and their resistance changes. By measuring the change in resistance, it is possible to determine the force or displacement applied to the end of the beam.

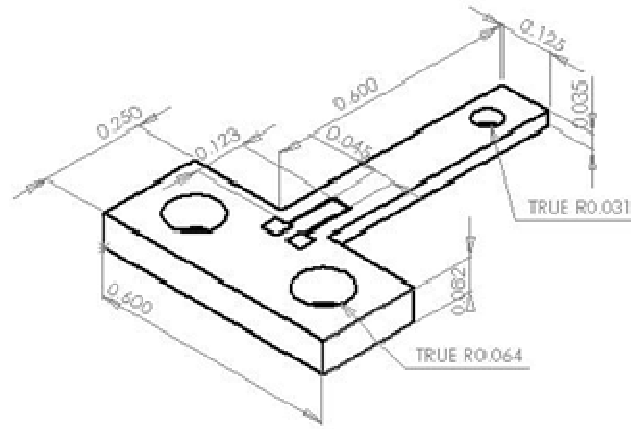


Figure 7.1. Test Structure Schematic (Units in Inches).

The base material for the test structure is variable since non-photolithographic manufacturing methods are suitable for many different types of materials. For the first set of tests, 6061-T6 aluminum was used for the beam, alumina was used as an insulating material between the beam and trace, titanium was used for the trace, and steel shim stock was used for the mask. Subsequent beams were made of acrylic. This allows the alumina deposition step to be eliminated and proof-of-concept polymer MEMS device to be created.

7.3.3 Fabrication

The test cantilever beams were cut from 1.52 mm (0.060") 6061-T6 aluminum stock using an Intellitek Benchman MX Desktop Mill. The toolpath was designed for a 1.59 mm (1/16") endmill running at 10,000 rpm. This allowed all features to be machined without a tool change. Total manufacturing time for each beam was 5 minutes. A jig was also made for mounting the cantilever to an optical table.

The placement of the CNT-based strain gauge onto the beam requires an electrical trace to be deposited onto the base of the beam. A physical $\sim 5 \mu\text{m}$ gap must be created in the trace measuring so that CNT-based piezoresistors can be integrated into the sensor. To this end, a shadow mask was manufactured using a Microlution 363-S micromill. The mask was cut from 0.127 mm (0.005") thick steel shim, using a 0.076 mm (.003") endmill running at 50,000 rpm. A

feed rate of 30 mm/min was used to cut the 100 μm wide trace path. A 1.59 mm (1/16") tool was then used to cut the mask from the stock material and to cut mounting holes in the mask so that the mask could be affixed to the cantilever beam.

In order to make the $\sim 5 \mu\text{m}$ gap in the wire traces, a tungsten wire tip was placed over the wire trace on the shadow mask. The tungsten wire tip was made by etching a 150 μm diameter tungsten wire. The tungsten wire was placed into a hole in a stainless steel fixture and etched using a 2M NaOH solution. A 2 VDC voltage was applied between the tungsten wire anode and the stainless steel cathode. The etching process takes several minutes and produces a long conical point on the wire coming to a final tip radius of $\sim 100\text{nm}$. The wire is then placed across the trace using a microscope to get alignment correct. Finally, the wire is fixed in place using tape on both sides of the mask as shown in Figure 7.2.

Trace deposition begins by smoothing the surface of the cantilever beam with a 3M microfine sanding paper. The beams are then cleaned using Terg-A-Zyme detergent in an ultrasonic cleaner. Finally they are washed with methanol and blown dry with nitrogen.

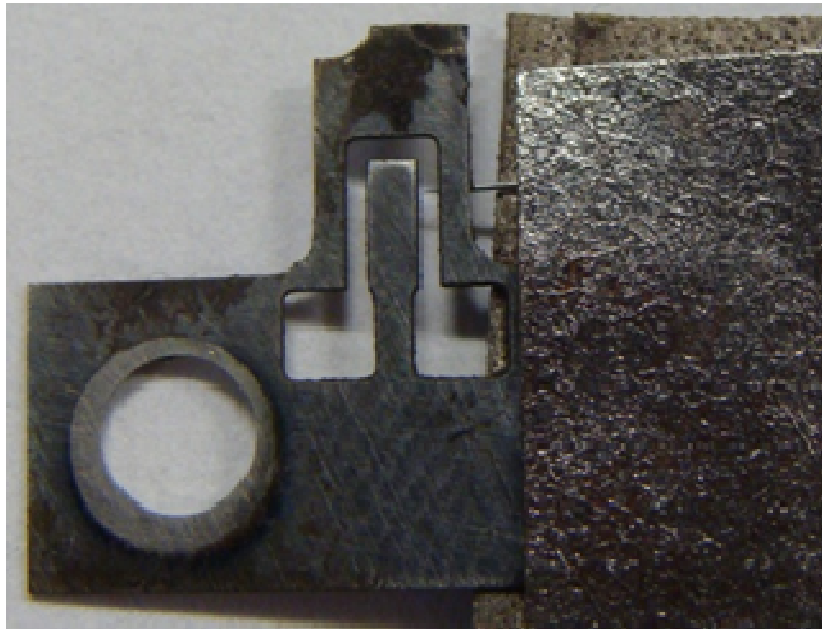


Figure 7.2. Shadow Mask with Tungsten Wire.

For metal deposition, the cantilevers are placed into an electron beam evaporator and pumped down to 10^{-5} torr. The cantilevers are first coated with 500 nm of aluminum oxide at a

rate of 0.5 nm/s. This provides an insulating layer between the metal trace and the aluminum substrate. Next, the shadow mask is affixed to the cantilever beam using standard nuts and bolts. 100 nm of titanium is then deposited through the shadow mask at a rate of 0.3 nm/s. The parts are then cooled under vacuum for 10 minutes and are removed from the chamber. Finally, the mask is unbolted and removed, and the traces inspected for defects. This method produces titanium traces on top of the insulating alumina layer on the cantilever beam, as shown in Figure 7.3. Prior tests in which the alumina was deposited through the shadow mask resulted in poor insulation between the conducting traces and the underlying aluminum due to unsatisfactory coating of the beam surface.



Figure 7.3. Test Structure with Metal Trace.

After the test structure fabrication is completed, CNTs are deposited across the gap in the wire traces. CNTs are deposited onto these test flexures via dielectrophoresis. A droplet of a 3 $\mu\text{g}/\text{mL}$ solution of SWCNTs in deionized water is placed on the electrodes of the test structure and a 5 MHz, 5V peak-to-peak AC voltage was used to direct the deposition of the SWCNTs. After 5 minutes, the test structure is rinsed with DI water and dried. Finally, the structure is coated with a thin ceramic layer to protect the sensor and mitigate noise [223].

7.3.4 Results

7.3.4.1 Metal Trace Deposition

Several different types of metals including gold, palladium, and titanium were tested for use in the metal traces. These metals were chosen because of their ohmic contact with CNTs [241]. Unfortunately, the gold and palladium contacts showed the tendency to flake off after deposition, as shown in Figure 7.4. However, the titanium contacts did not suffer from this flaking tendency. Therefore, titanium ultimately was chosen as the wire trace material due to its superior bonding to aluminum and its low Schottky barrier with carbon nanotubes.

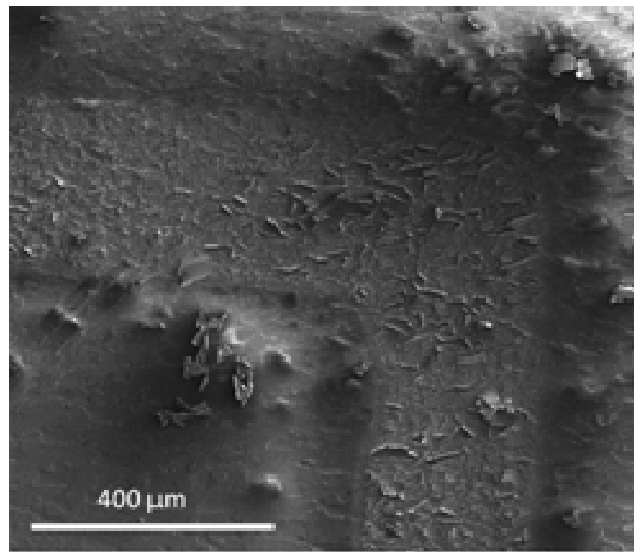


Figure 7.4. Flaking of Pd wire on Aluminum Beam.

7.3.4.2 Gap Fabrication with Tungsten Wire

The quality of the gap in the metal trace on the test structures is completely determined by the tungsten wire placement and geometry. When the tungsten wire is placed on top of the mask, and further away from the beam surface, it creates a blurred edge to the gap in the trace, as some atoms diffuse in after passing the wire. In fact, when the deposition thickness is great enough the gap can disappear entirely, as shown in Figure 7.5.

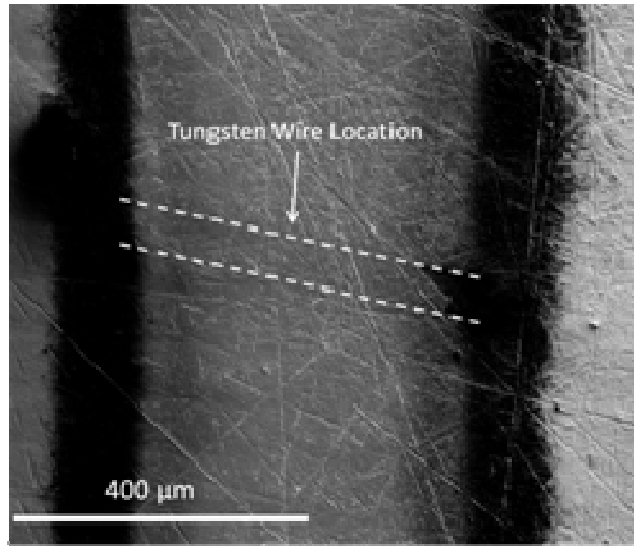


Figure 7.5. Trace fabricated with tungsten wire on the top of shadow mask.

When the tungsten wire is placed between the mask and the beam, a sharply defined gap is produced. The dimensions of the gap match that of the wire closely. This can be seen in Figure 7.6 where the gap in the metal trace matches the shape of the tungsten tip. Thus, with a long, narrow etching of the tungsten wire a well-controlled gap can reliably be produced in the trace, allowing robust placement of carbon nanotube strain gauges onto a MEMS device of any material.

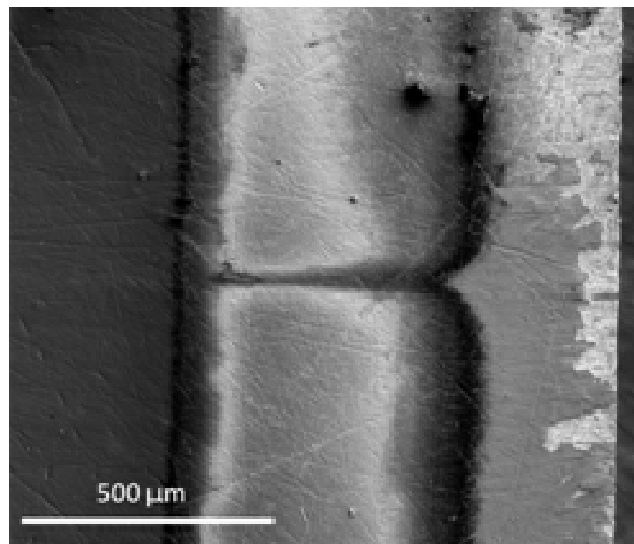


Figure 7.6. Trace fabricated with tungsten wire on the bottom of shadow mask.

7.3.4.3 Gap Fabrication with FIB & CNT Deposition

Gaps in the metal traces can also be fabricated using a focused ion beam. The FIB is capable of producing precise and uniform gaps in the metal traces, as shown in Figure 7.

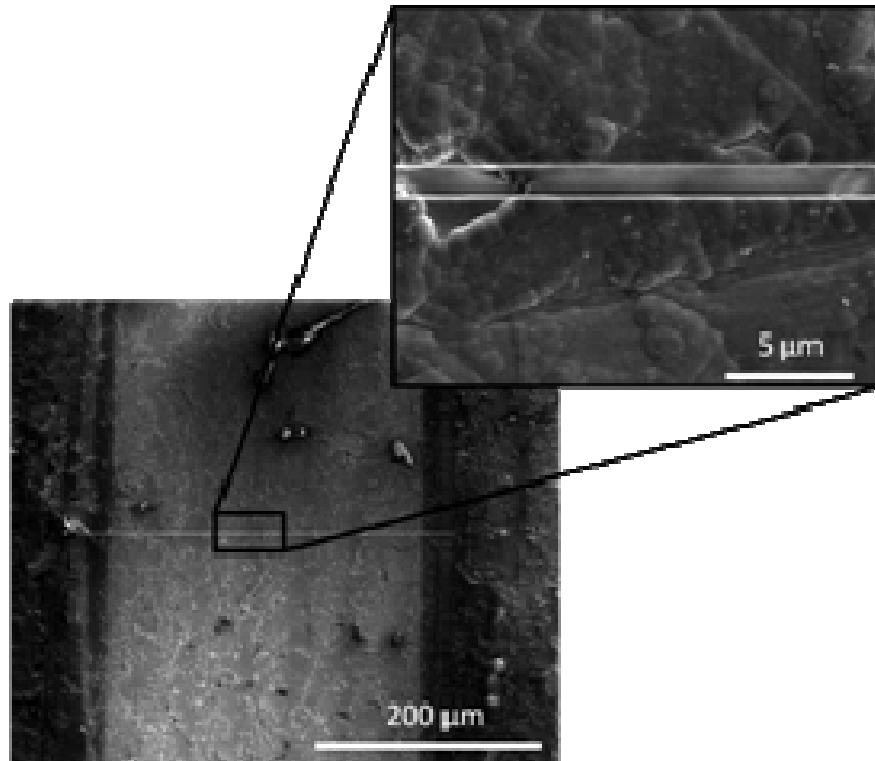


Figure 7.7. Test structure with gap cut with FIB.

However, the use of the FIB to fabricate the gaps doubles both the fabrication cost and time. Using the gaps fabricated with the FIB, it was possible to deposit CNT-based sensors onto the test structures, as shown in Figure 8.

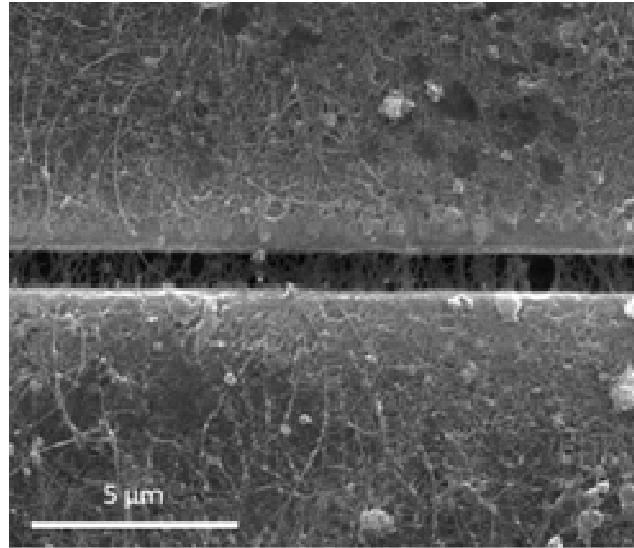


Figure 7.8. CNTs deposited on test structure.

7.3.5 Test Structure Performance

The cantilever test structures were tested by hanging weights off the end of the cantilever and measuring the deflection. The strain on the sensor was then calculated based on the force and the displacement applied to the cantilever beam. Results for both the cantilevers with the FIB cut gap and the gap created using the tungsten wire are presented in Figure 7.9. The measured gauge factor for the FIB cut gap of 73 is within experimental error for the measured gauge factor for the CNT test structures discussed in Chapter 4. This indicates that this fabrication procedure produces sensors that are nearly identical to the sensors produced using cleanroom microfabrication procedures. However, the gauge factor of the sensor produced using the tungsten wire is significantly lower than the measured gauge factor for the CNT test structures in Chapter 4. This is likely because the gap fabricated using the tungsten wire is more than 10 μm wide. Therefore, CNTs cannot directly connect one electrode to another. In order to span the gap, CNT to CNT connections must be made. These inter-tube connections tend to be high resistance, which reduces the overall sensitivity of the system. In addition to these inter-tube connections, the strain transfer to the CNTs in this large gap may not be as good as that for the CNTs that span the entire electrode gap. This could help to reduce the strain sensitivity of these piezoresistive sensors.

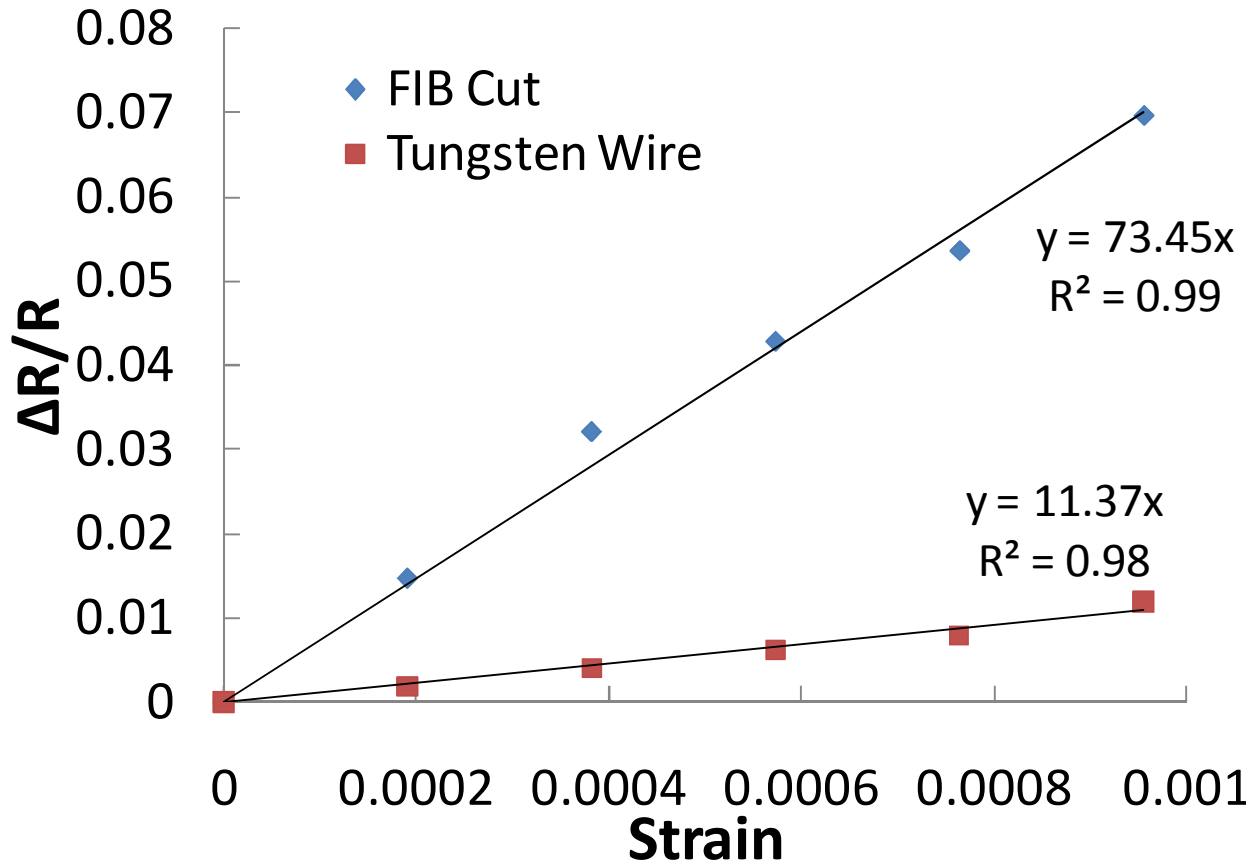


Figure 7.9. Results for FIB Cut and Tungsten Wire Gaps.

Even with the limitation that a FIB must be used to cut the gap in the electrodes, this non-cleanroom fabrication method offers several advantages over traditional microfab methods for product such as the HexFlex nanopositioner, where low volume production of mesoscale MEMS devices is required. For example, the lead time in the production of the first device is reduced from 3 months to 3 days using this new fabrication method. In addition, average cost of a device in a 36 device batch is reduced from about \$500 to \$20. These gains in fabrication time and cost are made without sacrificing performance. In fact, the CNT-based piezoresistive HexFlex should have a dynamic range that is slightly higher than the silicon based HexFlex devices that have been fabricated in recent years [239]. A comparison of Hexflex devices fabricated using traditional clean room processes and the non-lithographic process described in this section is presented in Table 7.1.

Table 7.1: Comparison of Potential performance of Microfabricated and Machined Hexflex Designs.

	Fabrication Cost	Fabrication Time	Gauge Factor	Noise
Silicon Hexflex with Polysilicon Piezoresistors	\$500	3 Months	18	30 μV_{RMS}
Non-Lithographic Hexflex with CNT Piezoresistors	\$20	3 Days	73	200 μV_{RMS}

7.3.6 Conclusions and Future Work for Non-photolithographic MEMS

This work shows that carbon nanotube-based sensors can be fabricated on mesoscale devices without the use of expensive IC fabrication equipment. This reduces the prototyping cost of such sensors from around \$10-30k to less than \$100 and reduces the fabrication time from about 3-6 months to less than 3 days. However, more work still needs to be done to improve the sensor fabrication using tungsten wire shadow masks. These improvements in device fabrication will help to increase device quality while reducing the fabrication cost and time.

7.4 Possible Future Applications

7.4.1 Heated Center Stage Tests

Heated stages are used in a variety of metrology and fabrication applications such as the measurement of the thermal conductivity of nanomaterials or the positioning of localized chemical reactions. These types of experiments offer a challenge for positioner designs that incorporate silicon or polysilicon piezoresistors. This is because the piezoresistive gauge factor of these sensors starts to significantly decrease after the temperature of the sensor increases above 80 °C. As shown in Figure 7.10 and Figure 7.11, when the central stage of the HexFlex force sensor is heated up to approximately 530 °C, there is a significant temperature gradient

over the length of the flexure beams. This is because the thermally grounded base of the flexure experiences virtually no change in temperature.

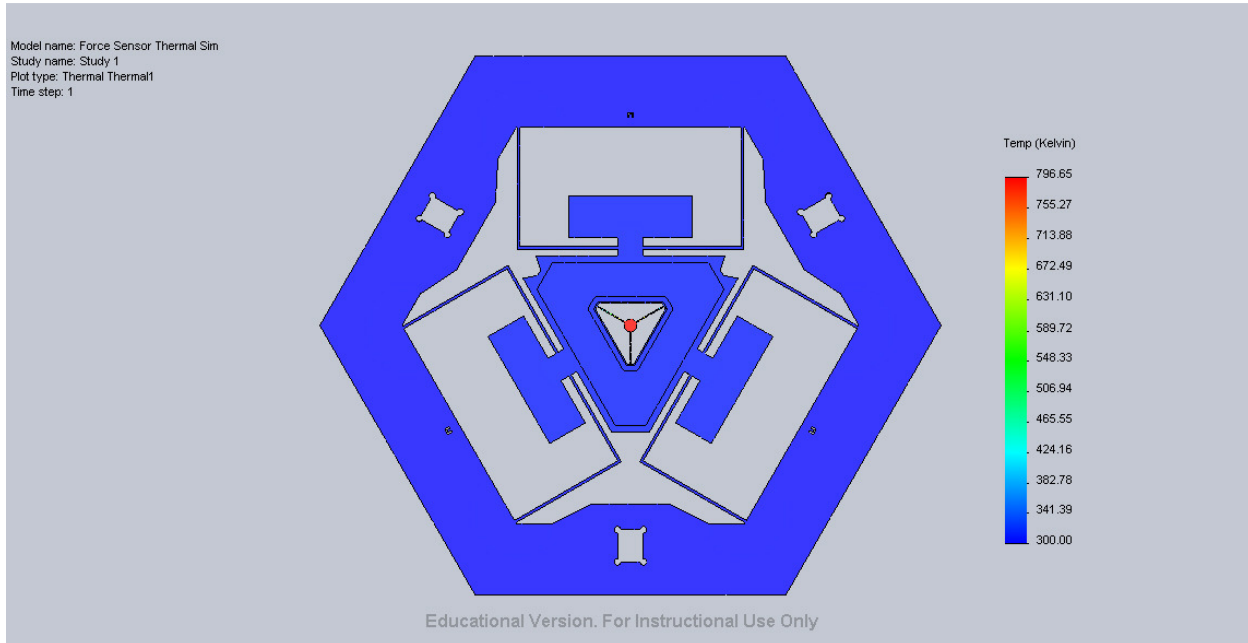


Figure 7.10. Force Sensor assembly with heated central stage.

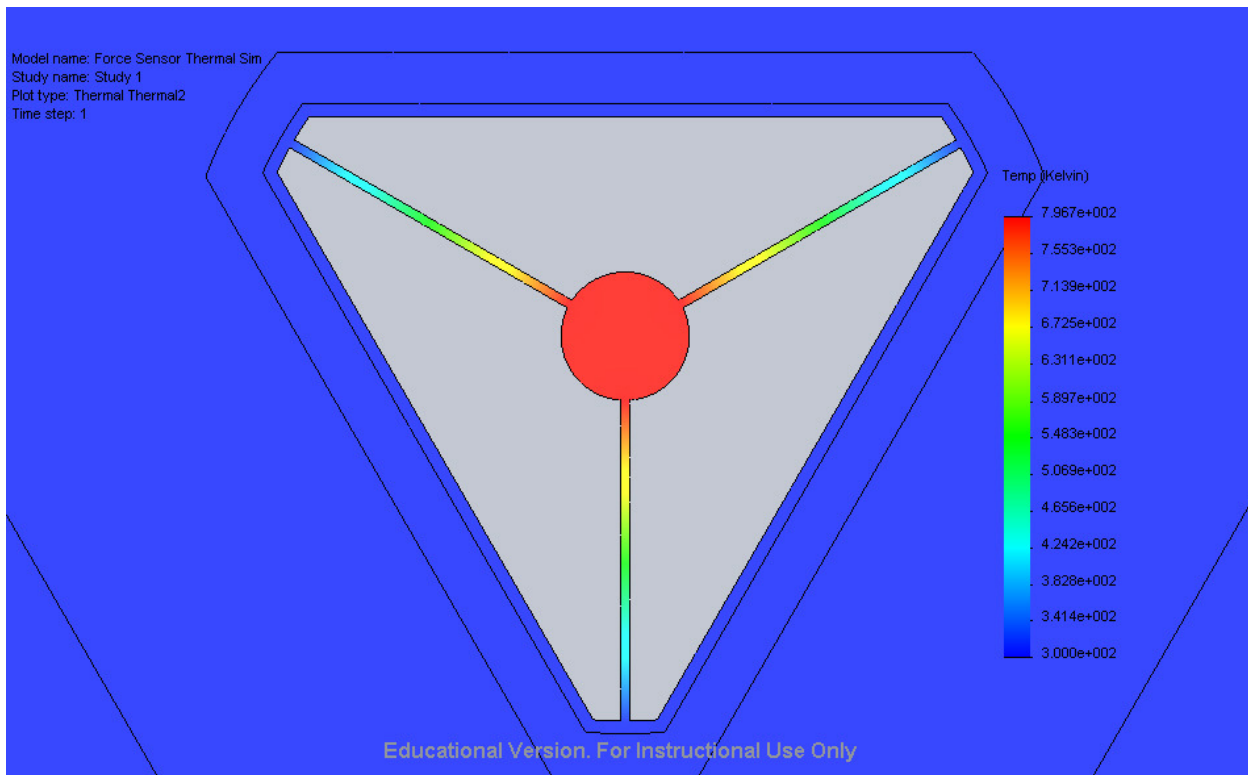


Figure 7.11. Force Sensor assembly with heated central stage.

Typically, in an optimized design involving silicon or polysilicon piezoresistors, the piezoresistors extend up to 1/3 of the beam length from the base of the flexure. Therefore, these piezoresistors can experience significant temperature gradients over their structure. However, CNT-based piezoresistors only extend a few microns onto the flexure beam. Therefore, the CNT-based piezoresistors experience virtually no change in temperature when the central stage is heated. This means that the performance of the CNT-based piezoresistors is unaffected by the heating of the central stage, which makes it possible to implement this type of heated stage design in real devices.

7.4.2 Self Sensing Nanoscale Bearings

As mechanical devices move towards the nanoscale, force and displacement sensing become challenging due to the limitation of traditional sensing techniques such as capacitive sensing and interferometry. Carbon nanotubes offer the potential to overcome these limitations due to their nanoscale size. In addition, carbon nanotubes are attractive as flexural materials at the nanoscale due to their high elastic modulus and yield strength. These properties give CNT-based flexures a large range and high natural frequency. For example, the linear flexural bearing shown in Figure 7.12 is capable of deformations of up to 25 percent of the device size.

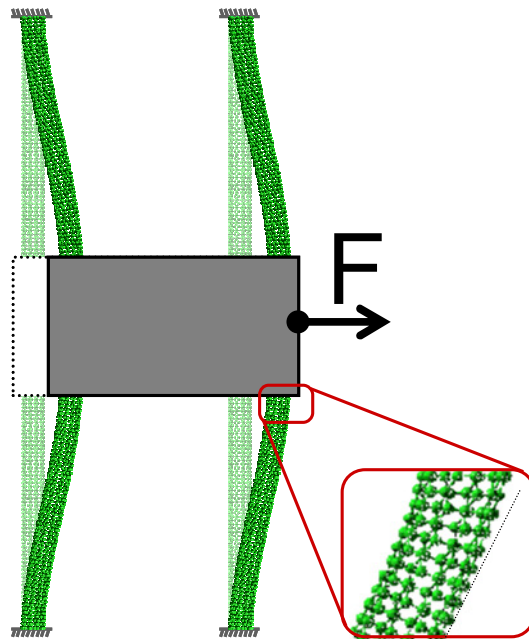


Figure 7.12. Nanoscale linear motion bearing with CNT-based flexures/sensors.

In addition to guiding the motion to the central linear stage, the nanoscale CNT bearings can also be used to determine the displacement of the central stage. This can be done by measuring the change in resistance of the CNTs as the stage is deflected. When the central stage is deflected, the CNT is subject to both localized bending and localized stretching, as demonstrated in Figure 7.13.

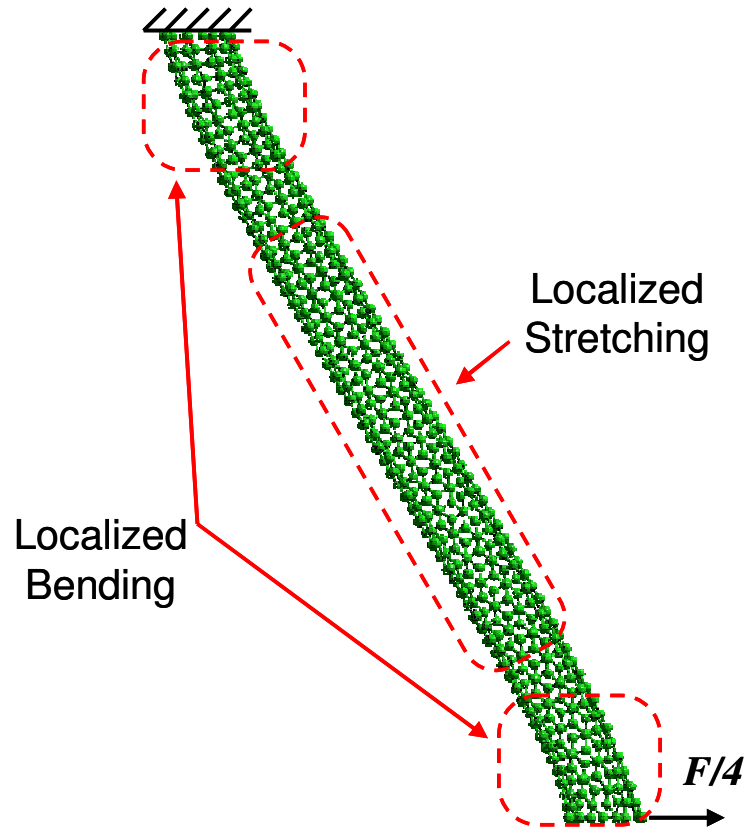


Figure 7.13. Deformation of CNT in linear motion bearing.

This bending and stretching of the CNT as the central stage is displaced should result in a significant change in the electrical resistance of the CNT due to the piezoresistive nature of CNTs. This change in resistance can be calibrated to provide a measurement of the force on the central stage or the displacement of the central stage. In fact, due to the small size of such devices, sensing using CNT-based piezoresistors may be one of the few integrated sensing options available as we move towards these types of NEMS devices.

REFERENCES

- [1] C. Stampfer, A. Jungen, R. Linderman, and D. Oberfell, S, “Nano-electromechanical displacement sensing based on single-walled carbon nanotubes,” *Nano Lett*, vol. 6, 2006, pp. 1449-1453.
- [2] J. Lu and L. Zhang, “Analysis of localized failure of single-wall carbon nanotubes,” *Computational Materials Science*, vol. 35, Apr. 2006, pp. 432-441.
- [3] W. Xue, B.V. Krishna, A. Bandyopadhyay, and S. Bose, “Processing and biocompatibility evaluation of laser processed porous titanium.,” *Acta biomaterialia*, vol. 3, Nov. 2007, pp. 1007-1018.
- [4] B.L. Pruitt and T.W. Kenny, “Piezoresistive cantilevers and measurement system for characterizing low force electrical contacts,” *Sensors and Actuators A: Physical*, vol. 104, 2003, p. 68–77.
- [5] S. Chen and M. Culpepper, “Design of a six-axis micro-scale nanopositioner— μ HexFlex,” *Precision Engineering*, vol. 30, Jul. 2006, pp. 314-324.
- [6] J. Tong and Y. Sun, “Toward carbon nanotube-based AFM cantilevers,” *IEEE transactions on nanotechnology*, vol. 6, 2007, pp. 519-523.
- [7] R.D. Piner, ““Dip-Pen” Nanolithography,” *Science*, vol. 283, Jan. 1999, pp. 661-663.
- [8] M. Cullinan, C. DiBiasio, and L. Howell, M, “Modeling of a Clamped-Clamped Carbon Nanotube Flexural Element for use in Nanoelectromechanical Systems,” *13th National Conference on Mechanisms and Machines*, 2007, pp. 105-110.
- [9] M. Cullinan and M. Culpepper, “Carbon nanotubes as piezoresistive microelectromechanical sensors: Theory and experiment,” *Physical Review B*, vol. 82, Sep. 2010, p. 115482.
- [10] R. Saito, G. Dresselhaus, and M.S. Dresselhaus, *Physical Properties of Carbon Nanotubes*, London: Imperial College Press, 2005.
- [11] C. Li and T.-wei Chou, “A structural mechanics approach for the analysis of carbon nanotubes,” *International Journal of Solids and Structures*, vol. 40, May. 2003, pp. 2487-2499.
- [12] M. Meyyappan, *Carbon Nanotubes: Science and Applications*, Boca Raton: CRC Press, 2005.

- [13] C.M. Dibiasio and M.L. Culpepper, "Design of a Six Degree of Freedom Nanopositioner for Use in Massively Parallel Probe-Based Nanomanufacturing," *Proceedings of the 2009 Annual Meeting of the American Society for Precision Engineering*, Monterey, CA: 2009.
- [14] M.A. Cullinan, R.M. Panas, and M.L. Culpepper, "Design of Micro-Scale Multi-Axis Force Sensors for Precision Applications," *Proceedings of the 2009 Annual Meeting of the American Society for Precision Engineering*, Monterey, CA: 2009.
- [15] L.L. Chu and Y.B. Gianchandani, "A micromachined 2D positioner with electrothermal actuation and sub-nanometer capacitive sensing," *Journal of Micromechanics and Microengineering*, vol. 13, Mar. 2003, pp. 279-285.
- [16] O. Schneegans, P. Chrétien, F. Houzé, and R. Meyer, "Capacitance measurements on small parallel plate capacitors using nanoscale impedance microscopy," *Applied Physics Letters*, vol. 90, 2007, p. 043116.
- [17] J.-I. Lee, X. Huang, and P.B. Chu, "Nanoprecision MEMS Capacitive Sensor for Linear and Rotational Positioning," *Journal of Microelectromechanical Systems*, vol. 18, Jun. 2009, pp. 660-670.
- [18] S.D. Senturia, *Microsystem Design*, Norwell, MA: Kluwer Academic Publishers, 2002.
- [19] J.J. Neumann, "Comparison of piezoresistive and capacitive ultrasonic transducers," *Proceedings of SPIE*, vol. 5391, 2004, pp. 230-238.
- [20] M. Li, H.X. Tang, and M.L. Roukes, "Ultra-sensitive NEMS-based cantilevers for sensing, scanned probe and very high-frequency applications.," *Nature nanotechnology*, vol. 2, Feb. 2007, pp. 114-20.
- [21] J. Thaysen, A. Boisen, O. Hansen, and S. Bouwstra, "Atomic force microscopy probe with piezoresistive read-out and a highly symmetrical Wheatstone bridge arrangement," *Sensors and Actuators A: Physical*, vol. 83, 2000, p. 47-53.
- [22] A. Barlian, W.-T. Park, J.R. Mallon, A.J. Rastegar, and B.L. Pruitt, "Review: Semiconductor Piezoresistance for Microsystems.," *Proceedings of the IEEE. Institute of Electrical and Electronics Engineers*, vol. 97, Jan. 2009, pp. 513-552.
- [23] J.A. Harley and T.W. Kenny, "1/F Noise Considerations for the Design and Process Optimization of Piezoresistive Cantilevers," *Journal of Microelectromechanical Systems*, vol. 9, Jun. 2000, pp. 226-235.
- [24] S.D. Senturia, *Microsystem Design*, Norwell, MA: Kluwer Academic Publishers, 2002.
- [25] *The Pressure Strain and Force Handbook*, Stamford, CT: Omega Engineering Inc., 2006.

- [26] G. Boero, I. Utke, T. Bret, N. Quack, M. Todorova, S. Mouaziz, P. Kejik, J. Brugger, R.S. Popovic, and P. Hoffmann, "Submicrometer Hall devices fabricated by focused electron-beam-induced deposition," *Applied Physics Letters*, vol. 86, 2005, p. 042503.
- [27] G. Pepka, "Position and level sensing using Hall-effect sensing technology," *Sensor Review*, vol. 27, 2007, pp. 29-34.
- [28] S.M. Sze, *Semiconductor Sensors*, New York, NY: John Wiley & Sons, Inc., 1994.
- [29] A.H. Slocum, *Precision Machine Design*, Eaglewood, NJ: Prentice-Hall, Inc., 1992.
- [30] G. Gautschi, *Piezoelectric Sensorics*, Berlin, Germany: Springer, 2002.
- [31] X.-H. Xu, Y. Feng, B.-Q. Li, and J.-R. Chu, "Integration of displacement sensor into bulk PZT thick film actuator for MEMS deformable mirror," *Sensors and Actuators A: Physical*, vol. 147, Sep. 2008, pp. 242-247.
- [32] *ICP® Accelerometer: Model 333B30*, Depew, NY: PCB Piezotronics, 2006.
- [33] A.H. Slocum, *Precision Machine Design*, Eaglewood, NJ: 1992.
- [34] D. Marioli, E. Sardini, and A. Taroni, "Flat Type Thick Film Inductive Sensors," *Active and Passive Electronic Components*, vol. 26, 2003, pp. 37-49.
- [35] P.L. Yu and R.B. Zmood, "Versatile microsensor for micromachine applications," *Proceedings of SPIE*, Spie, 1999, pp. 192-198.
- [36] D. Sadler, "On-chip eddy current sensor for proximity sensing and crack detection," *Sensors and Actuators A: Physical*, vol. 91, Jul. 2001, pp. 340-345.
- [37] A.H. Slocum, *Precision Machine Design*, Eaglewood, NJ: 1992.
- [38] H. Büchner, H. Stiebig, and V. Mandryka, E, "An optical standing-wave interferometer for displacement measurements," *Measurement*, vol. 14, Mar. 2003, pp. 311-316.
- [39] G. Jager, E. Manske, T. Hausotte, H. Buchner, and R. Grunwald, "Nanopositioning and -measuring technique," *Proceedings of SPIE*, vol. 4900, 2002, pp. 240-246.
- [40] F. Zhao, "Development of high-precision laser heterodyne metrology gauges," *Proceedings of SPIE*, vol. 5634, 2005, pp. 247-259.
- [41] M.L. Schattenburg, "The critical role of metrology in nanotechnology," *Proceedings of SPIE*, vol. 4608, 2002, pp. 116-124.
- [42] Z. Zhang and C.-H. Menq, "Laser interferometric system for six-axis motion measurement.," *The Review of scientific instruments*, vol. 78, Aug. 2007, p. 083107.

- [43] C.-M. Wu, "Heterodyne interferometric system with subnanometer accuracy for measurement of straightness.," *Applied optics*, vol. 43, Jul. 2004, pp. 3812-3816.
- [44] C. Chao, Z. Wang, and W. Zhu, "Modulated laser interferometer with picometer resolution for piezoelectric characterization," *Review of Scientific Instruments*, vol. 75, 2004, p. 4641.
- [45] G. Jager, E. Manske, T. Hausotte, R. Fussl, R. Grunwald, and H. Buchner, "Miniature interferometers for applications in microtechnology and nanotechnology," *Proceedings of SPIE*, vol. 5190, 2003, pp. 185-192.
- [46] T. Tombler, C. Zhou, L. Alexseyev, J. Kong, H. Dai, and L. Liu, "Reversible electromechanical characteristics of carbon nanotubes under local-probe manipulation," *Nature*, vol. 405, 2000, pp. 769-772.
- [47] E.D. Minot, Y. Yaish, V. Sazonova, J.-Y. Park, M. Brink, and P.L. McEuen, "Tuning carbon nanotube band gaps with strain," *Physical review letters*, vol. 90, Apr. 2003, p. 156401.
- [48] A. Maiti, A. Svizhenko, and M. Anantram, "Electronic transport through carbon nanotubes: Effects of structural deformation and tube chirality," *Physical review letters*, vol. 88, 2002, p. 126805.
- [49] A. Rochefort, D.R. Salahub, and P. Avouris, "The effect of structural distortions on the electronic structure of carbon nanotubes," *Chemical Physics Letters*, vol. 297, 1998, pp. 45-50.
- [50] J. Cao, Q. Wang, and H. Dai, "Electromechanical properties of metallic, quasimetallic, and semiconducting carbon nanotubes under stretching," *Physical review letters*, vol. 90, 2003, p. 157601.
- [51] R. Grow, Q. Wang, J. Cao, D. Wang, and H. Dai, "Piezoresistance of carbon nanotubes on deformable thin-film membranes," *Applied Physics Letters*, vol. 86, 2005, p. 093104.
- [52] Y. Chen and C. Weng, "Electronic properties of zigzag carbon nanotubes under uniaxial strain," *Carbon*, vol. 45, 2007, pp. 1636-1644.
- [53] L. Yang and J. Han, "Electronic structure of deformed carbon nanotubes," *Physical Review Letters*, vol. 85, 2000, pp. 154-157.
- [54] W. Xue and T. Cui, "Electrical and electromechanical characteristics of self-assembled carbon nanotube thin films on flexible substrates," *Sensors and Actuators A: Physical*, vol. 145-146, 2008, pp. 330-335.
- [55] Z. Li, P. Dharap, S. Nagarajaiah, E.V. Barrera, and J. Kim, "Carbon nanotube film sensors," *Advanced Materials*, vol. 16, 2004, p. 640-643.

- [56] X. Li, C. Levy, and L. Elaadil, "Multiwalled carbon nanotube film for strain sensing," *Nanotechnology*, vol. 19, Jan. 2008, p. 045501.
- [57] S.M. Vemuru, R. Wahi, S. Nagarajaiah, and P.M. Ajayan, "Strain sensing using a multiwalled carbon nanotube film," *The Journal of Strain Analysis for Engineering Design*, vol. 44, Oct. 2009, pp. 555-562.
- [58] S.V. Anand and D.R. Mahapatra, "The dynamics of polymerized carbon nanotubes in semiconductor polymer electronics and electro-mechanical sensing," *Nanotechnology*, vol. 20, 2009, p. 145707.
- [59] C. Gau, H. Ko, and H. Chen, "Piezoresistive characteristics of MWNT nanocomposites and fabrication as a polymer pressure sensor," *Nanotechnology*, vol. 20, 2009, p. 185503.
- [60] Z. Dang, M. Jiang, D. Xie, and S.-hong Yao, LQ, "Supersensitive linear piezoresistive property in carbon nanotubes/silicone rubber nanocomposites," *Journal of Applied Physics*, vol. 104, 2009, p. 024114.
- [61] M. Park, H. Kim, and J. Youngblood, "Strain-dependent electrical resistance of multi-walled carbon nanotube/polymer composite films," *Nanotechnology*, vol. 19, 2008, p. 055705.
- [62] N. Hu, Y. Karube, M. Arai, T. Watanabe, and C. Yan, "Investigation on sensitivity of a polymer / carbon nanotube composite strain sensor," *Carbon*, vol. 48, 2009, pp. 680-687.
- [63] I. Kang, M.J. Schulz, J.H. Kim, V. Shanov, and D. Shi, "A carbon nanotube strain sensor for structural health monitoring," vol. 15, 2006, pp. 737-748.
- [64] S.V. Anand and D. Roy Mahapatra, "Quasi-static and dynamic strain sensing using carbon nanotube/epoxy nanocomposite thin films," *Smart Materials and Structures*, vol. 18, Apr. 2009, p. 045013.
- [65] P. Dharap, Z. Li, S. Nagarajaiah, and E. Barrera, "Nanotube film based on single-wall carbon nanotubes for strain sensing," *Nanotechnology*, vol. 15, 2004, pp. 379-382.
- [66] C. Hierold, A. Jungen, C. Stampfer, and T. Helbling, "Nano electromechanical sensors based on carbon nanotubes," *Sensors and Actuators A*, vol. 136, 2007, pp. 51-61.
- [67] X. Yang, Z. Zhou, F. Zheng, M. Zhang, J. Zhang, and Y. Yao, "A high sensitivity single-walled carbon-nanotube-array-based strain sensor for weighing," *Solid-State Sensors, Actuators and Microsystems Conference, 2009. TRANSDUCERS 2009. International*, IEEE, 2009, p. 1493-1496.
- [68] Y. Xie and M. Tabib-Azar, "Telescoping self-aligned metal-catalyzed carbon nanotube piezoresistors as strain gauges," *IEEE Sensors 2006*, 2006, pp. 1407-1410.

- [69] S. Dohn, J. Kjelstruphansen, D. Madsen, K. Molhave, and P. Boggild, "Multi-walled carbon nanotubes integrated in microcantilevers for application of tensile strain," *Ultramicroscopy*, vol. 105, Nov. 2005, pp. 209-214.
- [70] N.-K. Chang, C.-C. Su, and S.-H. Chang, "Fabrication of single-walled carbon nanotube flexible strain sensors with high sensitivity," *Applied Physics Letters*, vol. 92, 2008, p. 063501.
- [71] H. Maune and M. Bockrath, "Elastomeric carbon nanotube circuits for local strain sensing," *Applied Physics Letters*, vol. 89, 2006, p. 173131.
- [72] C. Stampfer, T. Helbling, D. Oberfell, and B. Schöberle, MK, "Fabrication of single-walled carbon-nanotube-based pressure sensors," *Nano Lett*, vol. 6, 2006, pp. 233-237.
- [73] C. Stampfer, A. Jungen, and C. Hierold, "Fabrication of discrete nanoscaled force sensors based on single-walled carbon nanotubes," *Sensors Journal, IEEE*, vol. 6, 2006, p. 613-617.
- [74] V. Semet, V. Binh, D. Guillot, K. Teo, M. Chhowalla, G. Amaratunga, W.I. Milne, P. Legagneux, and D. Pribat, "Reversible electromechanical characteristics of individual multiwall carbon nanotubes," *Applied Physics*, vol. 87, 2005, p. 223103.
- [75] A. Hall, M. Falvo, R. Superfine, and S. Washburn, "Electromechanical response of single-walled carbon nanotubes to torsional strain in a self-contained device," *Nature Nanotechnology*, vol. 2, 2007, pp. 413-416.
- [76] J. Appenzeller, Y.-M. Lin, J. Knoch, Z. Chen, and P. Avouris, "1/f Noise in Carbon Nanotube Devices—On the Impact of Contacts and Device Geometry," *IEEE Transactions On Nanotechnology*, vol. 6, May. 2007, pp. 368-373.
- [77] P.G. Collins, M.S. Fuhrer, and A. Zettl, "1/F Noise in Carbon Nanotubes," *Applied Physics Letters*, vol. 76, 2000, pp. 894-896.
- [78] E.S. Snow, J.P. Novak, M.D. Lay, and F.K. Perkins, "1/F Noise in Single-Walled Carbon Nanotube Devices," *Applied Physics Letters*, vol. 85, 2004, pp. 4172-4174.
- [79] M. Ishigami, J.H. Chen, E.D. Williams, D. Tobias, Y.F. Chen, and M.S. Fuhrer, "Hooge's constant for carbon nanotube field effect transistors," *Applied Physics Letters*, vol. 88, 2006, p. 203116.
- [80] W. Liang, M. Bockrath, D. Bozovic, J.H. Hafner, M. Tinkham, and H. Park, "Fabry - Perot interference in a nanotube electron waveguide," *Nature*, vol. 411, Jun. 2001, pp. 665-9.
- [81] C. White and T. Todorov, "Carbon nanotubes as long ballistic conductors," *Nature*, vol. 393, 1998, pp. 240-242.

- [82] J. Tersoff, “Low-frequency noise in nanoscale ballistic transistors,” *Nano letters*, vol. 7, Jan. 2007, pp. 194-198.
- [83] B. Ilic, D. Czaplewski, M. Zalalutdinov, H.G. Craighead, P. Neuzil, C. Campagnolo, and C. Batt, “Single cell detection with micromechanical oscillators,” *Journal of Vacuum Science & Technology B: Microelectronics and Nanometer Structures*, vol. 19, 2001, p. 2825.
- [84] X. Ming, H. Huang, C.A. Zorman, and M.L. Roukes, “Nanodevice motion at microwave frequencies,” *Nature*, vol. 421, 2003, pp. 496-497.
- [85] Y.T. Yang, K.L. Ekinici, X.M.H. Huang, L.M. Schiavone, M.L. Roukes, C.A. Zorman, and M. Mehregany, “Monocrystalline silicon carbide nanoelectromechanical systems,” *Applied Physics Letters*, vol. 78, 2001, pp. 162-164.
- [86] V. Cimalla, F. Niebelschütz, and K. Tonisch, C, “Nanoelectromechanical devices for sensing applications,” *Sensors and Actuators B*, vol. 126, 2007, pp. 24-34.
- [87] D. Ramos, J. Tamayo, J. Mertens, M. Calleja, L.G. Villanueva, and a Zaballos, “Detection of bacteria based on the thermomechanical noise of a nanomechanical resonator: origin of the response and detection limits,” *Nanotechnology*, vol. 19, Jan. 2008, p. 035503.
- [88] K.L. Ekinici and M.L. Roukes, “Nanoelectromechanical systems,” *Review of Scientific Instruments*, vol. 76, 2005, p. 061101.
- [89] K.L. Ekinici, X.M.H. Huang, and M.L. Roukes, “Ultrasensitive nanoelectromechanical mass detection,” *Applied Physics Letters*, vol. 84, 2004, p. 4469.
- [90] C. Li and T.W. Chou, “Mass detection using carbon nanotube-based nanomechanical resonators,” *Applied Physics Letters*, vol. 84, 2009, p. 5246.
- [91] G. Cao, X. Chen, and J. Kysar, “Strain sensing of carbon nanotubes: Numerical analysis of the vibrational frequency of deformed single-wall carbon nanotubes,” *Physical Review B*, vol. 72, 2005, p. 195412.
- [92] D. Garcia-Sánchez, A. San Paulo, M.J. Esplandiú, F. Perez-Murano, L. Forró, A. Aguasca, and A. Bachtold, “Mechanical detection of carbon nanotube resonator vibrations,” *Physical review letters*, vol. 99, 2007, p. 85501.
- [93] M. Poot, B. Witkamp, M. Otte, and H. van Der Zant, “Modelling suspended carbon nanotube resonators,” *physica status solidi (b)*, vol. 244, 2007, p. 4252–4256.
- [94] V. Sazonova, Y. Yaish, H. Ustünel, D. Roundy, T.A. Arias, and P.L. McEuen, “A tunable carbon nanotube electromechanical oscillator.,” *Nature*, vol. 431, Sep. 2004, pp. 284-287.

- [95] C. DiBiasio, M.A. Cullinan, and M.L. Culpepper, "Difference between bending and stretching moduli of single-walled carbon nanotubes that are modeled as an elastic tube," *Applied Physics Letters*, vol. 90, 2007, p. 203116.
- [96] S. Iijima, C. Brabec, A. Maiti, and J. Bernholc, "Structural flexibility of carbon nanotubes," *The Journal of Chemical Physics*, vol. 104, 1996, p. 2089.
- [97] K.L. Ekinici, "Electromechanical transducers at the nanoscale: actuation and sensing of motion in nanoelectromechanical systems (NEMS)," *Small*, vol. 1, 2005, p. 786–797.
- [98] T.W. Kenny, W.J. Kaiser, H.K. Rockstad, J.K. Reynolds, J. a Podosek, and E.C. Vote, "Wide-bandwidth electromechanical actuators for tunneling displacement transducers," *Journal of Microelectromechanical Systems*, vol. 3, 1994, p. 97–104.
- [99] T. Kenny, "Nanometer-scale force sensing with MEMS devices," *IEEE sensors journal*, vol. 1, 2001, p. 148–157.
- [100] A. Cassell, N. Franklin, and T. Tomblor, EM, "Directed growth of free-standing single-walled carbon nanotubes," *J. Am. Chem.*, vol. 121, 1999, pp. 7975-7976.
- [101] D. Takagi, Y. Homma, and Y. Kobayashi, "Selective growth of individual single-walled carbon nanotubes suspended between pillar structures," *Physica E: Low-dimensional Systems*, vol. 24, 2004, pp. 1-5.
- [102] N. Franklin, Q. Wang, T. Tomblor, and A. Javey, M, "Integration of suspended carbon nanotube arrays into electronic devices and electromechanical systems," *Applied Physics*, vol. 81, 2002, pp. 913-915.
- [103] Y. Imaizumi, Y. Arakawa, and F. Arai, T, "Local growth of carbon nanotubes on the cantilever by chemical vapor deposition with FIB assist etching," *Proceedings of the 2005 5th IEEE Conference on Nanotechnology*, Nagoya, Japan: 2005.
- [104] C.C. Lin, P.L. Chen, C.T. Lin, and C.T. Kuo, "Selective growth of horizontally-oriented carbon nanotube bridges on patterned silicon wafers by electroless plating Ni catalysts," *Diamond and Related Materials*, vol. 14, 2005, p. 1867–1871.
- [105] H.T. Soh and C.F. Quate, "Integrated nanotube circuits : Controlled growth and ohmic contacting of single-walled carbon nanotubes," *Applied Physics Letters*, vol. 75, 1999, pp. 627-629.
- [106] A. Ural, Y. Li, and H. Dai, "Electric-field-aligned growth of single-walled carbon nanotubes on surfaces," *Applied Physics Letters*, vol. 81, 2002, pp. 3464-3466.
- [107] C.-chao Chiu, N.-hwa Tai, M.-kao Yeh, B.-yi Chen, S.-hao Tseng, and Y.-huang Chang, "Tip-to-tip growth of aligned single-walled carbon nanotubes under an electric field," *Journal of Crystal Growth*, vol. 290, 2006, pp. 171-175.

- [108] E. Joselevich and C.M. Lieber, "Vectorial Growth of Metallic and Semiconducting Single-Wall Carbon Nanotubes," *Nano Letters*, vol. 2, Oct. 2002, pp. 1137-1141.
- [109] M. Yu, M. Dyer, G. Skidmore, H. Rohrs, X. Lu, K. Ausman, J. Von Ehr, and R.S. Ruoff, "Three-dimensional manipulation of carbon nanotubes under a scanning electron microscope," *Nanotechnology*, vol. 10, 1999, pp. 244-252.
- [110] S. Fahlbusch, S. Mazerolle, J. Breguet, A. Stinecker, J. Angus, R. Perez, and J. Michler, "Nanomanipulation in a scanning electron microscope," *Journal of Materials Processing Technology*, vol. 167, 2005, pp. 371-382.
- [111] D. Cox, R. Forrest, P. Smith, V. Stolojan, and S. Silva, "Study of the current stressing in nanomanipulated three-dimensional carbon nanotube structures," *Applied Physics Letters*, vol. 87, 2005, p. 033102.
- [112] S. Lim, K. Kim, I. Lee, S. Jeong, S. Cho, J. Yoo, and Y. Lee, "Nanomanipulator-assisted fabrication and characterization of carbon nanotubes inside scanning electron microscope," *Micron*, vol. 36, 2005, pp. 471-476.
- [113] V. Grossi, L. Lozzi, and S. Santucci, with F. Bussolotti, LD'Ortenzi, "In situ manipulation and electrical characterization of multiwalled carbon nanotubes by using nanomanipulators under scanning electron microscopy," *Physical Review B*, 2007, pp. 1-7.
- [114] K. Molhave, T. Hansen, D. Madsen, and P. Bøggild, "Towards pick-and-place assembly of nanostructures," *Journal of Nanoscience and Nanotechnology*, vol. 4, 2004, pp. 279-282.
- [115] K. Mølhave, T. Wich, A. Kortschack, and P. Bøggild, "Pick-and-place nanomanipulation using microfabricated grippers," *Nanotechnology*, vol. 17, 2006, pp. 2434-2441.
- [116] V. Moore, M. Strano, E. Haroz, R. Hauge, and R. Smalley, "Individually Suspended Single-Walled Carbon Nanotubes in Various Surfactants," *Nano Letters*, vol. 3, Oct. 2003, pp. 1379-1382.
- [117] Z. Chen, Y. Yang, F. Chen, Q. Qing, Z. Wu, and Z. Liu, "Controllable interconnection of single-walled carbon nanotubes under ac electric field.," *The journal of physical chemistry. B*, vol. 109, Jun. 2005, pp. 11420-11423.
- [118] A. Subramanian, B.J. Nelson, L. Dong, and D. Bell, "Dielectrophoretic Nanoassembly of Individual Carbon Nanotubes onto Nanoelectrodes Overview of Individual Nanotube Based," *The 6th IEEE International Symposium on Assembly and Task Planning: From Nano to Macro Assembly and Manufacturing*, Montreal, Que.: 2005, pp. 200-205.

- [119] D. Xu, A. Subramanian, L. Dong, and B.J. Nelson, "Shaping Nanoelectrodes for High-Precision Dielectrophoretic Assembly of Carbon Nanotubes," *Nanotechnology, IEEE Transactions on*, vol. 8, 2009, p. 449–456.
- [120] L. An and C.R. Friedrich, "Process parameters and their relations for the dielectrophoretic assembly of carbon nanotubes," *Journal of Applied Physics*, vol. 105, 2009, p. 074314.
- [121] X.Q. Chen, T. Saito, H. Yamada, and K. Matsushige, "Aligning single-wall carbon nanotubes with an alternating-current electric field," *Applied Physics Letters*, vol. 78, 2001, pp. 3714-3716.
- [122] R. Krupke, F. Hennrich, H. Weber, M. Kappes, and H. Löhneysen, "Simultaneous deposition of metallic bundles of single-walled carbon nanotubes using ac-dielectrophoresis," *Nano Letters*, vol. 3, 2003, p. 1019–1023.
- [123] J. Li, Q. Zhang, N. Peng, and Q. Zhu, "Manipulation of carbon nanotubes using AC dielectrophoresis," *Applied Physics Letters*, vol. 86, 2005, p. 153116.
- [124] R. Krupke, F. Hennrich, M.M. Kappes, and H. v. Löhneysen, "Surface Conductance Induced Dielectrophoresis of Semiconducting Single-Walled Carbon Nanotubes," *Nano Letters*, vol. 4, Aug. 2004, pp. 1395-1399.
- [125] J. Chung, K. Lee, J. Lee, and R. Ruoff, "Toward large-scale integration of carbon nanotubes," *Langmuir*, vol. 20, 2004, pp. 3011-3017.
- [126] B.R. Burg, J. Schneider, M. Muoth, L. Durrer, T. Helbling, N.C. Schirmer, T. Schwamb, C. Hierold, and D. Poulikakos, "Aqueous dispersion and dielectrophoretic assembly of individual surface-synthesized single-walled carbon nanotubes.," *Langmuir : the ACS journal of surfaces and colloids*, vol. 25, Jul. 2009, pp. 7778-82.
- [127] A. Vijayaraghavan, S. Blatt, D. Weissenberger, M. Oron-Carl, F. Hennrich, D. Gerthsen, H. Hahn, and R. Krupke, "Ultra-large-scale directed assembly of single-walled carbon nanotube devices.," *Nano letters*, vol. 7, Jun. 2007, pp. 1556-60.
- [128] K.W.C. Lai, N. Xi, C.K.M. Fung, J. Zhang, H. Chen, Y. Luo, and U.C. Wejinya, "Automated Nanomanufacturing System to Assemble Carbon Nanotube Based Devices," *The International Journal of Robotics Research*, vol. 28, Apr. 2009, pp. 523-536.
- [129] S. Sorgenfrei, I. Meric, S. Banerjee, A. Akey, S. Rosenblatt, I.P. Herman, and K.L. Shepard, "Controlled dielectrophoretic assembly of carbon nanotubes using real-time electrical detection," *Applied Physics Letters*, vol. 94, 2009, p. 053105.
- [130] J. Li, Q. Zhang, D. Yang, and J. Tian, "Fabrication of carbon nanotube field effect transistors by AC dielectrophoresis method," *Carbon*, vol. 42, 2004, pp. 2263-2267.

- [131] R.H.M. Chan, C.K.M. Fung, and W.J. Li, "Rapid assembly of carbon nanotubes for nanosensing by dielectrophoretic force," *Nanotechnology*, vol. 15, 2004, p. S672-s677.
- [132] M. a Meitl, Z.-T. Zhu, V. Kumar, K.J. Lee, X. Feng, Y.Y. Huang, I. Adesida, R.G. Nuzzo, and J. a Rogers, "Transfer printing by kinetic control of adhesion to an elastomeric stamp," *Nature Materials*, vol. 5, Dec. 2005, pp. 33-38.
- [133] X. Feng, M.A. Meitl, A.M. Bowen, Y. Huang, R.G. Nuzzo, and J.A. Rogers, "Competing fracture in kinetically controlled transfer printing.," *Langmuir*, vol. 23, Dec. 2007, pp. 12555-12560.
- [134] S.J. Kang, C. Kocabas, H.-S. Kim, Q. Cao, M. a Meitl, D.-Y. Khang, and J. a Rogers, "Printed multilayer superstructures of aligned single-walled carbon nanotubes for electronic applications.," *Nano letters*, vol. 7, Nov. 2007, pp. 3343-8.
- [135] C.-M. Lin, L.-Y. Lin, and W. Fang, "Monolithic integration of carbon nanotubes based physical sensors," *2010 IEEE 23rd International Conference on Micro Electro Mechanical Systems (MEMS)*, Ieee, 2010, pp. 55-58.
- [136] T. a El-Aguizy, J.-hyun Jeong, Y.-B. Jeon, W.Z. Li, Z.F. Ren, and S.-G. Kim, "Transplanting carbon nanotubes," *Applied Physics Letters*, vol. 85, 2004, p. 5995.
- [137] M.A. Cullinan and M.L. Culpepper, "Control of carbon nanotube geometry via tunable process parameters," *Applied Physics Letters*, vol. 93, 2008, p. 103106.
- [138] D.A. Heller, R.M. Mayrhofer, S. Baik, Y.V. Grinkova, M.L. Usrey, and M.S. Strano, "Concomitant length and diameter separation of single-walled carbon nanotubes," *J. Am. Chem. Soc.*, vol. 126, 2004, p. 14567-14573.
- [139] C. Cheung, A. Kurtz, H. Park, and C. Lieber, "Diameter-controlled synthesis of carbon nanotubes," *J. Phys. Chem. B*, vol. 106, 2002, pp. 2429-2433.
- [140] M.A. Cullinan and M.L. Culpepper, "Controlling the Stiffness of Carbon Nanotube Based Compliant Mechanisms," *5th International Symposium on Nanomanufacturing*, Singapore: 2008, pp. 1-6.
- [141] F.H. Kaatz, M.P. Siegal, D.L. Overmyer, P.P. Provencio, and J.L. Jackson, "Diameter control and emission properties of carbon nanotubes grown using chemical vapor deposition," *Materials Science and Engineering C*, vol. 23, 2003, pp. 141-146.
- [142] C. Kuo, A. Bai, C. Huang, Y. Li, C. Hu, and C. Chen, "Diameter control of multiwalled carbon nanotubes using experimental strategies," *Carbon*, vol. 43, 2005, pp. 2760-2768.
- [143] W.Z. Li, D.Z. Wang, S.X. Yang, J.G. Wen, and Z.F. Ren, "Controlled growth of carbon nanotubes on graphite foil by chemical vapor deposition," *Chemical Physics Letters*, vol. 335, 2001, pp. 141-149.

- [144] Y. Li, W. Kim, Y. Zhang, M. Rolandi, D. Wang, and H. Dai, "Growth of Single-Walled Carbon Nanotubes from Discrete Catalytic Nanoparticles of Various Sizes," *J. Phys. Chem. B*, vol. 105, 2001, pp. 11424-11431.
- [145] M. Siegal, D. Overmyer, and P. Provencio, "Precise control of multiwall carbon nanotube diameters using thermal chemical vapor deposition," *Applied Physics Letters*, vol. 80, 2002, pp. 2171-2173.
- [146] I. Willems, Z. Konya, J. Colomer, and G.V. Tendeloo, "Control of the outer diameter of thin carbon nanotubes synthesized by catalytic decomposition of hydrocarbons," *Chemical Physics Letters*, vol. 317, 2000, pp. 71-76.
- [147] H. Shiozawa, C. Kramberger, R. Pfeiffer, H. Kuzmany, T. Pichler, Z. Liu, K. Suenaga, H. Kataura, and S.R.P. Silva, "Catalyst and Chirality Dependent Growth of Carbon Nanotubes Determined Through Nano-test tube Chemistry.," *Advanced materials*, vol. 22, Jun. 2010, pp. 3685-3689.
- [148] K.K.K. Koziol, C. Ducati, and A.H. Windle, "Carbon Nanotubes with Catalyst Controlled Chiral Angle," *Chemistry of Materials*, vol. 22, Sep. 2010, pp. 4904-4911.
- [149] J. Liu and M.C. Hersam, "Recent Developments in Carbon Nanotube Sorting and Selective Growth," *MRS Bulletin*, vol. 35, 2010, pp. 315-322.
- [150] R. Krupke, F. Henrich, H.V. Löhneysen, and M.M. Kappes, "Separation of metallic from semiconducting single-walled carbon nanotubes.," *Science (New York, N.Y.)*, vol. 301, Jul. 2003, pp. 344-7.
- [151] Y. Kim, S. Hong, S. Jung, M.S. Strano, J. Choi, and S. Baik, "Dielectrophoresis of surface conductance modulated single-walled carbon nanotubes using cationic surfactants.," *The journal of physical chemistry. B*, vol. 110, Feb. 2006, pp. 1541-5.
- [152] R.M. Tromp, a Afzali, M. Freitag, D.B. Mitzi, and Z. Chen, "Novel strategy for diameter-selective separation and functionalization of single-wall carbon nanotubes.," *Nano letters*, vol. 8, Feb. 2008, pp. 469-72.
- [153] A. Nish, J.-Y. Hwang, J. Doig, and R.J. Nicholas, "Highly selective dispersion of single-walled carbon nanotubes using aromatic polymers.," *Nature nanotechnology*, vol. 2, Oct. 2007, pp. 640-646.
- [154] A. a Green and M.C. Hersam, "Colored Semitransparent Conductive Coatings Consisting of Monodisperse Metallic Single-Walled Carbon Nanotubes," *Nano letters*, vol. 8, May. 2008, pp. 1417-1422.
- [155] A. a Green, M.C. Duch, and M.C. Hersam, "Isolation of single-walled carbon nanotube enantiomers by density differentiation," *Nano Research*, vol. 2, Mar. 2010, pp. 69-77.

- [156] X. Peng, N. Komatsu, S. Bhattacharya, T. Shimawaki, S. Aonuma, T. Kimura, and A. Osuka, "Optically active single-walled carbon nanotubes.," *Nature nanotechnology*, vol. 2, Jul. 2007, pp. 361-5.
- [157] X. Peng, N. Komatsu, T. Kimura, and A. Osuka, "Improved optical enrichment of SWNTs through extraction with chiral nanotweezers of 2,6-pyridylene-bridged diporphyrins.," *Journal of the American Chemical Society*, vol. 129, Dec. 2007, pp. 15947-53.
- [158] X. Peng, N. Komatsu, T. Kimura, and A. Osuka, "Simultaneous enrichments of optical purity and (n,m) abundance of SWNTs through extraction with 3,6-carbazolylene-bridged chiral diporphyrin nanotweezers.," *ACS nano*, vol. 2, Oct. 2008, pp. 2045-2050.
- [159] X. Tu, S. Manohar, A. Jagota, and M. Zheng, "DNA sequence motifs for structure-specific recognition and separation of carbon nanotubes.," *Nature*, vol. 460, Jul. 2009, pp. 250-253.
- [160] M.C. Hersam, "Nanotubes sorted using DNA," *Nature*, vol. 460, 2009, pp. 186-187.
- [161] L. Zhang, X. Tu, K. Welsher, X. Wang, M. Zheng, and H. Dai, "Optical characterizations and electronic devices of nearly pure (10,5) single-walled carbon nanotubes.," *Journal of the American Chemical Society*, vol. 131, Feb. 2009, pp. 2454-5.
- [162] Y. Sun, B. Nelson, D. Potasek, and E. Enikov, "A bulk microfabricated multi-axis capacitive cellular force sensor using transverse comb drives," *Journal of Micromechanics and Microengineering*, vol. 12, Nov. 2002, pp. 832-840.
- [163] F. Beyeler, S. Muntwyler, and B.J. Nelson, "A Six-Axis MEMS Force – Torque Sensor with Micro-Newton and Nano-Newtonmeter Resolution," *Journal of Microelectromechanical Systems*, vol. 18, Apr. 2009, pp. 433-441.
- [164] Y. Sun and B.J. Nelson, "MEMS capacitive force sensors for cellular and flight biomechanics.," *Biomedical materials*, vol. 2, Mar. 2007, p. S16-S22.
- [165] K. Kim, X. Liu, Y. Zhang, and Y. Sun, "Nanonewton force-controlled manipulation of biological cells using a monolithic MEMS microgripper with two-axis force feedback," *Micro*, vol. 18, 2008.
- [166] P. Eaton and P. West, *Atomic Force Microscopy*, New York, NY: Oxford University Press, 2010.
- [167] S.J. Koch, G.E. Thayer, A.D. Corwin, and M.P.D. Boer, "Micromachined piconewton force sensor for biophysics investigations," *Applied Physics*, vol. 89, 2009, p. 172901.
- [168] T. Stowe, K. Yasumura, T. Kenny, D. Botkin, K. Wago, and D. Rugar, "Attonewton force detection using ultrathin silicon cantilevers," *Applied Physics Letters*, vol. 71, 1997, p. 288–290.

- [169] J. Otero and M. Puig-Vidal, "Low-noise Instrumentation for the Measurement of Piezoresistive AFM Cantilever Deflection in Robotic Nanobiocharacterization Applications," *2008 IEEE Instrumentation and Measurement Technology Conference*, Victoria, Canada: Ieee, 2008, pp. 1392-1396.
- [170] J.C. Doll, S.-J. Park, and B.L. Pruitt, "Design optimization of piezoresistive cantilevers for force sensing in air and water.," *Journal of applied physics*, vol. 106, Sep. 2009, p. 64310.
- [171] X. Yu, J. Thaysen, O. Hansen, and A. Boisen, "Optimization of sensitivity and noise in piezoresistive cantilevers," *Journal of Applied Physics*, vol. 92, 2002, pp. 6296-6301.
- [172] R.M. Panas, M.A. Cullinan, and M.L. Culpepper, "A Systems Approach to Modeling of Piezoresistive MEMS Sensors," *Proceedings of the 2010 American Society for Precision Engineering, Control of Precision Systems Conference*, Boston, MA: 2010.
- [173] B. Chui, T. Kenny, H. Mamin, B. Terris, and D. Rugar, "Independent detection of vertical and lateral forces with a sidewall-implanted dual-axis piezoresistive cantilever," *Applied physics*, vol. 72, 1998, pp. 1388-1390.
- [174] T. Duc, J. Creemer, and P. Sarro, "Lateral nano-Newton force-sensing piezoresistive cantilever for microparticle handling," *Journal of Micromechanics and Microengineering*, vol. 16, 2006, p. S102-S106.
- [175] T.C. Duc, J. Creemer, and P.M. Sarro, "Piezoresistive cantilever beam for force sensing in two dimensions," *IEEE Sensors Journal*, vol. 7, 2007, p. 96-104.
- [176] J.R. Mallon, A.J. Rastegar, A.A. Barlian, M.T. Meyer, T.H. Fung, and B.L. Pruitt, "Low 1/f noise , full bridge , microcantilever with longitudinal and transverse piezoresistors," *Applied Physics Letters*, vol. 92, 2008, p. 033508.
- [177] Y. Matsuda, W.Q. Deng, and W.A. Goddard III, "Contact resistance properties between nanotubes and various metals from quantum mechanics," *J. Phys. Chem. C*, vol. 111, 2007, pp. 11113-11116.
- [178] D. Mann, A. Javey, J. Kong, Q. Wang, and H. Dai, "Ballistic transport in metallic nanotubes with reliable Pd ohmic contacts," *Nano Letters*, vol. 3, 2003, p. 1541-1544.
- [179] C. Chen, "A method for creating reliable and low-resistance contacts between carbon nanotubes and microelectrodes," *Carbon*, vol. 45, 2007, pp. 436-442.
- [180] D.N. Madsen, K. Mølhave, R. Mateiu, A.M. Rasmussen, M. Brorson, C.J.H. Jacobsen, and P. Bøggild, "Soldering of Nanotubes onto Microelectrodes," *Nano Letters*, vol. 3, Jan. 2003, pp. 47-49.
- [181] Y. Yang, Z. Dong, Y. Qu, M. Li, and W.J. Li, "A Programmable AFM-Based Nanomanipulation Method Using Vibration-Mode Operation," *Proceedings of the 3rd*

- IEEE Int. Conf. on Nano/Micro Engineered Molecular Systems*, Sanya, China: 2008, pp. 681-685.
- [182] Y. Kanda, "Optimum design considerations for silicon piezoresistive pressure sensors," *Sensors and Actuators A: Physical*, vol. 62, Jul. 1997, pp. 539-542.
- [183] N. Yazdi, F. Ayazi, and K. Najafi, "Micromachined inertial sensors," *Proceedings of the IEEE*, vol. 86, 1998, pp. 11640-1659.
- [184] P. French, "Polysilicon: a versatile material for microsystems," *Sensors and Actuators A: Physical*, vol. 99, Apr. 2002, pp. 3-12.
- [185] N.K. Upreti and S. Singh, "Grain boundary effect on the electrical properties of boron-doped polysilicon films," *Bulletin of Materials Science*, vol. 46, Dec. 1991, pp. 1331-1341.
- [186] R. Brederlow, W. Weber, and C. Dahl, "Low-frequency noise of integrated polysilicon resistors," *IEEE Transactions on Electron Devices*, vol. 48, Jun. 2001, pp. 1180-1187.
- [187] D. Ramos, J. Tamayo, J. Mertens, M. Calleja, L.G. Villanueva, and a Zaballos, "Detection of bacteria based on the thermomechanical noise of a nanomechanical resonator: origin of the response and detection limits," *Nanotechnology*, vol. 19, Jan. 2008, p. 035503.
- [188] S.D. Senturia, *Microsystem Design*, New York, NY: Kluwer Academic Publishers, 2001.
- [189] G. Franklin, J. Powell, and A. Emami-Naeini, *Feedback Control of Dynamic Systems*, Upper Saddle River, NJ: Pearson Prentice Hall, 2006.
- [190] L. Yang, M.P. Anantram, J. Han, and J.P. Lu, "Band-gap change of carbon nanotubes: Effect of small uniaxial and torsional strain," *Physical Review B*, vol. 60, 1999, pp. 13874-13878.
- [191] L. Yang, J. Han, M. Anantram, and R.L. Jaffe, "Bonding Geometry and Bandgap Changes of Carbon Nanotubes Under Uniaxial and Torsional Strain," *Computer Modeling in Engineering & Sciences*, vol. 3, 2002, pp. 675-685.
- [192] T. Ito, K. Nishidate, M. Baba, and M. Hasegawa, "First principles calculations for electronic band structure of single-walled carbon nanotube under uniaxial strain," *Surface Science*, vol. 514, 2002, pp. 222-226.
- [193] S. Reich, J. Maultzsch, C. Thomsen, and P. Ordejón, "Tight-binding description of graphene," *Physical Review B*, vol. 66, Jul. 2002, p. 035412.
- [194] J. Mintmire and C. White, "Universal Density of States for Carbon Nanotubes," *Physical Review Letters*, vol. 81, Sep. 1998, pp. 2506-2509.

- [195] C. White and J. Mintmire, "Density of states reflects diameter in nanotubes," *Nature*, vol. 394, Jan. 1998, pp. 29-30.
- [196] R.J. Grow, "Electromechanical Properties and Applications of Carbon Nanotubes," *Carbon Nanotubes: Properties and Applications*, M.J. O'Connell, ed., New York, NY: Taylor & Francis, 2006, pp. 187-212.
- [197] X. Blase, L. Benedict, E. Shirley, and S. Louie, "Hybridization effects and metallicity in small radius carbon nanotubes.," *Physical review letters*, vol. 72, Mar. 1994, pp. 1878-1881.
- [198] S. Reich, C. Thomsen, and J. Mausch, *Carbon Nanotubes: Basic Concepts and Physical Properties*, New York, NY: Wiley-VCH, 2004.
- [199] J. Ding, X. Yan, J. Cao, D. Wang, Y. Tang, and Q. Yang, "Curvature and strain effects on electronic properties of single-wall carbon nanotubes," *Journal of Physics: Condensed Matter*, vol. 15, 2003, p. L439-L445.
- [200] A. Kleiner and S. Eggert, "Band gaps of primary metallic carbon nanotubes," *Physical Review*, vol. 63, 2001, p. 073408.
- [201] R. Heyd, A. Charlier, and E. Mcrae, "Uniaxial-stress effects on the electronic properties of carbon nanotubes," *Physical Review B*, vol. 55, 1997, pp. 6820-6824.
- [202] T. Hertel, "Deformation of carbon nanotubes by surface van der Waals forces," *Physical Review B*, vol. 102, Nov. 1998, pp. 910-13873.
- [203] H. Son, G.G. Samsonidze, J. Kong, Y. Zhang, X. Duan, J. Zhang, Z. Liu, and M.S. Dresselhaus, "Strain and friction induced by van der Waals interaction in individual single walled carbon nanotubes," *Applied Physics Letters*, vol. 90, 2007, p. 253113.
- [204] S.M. Bachilo, M.S. Strano, C. Kittrell, R.H. Hauge, R.E. Smalley, and R.B. Weisman, "Structure-assigned optical spectra of single-walled carbon nanotubes.," *Science (New York, N.Y.)*, vol. 298, Dec. 2002, pp. 2361-6.
- [205] S. Ghosh, S.M. Bachilo, and R.B. Weisman, "Advanced sorting of single-walled carbon nanotubes by nonlinear density-gradient ultracentrifugation.," *Nature nanotechnology*, vol. 5, May. 2010, pp. 443-450.
- [206] X. Yang, Z.Y. Zhou, F.Z. Zheng, M. Zhang, Z. J., and Y.G. Yao, "A high sensitivity single-walled carbon-nanotube-array-based strain sensor for weighing," *Solid-State Sensors, Actuators and Microsystems Conference, 2009. TRANSDUCERS 2009. International*, Denver, CO: 2009, pp. 1493-1496.
- [207] F. Liu, K.L. Wang, D. Zhang, and C. Zhou, "Noise in carbon nanotube field effect transistor," *Applied Physics Letters*, vol. 89, 2006, p. 063116.

- [208] M. Briman, K. Bradley, and G. Gruner, "Source of $1/f$ noise in carbon nanotube devices," *Journal of Applied Physics*, vol. 100, 2006, p. 013505.
- [209] Y. Lin, J. Appenzeller, Z. Chen, and P. Avouris, "Electrical transport and $1/f$ noise in semiconducting carbon nanotubes," *Physica E: Low-dimensional Systems and Nanostructures*, vol. 37, Mar. 2007, pp. 72-77.
- [210] Y.-M. Lin, J. Appenzeller, J. Knoch, Z. Chen, and P. Avouris, "Low-frequency current fluctuations in individual semiconducting single-wall carbon nanotubes.," *Nano letters*, vol. 6, May. 2006, pp. 930-936.
- [211] D. Tobias, M. Ishigami, A. Tselev, P. Barbara, E. Williams, C. Lobb, and M. Fuhrer, "Origins of $1/f$ noise in individual semiconducting carbon nanotube field-effect transistors," *Physical Review B*, vol. 77, Jan. 2008, pp. 1-4.
- [212] Y.-M. Lin, J.C. Tsang, M. Freitag, and P. Avouris, "Impact of oxide substrate on electrical and optical properties of carbon nanotube devices," *Nanotechnology*, vol. 18, Jul. 2007, p. 295202.
- [213] V.K. Sangwan, V.W. Ballarotto, M.S. Fuhrer, and E.D. Williams, "Facile fabrication of suspended as-grown carbon nanotube devices," *Applied Physics Letters*, vol. 93, 2008, p. 113112.
- [214] S. Reza, Q.T. Huynh, G. Bosman, J. Sippel-Oakley, and A.G. Rinzler, " $1/f$ Noise in Metallic and Semiconducting Carbon Nanotubes," *Journal of Applied Physics*, vol. 100, 2006, p. 094318.
- [215] H.W.C. Postma, T.F. Teepen, Z. Yao, and C. Dekker, " $1/f$ Noise in Carbon nanotubes," *Proceedings of the XXXVIth Rencontres de Moriond*, Les Arcs, France: 2001.
- [216] R. Tarkiainen, L. Roschier, M. Ahlskog, M. Paalanen, and P. Hakonen, "Low-frequency current noise and resistance fluctuations in multiwalled carbon nanotubes," *Physica E: Low-dimensional Systems and Nanostructures*, vol. 28, Jun. 2005, pp. 57-65.
- [217] A. Behnam, G. Bosman, and A. Ural, " $1/f$ Noise in Single-Walled Carbon Nanotube Films," *Proceedings of SPIE Volume 7204*, 2009, p. 72040J.
- [218] A. Behnam, G. Bosman, and A. Ural, "Percolation scaling of $1/f$ noise in single-walled carbon nanotube films," *Physical Review B*, vol. 78, 2008, p. 085431.
- [219] S. Soliveres, J. Gyani, C. Delseny, a Hoffmann, and F. Pascal, " $1/f$ Noise and Percolation in Carbon Nanotube Random Networks," *Applied Physics Letters*, vol. 90, 2007, p. 082107.

- [220] A. Behnam, A. Biswas, G. Bosman, and A. Ural, "Temperature-dependent transport and 1/f noise mechanisms in single-walled carbon nanotube films," *Physical Review B*, vol. 81, Mar. 2010, p. 125407.
- [221] M. Lee, J. Lee, T.H. Kim, H. Lee, B.Y. Lee, J. Park, Y.M. Jhon, M.-J. Seong, and S. Hong, "100 Nm Scale Low-Noise Sensors Based on Aligned Carbon Nanotube Networks: Overcoming the Fundamental Limitation of Network-Based Sensors.," *Nanotechnology*, vol. 21, Feb. 2010, p. 055504.
- [222] U.J. Kim, K.H. Kim, K.T. Kim, Y.-S. Min, and W. Park, "Noise characteristics of single-walled carbon nanotube network transistors," *Nanotechnology*, vol. 19, Jul. 2008, p. 285705.
- [223] T. Helbling, C. Hierold, C. Roman, L. Durrer, M. Mattmann, and V.M. Bright, "Long term investigations of carbon nanotube transistors encapsulated by atomic-layer-deposited Al₂O₃ for sensor applications.," *Nanotechnology*, vol. 20, Oct. 2009, p. 434010.
- [224] G. Xu, F. Liu, S. Han, K. Ryu, A. Badmaev, B. Lei, C. Zhou, and K.L. Wang, "Low-frequency noise in top-gated ambipolar carbon nanotube field effect transistors," *Applied Physics Letters*, vol. 92, 2008, p. 223114.
- [225] S.K. Kim, Y. Xuan, P.D. Ye, S. Mohammadi, J.H. Back, and M. Shim, "Atomic layer deposited Al₂O₃ for gate dielectric and passivation layer of single-walled carbon nanotube transistors," *Applied Physics Letters*, vol. 90, 2007, p. 163108.
- [226] R. Lu, G. Xu, and J.Z. Wu, "Effects of thermal annealing on noise property and temperature coefficient of resistance of single-walled carbon nanotube films," *Applied Physics Letters*, vol. 93, 2008, p. 213101.
- [227] Y.-M. Lin, J. Appenzeller, C.C. Tsuei, A. Chen, and P. Avouris, "Reduction of 1/f Noise in Carbon Nanotube Devices," *64th Device Research Conference Digest*, 2006, pp. 179-180.
- [228] J.H. Back, S. Kim, S. Mohammadi, and M. Shim, "Low-frequency noise in ambipolar carbon nanotube transistors.," *Nano letters*, vol. 8, Apr. 2008, pp. 1090-1094.
- [229] T. Helbling, C. Roman, and C. Hierold, "Signal-to-noise ratio in carbon nanotube electromechanical piezoresistive sensors," *Nano letters*, vol. 10, Sep. 2010, pp. 3350-4.
- [230] H.M. Manohara, E.W. Wong, E. Schlecht, B.D. Hunt, and P.H. Siegel, "Carbon nanotube Schottky diodes using Ti-Schottky and Pt-Ohmic contacts for high frequency applications.," *Nano letters*, vol. 5, Jul. 2005, pp. 1469-74.
- [231] J.O. Lee, C. Park, J.J. Kim, J. Kim, J.W. Park, and K.H. Yoo, "Formation of low-resistance ohmic contacts between carbon nanotube and metal electrodes by a rapid

- thermal annealing method,” *Journal of Physics D: Applied Physics*, vol. 33, 2000, pp. 1953-1956.
- [232] Z. Chen, J. Appenzeller, J. Knoch, Y.-ming Lin, and P. Avouris, “The role of metal-nanotube contact in the performance of carbon nanotube field-effect transistors.,” *Nano letters*, vol. 5, Jul. 2005, pp. 1497-502.
- [233] S.C. Lim, J.H. Jang, D.J. Bae, G.H. Han, S. Lee, I.S. Yeo, and Y.H. Lee, “Contact resistance between metal and carbon nanotube interconnects: Effect of work function and wettability,” *Applied Physics Letters*, vol. 95, 2009, p. 264103.
- [234] M.P. Anantram, S. Datta, and Y. Xue, “Coupling of carbon nanotubes to metallic contacts,” *Physical Review B*, vol. 61, 2000, pp. 14219-14224.
- [235] Y. Matsuda, W.Q. Deng, and W.A. Goddard III, “Contact Resistance for ‘End-Contacted’ Metal-Graphene and Metal-Nanotube Interfaces from Quantum Mechanics,” *The Journal of Physical Chemistry C*, vol. 114, 2010, pp. 17845-17850.
- [236] K. Das, S. Bose, and A. Bandyopadhyay, “Surface modifications and cell – materials interactions with anodized Ti,” *Acta Biomaterialia*, vol. 3, 2007, pp. 573-585.
- [237] M. Tortonese, R.C. Barrett, and C.F. Quate, “Atomic resolution with an atomic force microscope piezoresistive detection,” *Review Literature And Arts Of The Americas*, 1993, pp. 34-36.
- [238] K. Van Vliet, “The biomechanics toolbox: experimental approaches for living cells and biomolecules,” *Acta Materialia*, vol. 51, Nov. 2003, pp. 5881-5905.
- [239] C.M. DiBiasio, “Concept Synthesis and Design Optimization of Meso-scale, Multi-Degree-of-Freedom Precision Flexure Motion Systems with Integrated Strain-based Sensors,” 2010.
- [240] S. a Tadigadapa and N. Najafi, “Developments in Microelectromechanical Systems (MEMS): A Manufacturing Perspective,” *Journal of Manufacturing Science and Engineering*, vol. 125, 2003, p. 816.
- [241] H. Dai, “Carbon nanotubes : opportunities and challenges,” *Surface Science*, vol. 500, 2002, pp. 218-241.

A

VARIABLE DEFINITIONS

A.1 Variable Definitions

Table A.1: Nomenclature for System Design Section

Symbol	Units	Definition	Symbol	Units	Definition
δ	m	Displacement of compliant structure	ν	--	Active fraction of ADC voltage range
F	N	Force on compliant structure	V_{range}	V	Full voltage range of ADC
V_S	V	Source voltage	σ_y	Pa	Flexural material yield stress
Ψ_M	m,	Signal output of sensor system	η	--	Flexural material safety factor to yield
Ψ	m, N	Signal input to sensor system	V_B		Bias voltage
σ_{Mv}	M	Ambient vibration displacement noise	σ_{Tb}	C	Bias voltage chip temperature noise
σ_{Mt}	M	Thermomechanical displacement noise	σ_{vb}	V	Bias voltage noise
$S_{Mt}(f)$	m ² /Hz	PSD of thermomechanical noise	$PSRR_B(s)$	--	Bias voltage power supply rejection ratio Laplace transform
k_B	m ² kg/K s ²	Boltzmann's constant			
T		Ambient temperature	α_{vb}	1/C	Bias voltage thermal sensitivity
k	N m	Compliant structure stiffness	$F_B(s)$		Bias voltage filter Laplace transform
ζ	--	Compliant structure damping ratio	σ_{vai}	V	Amplifier input voltage noise
ω_n	Rad/s	Compliant structure natural frequency	σ_{vao}	V	Amplifier output voltage noise

f	Hz	Frequency	Δ_{vai}	V	Amplifier input voltage offset
A	- , N/m	Mechanical noise scaling factor	Δ_{vao}	V	Amplifier output voltage offset
$F_F(s)$	--	Flexure mechanical filter Laplace transform	α_{vai}	V	Amplifier input offset thermal sensitivity
			α_{vao}	V	Amplifier output offset thermal sensitivity
ε_F	m^{-1}, N^{-1}	Flexure gain	$CMRR(s)$	--	Amplifier common mode rejection ratio Laplace transform
L_f	m	Flexure length			
b_f	m	Flexure width			
h_f	m	Flexure thickness	$PSRR_A(s)$	--	Amplifier power supply rejection ratio Laplace transform
E	Pa	Flexural material Young's Modulus			
N_b	--	Number of flexures in parallel	V_P	V	Power supply voltage
$\alpha_{\varepsilon F}$	1/C	Flexure gain thermal sensitivity	α_{vP}	1/C	Power supply voltage thermal sensitivity
σ_{Tw}	C	Bridge temperature noise	σ_{Tp}	C	Power supply thermal noise
G_{SG}	--	Strain geometry gain	σ_{vP}	V	Power supply voltage noise
$\varepsilon(x,y)$	--	Strain field over flexure	σ_{v_r}	V	Power supply ripple voltage noise
x	m	Distance along length of flexure	RR	--	Power supply ripple rejection ratio
y	m	Distance off neutral axis of flexure	$F_P(s)$	--	Power supply filter Laplace transform
L_r	m	Piezoresistor length	σ_{v_c}	V	ADC voltage noise
h_r	m	Piezoresistor thickness	α_{v_c}	1/C	ADC voltage thermal sensitivity
γ	--	Strain field constant	σ_{T_c}	C	ADC temperature noise
L_0	m	Piezoresistor offset from flexure boundary	Δ_{v_c}	V	ADC voltage offset
N_ε	--	Bridge strain type	$F_D(s)$	--	Digital noise filter Laplace transform
G_F	--	Piezoresistive gauge factor		(m, N)/V	Calibration coefficient
α_{GF}	1/C	Gauge factor thermal sensitivity	A	-	Coordinate transform matrix
N_{Tw}	--	Bridge thermal type	M	--	Axis noise summation vector
α_{Tw}	1/C	Bridge resistors thermal sensitivity	$S_{\psi M}(f)$	m^2/H z,	PSD of signal output from sensor system

N_{Tr}	-	Off-bridge thermal type		N^2/Hz	
α_{Tr}	1/C	Off-bridge resistors thermal sensitivity	f_m	Hz	Measurement frequency
Δ_{Rw}	--	Bridge imbalance	f_s	Hz	Sampling frequency
σ_{Vw}	V	Bridge piezoresistor voltage noise	f_n	Hz	Nyquist frequency
$S_{Vw}(f)$	V^2/Hz	PSD of piezoresistor noise	f_{filter}	Hz	Digital filter bandwidth frequency
R	Ω	Piezoresistor resistance	f_{sig}	Hz	Signal bandwidth frequency
α	--	Hooge constant for piezoresistor	σ_{Acc}	m, N	Sensor system accuracy st. dev.
C_C	1/m ³	Carrier concentration for piezoresistor	σ_{Res}	m, N	Sensor system resolution st. dev.
Ω	m ³	Piezoresistor volume	D	--	Dynamic range of sensor system
G_{STC}	--	Span temperature compensation (STC) gain	ρ	Ωm	Resistivity of piezoresistive material
			B	Hz	Bandwidth of sensor system
α_{STC}	1/C	STC gain thermal sensitivity	S_{Vai}	V^2/H	PSD of amplifier input voltage noise
α_{Rstc}	1/C	STC resistance thermal sensitivity	r	--	Sensor to signal bandwidth ratio
$F_T(s)$	--	Bridge thermal filter	P_{max}	W	Maximum power dissipated at sensor
α_{Vs}	1/	Source voltage thermal sensitivity	V_{max}	V	Maximum sensor source voltage
σ_{Ts}	C	Source voltage chip temperature noise	R_{cross}	Ω	Voltage/power regime boundary resistance
σ_{Vs}	V	Source voltage noise			
$PSRR_S(s)$	--	Source voltage power supply rejection ratio Laplace transform	Ω_{min}	m ³	Minimum piezoresistor volume
			Ω_{max}	m ³	Maximum piezoresistor volume
$F_S(s)$	--	Source voltage filter Laplace transform	N_r	--	Piezoresistor serpentine factor
G	--	Instrumentation amplifier gain	b_r	M	Width of resistor
α_G	/C	Amplifier gain thermal sensitivity	R_{min}	Ω	Minimum piezoresistor resistance
σ_{Ta}		Amplifier chip temperature noise	R_{max}	Ω	Maximum piezoresistor resistance

MASKS FOR MICROFABRICATION

B.1 Mask 1 – Polysilicon Piezoresistor

Mask 1 is used to define the polysilicon piezoresistors in the CNT test structures and the polysilicon based MEMS force sensors. The overall mask is shown in Figure B.1 while a close-up of the alignment features is given in Figure B.2.

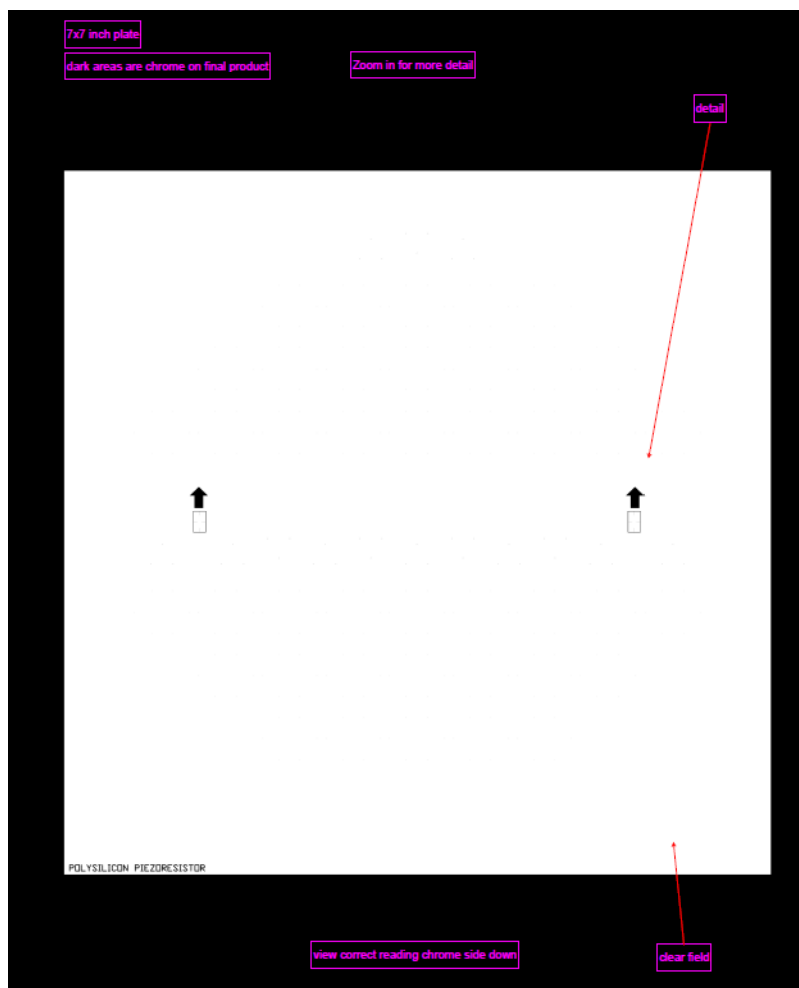


Figure B.1. Mask 1 defining polysilicon piezoresistors.

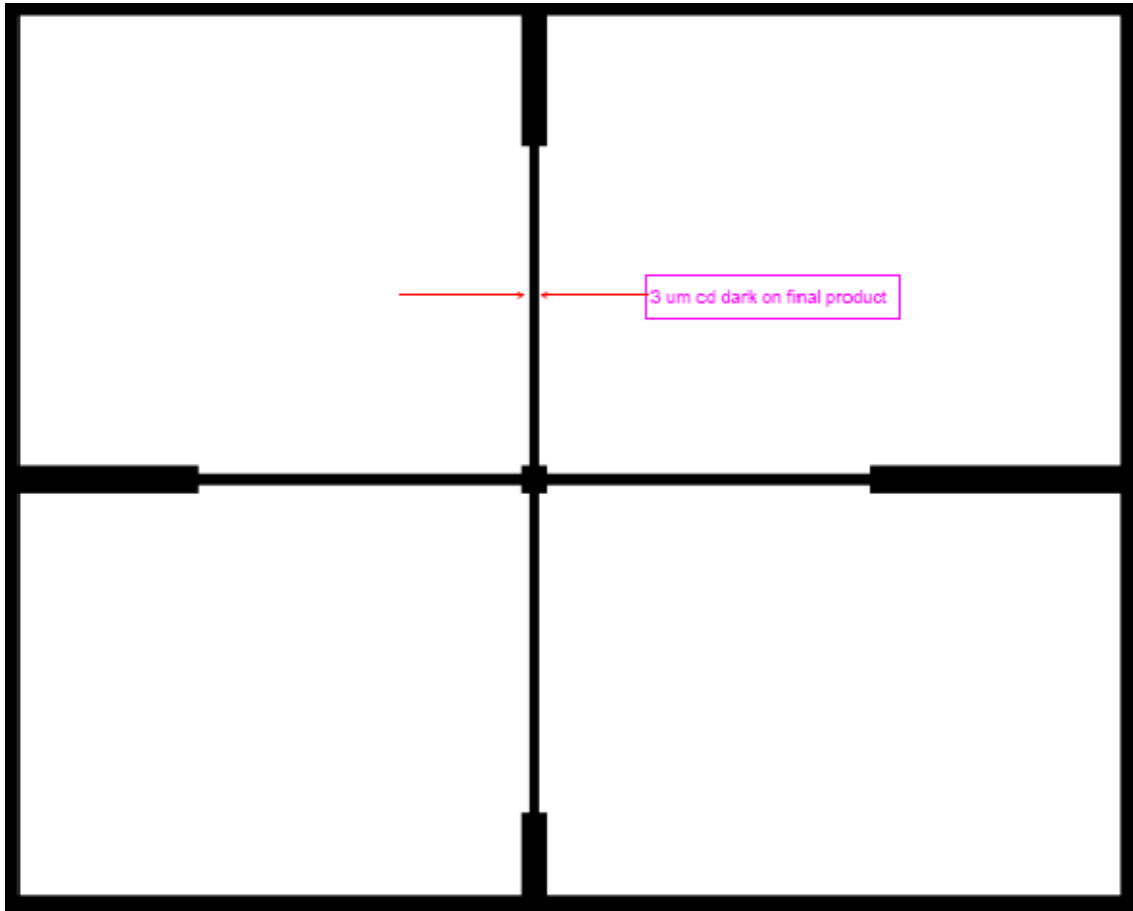


Figure B.2. Blowup of alignment mark in mask 1.

B.2 Mask 2 – Aluminum Bond Pads

Mask 2 is used to define the aluminum bond pads and wires in the CNT test structures and the MEMS force sensors. The overall mask design for the bond pads is given in Figure B.3 while Figure B.4 presents as close up of the electrode pattern for the CNT-based MEMS force sensor.

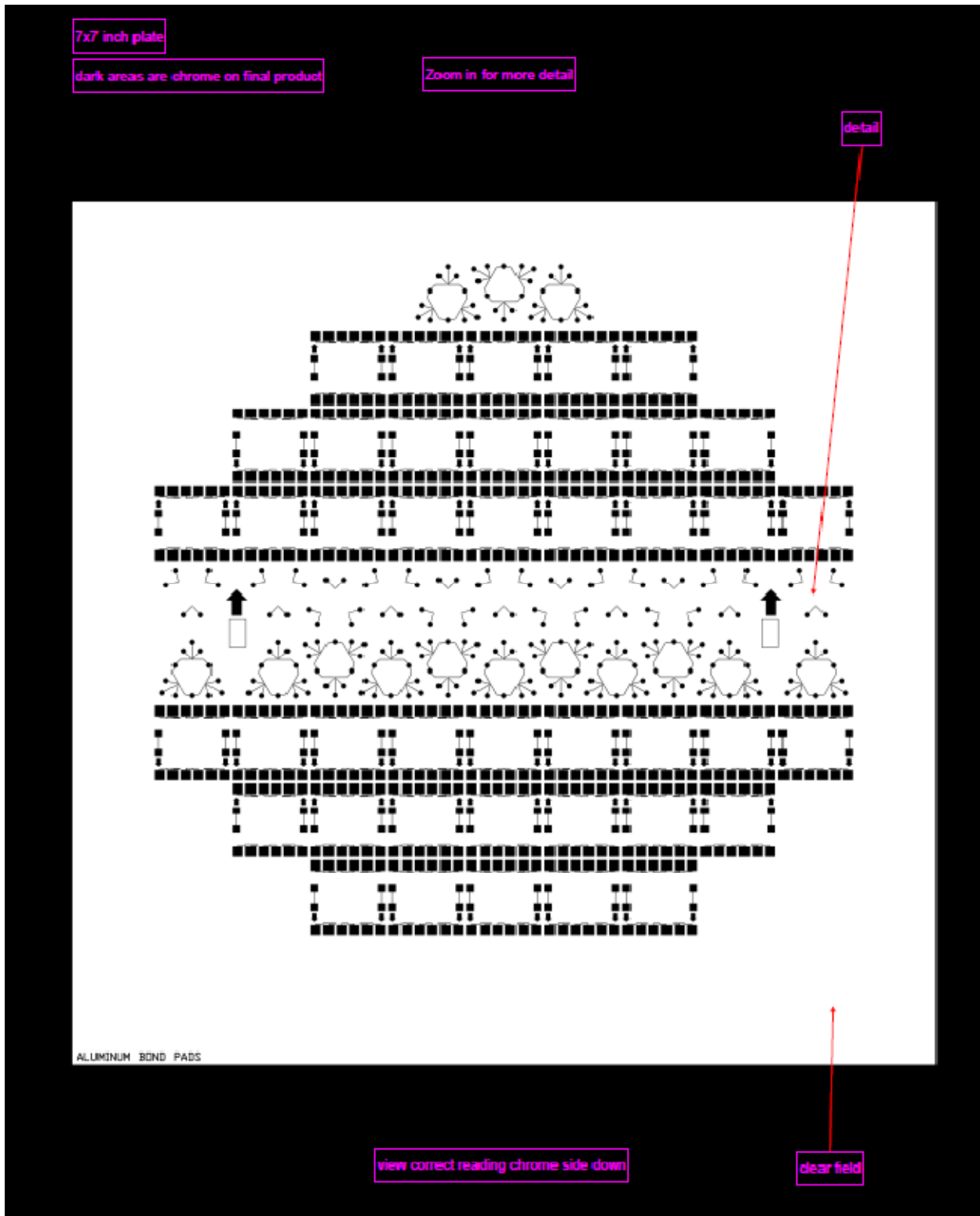


Figure B.3. Mask 2 defining aluminum bond pads and electrodes.

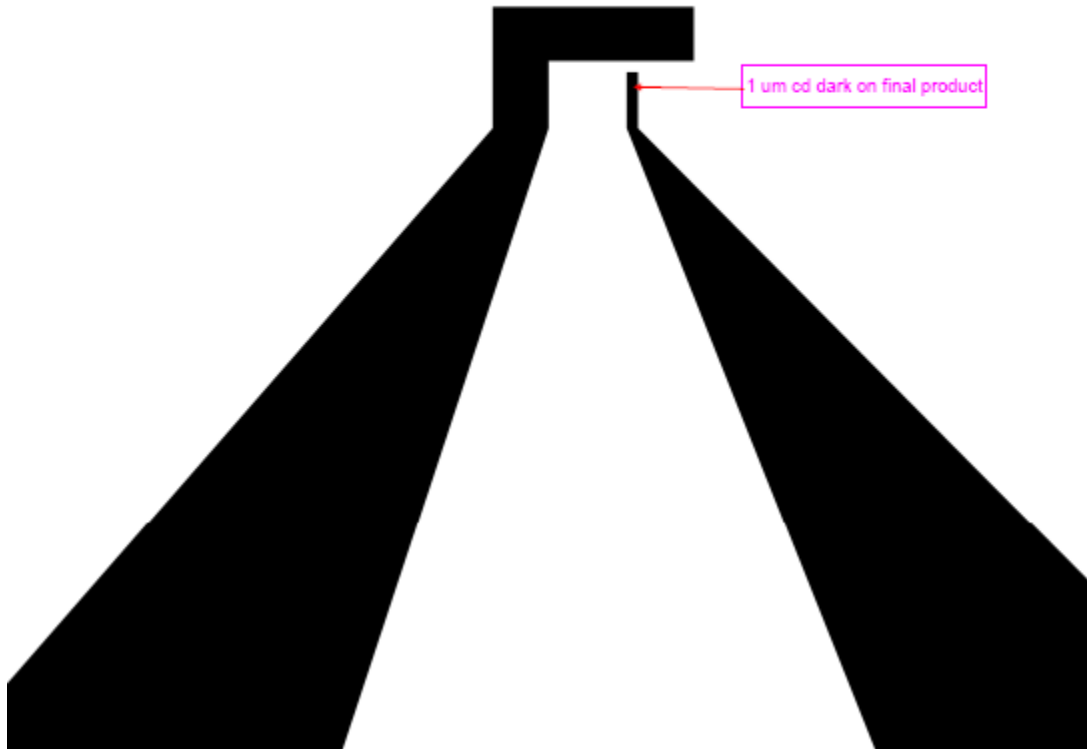


Figure B.4. Electrode pattern for CNT-based force sensor in mask 2.

B.3 Mask 3 – Frontside DRIE

Mask 3 is used to pattern the frontside of the SOI wafer. This mask is used to define the flexure structure in the CNT test structures and the MEMS force sensors. In addition, this mask is used to define the boundaries between the chips. Figure B.5 gives an overview of the pattern in mask 3 while Figure B.6 shows a close up of the frontside alignment marks.

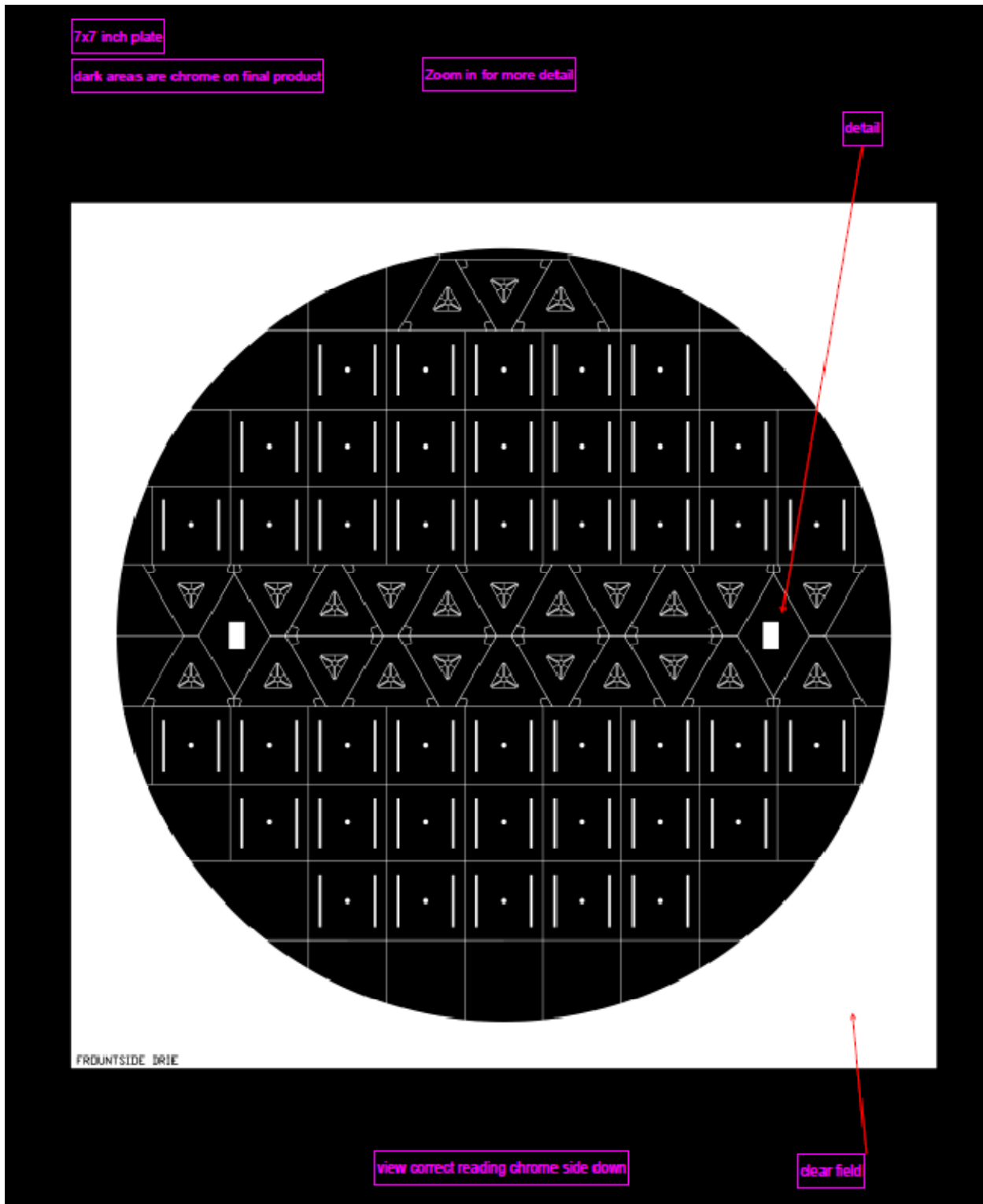


Figure B.5. Mask 3 defining frontside photoresist pattern.

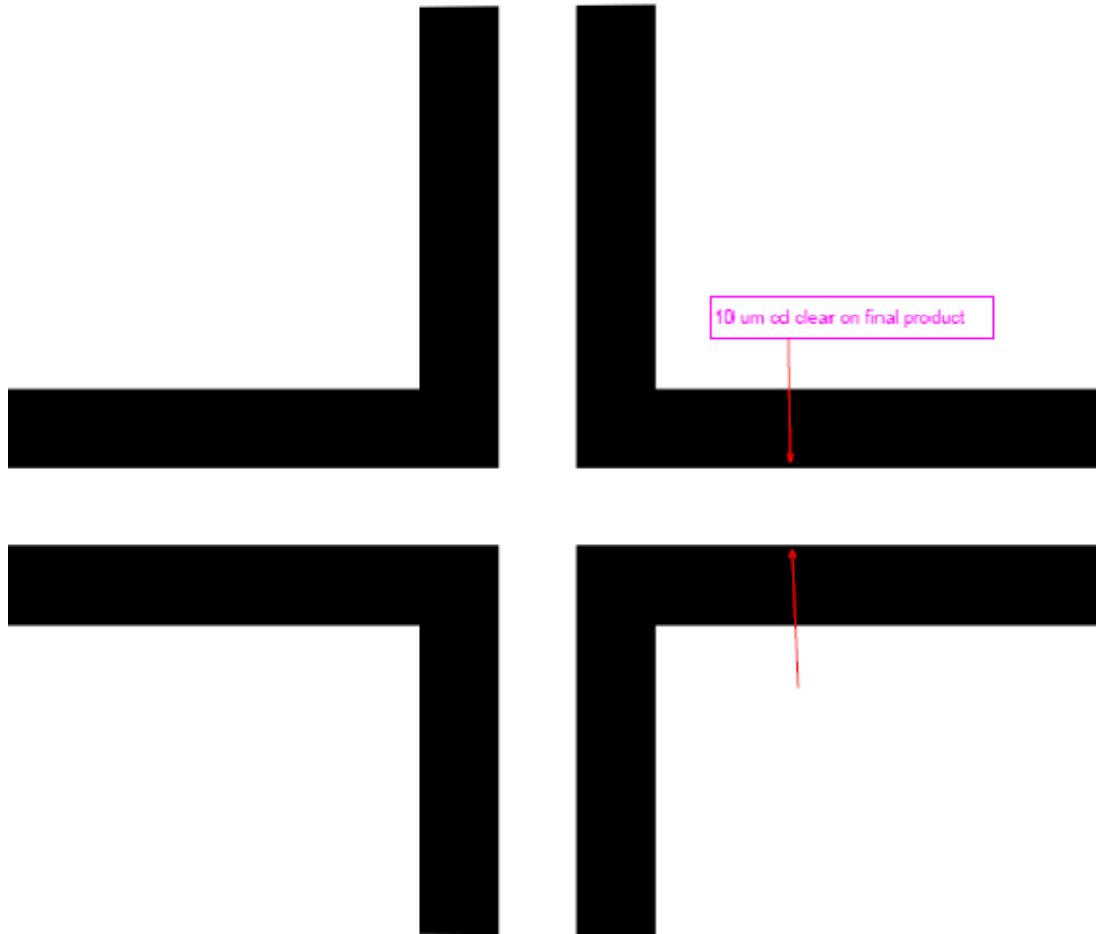


Figure B.6. Frontside alignment mark in mask 3.

B.4 Mask 4 – Backside DRIE

Mask 4 is used to define the pattern on the backside of the SOI wafer. This backside pattern is used to release the flexures in the frontside pattern and to separate the various chips within the wafer. Figure B.7 gives an overview of the pattern in mask 4 while Figure B.8 shows a close up of the backside alignment marks.

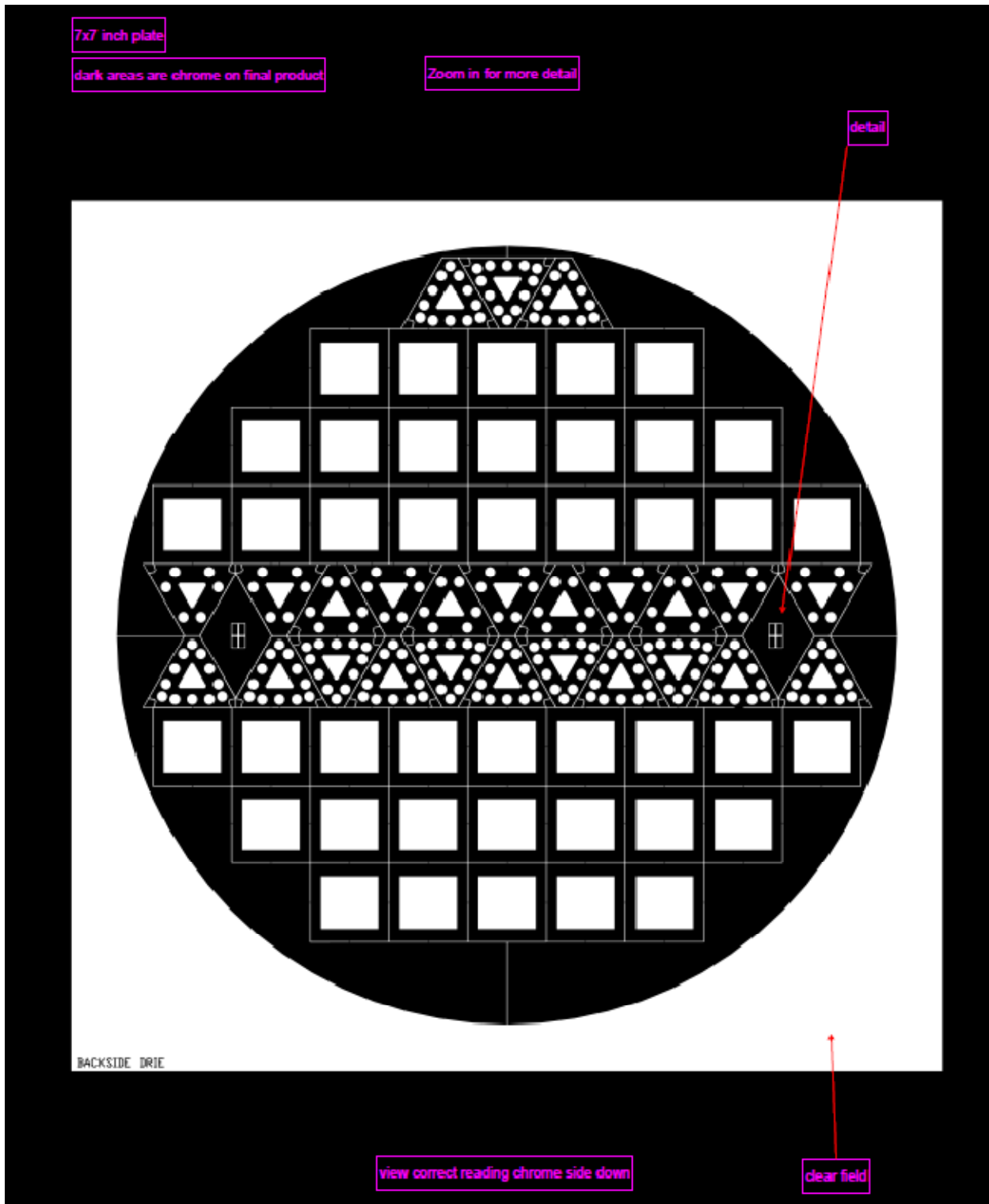


Figure B.7. Mask 4 defining backside photoresist pattern.

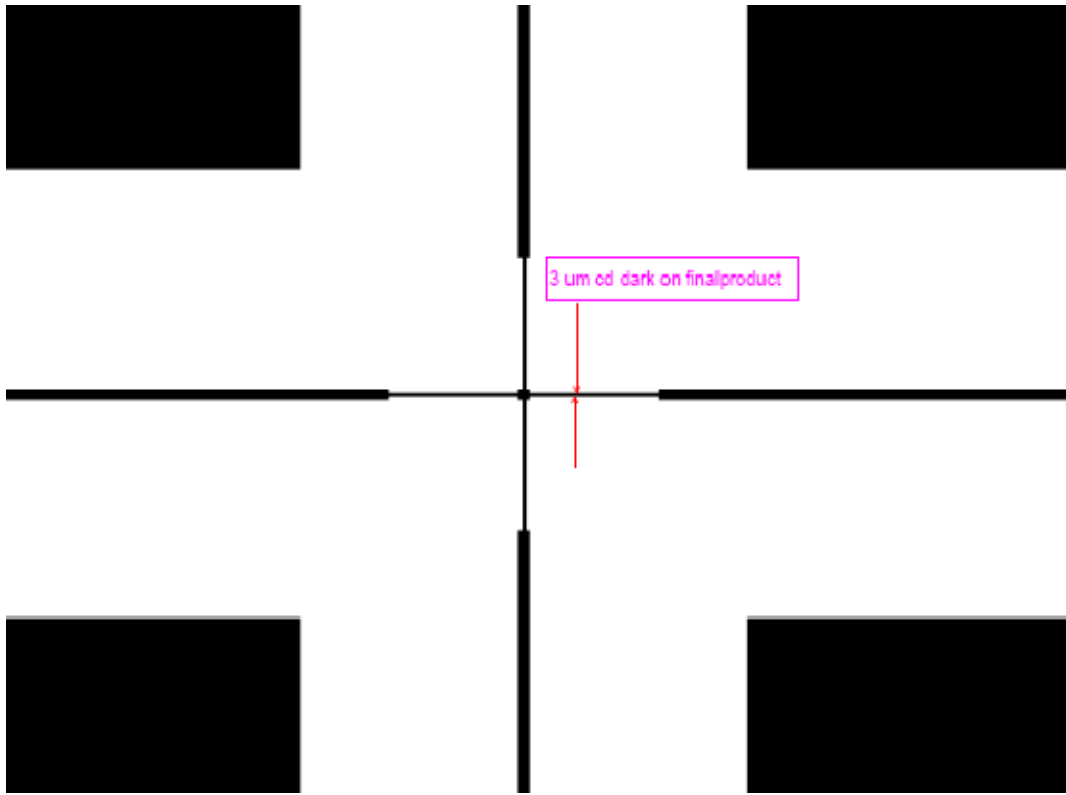


Figure B.8. Backside alignment mark in mask 3.